Geofluids

Flow, Transport, and Reactions in Coastal Aquifers

Lead Guest Editor: Xuan Yu
Guest Editors: Christopher J. Russoniello, Leanne Morgan, Gudrun Massmann, and Guizhi Wang

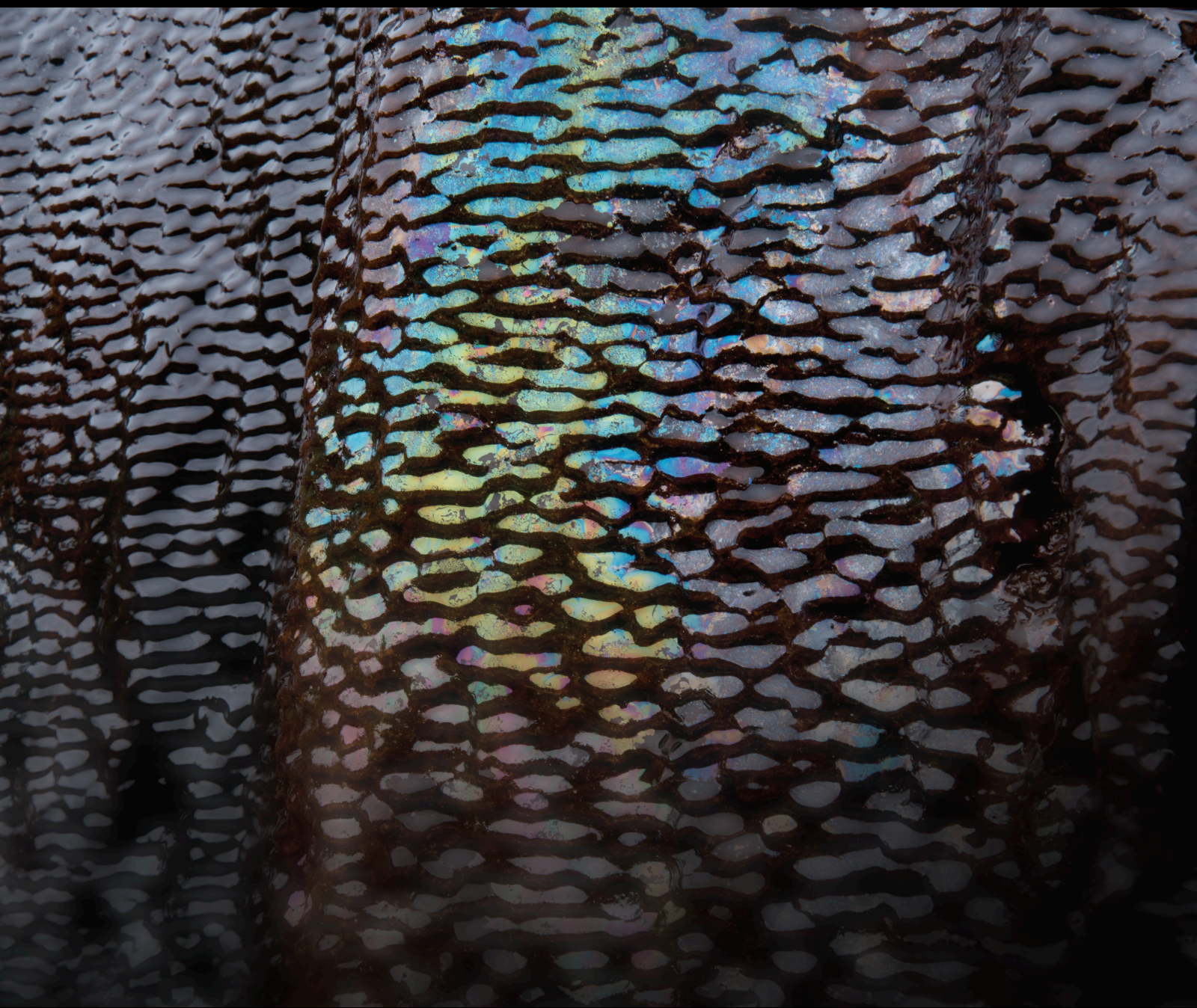

Flow, Transport, and Reactions in Coastal Aquifers

Geofluids

Flow, Transport, and Reactions in Coastal Aquifers

Lead Guest Editor: Xuan Yu
Guest Editors: Christopher J. Russoniello, Leanne Morgan, Gudrun Massmann, and Guizhi Wang

Editorial Board

Contents

Hindawi
Geofluids
Volume 2020, Article ID 3539052, 2 pages
https://doi.org/10.1155/2020/3539052

Editorial

Flow, Transport, and Reactions in Coastal Aquifers

Xuan Yu,[1,2,3] **Christopher J. Russoniello**,[4] **Leanne K. Morgan**,[5] **Gudrun Massmann**,[6] **and Guizhi Wang**[7]

[1]*School of Civil Engineering, Sun Yat-Sen University, Guangzhou, China*
[2]*Center for Water Resources and Environment, Sun Yat-Sen University, Guangzhou, China*
[3]*Southern Marine Science and Engineering Guangdong Laboratory (Zhuhai), Zhuhai 519082, China*
[4]*Department of Geology and Geography, West Virginia University, Morgantown, WV 26506, USA*
[5]*School of Earth and Environment, University of Canterbury, Christchurch, Private Bag 4800, Christchurch 8140, New Zealand*
[6]*Carl von Ossietzky University Oldenburg, Germany*
[7]*State Key Laboratory of Marine Environmental Science, Xiamen University, Xiang An District, Xiamen 361005, China*

Correspondence should be addressed to Xuan Yu; yuxuan7@mail.sysu.edu.cn

Received 27 January 2020; Accepted 28 January 2020; Published 4 February 2020

1. Motivations and Background

Coastal aquifers are a critically important water resource, which supports coastal populations and economies globally. Flow, transport, and geochemical reactions in coastal aquifers are hot interests of hydrologists and marine geochemists as well as policy makers in charge of environmental management and sustainable development. In this special issue, we cover recent scientific advances in seawater intrusion and submarine groundwater discharge (the flux of geofluids from coastal aquifers to the ocean), as well as field and laboratory methods and techniques that can be used to monitor and better understand the processes occurring in coastal aquifers.

2. Contents of the Special Issue

The purpose of this special issue is to present the most recent studies in these exciting fields. A brief summary of all accepted papers is provided below.

Yan et al. illustrate structured heterogeneity in porous media for a modified setting of the Elder problem. The effects of the permeability and the location (horizontal and vertical) of the low-/high-permeability inclusion on the free convection process are assessed using three assessment indicators: total solute mass (TM), Sherwood number (Sh), and solute center of gravity (COG). The result shows that heterogeneity in permeability makes the system more unstable. A high-permeability inclusion shows stronger effects on the free convectional process than a low-permeability inclusion at the early stage, with significantly unbalanced solute distributions and accelerated transport processes. Free convection is more sensitive to the low-/high-permeability inclusion vertically closer to the source zone.

Guo et al. investigate the effects of a fluctuating sea level and inland recharge on pumping-induced groundwater salinization in coastal multilayered aquifers. Through laboratory experiments and numerical simulations, they conclude that pumping could significantly enhance the amplitude of the groundwater level fluctuation. An increment of the pumping rate causes faster drawdown of the groundwater level in the aquifer. Inland recharge plays a major role in the seawater intrusion for the same pumping rate of groundwater in different seasons. Increasing or decreasing the hydraulic conductivities of the two layers is not able to reproduce the variation of the seawater wedge. Changing the dispersivity has no effect on the arrival time of the steady state saltwater wedge.

Levanon et al. investigate how a variable tidal boundary affects salinity, pressure, and saturation in a coastal aquifer. Tank experiments show that tidal variation affects not only hydraulic heads but also salinity across the freshwater-saltwater interface and saturation within the capillary fringe.

The speed of response varies—hydraulic heads respond quickly to the pressure signal—while both saturation and salinity responses lag tidal fluctuations. Numerical FEFLOW simulations that match the tank experiments allowed further investigation of the lagged response. Lag in the salinity response at the freshwater-saltwater interface increases with depth and lag of capillary fringe saturation response increases drastically toward the top of the capillary fringe.

Song et al. have developed an analytic solution relating to an offshore submarine aquifer. Specifically, they consider tidal groundwater head fluctuations in a submarine leaky confined aquifer overlain by a semipermeable seabed. Both the seabed and the confined aquifer are assumed to extend horizontally infinitely. A one-dimensional mathematical model is established to describe the problem, and the analytical solution is derived. The impacts of the tidal loading efficiency, hydraulic conductivity, and elastic storage of the semipermeable layer and aquifer on the groundwater head fluctuations in the aquifer system are analyzed and discussed. Solution analyses indicated that tidal loading effects tend to enhance the amplitude of the tidal groundwater fluctuation in the confined aquifer system and to reduce the phase shift between the groundwater head and the sea tide fluctuations.

Stoeckl et al. explore postpumping seawater intrusion (PP-SWI), which is the phenomenon of seawater intruding further inland than the location of a well, after pumping has ceased. The paper describes a laboratory-scale investigation of the phenomenon and demonstrates that PP-SWI can be reproduced within physical experiments. They also use numerical modelling to show that PP-SWI is caused by disequilibrium in the flow field following the cessation of pumping. Specifically, the cone of depression persisted after the cessation of pumping (first moving inland and then retreating toward the coastal boundary) which caused a lag in the reestablishment of fresh water flow toward the coast, after pumping had stopped. It was during this period of flow-field disequilibrium that PP-SWI occurred. They predict that systems with larger postextraction disequilibrium will be most susceptible to PP-SWI and recommended future research to improve understanding of the relationship between hydrogeological parameters, extraction rates, well location, and incidence of PP-SWI.

Holt et al. report on the evolution of a freshwater lens below a very young barrier island in the North Sea in Germany that only formed in the past decades. Combining field observations with transient numerical 2-D density-dependent modelling, they assess the impact of both geomorphological changes and storm tides on freshwater lens formation. Results show that the asymmetric freshwater lens is restricted to the elevated dune areas and has nearly reached quasisteady-state conditions. Further growth of the freshwater lens is largely inhibited by annual storm tides that, in the absence of coastal protection measures, regularly flood large parts of the island in winter. The authors conclude that direct implementation of storm floods into numerical models is necessary to explain the groundwater salinity distribution under such highly dynamic conditions.

Post et al. investigate the fate of the hydrological tracers ^{3}H and ^{3}He in freshwater lens, transition zone, and saltwater wedge below a barrier island in the North Sea, using numerical variable-density flow and transport models of different complexities. They conclude that bomb-related tritiogenic ^{3}He is a useful tracer to date young (<60 years) groundwater, as it is still mostly present in the freshwater lens, and shows that apparent ages may be biased up to 10 years due to differences in dispersive transport of ^{3}H and ^{3}He. They also illustrate the potential of ^{3}H from seawater as a tracer to study saltwater circulation patterns when it travels into the offshore part of the aquifer. They further explore the effect of mixing between freshwater and saltwater in the transition zone, highlighting remaining knowledge gaps and the need for more research to better understand its controlling factors (i.e., tides, lithological heterogeneity, or transience of recharge and pumping).

The study of Ngueleu et al. focuses on the biodegradation kinetics of benzene and naphthalene in a (semi)-arid saline coastal soil environment subject to saline conditions and continuous water level fluctuations. To quantify sorption and biodegradation, batch experiments considering different environmental conditions were conducted with samples collected at a beach in Qatar. The results show that removal of naphthalene is mainly due to sorption while benzene is mostly removed by biodegradation, whereby biodegradation of the two compounds is attributed to nitrate- and sulfate-reducing bacteria. Although during the experiments, the two petroleum hydrocarbons were considerably removed from the aqueous phase due to sorption and biodegradation processes, the latter is very slow with bulk rate coefficients in the order of 10^{-3} to 10^{-2} day^{-1} as quantified with kinetic models that match the experimental results well.

Conflicts of Interest

The authors declare that they have no conflict of interest.

Acknowledgments

We would like to express our gratitude to all authors who made this special issue possible. We hope this collection of articles will be useful to the coastal community.

Xuan Yu
Christopher J. Russoniello
Leanne K. Morgan
Gudrun Massmann
Guizhi Wang

Hindawi
Geofluids
Volume 2019, Article ID 8124716, 15 pages
https://doi.org/10.1155/2019/8124716

Research Article

Biodegradation Kinetics of Benzene and Naphthalene in the Vadose and Saturated Zones of a (Semi)-arid Saline Coastal Soil Environment

Stephane K. Ngueleu,[1,2] Riyadh I. Al-Raoush ,[1] Saeid Shafieiyoun,[1] Fereidoun Rezanezhad,[2] and Philippe Van Cappellen[2]

[1]*Department of Civil and Architectural Engineering, College of Engineering, Qatar University, P.O. Box, 2713 Doha, Qatar*
[2]*Ecohydrology Research Group and Water Institute, Department of Earth and Environmental Sciences, University of Waterloo, 200 University Avenue West, Waterloo, Ontario, Canada N2L 3G1*

Correspondence should be addressed to Riyadh I. Al-Raoush; riyadh@qu.edu.qa

Received 30 April 2019; Revised 18 October 2019; Accepted 4 December 2019; Published 23 December 2019

Guest Editor: Gudrun Massmann

Biodegradation is a key process for the remediation of sites contaminated by petroleum hydrocarbons (PHCs), but this process is not well known for the (semi)-arid coastal environments where saline conditions and continuous water level fluctuations are common. This study differs from the limited previous studies on the biodegradation of PHCs in Qatari coastal soils mainly by its findings on the biodegradation kinetics of the selected PHCs of benzene and naphthalene by indigenous bacteria. Soil samples were collected above, across, and below the groundwater table at the eastern coast of Qatar within a depth of 0 to -40 cm. Environmental conditions combining low oxygen and high sulfate concentrations were considered in this study which could favor either or both aerobic and anaerobic bacteria including sulfate-reducing bacteria (SRB). The consideration of SRB was motivated by previously reported high sulfate concentrations in Qatari soil and groundwater. Low- and high-salinity conditions were applied in the experiments, and the results showed the sorption of the two PHCs on the soil samples. Sorption was dominant for naphthalene whereas the biodegradation process contributed the most for the removal of benzene from water. Losses of nitrate observed in the biodegradation experiments were attributed to the activity of nitrate-reducing bacteria (NRB). The results suggested that aerobic, NRB, and most likely SRB biodegraded the two PHCs, where the combined contribution of sorption and biodegradation in biotic microcosms led to considerable concentration losses of the two PHCs in the aqueous phase (31 to 58% after 21 to 35 days). Although benzene was degraded faster than naphthalene, the biodegradation of these two PHCs was in general very slow with rate coefficients in the order of 10^{-3} to 10^{-2} day^{-1} and the applied kinetic models fitted the experimental results very well. It is relevant to mention that these rate coefficients are the contribution from all the microbial groups in the soil and not from just one.

1. Introduction

The process of biodegradation has been given considerable interest globally for the purpose of cleaning up the sites contaminated by petroleum hydrocarbons (PHCs) [1–6]. Attention has also been given to natural source zone depletion (NSZD) especially for contaminated sites at their later phases of remediation [7], in which, naturally occurring processes of dissolution, volatilization, and biodegradation result in mass losses of PHC constituents from the subsurface. In addition, bioremediation is a common and cost-effective technique for the treatment of media contaminated by PHCs [8]. A mechanistic understanding of the coupled geochemical and biological processes controlling PHC degradation and metabolisms of the microorganisms is the key for the success of bioremediation. Furthermore, in subsurface environments contaminated by PHCs, the geochemical conditions near the groundwater table, in particular the

availability of oxygen and other oxidative agents, moisture content, salinity, pH, redox potential, nutrient concentrations, and temperature, are key determinants of the biodegradation of PHCs [1, 9–14] and groundwater quality changes. Some studies have shown that tide-induced seawater circulations can cause frequent groundwater table fluctuations in coastal aquifers which in turn can enhance the biodegradation of PHCs after an oil spill (*e.g.,* [15–18]). This enhancement can occur as a result of the redistribution or diffusion of electron acceptors (*e.g.*, oxygen) and donors (*e.g.*, nonaqueous phase liquids or LNAPLs) across the groundwater table during water table rise and fall, thus helping local bacteria for their metabolisms. The variability of biodegradation with depth in PHC-contaminated coastal sediments was in general linked to the presence and distribution of electron acceptors in the subsurface, with oxygen dominating near the surface while for example nitrate, manganese, iron, and sulfate could become dominant with depth [19]. Some studies have also investigated the potential of microbial communities to biodegrade PHCs in coastal environments after their exposure to these contaminants by oil spills. Kostka et al. [20] characterized the microbial community involved in the biodegradation of PHCs (C_8 to C_{40}) in Gulf of Mexico beach sands which were exposed to heavy oil contamination from the well-known Deepwater Horizon oil spill in 2010. They identified up to 24 bacterial strains capable of degrading these PHCs. The biodegradation of naphthalene in seawater-impacted coastal sediments was studied by Jin et al. [21] with enriched cultures established using seawater and modified minimal media containing naphthalene. Their results showed that naphthalene and other polycyclic aromatic hydrocarbons (PAHs) such as phenanthrene and anthracene could be degraded in the sediments over time.

Biodegradation studies generally focus on determining the microbial species involved in the mineralization of various compounds and also on the quantification of this process by kinetic or equilibrium parameters. While these two types of studies have been conducted considerably for saline and nonsaline environments in mostly nonarid regions of the world, there is still limited information available on quantitative kinetic parameters of the biodegradation of PHCs in (semi)-arid saline coastal environments such as in Qatar. This study therefore considers the saline coastal environment of Qatar as an example of a (semi)-arid region to generate more information on such quantitative kinetic parameters. Situated in the Arabian Peninsula, Qatar has a (semi)-arid climate with an average annual evaporation rate of 30 times greater than a negligible amount of precipitation [22, 23]. Its main source of economy is from the energy sector as the country possesses large oil and natural gas reservoirs and thus, production of PHCs is very large. The North Gas Field and Al-Shaheen Oil Field are the two largest oil and natural gas fields of Qatar and they are located offshore and northeast of the country. The energy sector is also represented in the northeast coastal city of Ras Laffan by PHC facilities such as the Oryx and Pearl gas-to-liquid plants [24]. Based on the above characteristics, the northeastern and eastern coasts of Qatar can be classified as areas with high risk to environmental contamination by PHCs. Moreover, due to the strong dynamics and interaction of seawater and groundwater at the coast, PHC contaminants could migrate from the sea to aquifers and vice versa. Sediment contamination was shown by Soliman et al. [25] who measured concentrations of total PAHs between 2.6 and 1025 $ng\,g^{-1}$ in sediments from the eastern coast of Qatar and offshore between oil and gas fields. Offshore and mainly harbor locations generally had higher concentrations of PAHs compared to other coastal locations. The analysis of concentration ratios between pairs of PAHs suggested that PHC was the main source of contamination at most of the locations while it was pyrolysis of fossil fuels (*e.g.*, for residential heating [26]) at some inshore locations.

Despite the limited amount of previous studies on PHC contaminants in Qatari soil and groundwater environments, volatilization, dissolution, sorption, and biodegradation are among the key processes which can control the fate of PHC in subsurface coastal soil environments. Based on a crude oil report of Al-Shaheen Oil Field showing an American Petroleum Institute (API) gravity > 10 (*i.e.,* lighter than water) [27], PHCs in Qatar could behave like LNAPLs. They can then float on the shallow groundwater table and undergo both volatilization to the vadose zone and, due to groundwater table fluctuations, dissolution into groundwater. Ngueleu et al. [28], using batch experiments, showed that the benzene and naphthalene sorbed on a coastal soil from the eastern coast of Qatar at different magnitudes and sorption increased in general when the temperature decreased and the salinity increased. Studies on biodegradation of PHCs in Qatari soils are very limited. The existing few studies include the work of Al Disi et al. [29] who studied the effects of oil weathering due to long exposure to harsh weather conditions on the diversity, adaptation, and activity of hydrocarbon-degrading bacteria using contaminated soils from autoworkshops and industry waste management sites. In their study, with a purpose to help bioaugmentation strategies, the bacteria were isolated by growing them in the laboratory on the collected soils and using culture media with specific composition. Another study by Al-Thani et al. [30] was on a laboratory extraction of PAH-degrading bacteria from Qatari soils collected at an industrial zone. They used an enrichment medium with a specific composition and either naphthalene, phenanthrene, or anthracene as the sole source of carbon and energy. The increase of optical densities of the isolates showed that they were able to grow on the tested PAHs, and their results showed the potential of using soil bacteria for the bioremediation of sites contaminated by PAHs. The above studies are great contributions for the bioremediation of sites contaminated by PHCs in Qatar and other (semi)-arid regions, but information in this field is still limited especially for the coastal area where a particularly saline environment with continuous water table dynamics exists. An important information still missing is the quantitative evaluation of PHC losses and associated rate coefficients due to biodegradation at the Qatari coastal soil and groundwater environments, and this is the main focus of our study.

We hypothesized that high sulfate concentrations in Qatari coastal soil and groundwater [22, 28] indicate the

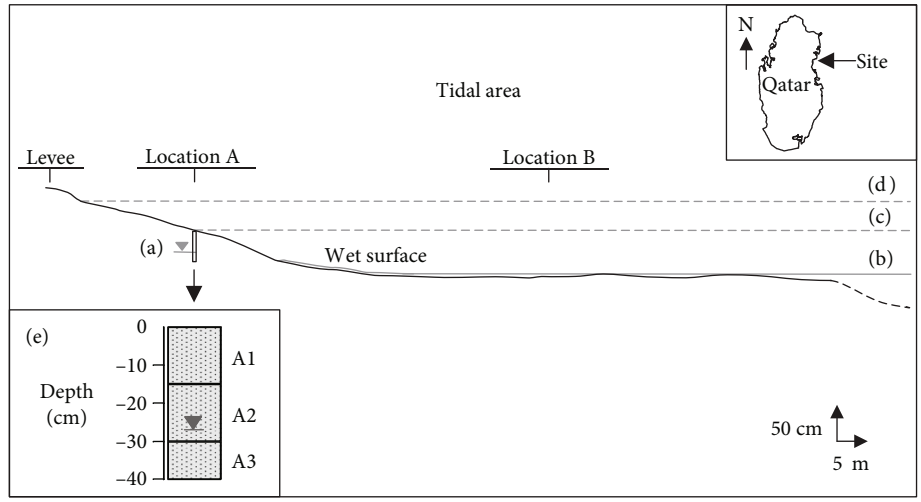

Figure 1: Schematic cross-sectional view of the sampling site between locations A and B. Elements with brackets indicate the following at the time of sampling: (a) the groundwater table, (b) the seawater level at low tide, (c) the normal high tide, and (d) the storm high tide. (e) The soil profile at location A with depths of the soil samples A1, A2, and A3.

potential presence of sulfate-reducing bacteria (SRB). Therefore, aerobic and anaerobic bacteria could coexist in the vadose and shallow groundwater zones with low oxygen concentration. The main objectives of this study were (1) to quantify the biodegradation kinetics of two PHCs in a (semi)-arid saline coastal soil, which was influenced by groundwater table fluctuations and seawater intrusion, by indigenous bacteria at a low oxygen concentration; (2) to investigate the potential difference in biodegradation behavior with depth by considering the vadose and saturated zones of shallow coastal soil environment of Qatar, and the effect of salinity on biodegradation due to seawater intrusion, and (3) to propose a model which takes into account the biodegradation kinetics of the PHCs used in this study to predict the fate of PHCs in (semi)-arid saline coastal soil environments.

2. Materials and Methods

2.1. Field Site and Sampling. The coastal soil, seawater, and groundwater samples were collected from the Sumaysimah beach located on the eastern coast of Qatar. In this site, vertical fluctuations of water levels at the shoreline occur in both the sea and the coastal aquifer due to their continuous interaction. An oil spill at the site could then result in the formation of a smear zone of light PHCs (*i.e.*, LNAPLs) in the shallow subsurface. It was then planned to collect soil samples at different shallow depths including the vadose and saturated aquifer zones (see below). Prior to sampling, the Sumaysimah beach site was investigated for relevant site features and a cross-sectional view of the beach site from the south is shown in Figure 1. This view shows the tidal area between a human-made levee and the sea, and it is along two locations denoted as location A (N25°34′20.9″; E51°29′20.3″) and location B (N25°34′21.8″; E51°29′21.7″), which were situated on sloping and flat areas, respectively. The soil at location A was sandy and contained some small seashells, whereas the soil at location B was silty and clayey at the surface but mostly sandy with some small seashells after a depth of a few centimeters. Visible organic matter was negligible. Seawater was visible at about 100 m from location A and was at low tide (Figure 1(b)) because a clear line made of leaves released by the sea and passing through location A was visible along the shoreline, indicating that the normal high tide was at location A (Figure 1(c)). It was also interpreted that the storm high tide was at or near the foot of the levee (Figure 1(d)). Soil and groundwater samples used in this study were collected at location A in order to have samples within the observed vertical fluctuation zone of seawater (Figures 1(b) and 1(d)) whose amplitude was similar to the amplitude of historical seawater levels of about 1 to 2 m [31].

Soil samples were aseptically collected with a clean shovel at location A at different depths, and they were labeled from the ground surface as A1 (0 to -15 cm), A2 (-15 to -30 cm), and A3 (-30 to -40 cm) (Figure 1(e)). Groundwater was encountered at a depth of about -27 cm below the A2 layer. A2 and A3 were collected saturated with groundwater to preserve their microbial communities and stored saturated. The soil samples were collected disturbed in doubled black plastic bags placed in sturdy boxes which were afterwards tightly closed. Soil sampling and packaging were performed quickly to minimize the potential effect of oxygen on potential anaerobic bacteria including SRB. 0.5 L of groundwater at location A was collected in an amber glass bottle, and 50 L of seawater was collected in a plastic container. The pH and the electrical conductivity (EC) were measured for groundwater on site using a portable pH meter (Horiba LAQUAtwin B-713) and a conductivity meter (Hach sensION 5). The groundwater table rose after sampling and a height difference of 4 cm was measured between a defined time interval dt of 55 minutes. As the hole made during sampling had a circular cross section (radius of ~20 cm) and a cylindrical shape, it was then possible to estimate upward groundwater flow parameters such as the flow rate (volume of water which filled up the hole during dt divided by dt) and the Darcy velocity (flow rate divided by the cross-sectional area of the hole) [32]. This estimation assumes that the dominant flow

component is vertical in case any potential horizontal flow component may have also contributed.

Groundwater and seawater samples were later analyzed for ion compositions by a Metrohm 850 professional ion chromatography (IC) instrument with two columns for anion (Metrosep A Supp 5-150/4.0, flow rate: 0.7 mL min^{-1}, pressure: 10.30 MPa, and temperature: 24.2°C) and cation (Metrosep C 4-150/4.0, flow rate: 0.9 mL min^{-1}, pressure: 8.33 MPa, and temperature: 24.2°C) analyses. About 55 to 65 g of fresh soils A1, A2, and A3 was previously put in the oven and dried at 105°C for 48 hours in order to determine their water content gravimetrically. The soil and seawater samples were stored in the lab at a room temperature of 22°C until their use in batch experiments. Measures were taken to minimize the exposure of potential anaerobic bacteria to oxygen by purging the bags containing the soils with argon gas from time to time and the experiments started 14 days after soil sampling.

2.2. Petroleum Hydrocarbons and Analysis. The PHCs of interest in this study were benzene (C_6H_6) and naphthalene ($C_{10}H_8$) because they are among the common aromatic products of oil companies in Qatar and can then become source of hydrocarbon contaminants in the soil and groundwater environments [28]. Liquid benzene (99.9+%, Sigma-Aldrich, #270709) and naphthalene in crystal form (99+%, Sigma-Aldrich, #184500) at high purity grade were used in the batch biodegradation experiments. Based on the data shown in Table 1, benzene is lighter (molecular weight), less hydrophobic (K_{ow}) and has a lower affinity to organic carbon (K_{oc}) than naphthalene; however, benzene is more soluble than naphthalene [28].

A solution of the organic solvent dichloromethane (CH_2Cl_2) containing the internal standard metafluorotoluene (C_7H_7F) was used for the microextraction of benzene and naphthalene from aqueous samples, and extracted samples were analyzed by gas chromatography (GC). The instrument was an Agilent 7890A GC Series equipped with a GC Sampler 80 and flame ionization detector (minimum detection limit: 0.005 mg L^{-1}, DB5 capillary column: 0.25 mm × 30 m with a film thickness of 0.25 μm, injection port temperature: 275°C, initial column temperature: 35°C, heating rate: 15°C min^{-1}, final temperature: 300°C, and detector temperature: 325°C).

2.3. Batch Biodegradation Experiments. Ngueleu et al. [28] studied the sorption of benzene and naphthalene on a saline coastal soil from the Sumaysimah beach site, where the soil was similar to the soil used in this study whose properties are assumed to also be similar. Their leaching experiment conducted with samples of the coastal soil did not show any sign of contamination by benzene and naphthalene [28]. In the current study, the focus was on the biodegradation of benzene and naphthalene, even if sorption and biodegradation processes had to be run simultaneously and then separated during the analysis. Since the soil samples were collected at different depths and the seawater sample was available, it was possible to consider different environmental conditions for simultaneous sorption and biodegradation

Table 1: Properties of benzene and naphthalene used in this study. K_{ow} and K_{oc} are the octanol-water partitioning coefficient and organic carbon-water partitioning coefficient from Mabey et al. [33], respectively.

Compound	Molecular weight (g Mol^{-1})	K_{ow} (-)	K_{oc} (-)
Benzene	78.11	135	65
Naphthalene	128.17	1950	940

experiments, namely, (i) three biodegradation zones which were defined as above the groundwater table when using the soil A1, slightly across the groundwater table when using the soil A2, and below the groundwater table when using the soil A3 and (ii) the salinity levels of the soil which were natural when using Millipore water, denoted hereafter as low salinity, and a salinity level much higher than natural when using seawater, denoted hereafter as high salinity. The low and high salinities corresponded to EC values measured in saturated soil microcosms averaging 3.1 ± 0.3 and 60.0 ± 0.9 mS cm^{-1}, respectively. Four batch experiments at a constant temperature of 22°C were conducted by combining the above conditions as follows: soil A1 at low salinity, soil A2 at low salinity, soil A3 at low salinity, and soil A3 at high salinity. The latter experiment could help to understand the effect of seawater intrusion on the processes investigated because the EC of groundwater was smaller than that of seawater at the time of sampling (Section 3.1). This study primarily considers that sulfate [28] and oxygen are the main electron acceptors available in the coastal shallow subsurface at the site. It was later found in the results of the investigation that nitrate is also another electron acceptor available in the soil but at low concentrations (see Section 3.2). Therefore, the relevant biodegradation pathways in this study were ultimately three of those described by Acosta-González and Marqués [19] for tidal zones and driven by aerobic bacteria (Equations (1) and (2)), SRB (Equations (3) and (4)), and nitrate-reducing bacteria (NRB) (Equations (5) and (6)):

$$C_6H_6 + 7.5O_2 + 3H_2O \longrightarrow 6HCO_3^- + 6H^+ \quad (1)$$

$$C_{10}H_8 + 12O_2 + 6H_2O \longrightarrow 10HCO_3^- + 10H^+ \quad (2)$$

$$C_6H_6 + 3.75SO_4^{2-} + 3H_2O \longrightarrow 6HCO_3^- + 3.75HS^- + 2.25H^+ \quad (3)$$

$$C_{10}H_8 + 6SO_4^{2-} + 6H_2O \longrightarrow 10HCO_3^- + 6HS^- + 4H^+ \quad (4)$$

$$C_6H_6 + 15NO_3^- + 3H_2O \longrightarrow 6HCO_3^- + 15NO_2^- + 6H^+ \quad (5)$$

$$C_{10}H_8 + 24NO_3^- + 6H_2O \longrightarrow 10HCO_3^- + 24NO_2^- + 10H^+ \quad (6)$$

where the presence of oxygen could however inhibit the activity of anaerobic bacteria [34].

The methodology applied for the batch biodegradation experiments through a simultaneous sorption and biodegradation approach was similar to that of the batch sorption experiments reported in Ngueleu et al. [28] with some

modifications. The soils were not homogenized prior to sample preparation to limit the exposure of potential anaerobic bacteria to oxygen. Aseptic technique was employed throughout the experiments. For each batch biodegradation experiment at the low or high salinity, two separate 2.6 or 3.9 L solutions of benzene and naphthalene were prepared in amber bottles by first purging Millipore water or seawater with argon gas until the dissolved oxygen (O_2) was about 0.058 mmol L^{-1}. This treatment allowed to have a background solution with a low oxygen concentration to represent groundwater into which oxygen would have slowly diffused from the vadose zone due to water table fluctuations. Teflon-coated magnetic stir bars and 10 mmol L^{-1} of sulfate as electron acceptor for SRB from anhydrous sodium sulfate (Na_2SO_4) were then quickly added in each solution. The final concentrations of sulfate were about 10 and 43.9 mmol L^{-1} with Millipore water and seawater, respectively. Although oxygen could inhibit the activity of SRB, the addition of sulfate was because the soil samples also contained it as a major anion based on the work of Ngueleu et al. [28] and it was also measured in groundwater (in contact with A2 and A3 on site) and seawater samples (see Section 3.1). The only electron donors and energy or carbon source available for the indigenous soil bacteria were benzene and naphthalene. The solutions were then spiked separately with benzene and naphthalene to get concentrations of about 0.2 and 0.1 mmol L^{-1}, respectively. The bottles were immediately tightly closed with caps having Tefon-faced septa. The solutions were afterward put on two stirrers to dissolve benzene and naphthalene for about 1 to 2 weeks. When dissolution was complete, duplicate 19 mL samples of the solutions of benzene and naphthalene were collected and a microextraction of benzene and naphthalene was performed using the previously prepared solution of dichloromethane containing metafluorotoluene. For a more detailed explanation of the applied microextraction method, the reader is referred to Ngueleu et al. [28]. The extracted samples were analyzed for benzene and naphthalene concentrations by GC to confirm the concentrations in initial solutions. In order to inhibit microbial activities in controls, a stock solution of 230.2 mmol L^{-1} of the biocide mercury(II) chloride ($HgCl_2$) was also prepared using Millipore water deoxygenated with argon gas to about 0.058 mmol L^{-1} DO.

For each hydrocarbon (benzene or naphthalene), thirty-five 73 mL glass serum bottles were sterilized by heating them in an oven at 121 to 130°C for a minimum of 6 hours. The day before the start of the batch experiment, a glove bag was inflated with argon gas to a volume enough to store all the serum bottles. These bottles were then filled outside the glove bag in series of five bottles (for triplicate biotic microcosms and duplicate abiotic controls), each bottle with 35 g of a selected soil sample (A1, A2, or A3). Sampling would later be done by collecting series of five bottles assembled in this way. Coarse soil particles and seashells were discarded when filling the bottles with the soil, so that the size fraction of the soil in the bottles and thus sorption would be similar to sorption results shown in Ngueleu et al. [28]. The bottles were filled as quick as possible in an open-top box which was purged with argon gas from time to time to minimize the concentration of oxygen in the bottles. Once series of five bottles were filled with the soil, they were quickly moved to the previously inflated glove bag. Because filling of the bottles with the soil was conducted during the whole day, they were left overnight in the glove bag and in the dark for 12 hours before starting the next step of sample preparation. Each bottle was then taken out of the glove bag, purged inside with argon gas using a cannula, and finally filled with the solution of either benzene or naphthalene using a bottle-top dispenser having a PTFE inlet tubing. Small volumes of the initial solution were sampled before and after dispensing into the serum bottles to validate the initial concentrations of benzene, naphthalene, and sulfate. For each sampling time during the batch biodegradation experiments, there were three bottles which received only either benzene or naphthalene, denoted hereafter as biotic microcosms, and two bottles which received 0.280 mL of the stock solution of mercury(II) chloride in addition to either benzene or naphthalene, denoted hereafter as abiotic controls. The final concentration of mercury(II) chloride in the abiotic controls was about 1.1 mmol L^{-1} and provided the minimum of 500 mg of mercury(II) chloride per kg of soil to inhibit microbial activities [35]. Controls and biotic microcosms were employed to distinguish between mass losses by sorption and by combination of sorption and biodegradation, respectively. The volumes of the aqueous phases were determined gravimetrically, and the final liquid-to-solid ratio (*LS*) was 1.6 mL g^{-1} (56 ± 0.4 mL of solution divided by 35.1 ± 0.08 g of soil). The headspace was minimized in all bottles in order to limit the loss by volatilization. The bottles were immediately closed using open-top unlined aluminum caps with Teflon-faced septa, then firmly crimped and placed on their side in a large black plastic bag in an open-top box. The box was placed and sealed in a dark-shaking incubator in a room with temperature maintained at 22°C, then shaken at 160 rounds per minute to keep the soil particles in suspension and allow the dissolution of salts that bacteria could need for their metabolism.

Sampling of the aqueous phase for hydrocarbon (benzene and naphthalene) and ion (sulfate, calcium, and magnesium) analyses occurred successively after 2 hours and 1, 4, 7, 14, 21, and 35 days. Sampling for the experiments with soil A3 at high salinity was stopped after 21 days as the rates of combined sorption and biodegradation reached the same magnitude as observed with the other conditions at 35 days (Section 3.2). At each sampling time, the pH of the aqueous phase was measured and aqueous samples were analyzed for hydrocarbons and ions by GC and IC, respectively.

2.4. Numerical Modeling. The kinetics of simultaneous sorption and biodegradation of benzene and naphthalene data were determined using the two-site sorption kinetic model presented in Ngueleu et al. [28]. (Note: Ngueleu et al. [28] only studied the sorption process, not the biodegradation.) In brief, the model assumes that two sorption sites exist on the soil particles and while sorption is instantaneously in equilibrium on one site, it is rate-limited on the other site and the Langmuir sorption isotherm was used to define the sorption on the equilibrium site. The model can

Table 2: Major cations and anions of groundwater and seawater samples.

Water type	Na^+ (mmol L^{-1})	K^+ (mmol L^{-1})	Ca^{2+} (mmol L^{-1})	Mg^{2+} (mmol L^{-1})	Cl^- (mmol L^{-1})	Br^- (mmol L^{-1})	SO_4^{2-} (mmol L^{-1})
Groundwater	40.61 ± 1.16	1.35 ± 0.05	6.62 ± 0.19	3.66 ± 0.12	43.86 ± 0.92	0.03 ± 0.00	10.83 ± 0.14
Seawater	532.71 ± 93.98	11.76 ± 1.35	10.59 ± 2.36	55.92 ± 14.26	702.81 ± 129.00	0.78 ± 0.19	33.80 ± 11.52

therefore be written in its more general form by adding a reaction term R (mmol day^{-1}) as follows:

$$\begin{cases} V\dfrac{\partial C}{\partial t} + m\left(\dfrac{\partial S_1}{\partial t} + \dfrac{\partial S_2}{\partial t}\right) = R, \\ \dfrac{\partial S_1}{\partial t} = \dfrac{\partial}{\partial t}\left[f_{eq}\left(\dfrac{S_{max}C}{K+C}\right)\right], \\ \dfrac{\partial S_2}{\partial t} = \lambda\left[\left(1-f_{eq}\right)\left(\dfrac{S_{max}C}{K+C}\right) - S_2\right], \end{cases} \tag{7}$$

where V (L) is the volume of the aqueous solution in the serum bottles, C (mmol L^{-1}) is the aqueous concentration of benzene or naphthalene, t (s) is the time, m (kg) is the mass of the soil in the serum bottles, S_1 (mmol kg^{-1}) is the sorbed concentration at the site with instantaneous equilibrium sorption, S_2 (mmol kg^{-1}) is the sorbed concentration at the site with kinetic sorption, f_{eq} (-) is the fraction of equilibrium sorption with values between 0 and 1, S_{max} (mmol kg^{-1}) is the maximum sorbed concentration, K (mmol L^{-1}) is the half-saturation concentration, and λ (day^{-1}) is the first-order rate coefficient of kinetic sorption. The results of the abiotic controls from batch experiments containing inactive bacteria and those of the biotic microcosms containing active bacteria were then modeled separately. For the controls, the model denoted hereafter as model M1 was the same as described in Ngueleu et al. [28] by setting the reaction term R equals to zero. For the biotic microcosms, the model denoted hereafter as model M2 was defined by assuming that biodegradation can be described by a first-order biodegradation rate, which led to R having the following expression:

$$R = -k_b CV, \tag{8}$$

where k_b (day^{-1}) is the first-order biodegradation rate coefficient. For each batch experiment, model M1 was first run and the fitting parameters were f_{eq}, λ, S_{max}, and K. The MATLAB function fminsearchbnd was used to fit the experimental data, and the boundaries were applied to the above four parameters except λ. The boundary values of S_{max} and K were taken from Ngueleu et al. [28] and corresponded to the ranges of the parameters of Langmuir sorption isotherm of their experiments conducted at 25°C and natural salinity. The average mass of soil (~35.1 g) and volume of aqueous phase (~56 mL) were among the input variables. The root mean square error (RMSE) between measured and simulated data was minimized during model fitting and was used as a criterion to evaluate the goodness of the fit. Since the abiotic controls were run in parallel with the biotic microcosms, it was then possible to assume that the process of sorption was the same in both types of experiments. Therefore, the simulated values of f_{eq}, λ, S_{max}, and K from model M1 were used in model M2, which was set up similarly to model M1 except that the only fitting parameter was k_b.

3. Results and Discussions

3.1. Properties of Groundwater, Seawater, and Soil Samples. The EC, pH, and temperature of the field sampled groundwater were measured as 5.3 mS cm^{-1}, 7.4, and 25°C, respectively. In the laboratory at 22°C, before starting the batch experiments, the EC and pH of the groundwater sample were measured again and the values were the same as in the field and the EC and pH of the seawater sample were 63.3 mS cm^{-1} and 8.2, respectively. Note that a seawater pH scale was not used because calibration of the pH meter was not done using a buffer made of a synthetic seawater medium such as Tris buffers [36, 37]. The seawater was more saline than the groundwater based on the above EC values. The groundwater was near-neutral whereas the seawater was slightly alkaline but the difference between their pH was fairly small. In general, it would be possible that the EC and pH of groundwater are within or near the ranges defined by both groundwater and seawater values due to the interaction between the two water sources in the coastal area. This statement is consistent with the study of Shomar [22] who reported the EC and pH in inland and coastal groundwater in Qatar in the ranges of 0.022-30.6 mS cm^{-1} and 7-8.22, respectively.

The concentrations of major cations and anions measured in the groundwater and seawater samples are presented in Table 2. Sodium (Na^+) and chloride (Cl^-) had the highest concentrations in both waters. The relative abundance of major ions in groundwater followed the same pattern presented in Kuiper et al. [38], where the concentrations of cations were as sodium (Na^+) > calcium (Ca^{2+}) > magnesium (Mg^{2+}) > potassium (K^+) and for anions as chloride (Cl^-) > sulfate (SO_4^{2-}) > bromide (Br^-). For seawater, the relative abundance was the same as in groundwater for anions but different for cations ($Na^+ > Mg^{2+} > K^+ > Ca^{2+}$). The origin of major ions in groundwater was linked to the limestone and gypsum composition of the native rock and soil as well as sea salt aerosols [38]. Shomar [22] also stated that dissolved ions could precipitate as calcite and gypsum in the vadose zone after the evaporation of groundwater. The concentration of Mg^{2+} in seawater is close to that of standard seawater [39]. The concentration of SO_4^{2-} used in the batch biodegradation experiments in this study was similar to the concentration in the groundwater (natural or low-salinity condition).

The calculated water contents of the sandy soils A1, A2, and A3 were 15%, 21%, and 21%, respectively. The estimated upward groundwater flow rate and Darcy velocity were

1.30×10^5 cm^3 day^{-1} and 1.04×10^2 cm day^{-1}, respectively, reflecting the observed high flow caused by the tide-induced movements of water at the coastal site. These values are also comparable to groundwater flow parameters reported by Baalousha [40] for the shallow aquifer material at the field site. Based on field observations, one could deduce that the shallow aquifer was unconfined and the rise of the groundwater table was due to fluctuation which can also cause the exchange of oxygen across the groundwater table. In addition, it can be assumed that the sandy coastal soil provides a good hydraulic connection between the shallow aquifer and the sea, which would suggest that the observed vertical amplitude of the seawater fluctuation zone (about 1 to 2 m, see Section 2.1) could also correspond to the length of the interval in which the groundwater table fluctuates. In general, the topographical and hydrological features observed at the tidal area were similar to those described by other studies in coastal sabkha areas in the Arabian Peninsula [41, 42]. The soil used in this study was attributed to the class of beach sand and sabkha soils [28].

3.2. Kinetics of Sorption and Biodegradation. The results of the biodegradation experiments are shown in Figures 2–4. The measured mean concentrations of Ca^{2+} and Mg^{2+} at the low-salinity condition were slightly higher in the abiotic controls (2.97-4.09 mmol L^{-1} for Ca^{2+} and 0.76-1.19 mmol L^{-1} for Mg^{2+}) than in the biotic microcosms (1.17-2.74 mmol L^{-1} for Ca^{2+} and 0.49-0.89 mmol L^{-1} for Mg^{2+}). The lower concentrations in the biotic microcosms were possibly due to the uptake of Ca^{2+} and Mg^{2+} by bacteria for their metabolism because of the results discussed below (Figures 2 and 3) showing that the benzene and naphthalene were biodegraded in all experiments. Another possible explanation is the sorption of these divalent ions to the soil due to the lower ionic strength in the biotic microcosms [43], which would decrease their concentrations in the aqueous phase. Conversely, the higher ionic strength in the abiotic controls (due to the biocide) could have an important influence on cation exchange and limit the sorption of Ca^{2+} and Mg^{2+}. Because carbonate minerals are among the major constituents of Qatari soils [22], their chemical elements such as Ca^{2+} and Mg^{2+}, therefore, leached from the soil samples during the experiments. As a consequence to the microbial uptake or sorption of Ca^{2+} and Mg^{2+}, all experiments showed a slightly higher pH value in the biotic microcosms than in the controls, because the carbonate ions left in solution led to an increase of the pH. For the experiments with all soil samples at the low-salinity condition, the pH values in the biotic microcosms were between 8.6 ± 0.3 and 8.7 ± 0.2, whereas they were between 8.2 ± 0.2 and 8.4 ± 0.1 in the controls. For the experiments with soil A3 at high salinity, the pH values in the biotic microcosms were between 7.7 ± 0.1 and 7.8 ± 0.2, whereas they were about 7.7 ± 0.2 in the controls. Note that despite the small difference in pH values of the biotic and abiotic samples, their respective pH values were in general stable during the experiments. The low-salinity level in the biotic microcosms containing benzene corresponded to average EC values of 3.2 ± 0.1, 3.3 ± 0.2, and 2.6 ± 0.0 mS cm^{-1} with soils A1, A2, and A3, respectively, and similar values were obtained with naphthalene as they were 3.4 ± 0.1, 3.3 ± 0.1, and 2.6 ± 0.1 mS cm^{-1} with soils A1, A2, and A3, respectively. The higher EC values in soils A1 and A2 are due to the evaporation of water in the vadose zone at the sampling site which increases the salt content. The high-salinity level in the biotic microcosms prepared with only soil A3 corresponded to average EC values of 59.4 ± 0.4 and 60.6 ± 0.8 mS cm^{-1} with benzene and naphthalene, respectively.

Figure 2 shows the time series normalized concentrations of benzene, naphthalene, and SO_4^{2-} from the experiments with soils A1, A2, and A3 at low salinity. For the experiments with the deepest soil A3 at high salinity, the results are shown in Figure 3. After 1 day at low salinity, the normalized mean concentrations of benzene in the abiotic controls decreased due to sorption by about 7%, 11%, and 11% on soils A1, A2, and A3, respectively (Figures 2(a), 2(c), and 2(e)), and the concentrations remained relatively stable until 35 days due to equilibrium state with losses of about 7-9%, 7-18%, and 11-19% on soils A1, A2, and A3, respectively. With soil A3 and high salinity, the analysis of the normalized mean concentrations of benzene in the abiotic controls showed that the losses by sorption also stabilized after 1 day between 10 and 17%, and this behavior was similar to the case of soil A3 at low salinity (Figure 3(a)). These results are almost all similar to those shown in Ngueleu et al. [28], where a loss by sorption of 12-14% was measured and reached equilibrium after 1 to 2 days for benzene at 25°C and at natural salinity. The slight difference (lower) in loss by sorption on soil A1 at low salinity (7-9%), in this study, is due to the fact that the sorption followed the Langmuir sorption model and Ngueleu et al. [28] used the same mass of sorbent of 35 g (*i.e.*, same number of sorption sites) but a smaller LS of 1.28 ± 0.01 mL g^{-1} and a lower initial concentration (C_0) of $\sim 1.3 \times 10^{-2}$ mmol L^{-1}, which resulted in slightly lower C/C_0 values in their study. Note, however, that although the sorbed concentration (S) is proportional to LS ($S = (C_0 - C) \times LS$), the magnitudes of the equilibrium parameters S_{max} and K (Equation (7)) should not be affected by LS especially that the Langmuir sorption model is limited to one sorption layer.

Losses of about 7 to 25% of aqueous concentrations of naphthalene also occurred in the abiotic controls after 1 day due to sorption on the soils at low salinity (Figures 2(b), 2(d), and 2(f)). These concentrations continued to decreased until equilibrium sorption was reached for naphthalene after 7 days (21% loss), 14 days (28% loss), and 7 days (36-40% loss) with soils A1, A2, and A3, respectively. For naphthalene with soil A3 at high salinity (Figure 3(b)), although the decrease in the controls of 31% at 1 day is almost similar to the case of soil A3 at low salinity (Figure 2(f)), losses by sorption kept increasing until 14 days when an equilibrium was reached at a loss of 47 to 49%. Similarly to the case of benzene with soil A1 at low salinity, the above equilibrium sorption rate and time of naphthalene were also different from those shown in Ngueleu et al. [28] at 25°C and at natural salinity where the rate was measured as 75% at the equilibrium time of 2 days. These differences were due to the same reason given above for benzene and suggest

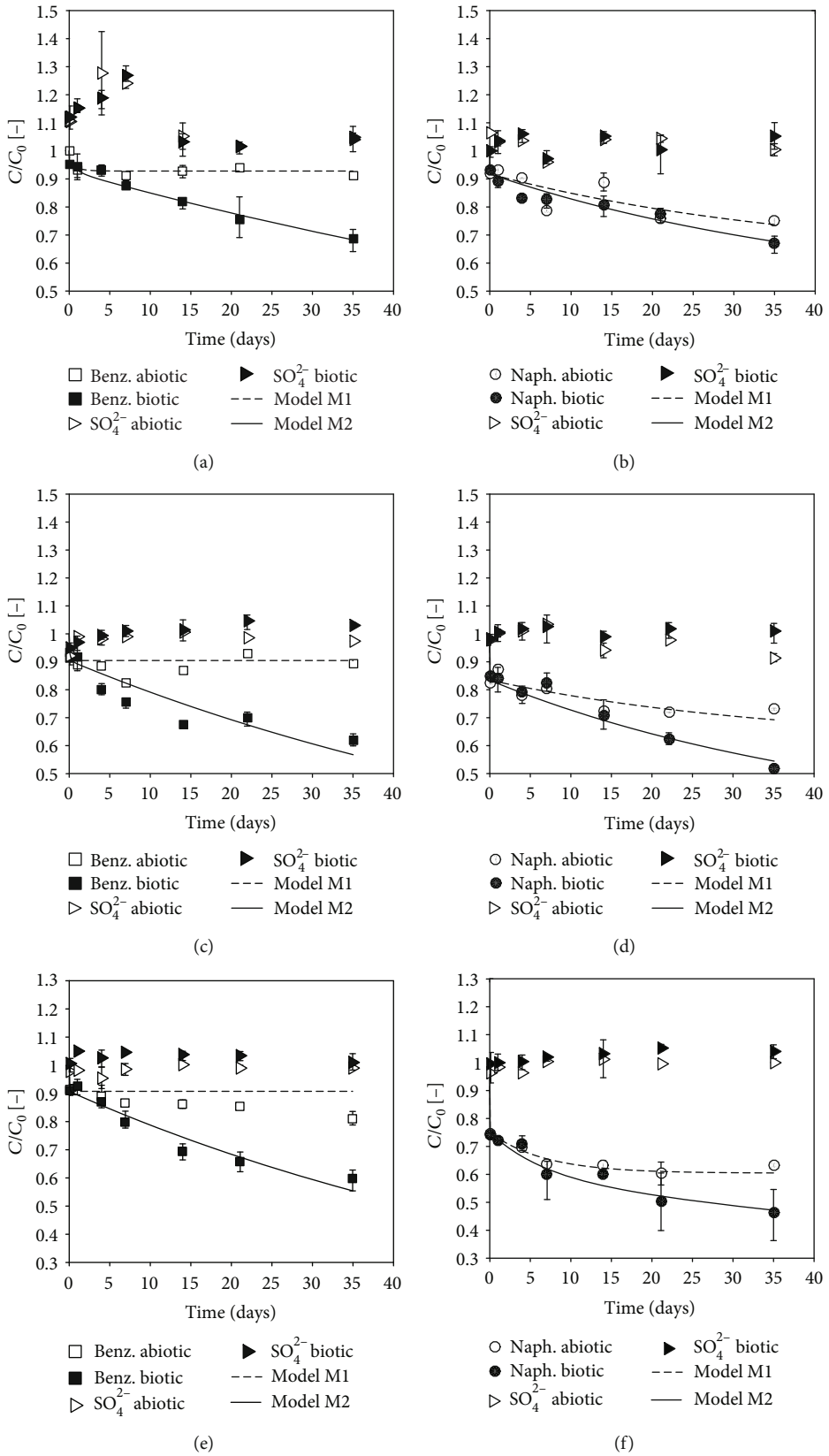

Figure 2: Sorption and biodegradation kinetics of benzene (Benz.) and naphthalene (Naph.) with soils A1 (a and b), A2 (c and d), and A3 (e and f) at low salinity. In Figures 2–4, the symbols are mean concentrations while the error bars are intervals between maxima and minima and they are within the width of the symbols when not visible. Aqueous concentrations at sampling time (C) are normalized by their respective initial concentrations (C_0).

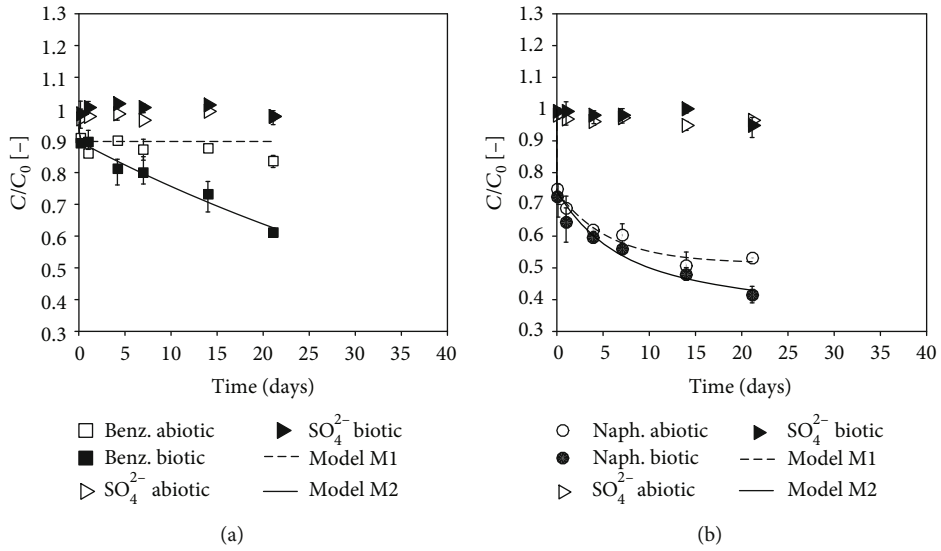

Figure 3: Sorption and biodegradation kinetics of benzene (a) and naphthalene (b) with soil A3 at high salinity (seawater).

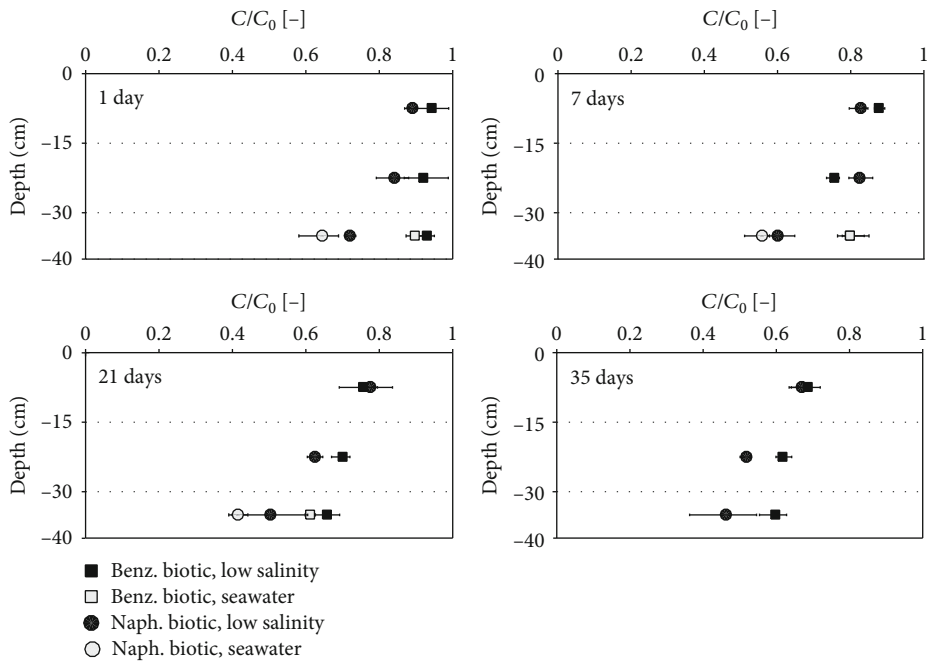

Figure 4: Summary of normalized aqueous concentration losses of benzene (Benz.) and naphthalene (Naph.) due to simultaneous sorption and biodegradation in biotic microcosms as a function of depth and salinity. The horizontal gray lines represent the limits between the soils A1, A2 and A3 from the top.

that sorption kinetics on the Qatari soil varies with LS and C_0, especially for naphthalene in which the highest difference in the sorption rate at equilibrium was observed.

Overall, the above results on sorption show that naphthalene sorbed stronger than benzene for all the scenarios considered and this was due to its higher affinity to organic carbon, reported in [28] for similar soils at $0.84 \pm 0.47\%$ dry, and to its higher hydrophobicity (see Table 1). Sorption at low salinity for benzene was in general similar and slightly stronger with soils A2 (7-18%) and A3 (11-19%) than with soil A1 (7-9%). For naphthalene, the loss by sorption at the low salinity was the strongest with soil A3 (36-40%). At the low-salinity level, the increase of sorption with depth cannot be attributed to salinity because the EC of the deepest soil A3 was slightly smaller than those of soils A1 and A2. Ngueleu et al. [28] also showed that the sorption of naphthalene was not affected by salinity at the low-salinity level. A probable reason for the increase of sorption with depth is the

heterogeneous physicochemical properties of the soil samples. However, when the results of the low- and high-salinity levels are considered, the higher concentration losses at the high salinity of only naphthalene suggest that the sorption of this compound could increase with salinity (36-40% to 47-49% with soil A3 at low- and high-salinity levels, respectively).

In Figure 2, the decrease of the normalized mean concentration of benzene in the biotic microcosms at low salinity was the same as in the controls after 4, 1, and 4 days with soils A1, A2, and A3, respectively. The concentration of benzene in soil A1 then deviated from the sorption equilibrium level with a constant slope from the 7^{th} to the 35^{th} day at reductions of 12% and 31%, respectively. The latter observation indicates that the biodegradation of benzene occurred in the biotic microcosms after a lag phase of about 7 days, and biodegradation alone accounted for about 22% of concentration loss on the 35^{th} day. The biodegradation of benzene with soils A2 and A3 was also observed from and after the 4^{th} day with the maximum differences of 28% and 21% measured on the 35^{th} day, respectively. Concerning naphthalene in soil A1 at low salinity, its normalized mean concentration in the biotic microcosms decreased in general in the same manner as in the controls. With this soil, differences in concentration due to biodegradation were observed from the 4^{th} day, but due to fluctuating concentrations in the controls, a clear difference was noticeable after 21 days. Without considering the fluctuations, biodegradation alone accounted for about 8% of concentration loss on the 35^{th} day. The lag phase of biodegradation of naphthalene with soils A2 and A3 at low salinity was about 14 days because clear differences in concentration were observed afterwards, with the highest reductions due to biodegradation of 21% and 17% on the 35^{th} day, respectively.

In Figure 3, the results for soil A3 at high salinity showed that the maximum mean losses of about 39% and 58% at 21 days of the combined sorption and biodegradation in biotic microcosms were similar to those measured at low salinity at 35 days (about 40% and 54%) for benzene and naphthalene, respectively. The total significant reduction of naphthalene from the aqueous phase at high salinity was mostly due to sorption not biodegradation. The lag phases of biodegradation were about 4 and 7 days for benzene and naphthalene, respectively. The losses due to biodegradation of benzene and naphthalene at high salinity were about 22% and 11%, while the corresponding losses at 21 days with soil A3 at low salinity were 19% and 10%, respectively. The above results indicate that the coastal indigenous bacteria were capable of metabolizing the hydrocarbons in soil A3 in both low- and high-salinity conditions and at similar rates.

For all the scenarios considered, the normalized mean concentrations of SO_4^{2-} were quite similar in abiotic and biotic samples (Figures 2 and 3) and they were in general equal to approximately 1.0 with some exceptions. The exceptions include for example the normalized mean concentration of SO_4^{2-} of about 1.3 from the experiment with benzene in soil A1 at low salinity (Figure 2(a)). Normalized SO_4^{2-} concentrations higher than 1.0 suggest that it leached from the soil during the experiment as observed by Ngueleu et al. [28]; the difference in concentrations at different times is indicative of the nonuniform distribution of SO_4^{2-} in the coastal soil. Serum bottles could have indeed received fractions of the coastal soil with slightly different SO_4^{2-} concentrations since the homogenization of the soil prior to filling the serum bottles was not done.

For the low-salinity condition, nitrate (NO_3^-) was also detected at low concentrations but generally higher in controls than in biotic samples, and this finding suggests that NRB are also among the microbial groups in the coastal soil because nitrate was not added in the background solutions. The ability of NRB to biodegrade benzene and naphthalene is well documented (*e.g.*, [44–47]). For the experiments with benzene, the absolute mean concentrations of NO_3^- in the abiotic and biotic samples were, respectively, 0.073 ± 0.013 and $0.0 \pm 0.0\,\text{mmol L}^{-1}$ with soil A1, 0.0 ± 0.0 and $0.0 \pm 0.0\,\text{mmol L}^{-1}$ with soil A2, and 0.039 ± 0.027 and $0.02 \pm 0.028\,\text{mmol L}^{-1}$ with soil A3. For the experiments with naphthalene, these concentrations of NO_3^- in the abiotic and biotic samples were, respectively, 0.072 ± 0.009 and $0.005 \pm 0.007\,\text{mmol L}^{-1}$ with soil A1, 0.027 ± 0.024 and $0.004 \pm 0.005\,\text{mmol L}^{-1}$ with soil A2, and 0.024 ± 0.033 and $0.005 \pm 0.013\,\text{mmol L}^{-1}$ with soil A3. Due to low NO_3^- concentrations in the soil, it was not detected in samples from the high-salinity condition because the dilution of the corresponding IC samples was high in order to determine the major anion SO_4^{2-} which was prepared at an elevated concentration.

The measurement of dissolved O_2 was performed in biotic microcosms and the observed lowest and consumed absolute concentrations of this electron acceptor along with those of NO_3^- are shown in Table 3. Based on the observed maximum concentrations of O_2 and NO_3^- consumed, the maximum concentrations of the two PHCs that could be mineralized by aerobic bacteria and NRB are also presented in Table 3. The calculations of PHC concentrations were performed by using the stoichiometry ratios between the PHCs and O_2 (7.5 : 1 and 12 : 1 for benzene and naphthalene, respectively) and between the PHCs and NO_3^- (15 : 1 and 24 : 1 for benzene and naphthalene, respectively) (Equations (1) and (2) and (5) and (6), respectively). Mass balance calculations were not performed with SO_4^{2-} because considerable leaching of this anion occurred during the experiments that did not enable to clearly determine losses associated with biodegradation by SRB. For the low-salinity condition, the results in Table 3 show that the calculated PHC concentrations biodegraded by both aerobic bacteria and NRB vary between about 11% and 85% of the actually observed maximum concentrations of PHCs biodegraded in the experiments, with the highest microbial contribution being for the case of naphthalene in soil A1.

An estimate of the remainder of PHC concentrations not associated to O_2 and NO_3^- losses in all scenarios can be determined by neglecting the contribution of NRB at the high-salinity condition due to the lack of NO_3^- data (Table 3). This remainder varies between 0.038 and $0.055\,\text{mmol L}^{-1}$ for benzene and between 0.001 and $0.021\,\text{mmol L}^{-1}$ for naphthalene. The calculated concentration losses of SO_4^{2-} needed to

Table 3: Mass balance between oxygen and nitrate consumption and petroleum hydrocarbon degradation.

Compound	Soil and environmental condition	Electron acceptor	Observed lowest concentration of an electron acceptor in biotic samples (mmol L^{-1})	Observed maximum consumption of an electron acceptor* (mmol L^{-1})	Maximum concentration of PHCs biodegraded based on maximum electron acceptor consumed# (mmol L^{-1})		Observed actual maximum concentration of PHCs biodegraded in the experiment including an assumed contribution of SRB (mmol L^{-1})
Benzene	A1 (low salinity)	O_2	0.005	0.053	0.007	Total = 0.013	0.051
		NO_3^-	0	0.083	0.006		
	A2 (low salinity)	O_2	0.009	0.049	0.007	Total = 0.007	0.062
		NO_3^-	0	0	0		
	A3 (low salinity)	O_2	0.020	0.038	0.005	Total = 0.010	0.050
		NO_3^-	0	0.068	0.005		
	A3 (high salinity)	O_2	0.011	0.048	0.006	—	0.046
		NO_3^-	No data	No data	No data		
Naphthalene	A1 (low salinity)	O_2	0	0.058	0.005	Total = 0.008	0.009
		NO_3^-	0	0.068	0.003		
	A2 (low salinity)	O_2	0.037	0.022	0.002	Total = 0.04	0.025
		NO_3^-	0	0.037	0.002		
	A3 (low salinity)	O_2	0.004	0.054	0.005	Total = 0.008	0.019
		NO_3^-	0	0.073	0.003		
	A3 (high salinity)	O_2	0.025	0.033	0.003	—	0.012
		NO_3^-	No data	No data	No data		

The evaluation was performed with the mean concentrations of triplicate biotic samples and duplicate controls. *The consumption or losses of O_2 and NO_3^- are reductions from the initial concentration of O_2 and concentrations of NO_3^- in controls, respectively. #The calculations were based on the stoichiometry ratios in Equations (1) and (2) and (5) and (6).

Table 4: Separate statistical regression analyses of the results of biodegradation kinetics as a function of depth and salinity as EC.

Compound	Percent losses at low salinity by sorption and biodegradation versus depth				Percent losses by sorption and biodegradation versus salinity as EC		k_b values at low salinity versus depth		k_b values versus salinity as EC	
	21 days		35 days		21 days					
	R^2	p value	R^2	p value	R^2	p value	R^2	p value	R^2	p value
Benzene	1.00	0.04	0.93	0.16	0.57	0.24	0.89	0.22	0.52	0.28
Naphthalene	1.00	0.007	0.96	0.12	0.46	0.32	0.95	0.15	0.48	0.31

mineralize these concentrations of benzene, based on the stoichiometry ratio of 3.75 : 1 (Equation (3)), are between 0.144 and 0.208 mmol L^{-1}; and naphthalene, based on the stoichiometry ratio of 6 : 1 (Equation (4)), are between 0.008 and 0.127 mmol L^{-1}. These losses of SO_4^{2-} are less than 3% of its initial concentrations (10 and 43.9 mmol L^{-1} at the low- and high-salinity conditions, respectively). These results suggest that aerobic bacteria, NRB and most likely SRB biodegraded benzene and naphthalene in the biotic microcosms for the period investigated. The expected losses of SO_4^{2-} (<3%) were very low that they could explain why a clear decreasing trend of the concentration of SO_4^{2-} in the biotic microcosms could not be seen in Figures 2 and 3. If oxygen inhibited the activity of the anaerobic bacteria at some time during the experiment [34], it would imply that the performance of the anaerobic bacteria observed in this study is among the best because groundwater at the site could continuously be supplied by oxygen due to frequent groundwater table fluctuation. Dobson et al. [48], who conducted laboratory thin-slab sandy aquifer experiments in water-fluctuating and non-fluctuating conditions and using a solution containing O_2, NO_3^-, and SO_4^{2-}, also observed both aerobic and anaerobic biodegradations in their experiments as indicated by minor losses of SO_4^{2-} for a short period and significant losses of O_2 and NO_3^-.

In general, the experimental results from the biotic microcosms and abiotic controls show that sorption was the dominant process for naphthalene whereas biodegradation was the main process controlling the fate of benzene. Regarding biodegradation at low salinity, the losses of aqueous concentration for benzene after 35 days were slightly higher in soil A2 (28 ± 2%) than in soils A1 (22 ± 4%) and A3 (21 ± 2%). This conclusion cannot be clearly drawn for naphthalene because of the large standard deviation obtained with soil A3 (8 ± 3%, 21 ± 1%, and 17 ± 9% for soils A1, A2, and A3, respectively). Since soil A2 was located across the groundwater table at the time of sampling, the latter rates would suggest that the interface between the vadose zone and the groundwater system could be a hot spot for the biodegradation of at least benzene at low salinity. However, due to the possible good hydraulic connection between the shallow aquifer and the sea, as suggested by the type of coastal soil (sandy) and by the rise of the groundwater table during sampling, soils A1 and A3 would also frequently intersect with the groundwater table similarly to soil A2. That being said, microbial activities in these three soil samples would in general be similar.

A summary of the combined contribution of sorption and biodegradation on the kinetic removal of benzene and naphthalene from the aqueous phase as a function of depth and salinity is shown in Figure 4. Visually, the plots clearly show that the removal increased with depth and salinity and as stated before, the dominant removal process was biodegradation for benzene and sorption for naphthalene. It is possible that the weaker sorption of benzene, as compared to naphthalene, made it easily bioavailable to bacteria in the aqueous phase. The fact that benzene also has a smaller molecular weight than naphthalene, it could have also facilitated its relatively faster biodegradation because the lighter PHCs are generally more susceptible to microbial degradation than the heavier ones [5, 14]. A statistical regression analysis of the percent losses of PHCs $((1 - C/C_0) \times 100)$ due to sorption and biodegradation versus depth and salinity as EC (separately) was performed for selected sampling times. These times corresponded to the results showing stronger visual relationships with depth and EC separately. The data sets selected were then those obtained at 21 and 35 days when using depth data (*i.e.*, means of soil intervals of 7.5, 22.5, and 35 cm), and only at 21 days when using salinity data (*i.e.*, mean of EC data of 3.2, 3.3, 2.6, and 59.4 mS cm^{-1} for benzene and 3.4, 3.3, 2.6, and 60.6 mS cm^{-1} for naphthalene). This analysis was carried out using the Microsoft Office Excel Program Analysis ToolPak which provided the square of the Pearson correlation coefficient (R^2) and the p value between two variables. As shown in Table 4, R^2 values of 1.0 indicate good linear correlations between percent loss (y) and depth (x) after 21 days for benzene ($y = 0.36x + 21.43$) and naphthalene ($y = 0.98x + 15.71$) and, based on a significance level (α) of 0.05, these relationships were statistically significant (p values < 0.05). Good linear correlations also existed after 35 days for benzene ($y = 0.33x + 29.14$) and naphthalene ($y = 0.77x + 28.29$), but they were not statistically significant because p values were greater than 0.05. No statistically reasonable relationship was obtained between the percent losses and EC data at 21 days but this could somehow be due to the fact that three of the four EC data were fairly similar, therefore not providing any possible trend. However, the lack of relationship with the EC would support the interpretation previously mentioned that the indigenous bacteria metabolized the two PHCs at low- and high-salinity conditions and at similar rates (using soil A3).

The best fits of the models M1 and M2 are plotted in Figures 2 and 3, and the model parameters are presented in Table 5 along with RMSE values which reflect the very good

Table 5: Initial concentrations and parameters of the two-site sorption and biodegradation kinetic models M1 and M2.

Compound	Soil and environmental condition	C_0 (mmol L^{-1})	S_{max} (mmol kg^{-1})	K (mmol L^{-1})	f_{eq} (-)	λ (day^{-1})	k_b (day^{-1})	Model M1 RMSE (-)	Model M2 RMSE (-)
Benzene	A1 (low salinity)	0.23	0.038	0.091	0.6	9.33×10^{-1}	8.99×10^{-3}	0.02	0.01
	A2 (low salinity)	0.23	0.050	0.091	0.55	5.56	1.38×10^{-2}	0.04	0.05
	A3 (low salinity)	0.23	0.050	0.091	0.58	12.8	1.46×10^{-2}	0.05	0.03
	A3 (high salinity)	0.21	0.050	0.091	0.54	8.04	1.77×10^{-2}	0.03	0.02
Naphthalene	A1 (low salinity)	0.12	0.236	0.163	0.17	1.99×10^{-2}	2.53×10^{-3}	0.04	0.02
	A2 (low salinity)	0.12	0.236	0.163	0.35	2.28×10^{-2}	7.54×10^{-3}	0.03	0.03
	A3 (low salinity)	0.11	0.236	0.163	0.56	1.28×10^{-1}	9.16×10^{-3}	0.02	0.03
	A3 (high salinity)	0.11	0.299	0.153	0.43	1.37×10^{-1}	1.19×10^{-2}	0.02	0.02

agreement of the fits. For their batch sorption experiments at 25°C and natural salinity, Ngueleu et al. [28] determined that the ranges of S_{max} and K for benzene were 0.031-0.050 mmol kg^{-1} and 0.091-0.193 mmol L^{-1}, whereas for naphthalene they were 0.236-0.464 mmol kg^{-1} and 0.070-0.163 mmol L^{-1}, respectively. The values of S_{max} and K in Table 5 are all within these ranges. The values of f_{eq} and λ indicate that equilibrium sorption dominated over kinetic sorption for benzene ($f_{eq} > 0.5$ and higher λ) whereas except for the experiment with soil A3 at low salinity, kinetic sorption was dominant for naphthalene. The magnitudes of k_b values suggest that biodegradation occurred at very slow rates. The slowest biodegradation rates were for naphthalene with soils A1 and A2 at the low-salinity condition. The slow rates could represent cases of first microbial exposure to PHCs since the soil was not contaminated at the site because cases of prior microbial exposure could exhibit faster biodegradation rates [46]. Suarez and Rifai [49] conducted a comprehensive review of biodegradation rates of fuel hydrocarbons from 133 field and laboratory studies which were conducted under either aerobic, anaerobic, or mixed aerobic/anaerobic conditions. From their statistical analysis of the results, median rate coefficients for benzene, ethylbenzene, and xylenes of $(3 \text{ to } 4) \times 10^{-3}$ day^{-1} were estimated from all the studies. These values are similar or close to the values estimated in this study. It is relevant to remind that aerobic and anaerobic bacteria mineralized benzene and naphthalene in this study, and therefore, the observed losses of these PHCs (Figures 2 and 3) and the simulated kinetic rate coefficients (Table 5) represent their combined contribution. These results should then not be extrapolated to other studies with differing availability of electron acceptors (*e.g.*, studies with single redox conditions). A statistical regression analysis of k_b versus depth and salinity as EC (separately) was also performed and the results are presented in Table 4. Similarly to the analysis using the percent losses, good linear correlations were also obtained between k_b (y) and depth (x) for benzene ($y = 2 \times 10^{-4}x + 8 \times 10^{-3}$) and naphthalene ($y = 2 \times 10^{-4}x + 1.1 \times 10^{-3}$), but they were not statistically significant since p values were greater than 0.05. No statistically reasonable relationship was also obtained between the k_b and EC data.

4. Conclusions

The findings of this study indicated that the dominant process in the batch experiments was sorption for naphthalene and biodegradation for benzene. It was suggested that the increase of sorption of these two PHCs with depth is likely due to the heterogeneous physicochemical properties of the coastal soil. Biodegradation at the low O_2 and high SO_4^{2-} concentrations could be attributed to aerobic bacteria, NRB, and most likely SRB for the period investigated, with the contribution of NRB deduced from losses of NO_3^- during the experiments. The lag phases of benzene and naphthalene biodegradation were between 1 and 4 days and between 4 and 14 days, respectively. In general, the 0.2 mmol L^{-1} benzene was degraded faster than the 0.1 mmol L^{-1} naphthalene, and similar biodegradation rates were determined at low- and high-salinity conditions for the soil sample collected below the groundwater table. The biodegradation of benzene and naphthalene was, however, very slow as their simulated first-order biodegradation rate coefficients varied between 8.99×10^{-3} and 1.77×10^{-2} day^{-1} and between 2.53×10^{-3} and 1.19×10^{-2} day^{-1}, respectively. Overall, sorption and biodegradation together, which were statistically found to increase with depth at selected times when combined, can help to achieve remediation goals at PHC-contaminated coastal soil and groundwater environments in Qatar. These findings also add up to the limited quantitative information on biodegradation kinetics of PHCs at (semi)-arid saline coastal soil environments.

Data Availability

The data used to support the findings of this study are available from the corresponding author upon request.

Disclosure

The findings achieved herein are solely the responsibility of the authors.

Conflicts of Interest

The authors declare that they have no conflicts of interest.

Acknowledgments

This publication was made possible by the NPRP grant # NPRP9-93-1-021 from the Qatar National Research Fund (a member of Qatar Foundation). We also would like to acknowledge the funding provided by the Canada Excellence Research Chair Program in Ecohydrology. We are thankful to Marianne Vandergriendt, Reem Ismail, Reem Azzam, Jamal Hannun, and Lindsay Norwood for their valuable assistance during the experiments and analyses. We also thank the Environmental Science Center of Qatar University and Shirley Chatten at University of Waterloo for gas chromatography analysis.

References

[1] J. L. Sims, R. C. Sims, R. R. Dupont, J. E. Matthews, and H. H. Russell, "Engineering issue: in situ bioremediation of contaminated unsaturated subsurface soils," 1993, EPA/540/S-93/501.

[2] J. T. K. Akoachere, T. N. Akenji, F. N. Yongabi, G. Nkwelang, and R. N. Ndip, "Lubricating oil-degrading bacteria in soils from filling stations and auto-mechanic workshops in Buea, Cameroon: occurrence and characteristics of isolates," *African Journal of Biotechnology*, vol. 7, no. 11, pp. 1700–1706, 2008.

[3] Q. Liu, J. Tang, K. Gao, R. Gurav, and J. P. Giesy, "Aerobic degradation of crude oil by microorganisms in soils from four geographic regions of China," *Scientific Reports*, vol. 7, no. 1, article 14856, 2017.

[4] F. Chaillan, A. Le Flèche, E. Bury et al., "Identification and biodegradation potential of tropical aerobic hydrocarbon-degrading microorganisms," *Research in Microbiology*, vol. 155, no. 7, pp. 587–595, 2004.

[5] N. Das and P. Chandran, "Microbial degradation of petroleum hydrocarbon contaminants: an overview," *Biotechnology Research International*, vol. 2011, Article ID 941810, 13 pages, 2011.

[6] M. Schirmer, B. J. Butler, J. F. Barker, C. D. Church, and K. Schirmer, "Evaluation of biodegradation and dispersion as natural attenuation processes of MTBE and benzene at the Borden field site," *Physics and Chemistry of the Earth, Part B: Hydrology, Oceans and Atmosphere*, vol. 24, no. 6, pp. 557–560, 1999.

[7] S. Garg, C. J. Newell, P. R. Kulkarni et al., "Overview of natural source zone depletion: processes, controlling factors, and composition change," *Groundwater Monitoring & Remediation*, vol. 37, no. 3, pp. 62–81, 2017.

[8] S. J. Varjani, "Microbial degradation of petroleum hydrocarbons," *Bioresource Technology*, vol. 223, pp. 277–286, 2017.

[9] E. A. Paul, *Soil Microbiology, Ecology, and Biochemistry*, Academic Press, San Diego, Third edition, 2007.

[10] N. R. Zeman, M. Irianni Renno, M. R. Olson, L. P. Wilson, T. C. Sale, and S. K. De Long, "Temperature impacts on anaerobic biotransformation of LNAPL and concurrent shifts in microbial community structure," *Biodegradation*, vol. 25, no. 4, pp. 569–585, 2014.

[11] S. J. D. Grosso, W. J. Parton, A. R. Mosier et al., "General CH_4 oxidation model and comparisons of CH_4 oxidation in natural and managed systems," *Global Biogeochemical Cycles*, vol. 14, no. 4, pp. 999–1019, 2000.

[12] N. D. Gray, A. Sherry, C. Hubert, J. Dolfing, and I. M. Head, "Chapter 5 - methanogenic degradation of petroleum hydrocarbons in subsurface environments: remediation, heavy oil formation, and energy recovery," in *Advances in Applied Microbiology*, A. I. Laskin, S. Sariaslani, and G. M. Gadd, Eds., vol. 72, pp. 137–161, Academic Press, 2010.

[13] B. A. Bekins, F. D. Hostettler, W. N. Herkelrath, G. N. Delin, E. Warren, and H. I. Essaid, "Progression of methanogenic degradation of crude oil in the subsurface," *Environmental Geosciences*, vol. 12, no. 2, pp. 139–152, 2005.

[14] A. B. Al-Hawash, M. A. Dragh, S. Li et al., "Principles of microbial degradation of petroleum hydrocarbons in the environment," *The Egyptian Journal of Aquatic Research*, vol. 44, no. 2, pp. 71–76, 2018.

[15] C. Robinson, A. Brovelli, D. A. Barry, and L. Li, "Tidal influence on BTEX biodegradation in sandy coastal aquifers," *Advances in Water Resources*, vol. 32, no. 1, pp. 16–28, 2009.

[16] Y. Xia, H. Li, M. C. Boufadel, and Y. Sharifi, "Hydrodynamic factors affecting the persistence of the Exxon Valdezoil in a shallow bedrock beach," *Water Resources Research*, vol. 46, no. 10, 2010.

[17] X. Geng, M. C. Boufadel, K. Lee, S. Abrams, and M. Suidan, "Biodegradation of subsurface oil in a tidally influenced sand beach: impact of hydraulics and interaction with pore water chemistry," *Water Resources Research*, vol. 51, no. 5, pp. 3193–3218, 2015.

[18] X. Geng, M. C. Boufadel, and F. Cui, "Numerical modeling of subsurface release and fate of benzene and toluene in coastal aquifers subjected to tides," *Journal of Hydrology*, vol. 551, pp. 793–803, 2017.

[19] A. Acosta-González and S. Marqués, "Bacterial diversity in oil-polluted marine coastal sediments," *Current Opinion in Biotechnology*, vol. 38, pp. 24–32, 2016.

[20] J. E. Kostka, O. Prakash, W. A. Overholt et al., "Hydrocarbon-degrading bacteria and the bacterial community response in Gulf of Mexico beach sands impacted by the Deepwater Horizon oil spill," *Applied and Environmental Microbiology*, vol. 77, no. 22, pp. 7962–7974, 2011.

[21] H. M. Jin, J. M. Kim, H. J. Lee, E. L. Madsen, and C. O. Jeon, "Alteromonas as a key agent of polycyclic aromatic hydrocarbon biodegradation in crude oil-contaminated coastal sediment," *Environmental Science & Technology*, vol. 46, no. 14, pp. 7731–7740, 2012.

[22] B. Shomar, "Geochemistry of soil and groundwater in arid regions: Qatar as a case study," *Groundwater for Sustainable Development*, vol. 1, no. 1-2, pp. 33–40, 2015.

[23] B. Shomar, M. Darwish, and C. Rowell, "What does integrated water resources management from local to global perspective mean? Qatar as a case study, the very rich country with no water," *Water Resources Management*, vol. 28, no. 10, pp. 2781–2791, 2014.

[24] D. J. Ramberg, Y. H. Henry Chen, S. Paltsev, and J. E. Parsons, "The economic viability of gas-to-liquids technology and the crude oil-natural gas price relationship," *Energy Economics*, vol. 63, pp. 13–21, 2017.

[25] Y. S. Soliman, E. M. S. Al Ansari, and T. L. Wade, "Concentration, composition and sources of PAHs in the coastal sediments of the exclusive economic zone (EEZ) of Qatar, Arabian Gulf," *Marine Pollution Bulletin*, vol. 85, no. 2, pp. 542–548, 2014.

[26] K. H. Jung, B. Yan, S. N. Chillrud et al., "Assessment of benzo(a)pyrene-equivalent carcinogenicity and mutagenicity of residential indoor versus outdoor polycyclic aromatic

hydrocarbons exposing young children in New York City," *International Journal of Environmental Research and Public Health*, vol. 7, no. 5, pp. 1889–1900, 2010.

[27] C. Brett, "Crude assay report on crude oil sample marked AL Shaheen Crude Oil, behalf of Maersk Oil Qatar AS," 2006, March 2019, https://www.qp.com.qa/en/marketing/Documents/Al-Shaheen%20Assay%2010Apr2006.pdf.

[28] S. K. Ngueleu, F. Rezanezhad, R. I. Al-Raoush, and P. Van Cappellen, "Sorption of benzene and naphthalene on (semi)-arid coastal soil as a function of salinity and temperature," *Journal of Contaminant Hydrology*, vol. 219, pp. 61–71, 2018.

[29] Z. Al Disi, S. Jaoua, D. Al-Thani, S. Al-Meer, and N. Zouari, "Considering the specific impact of harsh conditions and oil weathering on diversity, adaptation, and activity of hydrocarbon-degrading bacteria in strategies of bioremediation of harsh oily-polluted soils," *BioMed Research International*, vol. 2017, Article ID 8649350, 11 pages, 2017.

[30] R. F. Al-Thani, D. A. M. Abd-El-Haleem, and M. Al-Shammri, "Isolation and characterization of polyaromatic hydrocarbons-degrading bacteria from different Qatari soils," *African Journal of Microbiology Research*, vol. 3, no. 11, pp. 761–766, 2009.

[31] Qatar Meteorology Department, "Climate and marine information for Qatar," 2018, https://qweather.gov.qa/Index.aspx.

[32] R. A. Freeze and J. A. Cherry, *Groundwater*, Prentice-Hall, Inc., Englewood Cliffs, NJ, USA, 1979.

[33] W. Mabey, J. Smith, R. Podoll et al., "Aquatic fate process data for organic priority pollutants," Technical Report No. 440/4-81-014, U.S. Environmental Protection Agency (USEPA), 1982.

[34] K. U. Kjeldsen, C. Joulian, and K. Ingvorsen, "Oxygen tolerance of sulfate-reducing bacteria in activated sludge," *Environmental Science & Technology*, vol. 38, no. 7, pp. 2038–2043, 2004.

[35] J. T. Trevors, "Sterilization and inhibition of microbial activity in soil," *Journal of Microbiological Methods*, vol. 26, no. 1-2, article 0167701296008433, pp. 53–59, 1996.

[36] B. V. Nemzer and A. G. Dickson, "The stability and reproducibility of Tris buffers in synthetic seawater," *Marine Chemistry*, vol. 96, no. 3-4, pp. 237–242, 2005.

[37] G. M. Marion, F. J. Millero, M. F. Camões, P. Spitzer, R. Feistel, and C. T. A. Chen, "pH of seawater," *Marine Chemistry*, vol. 126, no. 1-4, pp. 89–96, 2011.

[38] N. Kuiper, C. Rowell, and B. Shomar, "High levels of molybdenum in Qatar's groundwater and potential impacts," *Journal of Geochemical Exploration*, vol. 150, pp. 16–24, 2015.

[39] F. J. Millero, R. Feistel, D. G. Wright, and T. J. McDougall, "The composition of Standard Seawater and the definition of the Reference-Composition Salinity Scale," *Deep Sea Research Part I: Oceanographic Research Papers*, vol. 55, no. 1, pp. 50–72, 2008.

[40] H. M. Baalousha, "Groundwater vulnerability mapping of Qatar aquifers," *Journal of African Earth Sciences*, vol. 124, pp. 75–93, 2016.

[41] A. M. Alnuaim and M. H. El Naggar, "Performance of foundations in sabkha soil: numerical investigation," *Geotechnical and Geological Engineering*, vol. 32, no. 3, pp. 637–656, 2014.

[42] W. Akili and J. K. Torrance, "The development and geotechnical problems of sabkha, with preliminary experiments on the static penetration resistance of cemented sands," *Quarterly Journal of Engineering Geology and Hydrogeology*, vol. 14, no. 1, pp. 59–73, 1981.

[43] C. A. J. Appelo and D. Postma, *Geochemistry, Groundwater and Pollution*, A.A. Balkema Publishers, Leiden, The Netherlands, 2nd edition, 2005.

[44] C. Vogt, S. Kleinsteuber, and H.-H. Richnow, "Anaerobic benzene degradation by bacteria," *Microbial Biotechnology*, vol. 4, no. 6, pp. 710–724, 2011.

[45] S. Atashgahi, B. Hornung, M. J. van der Waals et al., "A benzene-degrading nitrate-reducing microbial consortium displays aerobic and anaerobic benzene degradation pathways," *Scientific Reports*, vol. 8, no. 1, article 4490, 2018.

[46] J. Dou, X. Liu, and A. Ding, "Anaerobic degradation of naphthalene by the mixed bacteria under nitrate reducing conditions," *Journal of Hazardous Materials*, vol. 165, no. 1-3, pp. 325–331, 2009.

[47] K. J. Rockne and S. E. Strand, "Anaerobic biodegradation of naphthalene, phenanthrene, and biphenyl by a denitrifying enrichment culture," *Water Research*, vol. 35, no. 1, pp. 291–299, 2001.

[48] R. Dobson, M. H. Schroth, and J. Zeyer, "Effect of water-table fluctuation on dissolution and biodegradation of a multi-component, light nonaqueous-phase liquid," *Journal of Contaminant Hydrology*, vol. 94, no. 3-4, pp. 235–248, 2007.

[49] M. P. Suarez and H. S. Rifai, "Biodegradation rates for fuel hydrocarbons and chlorinated solvents in groundwater," *Bioremediation Journal*, vol. 3, no. 4, pp. 337–362, 1999.

Hindawi
Geofluids
Volume 2019, Article ID 8609682, 11 pages
https://doi.org/10.1155/2019/8609682

Research Article

Impact of Low- or High-Permeability Inclusion on Free Convection in a Porous Medium

Min Yan,[1] Chunhui Lu,[1] Jie Yang,[1] Yifan Xie,[1] and Jian Luo[2]

[1]*State Key Laboratory of Hydrology-Water Resources and Hydraulic Engineering, Hohai University, Nanjing, China*
[2]*School of Civil and Environmental Engineering, Georgia Institute of Technology, Atlanta, GA 30332-0355, USA*

Correspondence should be addressed to Chunhui Lu; clu@hhu.edu.cn

Received 4 July 2019; Revised 19 September 2019; Accepted 27 September 2019; Published 26 November 2019

Guest Editor: Xuan Yu

Density-driven free convection in porous media is highly affected by large-scale heterogeneity, typical of which are low- or high-permeability inclusions imbedded in homogeneous porous media. In this research, we applied the modified Elder problem to investigate the impact of low- or high-permeability inclusions on the migration of a dense, unstable salt plume. Sensitivity analyses were conducted in terms of the permeability contrast, the effective area (the area of the inclusion beneath the source zone), and the distance of the inclusion from the source zone, all of which were found to play a significant role in controlling the total mass flux released from the source into the media. Results show that (1) a high-permeability inclusion has stronger effects than low-permeability inclusion, due to significantly unbalanced solute distributions caused by accelerated solute transport, (2) the inclusion with a larger effective area has more potential to influence free convection, (3) free convection is more sensitive to the low-/high-permeability inclusion vertically closer to the source zone, and (4) free convection is more susceptible to the low-permeability inclusion horizontally closer to the source zone. For high-permeability inclusions, the inclusion horizontally closer to the source zone influences the transport process more significantly at the early stage, and conversely, the inclusion far from the source zone has a later impact. The results obtained could offer significant implications for understanding unstable density-driven flow and solute transport in porous media with structured heterogeneity.

1. Introduction

In groundwater systems, the fluid density gradient may vary as a function of concentration, temperature, and/or pressure of the fluid, which is of particular importance in the migration of solutes. The density gradient caused by a denser fluid overlying a light one may lead to the onset of the gravity-induced instabilities. Firstly, a boundary layer develops at the source zone through diffusion and grows to a certain critical thickness and then breaks into fingers moving downward rapidly, generating the instability (free convection) [1–3]. Over the years, numerical, laboratory, and field experiments have analyzed numerous examples of naturally occurring free convection, including seawater intrusion in coastal aquifers, leachate infiltration from waste disposal, salt lakes and saline disposal basins, and interaction between groundwater-surface water [e.g., [4–12]]. Free convection significantly enhances the hydrodynamic mixing of denser solute with its ambient groundwater over lager spatial scales within shorter time scales compared with diffusion alone.

Heterogeneity in porous media can significantly affect the transport processes of free convection. In addition to the common assumption of homogeneous and isotropic hydrogeological settings in the studies of free convection processes (for exhaustive reviews on this topic, see [13–16]), heterogeneity has also been frequently investigated in previous studies. [8] conducted an experimental investigation of free convection in homogeneous, layered, and lenticular porous media to study the roles played by the heterogeneity. They noted that local-scale nonhomogeneity of the flow results in a complex and highly dispersed plume. [17] found that in flow through natural porous media, heterogeneity can cause perturbation or interfacial disturbances over many spatial scales (from slight differences in pore geometry to larger heterogeneities on the scale of the dense plume source). [18] improved our understanding of instability phenomena

that increased correlation length scales and increased variance of the permeability field could promote stability. The experimental and theoretical studies mentioned above have proved that the passive solute transport in natural porous media is controlled by the spatial variations in heterogeneous fields. Another notable result in the field of free convection was the quantitative indicators developed by [19], which include solute fluxes, solute presence, center of gravity, and finger penetration depth, providing visual inspection to assess numerical outputs (e.g., [20–23]). [15] carried out a numerical investigation of free convection and considered various patterns of heterogeneity ranging from periodically structured to random permeability fields. The results suggested that heterogeneity triggers the onset of instabilities and also tend to dissipate them at later times by enhancing dispersive mixing. They also found that structured heterogeneity allows instabilities to propagate at a modest combination of fracture aperture and separation distances, while disordered heterogeneity tends to dissipate convection through dispersive mixing. [24] evaluated free thermal convection in randomly heterogeneous media.

In heterogeneous porous media, low- or high-permeability inclusions imbedded in homogeneous porous media are particularly common representations of large-scale heterogeneity that can significantly influence solute transport [25]. Post and Simmons [26] used sand tank experiments and numerical models to investigate how discrete low-permeability structures affect free convection at the scale of individual lenses. They found two different mechanisms exist: interlayer convection for high-permeability regions and intralayer convection for low-permeability regions. The result demonstrates that the solute transport driven by a source zone at the top of the domain is a complicated function of the geometry of the permeability structure and contrast between low- and high-permeability regions.

Moreover, modes of free convection in fractured low-permeability media have been explored by [27]. Their results showed that free convection may be common in thick shale sequences, and analyses neglecting both inter- and intrafracture convection modes may significantly underestimate the likelihood of the occurrence of free convection. [28] studied fracture networks containing continuous, discontinuous, orthogonal, and/or inclined discrete fractures embedded in a low-permeability rock matrix and found that fracture networks can inhibit or promote convection depending on the fracture network geometry. [29] investigated combined inter- and intrafracture free convection in fractured porous rock and suggested that it is challenging to predict the convective pattern under such conditions.

In this paper, we focus on investigating the effects of the distribution of low- or high-permeability inclusions on free convection. We introduce structured heterogeneity in porous media in a modified setting of the Elder problem [30, 31], which is a commonly used example of free convection. The variable-density flow and solute transport in the system were simulated using SEAWAT-2000 [32]. The permeability and location (horizontal and vertical) of the low- or high-permeability inclusions were set to be variable. Their effects on free convection were quantitatively assessed using three assessment indicators, including the total solute mass (TM), Sherwood number (Sh), and solute center of gravity (COG). The main objective of the current study was to test the sensitivity of the location of the low-/high-permeability inclusions on free convection. The expected results will advance our understanding of unstable density-drive flow and solute transport processes under the effect of structured heterogeneity.

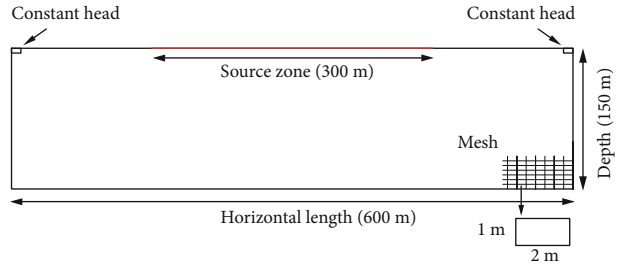

Figure 1: Model geometry of the Elder problem.

2. Methodology

2.1. Modified Elder Problem. The Elder problem is a classic example of free convection phenomena [33, 34]. It was first studied by [30, 31] for thermal convection (referred as "original" Elder problem) and developed later by [35] into a solute transport problem (referred as "classic" Elder problem). The Elder problem is chosen here for two reasons: (1) it is a classic example for free convection in which the flow is purely driven by density gradients and (2) the Elder problem, especially under the homogeneous condition, has been extensively investigated and discussed in both experimental and numerical simulation researches.

The Elder problem used in this study (Figure 1) is modified from the one used in [21], by transforming the fixed-concentration boundary at the bottom into a no-flux boundary while keeping the domain geometry and boundary conditions unchanged. This transformation makes the solute transport process more realistic under natural conditions. Initially, the domain is filled with freshwater with a hydrostatic head distribution. The two-dimensional domain has a length of 600 m and a depth of 150 m. The domain boundaries are impermeable except that constant heads are prescribed at the top left and right corners as two outlets for fluid and solute. A fixed concentration boundary condition (C_{source} = 280 kg/m^3 [20, 23]) is imposed at the source zone. The density of the source zone (ρ_{source}) is 1200 kg/m^3, which corresponds to a salt concentration of C_{source} = 280 kg/m^3. As abundant solutes diffused from the source zone accumulate at the top boundary, flow is generated by density gradients in the model domain.

2.2. Numerical Simulations

2.2.1. Simulation Tool. As indicated above, we employ SEAWAT-2000 [32] to simulate variable-density groundwater flow and solute transport in porous media, which combines

MODFLOW-2000 and MT3DMS into a single computer program.

The governing equation for saturated variable-density groundwater flow in terms of freshwater head is expressed by [36]

$$\nabla \cdot \left[\rho \mathrm{K}_f \left(\nabla \cdot \mathrm{h}_f + \frac{\rho - \rho_0}{\rho_0} \cdot \nabla z\right)\right] = \rho S_f \frac{\partial h_f}{\partial t} + n \frac{\partial \rho}{\partial t} + \rho_s q_s, \tag{1}$$

where z (L) is the vertical coordinate directed upward; h_f (L) is the equivalent freshwater head; K_f (LT^{-1}) is the equivalent freshwater hydraulic conductivity; ρ (ML^{-3}), ρ_0 (ML^{-3}), and ρ_s (ML^{-3}) are the densities of fluid, freshwater, and source/-sink, respectively; n (-) is effective porosity; S_f (L^{-1}) is the equivalent freshwater storage coefficient; t (T) is the time; and q_s (T^{-1}) is the flow rate per unit volume of aquifer of the source/sink.

The solute transport model involving advection, molecular diffusion, and mechanical dispersion is given as

$$\frac{\partial C}{\partial t} = \nabla \cdot (D \nabla C) - \nabla \cdot (vC), \tag{2}$$

where C (ML^{-3}) is dissolved concentration; D ($\mathrm{L}^2\mathrm{T}^{-1}$) is the hydrodynamic dispersion coefficient tensor; and v (LT^{-1}) is the pore water velocity vector.

An empirical linear relationship is present between salt concentration C and density ρ (e.g., [37, 38]):

$$\rho = \rho_0 + \varepsilon C, \tag{3}$$

where ε (-) has a dimensionless value of 0.7143 [32].

2.2.2. Instability Descriptor. Stratification formed by a denser fluid overlying a lighter fluid develops high a density gradient and causes gravity-driven instability. The instability of the Elder problem can be quantified by the dimensionless Rayleigh number [15]:

$$\mathrm{Ra} = \frac{k \rho_0 g \alpha H}{\mu n D}, \tag{4}$$

where $\alpha = (\rho_{\mathrm{source}} - \rho_0)/\rho_0$ is the dimensionless density contrast coefficient; H (L) is the height of the model domain; g (LT^{-2}) is the gravitational acceleration; μ ($\mathrm{ML}^{-1}\mathrm{T}^{-1}$) is the dynamic viscosity; D ($\mathrm{L}^2\mathrm{T}^{-1}$) is the molecular diffusion coefficient; and k (L^2) is the intrinsic permeability. The value of Ra measures the relation between buoyancy-driven transport and diffusion. The values of the parameters in the equation can be found in Table 1. The critical Ra is 4π for Horton-Rogers-Lapwood problem with infinitely extended horizontal porous layer and constant temperature at upper and lower boundaries, but is zero for the classic Elder problem [23, 39] since the fixed concentration boundary at both upper and lower boundaries decides the inevitable concentration gradient and thus free convection. The calculated Rayleigh number of our modified Elder problem approaches 400, which is far greater than the critical value $\mathrm{Ra}_{\mathrm{cr}}$, ensuring the occurrence of free convection. Note that when considering a low-/high-permeability inclusion in the domain, the value of Ra alters accordingly.

Table 1: Simulation parameters for the modified Elder problem [35].

Parameter	Variable	Value	Unit
Model length	L	600	m
Model depth	H	150	m
Porosity	n	0.1	—
Intrinsic permeability	k_c	4.845×10^{-13}	m^2
Hydraulic conductivity	K_c	0.4017	m/d
Molecular diffusion coefficient	D	3.565×10^{-6}	$\mathrm{m}^2 \cdot \mathrm{s}^{-1}$
Dynamic viscosity	μ	1.0×10^{-3}	$\mathrm{kg} \cdot \mathrm{m}^{-1} \cdot \mathrm{s}^{-1}$
Gravitational acceleration	g	9.81	$\mathrm{m} \cdot \mathrm{s}^{-2}$
Specific storage	S_s	1.0×10^{-4}	m^{-1}
Density of freshwater	ρ_0	1000	$\mathrm{kg} \cdot \mathrm{m}^{-3}$
Density of source zone	ρ_{source}	1200	$\mathrm{kg} \cdot \mathrm{m}^{-3}$
Concentration of source zone	C_{source}	280	$\mathrm{kg} \cdot \mathrm{m}^{-3}$

2.2.3. Spatial and Temporal Discretization. Previous studies have proved that free convection processes in the Elder problem are largely influenced by grid discretization [19, 40]. [18] showed that too coarse grid discretization may result in large errors and numerical dispersion, which can reshape the salt plumes and transform the developments of unstable fingers after their generation. As suggested by [41], $\Delta x = 2$ m (horizontal) and $\Delta z = 1$ m (vertical) are adopted in this study to avoid the influences of grid discretization, resulting in a total of 300×150 rectangular cells.

As the bottom boundary condition of the modified Elder problem is transformed to be a no-flux boundary, the system cannot reach its steady state until the entire domain is filled with saltwater with a concentration equal to that of the source zone. Therefore, the simulation time is extended to 18,250 days (50 yrs), such that a significant amount of solute mass could enter into the domain.

2.2.4. Low- or High-Permeability Inclusion. A low-/high-permeability (kv) inclusion is imbedded in the modeled porous media of constant permeability (kc). The permeability contrast k_v/k_c is set to be 0.01 and 0.1 for a low-permeability inclusion, 10, 100, and 1000 for a high-permeability inclusion, and 1 for the homogeneous porous media as a reference case.

Due to the symmetry of the model domain, only the left half of the domain was subjected to the simulations (Figure 2). Sixteen zones were selected for the low-/high-permeability inclusion, each with a rectangular area of 40 m × 20 m. Their locations, labeled by their horizontal and vertical positions (Figure 2), were selected to assess the behavior of

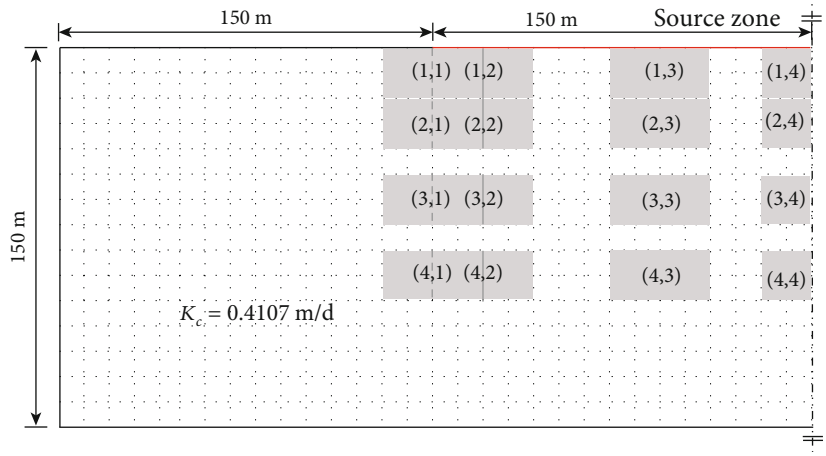

Figure 2: The selected locations to place the low-/high-permeability inclusion (the grey rectangles). The locations are labeled by their horizontal and vertical positions, e.g., the low-/high-permeability region is placed close to the source zone center at (1, 4) and far from the source zone at (1, 1). Note that the regions at the furthest locations ((1, 1), (2, 1), (3, 1), and (4, 1)) are partially out of the range of the source zone.

Table 2: Setup of the simulation cases, with a permeability contrast ranging from 0.01 to 1000, and different positions to placing the low (high)-permeability region. The positions are marked in Figure 2.

k_v/k_c	Position	Total time (yrs)	Step size (d)
0.01	(1, 1)~(1, 4)		2
0.1	(1, 1)~(4, 4)		2
10	(1, 1)~(4, 4)	50	2
100	(1, 1)~(1, 4)		0.5
1000	(1, 1)~(1, 4)		0.2

the free convection in response to the changing location of the low (high)-permeability inclusion. Note that the leftmost two inclusions are partially overlapped. Preliminary simulations showed that the low (high)-permeability inclusions located close to the top boundary affect the free convection mostly. Therefore, emphasis was more put on the low (high)-permeability inclusions situated in regions from (1, 1) to (1, 4) (Figure 2). For cases of $kv/kc = 0.01$, 100, and 1000, four positions of inclusions are considered (i.e., from (1, 1) to (1, 4)), while for cases of $kv/kc = 0.1$ and 10, 16 positons are adopted (i.e., from (1, 1) to (4, 4)). Table 2 lists the cases with low (high)-permeability inclusions. By considering a homogeneous case, a total of 45 cases are simulated.

2.3. Assessment Indicators. To quantify the behavior of free convection in response to the permeability/location of the low-/high-permeability inclusions, three assessment indicators [19, 21–23] are used in this study.

2.3.1. Total Solute Mass (TM). TM is a parameter to quantify time-variable solute mass (normalized) present in the model domain, calculated as [21]

$$\mathrm{TM} = \frac{1}{LH}\int_{x=0}^{x=L}\int_{z=0}^{z=H} C_{x,z}\,dxdz, \tag{5}$$

where $C_{x,z}$ is the normalized concentration ranging within [0, 1] at (x, z). The value of TM varies from 0 when the domain has no solute mass to 1 when the domain is fully filled with saltwater.

2.3.2. Sherwood Number (Sh). Sh is defined as the ratio of actual mass transfer due to free convection during the transient state to the rate of mass transfer due to diffusion, calculated as [14]

$$\mathrm{Sh} = \frac{QH}{WL_sD\Delta C}, \tag{6}$$

where Q is the solute mass flux across the top boundary, W and L_s are the width and length of the source zone, and ΔC ($\Delta C = 280\ \mathrm{kg/m^3}$) is the maximum concentration difference between freshwater and saltwater. A stable system with only diffusive transport has Sh = 1. Conversely, an unstable system with convection and diffusion, such as the classic Elder problem, has Sh > 1.

2.3.3. Center of Gravity (COG) of the Plume. COG describes the horizontal and vertical transient gravity center of solute plume present in the domain. It is one of the most important stochastic characteristics and can be calculated through spatial moments:

$$M(m, n) = \sum_j \sum_i x_i^m z_j^n C_{ij}, \tag{7}$$

where the summation is executed for all cells of the model grid; C_{ij} is the normalized concentration of cell (i, j); x_i and z_j are coordinates of the cell; and m and n are integer power

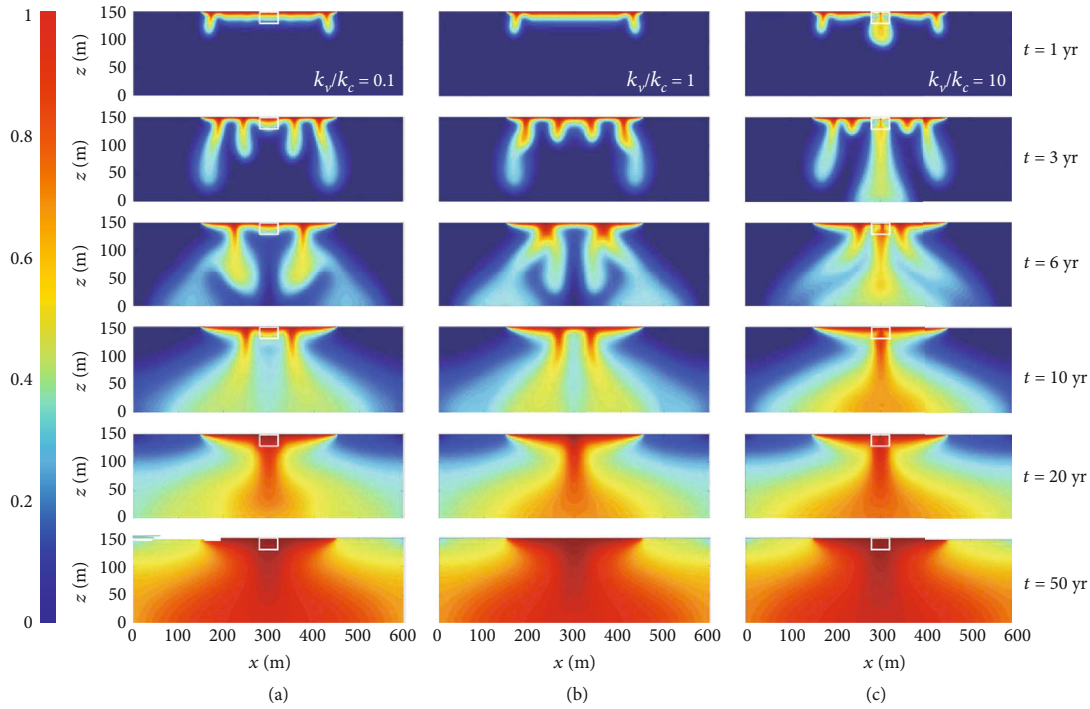

FIGURE 3: Concentration distributions of the homogeneous case ($k_v/k_c = 1$) and heterogeneous cases ($k_v/k_c = 0.1$, 10) at different times. The low-/high-permeability regions are marked by the white rectangles.

exponents that define the moment order. Subsequently, the gravity center (x_0, z_0) is expressed by

$$\left.\begin{aligned} x_0 &= \frac{M(1,0)}{M(0,0)} \\ z_0 &= \frac{M(0,1)}{M(0,0)} \end{aligned}\right\}. \tag{8}$$

COG can indicate the movement of the salt plumes in the heterogeneous porous media in both vertical and horizontal direction.

3. Results and Discussion

3.1. Plume Development. Comparing the concentration distributions for the case of low-permeability inclusion ($k_v/k_c = 0.1$, Figure 3(a)), the homogeneous case ($k_v/k_c = 1$, Figure 3(b)), and the case of high-permeability inclusion ($k_v/k_c = 10$, Figure 3(c)), it can be observed that after three years five separate fingers were developed in the case of high-permeability region with one main finger generated underneath the high-permeability region in the middle, while only four fingers were generated in the case of low-permeability region and the homogeneous case. This indicates that a higher instability existed in the system of high-permeability region than the other two cases. The high-permeability region aggravates the imbalance by accelerating its transport in the local region, resulting in the deeper and wider penetration of the salt plumes. Conversely, the low-permeability region slows down the process of descending and spreading, such that the solute distributes more uniformly. Conclusion can be made that, in terms of instability, a higher permeability region in the domain has a pronounced impact on free convection, which would result in more solute mass entering into the domain at the same loading time. Hence, emphasis for discussion will be put on the cases with higher permeability region ($k_v/k_c > 1$) afterwards.

The concentration distributions in the domain with the high-permeability inclusion ($k_v/k_c = 10$) located at three different horizontal positions are plotted in Figure 4. The salt plumes tend to preferentially develop underneath the high-permeability region, consistent with our aforementioned conclusion that a higher permeability region can result in a faster flow speed and a less uniform concentration distribution. After one year, an additional finger is generated when the high-permeability region is located within the source zone (Figure 4(c)). By three years, except case (1, 1) with a less effective area, the main finger developed from the high-permeability region starts to reach the domain bottom, earlier than that in the homogeneous case. Surprisingly, at approximately 15 years, all fingers have merged into a single dense plume. This may be because the area of the higher-permeability inclusion is relatively small in comparison to the total domain area. The development of the salt plumes under all cases experiences such a process, i.e., individual fingers developed firstly and merged into one large plume later. However, diversity existed in the solute migration paths that depended on the position of the high-permeability region. Eventually, as the density gradient dissipates, diffusion becomes the primary transport mechanism, indicating that the system state was gradually transformed from instability to stability.

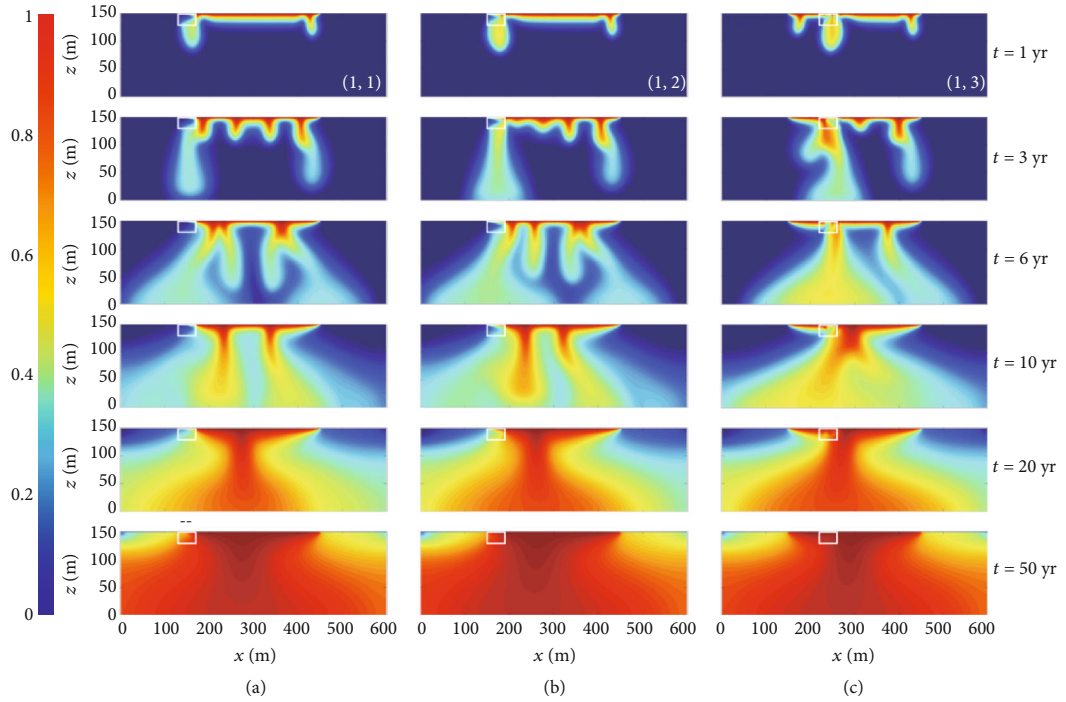

FIGURE 4: Concentration distributions in the domain with the high-permeability region ($k_v/k_c = 10$) placed at different locations and at different times. The high-permeability regions are marked by the white rectangles.

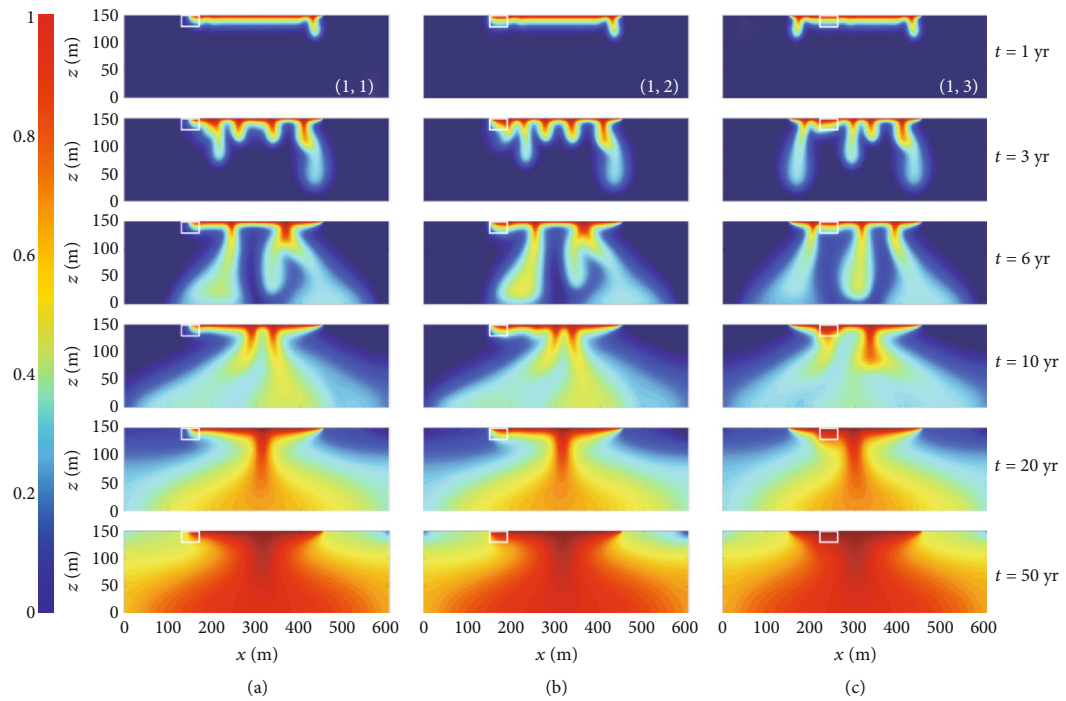

FIGURE 5: Concentration distributions in the domain with the low-permeability region ($k_v/k_c = 0.1$) placed at different locations and at different times. The low-permeability regions are marked by the white rectangles.

The concentration distributions for the domain with low-permeability regions ($k_v/k_c = 0.1$) located at three horizontal positions are different (Figure 5) from that for the high-permeability regions. By one year, it can be observed that downward solutes transport in all heterogeneous cases tends to be blocked by the low-permeability region, such that

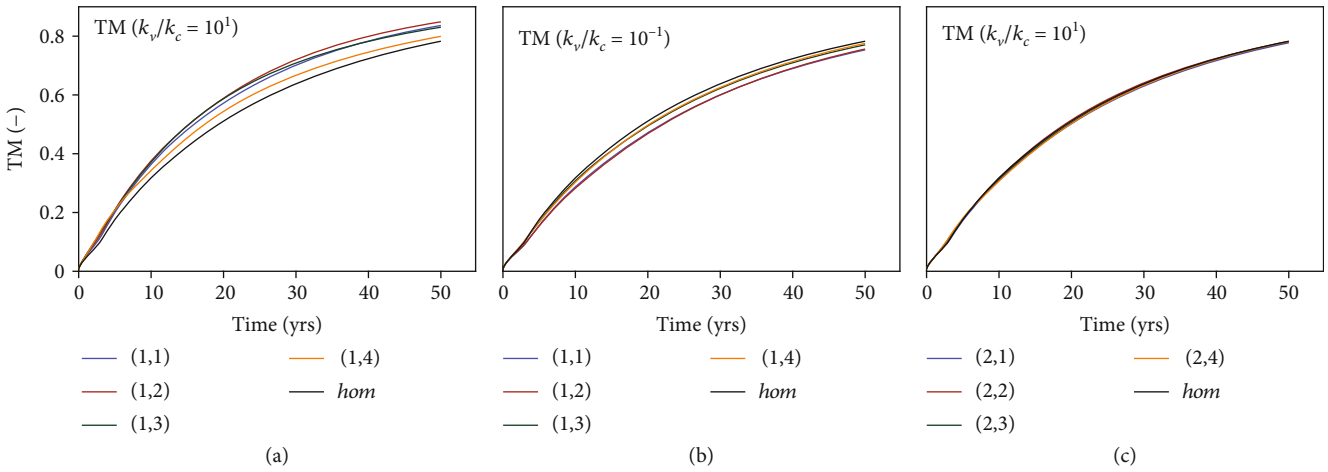

Figure 6: The calculated time-variable total solute mass (TM) for simulation cases with different permeability contrasts and locations.

only one finger was developed in two of the cases (Figures 5(a) and 5(b)). Three years after, the distributions show that part of salt plumes immigrate bypass the low-permeability regions rather than passing through them. Fifty years after, the systems approached their steady state with the plumes symmetrically distributed.

Insights into the plume development have provided qualitative explanations for the ways how the presence of a spatially varied low-/high-permeability zone affects free convection. It can be concluded that the high-permeability region ($k_v/k_c > 1$) in the domain has more potential to influence the transport process of free convection in time and space (e.g., fingering speed, number, and pattern). Quantitative evaluation of the behavior of the system in response to the presence of a low-/high-permeability region requires further investigation using the assessment indicators.

3.2. Quantitative Assessment

3.2.1. Effects on Total Solute Mass (TM). The breakthrough curves for TM of the model domain with different configurations of the low-/high-permeability region were plotted in Figure 6. It can be concluded that the high-permeability region accelerates the mass transport into the domain and the low-permeability region slows down that transport processes, evidenced by TM curves overtopping (Figure 6(a)) and underneath (Figure 6(b)) the one for homogeneous case, respectively. The TM curves almost coincide with each other when the high-permeability region is placed vertically further from the source zone (Figure 6(c)). This indicates that the high-permeability region vertically closer to the source zone affects the mass transport in terms of TM more significantly.

For the domain with high-permeability regions close to the source zone (Figure 6(a)), linear increasing trends of the TM can be identified at an early stage (<5 yr) while the big main fingers develop under high concentration gradients (Figure 4). Additionally, the transient TM is higher when the high-permeability region is closer to the source zone (position (1, 4), Figure 6(a)) at the early stage. The TM increasing speeds slow down gradually when salt is filling the domain after the stage of finger developing.

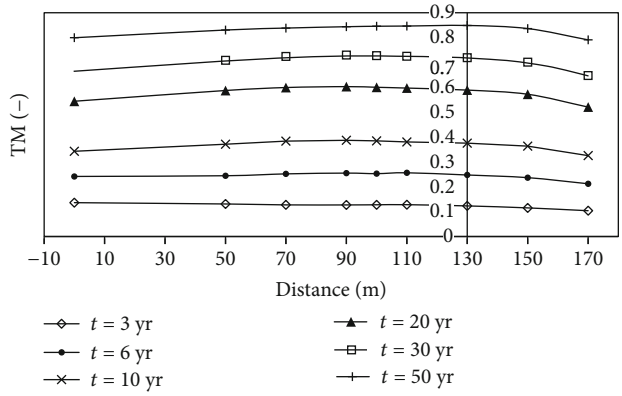

Figure 7: The calculated total solute mass (TM) in the domain with the high-permeability region ($k_v/k_c = 10$) being placed at different horizontal distances to the source zone center.

To test how the horizontal distance between the source zone center and the high-permeability region ($k_v/k_c = 10^1$) affects the mass transport process, TM values are calculated individually when the high-permeability region is horizontally moved from the source zone center (distance = 0, Figure 7) to the side of the source zone (distance = 170, Figure 7). At the early stage, e.g., $t = 3$ yr, the TM shows a monotonic decreasing function, i.e., mass transports faster when the high-permeability region is close to the source zone due to easier finger generation. However, this trend does not exist anymore at the later stage, within which the maximum TM is found when the high-permeability region is close to the border of the source zone (distance = 130 m, still with the range of the source zone). When the high-permeability region is placed further sideward out of the range of the source zone (distance > 130 m), the acceleration effect on mass transport process becomes less pronounced. In summary, the distance between the high-permeability region and the source zone significantly determines their effect on the transport process in terms of total mass. The trends differ between different stages of the transport process. Initially, the location of the inclusion dominates the solute loading

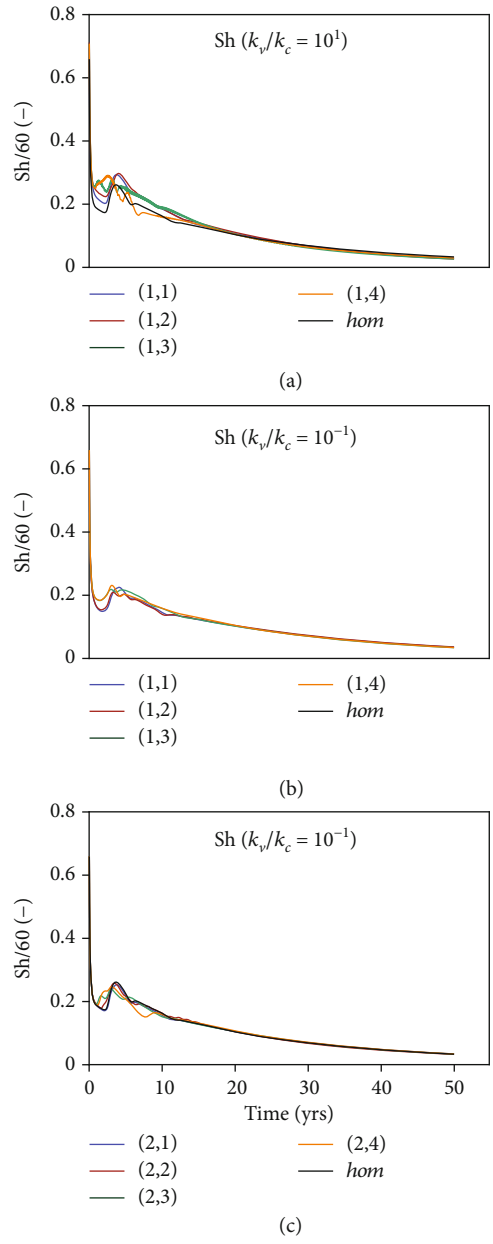

Figure 8: The calculated time-variable Sherwood number (Sh) for simulation cases with different permeability contrasts and locations.

process, while the total mass in the domain controls the speed of solute entering in to the domain at larger times. The time dependence of the TM on the location of inclusion is similar to the effect of dual domain mass transfer found in our previous study [20].

3.2.2. Effects on Sherwood Number (Sh). The calculated Sh values for the domain with different configurations of the low-/high-permeability regions are plotted in Figure 8, in which the Sh value is divided by 60 for better presentation. The results suggested that the high-permeability regions have upgraded the convectional mass transport, proved by higher Sh values than the homogeneous case (Figure 8(a)). At the early stage, this upgrading effect is more pronounced when the high-permeability region is placed at the source zone center (position (1, 4), Figure 8(a)). The upgradation is more pronounced when the high-permeability region is placed vertically further from the source zone (Figure 8(c)). Conversely, the low-permeability regions tend to degrade the convectional mass transport with lower Sh numbers than the homogenous case (Figure 8(b)). However, these upgradation or degradation of convectional mass transport becomes less significant at the later stage with the Sh values of all cases converging to a single value.

3.2.3. Effects on the Center of Gravity (COG). Nonuniform concentration distributions and fingering processes can certainly result in horizontal and vertical bias of the COG. Generally, solutes transport preferentially takes the path through more permeable area, i.e., salt plumes bypass the low-permeability region and preferentially passes through the high-permeability region. As a result, the horizontal COG (COG-x) shows right-side biases from the middle of the domain under the presence of the low-permeability region (Figure 9(a)) in the domain and left-side biases under the presence of the high-permeability region (Figure 9(b)). Note that the COG-x shows no difference from the homogenous case when the low (high)-permeability regions are placed in the middle of the domain (position (1, 4), Figure 9) due to the symmetric distribution of the salt plumes. For the domain with low-permeability regions (Figure 9(a)), fingers preferentially develop on the right side of the domain, with the bias of the COG-x reaching their maximums when the main fingers touch the domain bottom. Later, the plumes start to develop horizontally with the bias of COG-x being continuously reduced. However, double peaks of the bias of COG-x can be observed for the cases of high-permeability regions (Figure 9(b)), with the first one reached when the main finger touches the domain bottom and the second one reached due to a large amount of solute accumulation and diffusion on the left side of the domain. Additionally, the low-/high-permeability region placed the farthest from the source zone (but still within the source zone, position (1, 2), Figure 9) causes the most significant bias of COG-x. At the late stage, the COG-x moves continuously towards the domain center as secondary fingers go reach the bottom and salt plumes spread by diffusion to the entire space of the domain.

The vertical COG (COG-y) for all cases shows that the stage of fast descend due to the penetration of the fingers, followed by a stable stage during which the COG-y slightly rebounds since the fingers touch the domain bottom. The location of the low-permeability region in the domain (Figure 9(c)) has less effect on the COG-y than that of the high-permeability region (Figure 9(d)). In particular, for the domain with high-permeability region in the domain, deeper COG can be reached when the region is closer to the source (position (1, 4), Figure 9(d)) due to less lateral transport of the solute at the early stage.

4. Summary and Conclusion

In this study, we focused on investigating the influence of permeability inclusions on density-driven free convection.

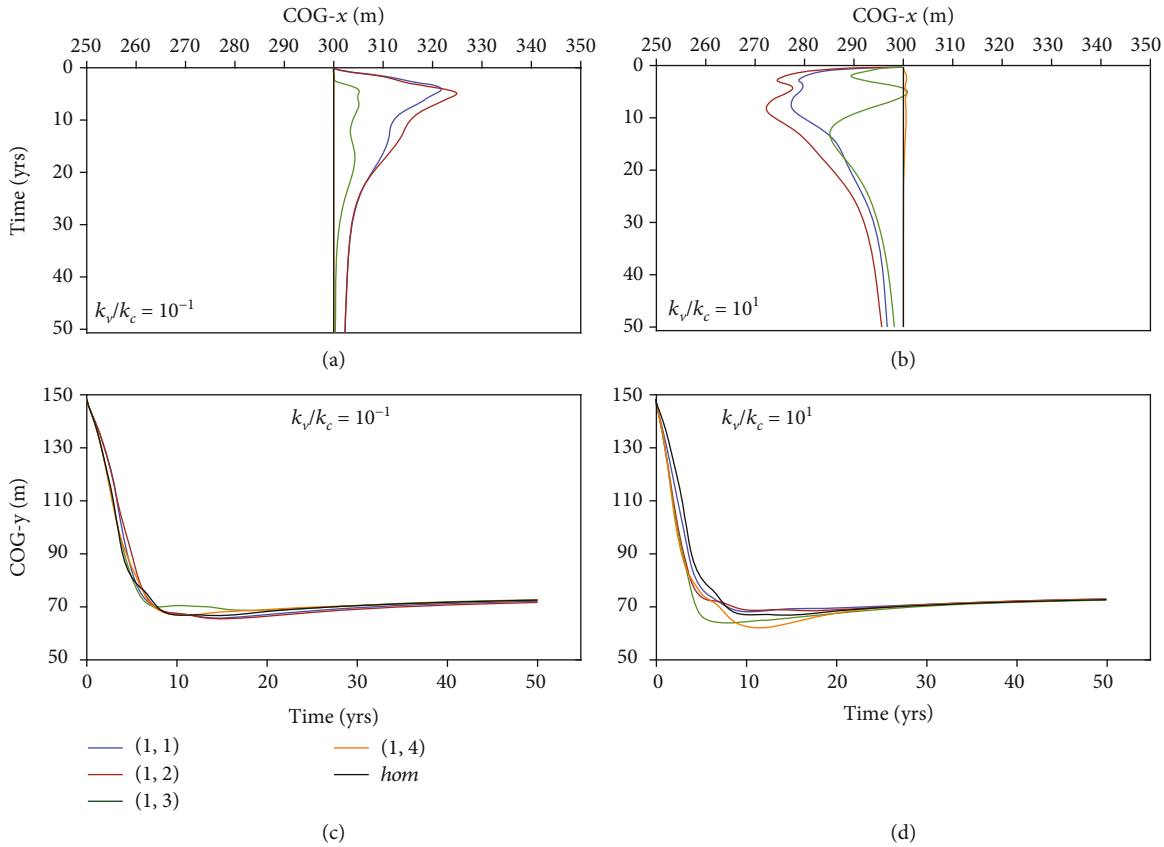

FIGURE 9: The calculated horizontal and vertical gravity center of the salt mass (COG-x and COG-y) in the domain with (a, c) low-permeability regions ($k_v/k_c = 0.1$) and with (b, d) high-permeability regions ($k_v/k_c = 10$).

We introduced the structured heterogeneity in porous media for a modified setting of the Elder problem. The effects of the permeability and the location (horizontal and vertical) of the low-/high-permeability inclusion on the free convection process were assessed using three assessment indicators: total solute mass (TM), Sherwood number (Sh), and solute center of gravity (COG). Despite the simplified model assumed, the obtained numerical results have important implications for understanding the unstable density-driven flow and solute transport processes in the presence of structured heterogeneity. The key findings of the study are as follows:

(1) In comparison to homogeneous systems, heterogeneity in permeability makes the system more unstable. A high-permeability inclusion shows stronger effects on the free convectional process than a low-permeability inclusion at the early stage, with significantly unbalanced solute distributions and accelerated transport processes

(2) Free convection is more sensitive to the low-/high-permeability inclusion vertically closer to the source zone, revealed in the mostly influenced breakthrough curves for total solute mass and Sherwood number

(3) Free convection is more susceptible to the low-permeability inclusion horizontally far from the source zone center. For high-permeability inclusions, by contrast, the inclusion horizontally closer to the source zone center influences the convectional transport process more significantly at the early stage, while the inclusion far from the source zone center has more significant influences at the late stage

The results obtained in the current study are based on the Elder problem, which neglects the boundary conditions in real situations. For example, in a coastal setting, one of the vertical boundaries should be the coastal boundary. Under such conditions, a constant head inland boundary with a constant salt concentration is usually defined, resulting in seawater intrusion in a coastal aquifer. The consideration of real situations incorporated with the effect of a low-/high-permeability inclusion should be included in future studies.

Data Availability

The data used to support the findings of this study are included within the article.

Conflicts of Interest

The authors declare that they have no conflicts of interest.

Acknowledgments

C. Lu acknowledges the financial support from the National Key Research Project (2018YFC0407200), the National Natural Science Foundation of China (51679067 and 51879088), the Fundamental Research Funds for the Central Universities (2018B42814), and the "111" Project (B17015). Y. Xie acknowledges the financial support from the National Natural Science Foundation of China (41702243). All the results/data have been included in the paper.

References

[1] R. A. Wooding, "Free convection of fluid in a vertical tube filled with porous material," *Journal of Fluid Mechanics*, vol. 13, no. 1, pp. 129–144, 1962.

[2] R. A. Wooding, S. W. Tyler, and I. White, "Convection in groundwater below an evaporating Salt Lake: 1. Onset of instability," *Water Resources Research*, vol. 33, no. 6, pp. 1199–1217, 1997.

[3] R. A. Wooding, S. W. Tyler, I. White, and P. A. Anderson, "Convection in groundwater below an evaporating Salt Lake: 2. Evolution of fingers or plumes," *Water Resources Research*, vol. 33, no. 6, pp. 1219–1228, 1997.

[4] E. O. Frind, "Simulation of long-term transient density-dependent transport in groundwater," *Advances in Water Resources*, vol. 5, no. 2, pp. 73–88, 1982.

[5] P. S. Huyakorn, P. F. Andersen, J. W. Mercer, and H. O. White Jr., "Saltwater intrusion in aquifers: development and testing of a three-dimensional finite element model," *Water Resources Research*, vol. 23, no. 2, pp. 293–312, 1987.

[6] H. Kooi, J. Groen, and A. Leijnse, "Modes of seawater intrusion during transgressions," *Water Resources Research*, vol. 36, no. 12, pp. 3581–3589, 2000.

[7] H. A. Michael, K. C. Scott, M. Koneshloo, X. Yu, M. R. Khan, and K. Li, "Geologic influence on groundwater salinity drives large seawater circulation through the continental shelf," *Geophysical Research Letters*, vol. 43, no. 20, pp. 10,782–10,791, 2016.

[8] R. A. Schincariol and F. W. Schwartz, "An experimental investigation of variable density flow and mixing in homogeneous and heterogeneous media," *Water Resources Research*, vol. 26, no. 10, pp. 2317–2329, 1990.

[9] R. A. Schincariol, F. W. Schwartz, and C. A. Mendoza, "On the generation of instabilities in variable density flow," *Water Resources Research*, vol. 30, no. 4, pp. 913–927, 1994.

[10] C. T. Simmons and K. A. Narayan, "Mixed convection processes below a saline disposal basin," *Journal of Hydrology*, vol. 194, no. 1–4, pp. 263–285, 1997.

[11] J. D. Stevens, J. M. Sharp Jr., C. T. Simmons, and T. R. Fenstemaker, "Evidence of free convection in groundwater: field-based measurements beneath wind-tidal flats," *Journal of Hydrology*, vol. 375, no. 3-4, pp. 394–409, 2009.

[12] R. L. Van Dam, C. T. Simmons, D. W. Hyndman, and W. W. Wood, "Natural free convection in porous media: first field documentation in groundwater," *Geophysical Research Letters*, vol. 36, no. 11, 2009.

[13] B. Gebhart, Y. Jaluria, R. L. Mahajan, and B. Sammakia, *Buoyancy-Induced Flows and Transport*, Hemisphere Publishing Corp., Washingtong DC., 1988.

[14] D. A. Nield and A. Bejan, *Convection in Porous Media*, Springer-Verlag, New York, 2013.

[15] C. T. Simmons, T. R. Fenstemaker, and J. M. Sharp Jr., "Variable-density groundwater flow and solute transport in heterogeneous porous media: approaches, resolutions and future challenges," *Journal of Contaminant Hydrology*, vol. 52, no. 1-4, pp. 245–275, 2001.

[16] C. T. Simmons, "Variable density groundwater flow: from current challenges to future possibilities," *Hydrogeology Journal*, vol. 13, no. 1, pp. 116–119, 2005.

[17] D. E. Moissis and M. F. Wheeler, "Effect of the structure of the porous medium on unstable miscible displacement," in *Dynamics of Fluids in Hierachical Porous Medida*, J. H. Cushman, Ed., pp. 243–271, Academic, San Diego, California, 1990.

[18] R. A. Schincariol, F. W. Schwartz, and C. A. Mendoza, "Instabilities in variable density flows: stability and sensitivity analyses for homogeneous and heterogeneous media," *Water Resources Research*, vol. 33, no. 1, pp. 31–41, 1997.

[19] A. Prasad and C. T. Simmons, "Unstable density-driven flow in heterogeneous porous media: A stochastic study of theElder[1967b] "short heater" problem," *Water Resources Research*, vol. 39, no. 1, pp. SBH 4-1–SBH 4-21, 2003.

[20] C. Lu, L. Shi, Y. Chen, Y. Xie, and C. T. Simmons, "Impact of kinetic mass transfer on free convection in a porous medium," *Water Resources Research*, vol. 52, no. 5, pp. 3637–3653, 2016.

[21] V. E. A. Post and H. Prommer, "Multicomponent reactive transport simulation of the Elder problem: effects of chemical reactions on salt plume development," *Water Resources Research*, vol. 43, no. 10, 2007.

[22] A. Prasad and C. T. Simmons, "Using quantitative indicators to evaluate results from variable-density groundwater flow models," *Hydrogeology Journal*, vol. 13, no. 5-6, pp. 905–914, 2005.

[23] Y. Xie, C. T. Simmons, A. D. Werner, and J. D. Ward, "Effect of transient solute loading on free convection in porous media," *Water Resources Research*, vol. 46, no. 11, 2010.

[24] V. T. Nguyen, T. Graf, and C. R. Guevara Morel, "Free thermal convection in heterogeneous porous media," *Geothermics*, vol. 64, pp. 152–162, 2016.

[25] J. Luo and O. A. Cirpka, "How well do mean breakthrough curves predict mixing-controlled reactive transport?," *Water Resources Research*, vol. 47, no. 2, 2011.

[26] V. E. A. Post and C. T. Simmons, "Free convective controls on sequestration of salts into low-permeability strata: insights from sand tank laboratory experiments and numerical modelling," *Hydrogeology Journal*, vol. 18, no. 1, pp. 39–54, 2010.

[27] C. T. Simmons, J. M. Sharp Jr., and D. A. Nield, "Modes of free convection in fractured low-permeability media," *Water Resources Research*, vol. 44, no. 3, 2008.

[28] K. Vujević, T. Graf, C. T. Simmons, and A. D. Werner, "Impact of fracture network geometry on free convective flow patterns," *Advances in Water Resources*, vol. 71, pp. 65–80, 2014.

[29] K. Vujevic and T. Graf, "Combined inter- and intra-fracture free convection in fracture networks embedded in a low-permeability matrix," *Advances in Water Resources*, vol. 84, pp. 52–63, 2015.

[30] J. W. Elder, "Transient convection in a porous medium," *Journal of Fluid Mechanics*, vol. 27, no. 3, pp. 609–623, 1967.

[31] J. W. Elder, "Steady free convection in a porous medium heated from below," *Journal of Fluid Mechanics*, vol. 27, no. 1, pp. 29–48, 1967.

[32] C. D. Langevin, W. B. Shoemaker, and W. Guo, "Modflow-2000, the US geological survey modular ground-water model–documentation of the SEAWAT-2000 version with the variable-density flow process (VDF) and the integrated MT3DMS transport process (IMT)," *U.S. Geological Survey Open-File Report*, vol. 03-426, p. 43, 2003.

[33] J. W. Elder, C. T. Simmons, H. J. Diersch, P. Frolkovič, E. Holzbecher, and K. Johannsen, "The Elder problem," *Fluids*, vol. 2, no. 1, p. 11, 2017.

[34] C. T. Simmons and J. W. Elder, "The Elder problem," *Groundwater*, vol. 55, no. 6, pp. 926–930, 2017.

[35] C. I. Voss and W. R. Souza, "Variable density flow and solute transport simulation of regional aquifers containing a narrow freshwater-saltwater transition zone," *Water Resources Research*, vol. 23, no. 10, pp. 1851–1866, 1987.

[36] C. D. Langevin and W. Guo, "MODFLOW/MT3DMS-based simulation of variable-density ground water flow and transport," *Groundwater*, vol. 44, no. 3, pp. 339–351, 2006.

[37] M. J. Simpson and T. P. Clement, "Theoretical analysis of the worthiness of Henry and Elder problems as benchmarks of density-dependent groundwater flow models," *Advances in Water Resources*, vol. 26, no. 1, pp. 17–31, 2003.

[38] H. Zhang and F. W. Schwartz, "Multispecies contaminant plumes in variable density flow systems," *Water Resources Research*, vol. 31, no. 4, pp. 837–847, 1995.

[39] M. van Reeuwijk, S. A. Mathias, C. T. Simmons, and J. D. Ward, "Insights from a pseudospectral approach to the Elder problem," *Water Resources Research*, vol. 45, no. 4, 2009.

[40] H. J. G. Diersch and O. Kolditz, "Variable-density flow and transport in porous media: approaches and challenges," *Advances in Water Resources*, vol. 25, no. 8–12, pp. 899–944, 2002.

[41] A. Al-Maktoumi, D. A. Lockington, and R. E. Volker, "SEAWAT 2000: modelling unstable flow and sensitivity to discretization levels and numerical schemes," *Hydrogeology Journal*, vol. 15, no. 6, pp. 1119–1129, 2007.

Hindawi
Geofluids
Volume 2019, Article ID 1494326, 16 pages
https://doi.org/10.1155/2019/1494326

Research Article

Behaviour of Tritium and Tritiogenic Helium in Freshwater Lens Groundwater Systems: Insights from Langeoog Island, Germany

Vincent E. A. Post,[1] **Georg J. Houben**,[1] **Leonard Stoeckl**,[1] **and Jürgen Sültenfuß**[2]

[1]*Federal Institute for Geosciences and Natural Resources (BGR), Stilleweg 2, D-30655 Hannover, Germany*
[2]*University of Bremen, Institute of Environmental Physics, Bremen, Germany*

Correspondence should be addressed to Vincent E. A. Post; vincent.post@bgr.de

Received 15 March 2019; Revised 13 July 2019; Accepted 21 July 2019; Published 7 October 2019

Academic Editor: Henrik Drake

Tritium (^{3}H) and its daughter product ^{3}He have been widely used as tracers in hydrological studies, but quantitative analyses of their behaviour in freshwater lenses and the transition zone in coastal aquifers are presently lacking. In this paper, the fate of ^{3}H and ^{3}He in the freshwater lens and the transition zone as well as the saltwater wedge is studied using numerical variable-density flow and transport models of different degrees of complexity. The models are based on the conditions on the German island of Langeoog, which is uniquely suited for this purpose because of the high ^{3}H concentration of the North Sea. It is found that most bomb-related tritiogenic ^{3}He still resides in the freshwater lens, making it a useful tracer for young (<60 years) groundwater. Differences in dispersive transport between ^{3}H and ^{3}He can cause an apparent age bias on the order of 10 years. Under favourable conditions, ^{3}H from seawater can penetrate deep into the offshore part of the aquifer and has potential to be used as a tracer to study saltwater circulation patterns. Our modelling suggests that the field-observed ^{3}H in the transition zone does not originate from seawater but from freshwater affected by the bomb peak. Yet in models with a low ($\alpha_L = 0.5$ m) dispersivity, no ^{3}H was sequestered into the transition zone and the transition zone width was underestimated. Better results were obtained with $\alpha_L = 5$ m, a value that is higher than in comparable modelling studies, which suggests that further work is needed to better understand the controls (tides, lithological heterogeneity, or transience of recharge and pumping) on transition zone mixing processes.

1. Introduction

Tritium (^{3}H) has been used extensively as a tracer in hydrogeological studies [1]. It is subject to beta-decay, and due to its half-life of 12.32 years, it is suitable to identify young groundwater. Tritium is naturally produced in the upper layers of the atmosphere but was also released in massive amounts by above-ground thermonuclear bomb testing in the 1950s and early 1960s [2]. Its atmospheric activity peaked around 1963-1964 and has been steadily falling since then.

When the tritium daughter product helium (^{3}He) is simultaneously analysed and after the so-called tritiogenic contribution (^{3}He$_{trit}$) is separated from other ^{3}He contributions (exchange with the atmosphere, excess air, and underground production), the apparent age τ (T) of a groundwater sample can be calculated based on the ratio of the ^{3}He$_{trit}$ over the ^{3}H concentration and the half-life constant:

$$\tau = \frac{1}{\lambda} \ln\left(1 + \frac{^3\mathrm{He}_{trit}}{^3\mathrm{H}}\right), \quad (1)$$

in which $\lambda = 0.05626$/yr is the radioactive decay rate of ^{3}H. Strong variations in recharge rates over time and mixing of groundwater of different ages are a source of uncertainty for the calculated value of τ [3]. Lumped parameter models provide another means to determine the age [4, 5] and are particularly useful for dealing with mixing effects. They are most effectively applied when tracer time series are available.

While tritium has been used extensively in terrestrial, fresh groundwater settings, it has seen less application in brackish and saline coastal environments. It has been mostly applied in freshwater lenses [6–8] to calculate recharge rates with the Vogel [9] model:

$$R = \frac{nB}{\tau} \ln\left(\frac{B}{(B-d)}\right), \quad (2)$$

where n is the porosity, B (L) is the lens thickness, and d (L) is the depth. The growing interest in the use of brackish and saline groundwater as feed water for desalination plants [10], however, necessitates a reevaluation of the usefulness of isotopic tracers for studying saltwater dynamics.

Tritium has been detected in brackish and saltwater in coastal aquifers in Tahiti [11], Israel [12], Morocco [13], the Netherlands [14], China [15], and Australia [16]. Sivan et al. [12] inferred the timing of seawater intrusion by comparing extrapolated tritium decay curves for saline groundwater samples to the history of ^{3}H concentrations in the Mediterranean Sea. Conclusive interpretations were not possible for the transition zone, as tritium may have derived from overlying freshwater and/or intruded seawater. That is, old, tritium-free seawater could have mixed with freshwater impacted by the bomb peak. In a similar manner, Han et al. [15] attributed the presence of ^{3}H in brackish groundwater to the mixing of young groundwater with old, ^{3}H-free saltwater from greater depth that is being drawn upwards by intensive groundwater abstraction.

While the tritium concentrations of most seas and oceans have returned to almost their prebomb era, natural background [17], a unique situation exists in northwestern Europe, where the discharge of water from nuclear processing plants sustains very high ^{3}H levels in the North Sea [18]. As a result, Stuyfzand et al. [14] were able to attribute ^{3}H values of up to ~30 TU (Tritium Units) in saline groundwater to the intrusion of ^{3}H-rich seawater. The main motivation for the present work was the discovery of ^{3}H in the transition zone between fresh and saline groundwater on the German island of Langeoog (Figure 1) during the study by Houben et al. [7]. They did not report these findings because their focus was on the freshwater lens, but tritium concentrations of up to 5.6 TU values were encountered in the transition zone that commences at 33 m below mean sea level (msl). It is conceivable that these values are due to the mixing of bomb peak-affected freshwater with intruded seawater, as put forward by Sivan et al. [12]. On the other hand, it may be that they originated from ^{3}H-enriched seawater, similar to the findings by Stuyfzand et al. [14].

The relationships between tritium, helium, and groundwater age in coastal aquifers have not been explored using quantitative models except for the highly simplified case of the Henry Problem [19]. This lack of quantitative analysis means that interpretations of the age structure of freshwater lenses and intruded seawater bodies often remain ambiguous. The North Sea's high tritium background concentrations provide an opportunity to study fresh and salt groundwater mixing processes along its coastlines. The objective of the present study is to extend the understanding of tritium dynamics in freshwater lenses in coastal aquifers. The focus is not only on the behaviour of ^{3}H within the freshwater but also on the fate of ^{3}H in the saltwater wedge and the offshore part of the aquifer. To this end, the spatiotemporal patterns arising from transient inputs and groundwater flow were investigated using numerical models, which are based on the hydrogeological conditions representative for Langeoog Island.

First, a set of models of increasing complexity was used to determine the influence for each of the various controlling factors separately. Attention is paid to the implications for submarine groundwater studies. The results are expected to be applicable to other study areas, especially along the North Sea shores, and also to other coastal localities where tritium concentrations persist above the natural background (e.g., [20]). Second, following a discussion of the model results, we address the issue of the origin of ^{3}H in the transition zone (i.e., whether it originates from the freshwater or the seawater). In what follows, the notation ^{3}He is used to indicate the tritiogenic ^{3}He contribution, omitting the subscript *trit*.

2. Study Area

The island of Langeoog is part of the chain of barrier islands that separate the shallow intertidal Wadden Sea from the North Sea (Figure 1). It first formed around 2,800 to 2,200 years before present as a sand bar, onto which dunes developed around the year 100 AD [21]. These remained largely unvegetated due to constant wind erosion until the 13th century. Thereafter, the formation of soils allowed the first human settlements. Over the following centuries, dune stabilization by vegetation and earthworks led to the formation of two parallel, west-east trending dune belts, which continue to dominate the island morphology.

Below the superficial dune and beach sands, the subsurface is made up of Holocene deposits of the Wadden Sea, underlain by mostly Pleistocene (glacio-) fluvial sediments [24]. Intercalated low-permeability sediments form an aquitard, which, because of glaciotectonic activity, is known to be spatially discontinuous (Figure 1(b)) and highly variable in thickness. In the northern part of the study area, the low-permeability unit consists of clay. No information is available about its offshore continuation. In the southern part, the unit is more heterogeneous and consists of fine sand, silt, and clay. It generally occurs below 20 m below mean sea level and, where well developed, it can reach a thickness of 10 m or more [23].

Three individual freshwater lenses exist on the island. Their separation is the result of occasional catastrophic storm flood inundations, storm floods, e.g., the Christmas flood of 1717, which caused large breaches of the dune belt in two locations [25]. Only the western lens is currently used, the outline of which can be inferred from the measured bulk apparent resistivity (Figure 1(c)) obtained from helicopter airborne electromagnetic (HEM) surveys [22]. Before the rise of tourism, the population obtained its water from rainwater and shallow dug wells. To satisfy the increasing demand, the

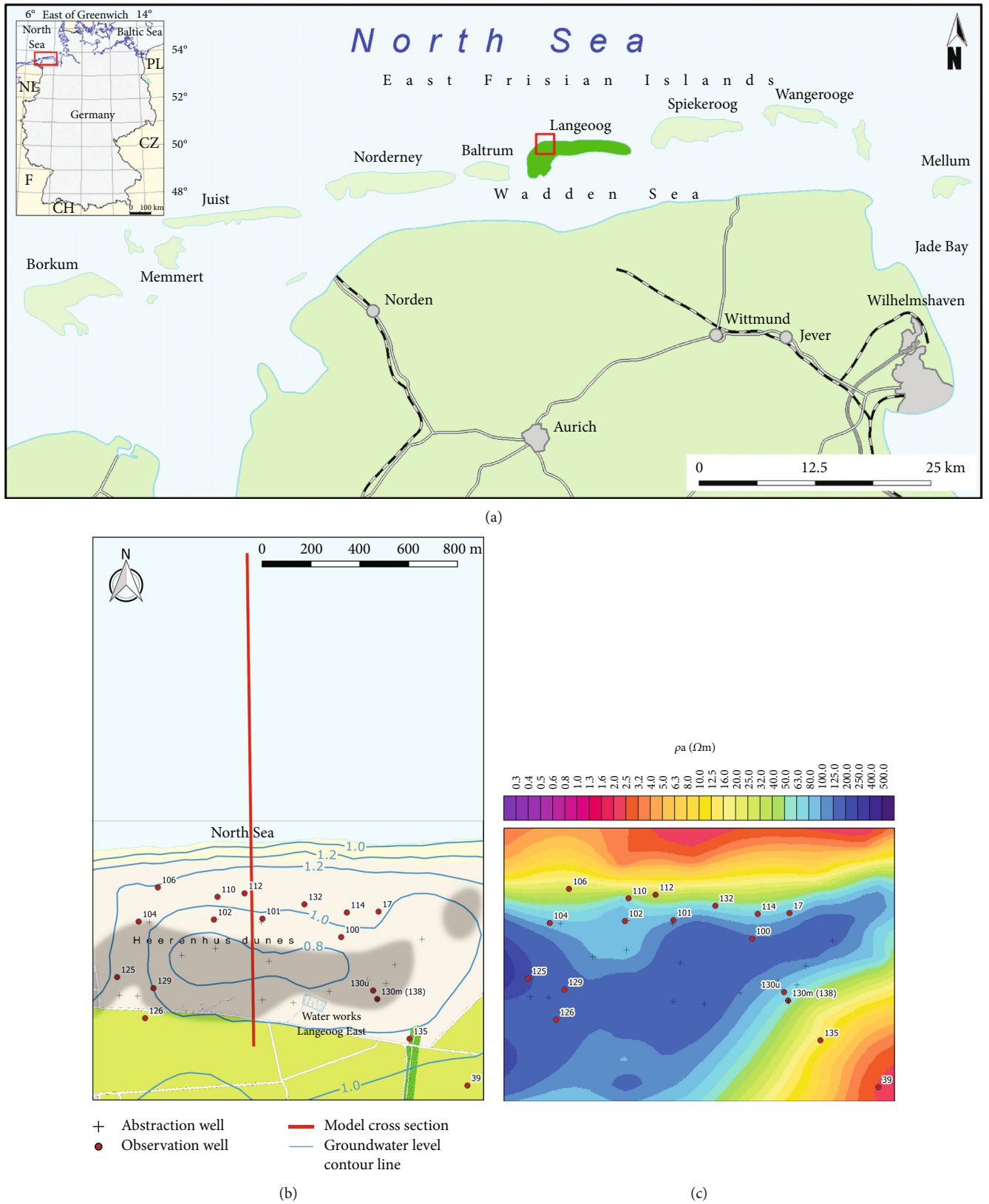

Figure 1: (a) Location of Langeoog Island, (b) map of the water supply area in the Heerenhus dune area showing the positions of the abstraction and observation wells, and (c) apparent bulk resistivity of the subsurface at 10 m below msl based on airborne electromagnetic measurements [22]. Blue lines in (b) represent the groundwater level elevation above msl during the summer of 1996, and the red line shows the projection of the model cross section. The shaded areas enclose the locations where Costabel et al. [23] found either no indication for the presence of the aquitard or found it to be <4 m thick. See their Figure 11 for the elevation of the top of the aquitard.

first three pumping wells were drilled in 1909 close to the village. After 1938, they were augmented and later replaced by wells drilled east of the village in the Heerenhus dunes, where a well field is still active today (Figure 1). Most wells are located in the Pirola Valley, which is situated between the two dune belts stretching W-E along the island's northern shoreline.

Extraction is done intermittently at pumping rates of 10 m^3/hr per well and is distributed over 20 small wells, with screens installed at varying depths between 10 and 18 m below sea level. As an effect of increasing tourism, water consumption continuously rose until the 1980s. It has significantly decreased since the 1990s due to the implementation of water-saving measures. Peak demand occurred in 1983 with 452,000 m^3/yr (Figure 2), while by 2011 the pumped volume was down to 333,000 m^3/yr, despite a mostly stable visitor number to the island since 1990 [7].

3. Methods

3.1. Sampling and Analysis. Basic information, such as well locations, groundwater levels, and pumping rates, were obtained from the local water supply company, the Oldenburgisch-Ostfriesischer Wasserverband (OOWV). Details about sampling and analytical techniques used to determine the chemical and isotopic composition of the groundwater samples were presented by Houben et al. [7]. He isotopes and tritium were analysed at the Institute of Environmental Physics of the University of Bremen [26]. The low detection limit for tritium (0.02 TU; 1 TU = $^3H/^1H$ ratio of $10^{-18} = 0.118$ TU) was achieved by using the ^3He accumulation method. For all sampling sites, duplicate samples were taken and analysed.

Transition zone water samples were obtained from observation well 17 (Figure 1), which has a long screen (from 33.6 to 57.6 m below sea level) reaching into the brackish water. Profiles of specific conductance (σ_{25}, i.e., the electrical conductivity for a reference temperature of 25°C) versus depth were obtained on two occasions, using an Ott™ Hydrolab multiparameter probe. After the first measurement, on 30 May 2013, the well was purged. An almost identical profile was afterwards established, as evidenced by a second measurement on 15 November 2013 (shown in Figure 3(a), alongside with model results that will be discussed later on). During the second sampling, three individual water samples were obtained by low-flow sampling using a Grundfos MP1 pump from three different depths, similar to Lee et al. [27]. It is known that coastal zone observation wells with long screens may indicate a higher position of the transition zone than in the aquifer [28, 29]. The resemblance between the specific conductance values of the three samples and the probe-derived values, as well as the HEM data [23], provides confidence though that the borehole data are representative for the groundwater.

3.2. Numerical Modelling. A two-dimensional section across the freshwater lens was considered (Figure 4). SEAWAT [31] was used to solve the following mass balance equations for fluid and solute, respectively,

$$\frac{\partial(n\rho)}{\partial t} + \nabla \cdot \left(\rho \vec{q}\right) = \bar{\rho} q_s, \tag{3}$$

$$\frac{\partial(nC)}{\partial t} = \nabla \cdot \left(n\vec{D} \cdot \nabla C\right) - \nabla \cdot \left(\vec{q} C\right) - q_s C_s + \Gamma, \tag{4}$$

where ρ is the fluid density ($M\,L^{-3}$), $\vec{q}$ is the Darcy flux ($L\,T^{-1}$), $\bar{\rho}$ is the density of water entering (or leaving) through a source (or sink) [$M\,L^{-3}$], q_s is the source's volumetric flow rate per unit volume of aquifer (T^{-1}), C is the concentration ($M\,L^{-3}$), $\vec{D}$ is the hydrodynamic dispersion tensor ($L^2\,T^{-1}$), and C_s is the solute concentration associated with water sources and sinks ($M\,L^{-3}$). The hydrodynamic dispersion tensor $\vec{D}$ is a function of the longitudinal (α_L) and transverse (α_T) dispersivity (L), as well as the effective molecular diffusion coefficient (D_e) ($L^2\,T^{-1}$).

The term Γ ($M\,L^{-3}\,T^{-1}$) in equation (4) accounts for the effects of radioactive decay. Three dissolved species, Cl, ^3H, and ^3He, were simulated. For Cl, $\Gamma = 0$, while for ^3H, the decay rate is $\Gamma = -\lambda C_H$, where the subscript H is used to indicate that C represents the ^3H concentration. For ^3He, $\Gamma = \lambda C_H$, i.e., the growth rate of tritiogenic ^3He is equal in magnitude but opposite in sign to the decay rate of ^3H. A modified version of the SEAWAT code was used to simulate this type of parent-daughter chain reaction based on the same approach as Bedekar et al. [32].

Nine different scenarios (A1-A9) were considered that each differ from each other by a single model variable (Table 1). The simplest simulation (simulation A1) had a constant recharge rate, a homogeneous and isotropic hydraulic conductivity, and no groundwater abstraction. The complexity of the model simulations A2 to A9 was increased in a stepwise manner as shown in Table 1. The most complex simulations (A7-A9) resemble the conditions on Langeoog Island the closest. In A8, the clay layer was made continuous in the offshore domain, but in A9, it was truncated 200 m offshore as there is considerable uncertainty about the spatial extent and the hydrodynamic significance of this layer [23]. The choice for 200 m was therefore also simply arbitrary. The model parameters and the boundary conditions are shown in Figure 1. A set of trial simulations was conducted to determine the model thickness at which the freshwater lens and the transition zone were not affected by boundary effects. The thickness of the aquifer sublayers was determined based on available borehole data [21, 23]. The hydraulic conductivities were taken from a calibrated three-dimensional finite element model for the entire island by Stoeckl [33], who used hydraulic conductivity estimates based on particle size by Marggraf and Naumann [34] and unpublished pumping test data.

The effect of the vertical anisotropy on the ^3H concentration distribution in the offshore domain due to the recirculation of seawater was investigated in an additional set of simulations labelled A3. The horizontal to vertical hydraulic conductivity ratio was varied between values $2 < K_x/K_z < 20$.

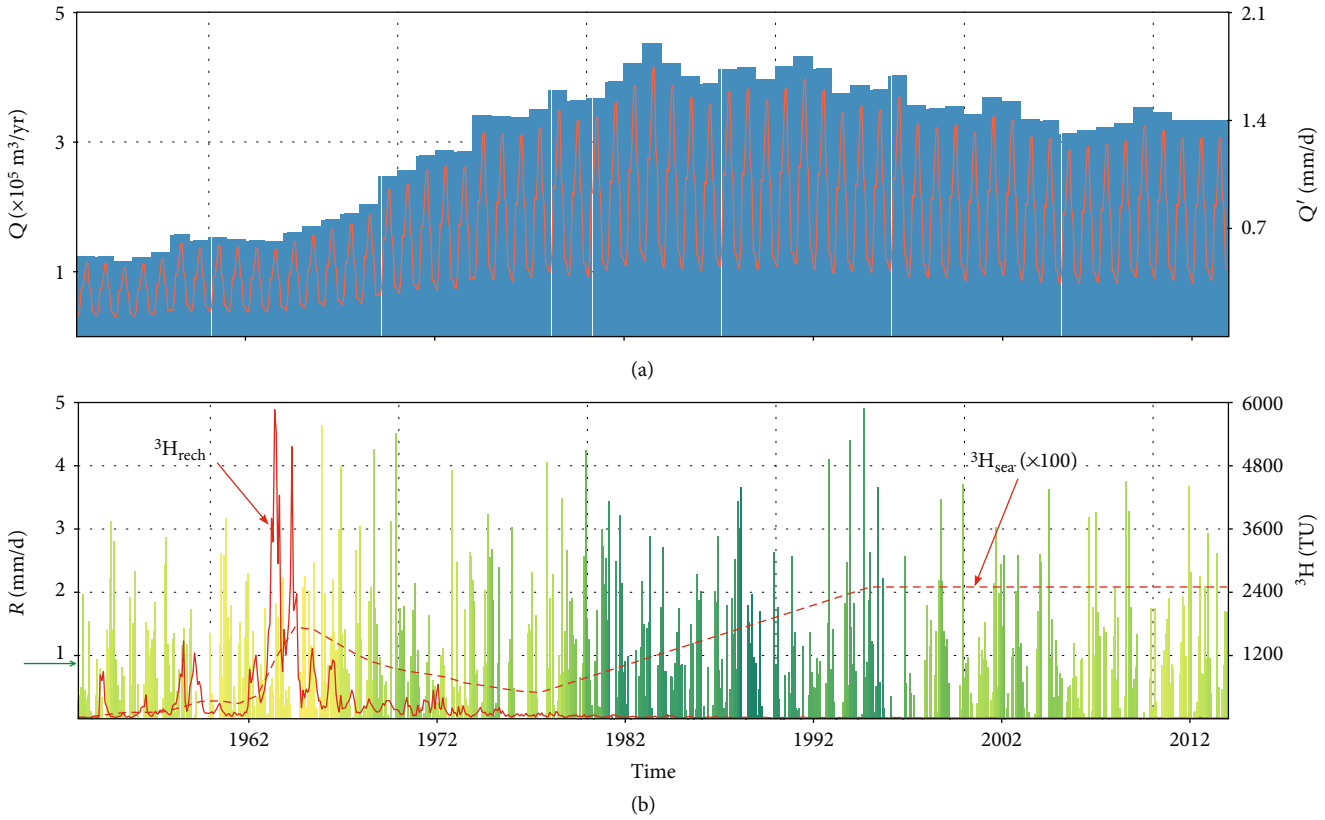

FIGURE 2: Time series data used in the model: (a) total annual abstraction (Q) from the freshwater lens (blue bars) as well as seasonally distributed abstraction per unit of surface area (Q') versus time (red line); (b) calculated groundwater recharge (R, bars) and ^{3}H concentration of groundwater recharge ($^3H_{rech}$, solid red line) and seawater ($^3H_{sea}$, dashed red line) as a function of time (see text for source of data). The colour of the bars in (b) indicates relatively dry (yellow) or wet (green) phases based on the cumulative deviation from the mean recharge rate. The small green arrow pointing to the y axis in (b) indicates the mean recharge rate (0.87 mm/d = 319 mm/yr) that was used in simulation A1.

This number was used as a subscript to indicate the simulation, e.g., $A3_5$ is for simulation A3 with $K_x/K_z = 5$. Since simulation A2 differs only from A3 in that it has $K_x/K_z = 1$, it has been equivalently labelled as $A3_1$. Some simulations with a constant ^{3}H input or a higher dispersivity were also run but not specifically labelled.

The transient simulation spanned the 61-year period from 1 January 1953, the earliest month for which the rainfall ^{3}H concentration could be estimated, to 31 December 2013. Groundwater recharge was calculated based on daily rainfall and evaporation measurements as described in Post and Houben [35], and monthly averages were used in the numerical model (Figure 2(b)). The ^{3}H concentration of the recharge was estimated from the measured concentrations of nearby rainfall stations of the global network of isotopes in precipitation (GNIP) [36]. The partial records of the German stations in Stuttgart and Cuxhaven as well as the Dutch station in Groningen were collated to form a continuous input time series (Figure 2(b)). Being the nearest to Langeoog (about 82 km), the Cuxhaven data (available from January 1978) were used as the principal time series. The time series was further completed with the Groningen data (85 km away, available from January 1970) and those from Stuttgart (available from February 1962). For the period prior to 1962, the data from Ottawa, Canada, were used. Due to the usually small depth to groundwater, it was assumed that the travel time across the unsaturated zone was short, so that the rainfall tritium concentration for a particular month could be assigned to the recharge of that month.

The ^{3}H concentration of seawater (Figure 2(b)) was estimated from different sources. Values prior to 1977 were assumed to be equal to those measured in the Atlantic Ocean [37, 38], while after 1995 a constant value of 30 TU was assumed, which is due to the disposal of tritium-enriched water into the English Channel from nuclear power and processing plants at the French coast [18]. This water flows from the English Channel along the southern coast of the North Sea to the Norwegian coast in a counter-clockwise pattern. A linear increase was assumed between 1977 and 1995, which was found to be in agreement with ^{3}H concentrations measured in the North Sea [39, 40] that can be attributed to increased emissions from nuclear power plants in France, Belgium, and Germany into rivers feeding the North Sea.

The initial conditions for the model (i.e., the heads and concentrations on 1 January 1953) were determined by simulating the 61-year period twice (i.e., 122 years spanning the period 1 January 1831–31 December 1952). With the exception of simulation A1, the initial conditions therefore do not

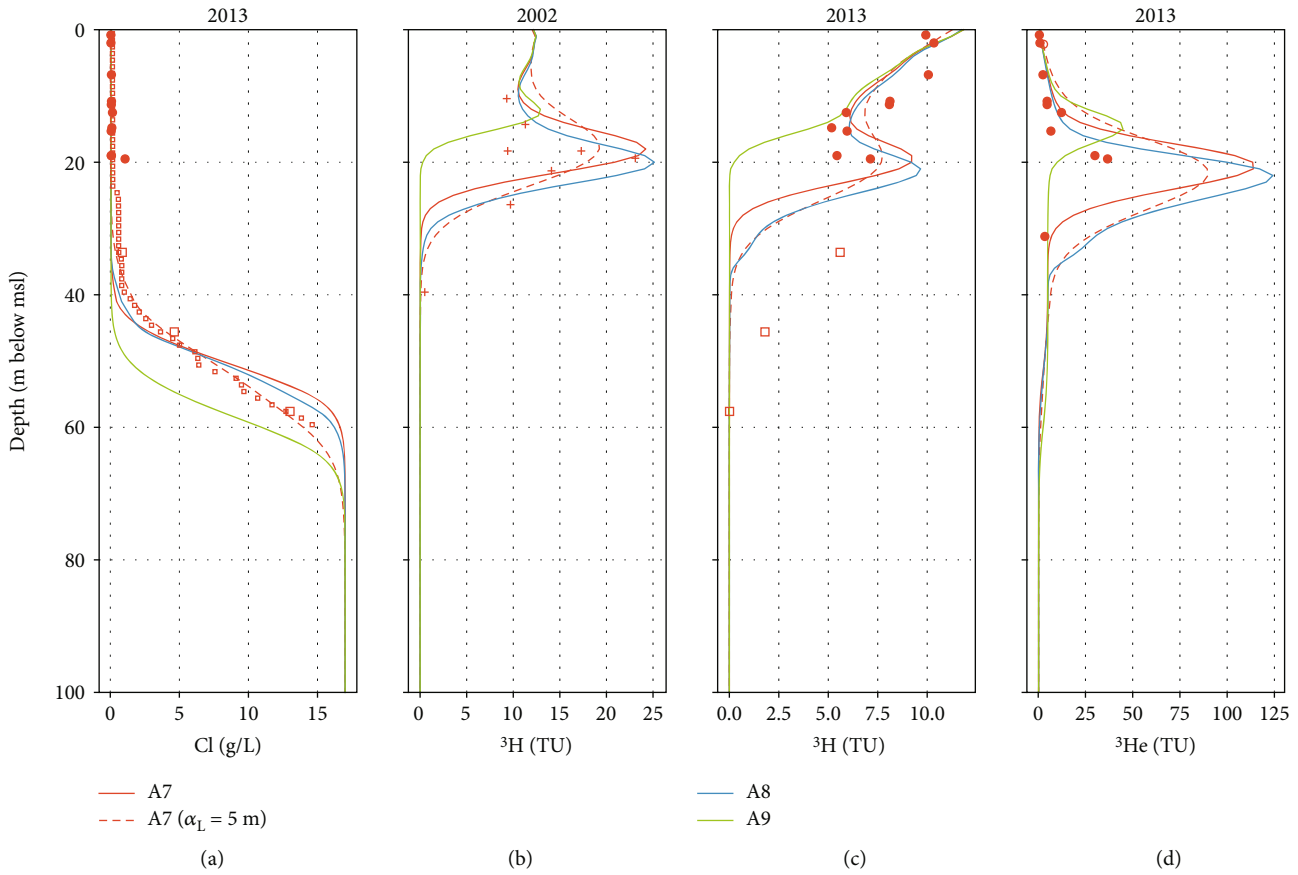

FIGURE 3: (a) Chloride concentration, (b, c) ^{3}H concentration, and (d) ^{3}He concentration as a function of depth for observation well 17. The small red square marker symbols in (a) indicate the chloride concentration calculated from the downhole σ_{25} log. Round symbol markers in (a), (c), and (d) represent samples collected in 2013 (previously published by Houben et al. [7]); square symbol markers are for the samples from well 17. Crosshair symbols in (b) are data for January 2002 from Marggraf [30]. The displayed samples are from different wells within 300 m of the model cross section. The solid lines represent the model outcomes (discussed later on) of simulations A7-A9; the dashed lines are for simulation A7 with longitudinal dispersivity α_L = 5 m. See Figure 1(b) for the location of observation well 17 and Figure 10 for its projected location on the modelled cross section.

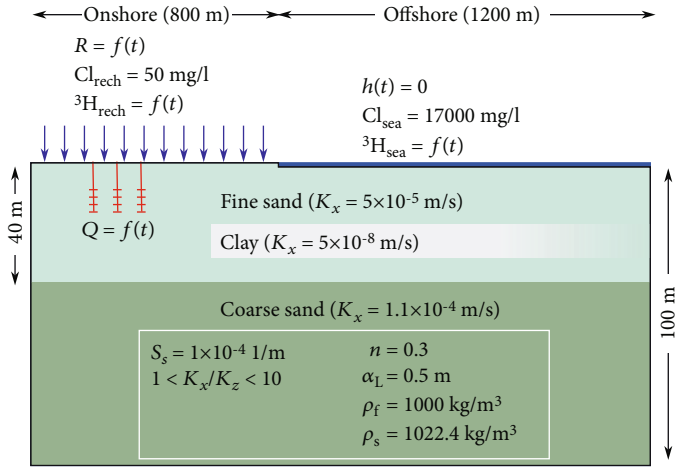

FIGURE 4: Cross section showing the model dimensions, boundary conditions, and hydraulic parameters for the layers used in the layered simulations. Parameter values in white font were constant in all model simulations. Along the left, bottom, and right boundaries, no-flow and nondispersive flux conditions were applied. The abstraction (Q) and recharge (R) time series used are shown in Figures 2(a) and 2(b), respectively. The input time series for ^{3}H in recharge ($^3H_{rech}$) and seawater ($^3H_{sea}$) are shown in Figure 2(b). The fading white colour of the clay layer indicates the uncertainty about its offshore extent.

Table 1: Overview of the model simulations.

	A1	A2 ($A3_1$)	A3	A4	A5	A6	A7	A8	A9
Transient recharge		X	X	X	X	X	X	X	X
Anisotropic K			X	X	X	X	X	X	X
Layered K				X	X	X	X	X	X
Clay layer					X			X	
Discontinuous clay layer						X			X
Abstraction							X	X	X

represent a steady-state situation, the reason being that the temporal variability of the recharge could not be neglected as it is responsible for a significant widening of the transition zone. Using a constant recharge to generate a steady-state starting point would thus result in an unrealistically narrow transition zone, as discussed below. During the 122-year period, all model parameters remained the same except that no abstraction was considered and that the ^{3}H concentration of the meteoric recharge was assigned a constant value of 5 TU, the estimated natural background (Craig and Lal, 1966; Roether, 1967). It was further assumed that seawater had ^{3}H = 0.2 TU prior to 1953 [38].

To include abstraction in the two-dimensional cross-sectional simulations, the reported abstraction volumes were divided by the estimated ground surface area of the well field zone of influence of 1.2×10^6 m^2. Groundwater withdrawal was distributed over the model cells between 200 and 400 m from the left boundary and 9.5 to 14.5 m below mean sea level (a total of 75 cells). This approach assumes that the effect of the withdrawal extends uniformly in the direction perpendicular to the cross section, which is a justifiable approximation as the water table elevation shows little variation in that direction (Figure 1(b)). Because pumping is highly seasonal, but the exact monthly amounts were not available for most of the years, an estimate of the intra-annual distribution of pumping rates was made based on monthly figures for the years 1995, 2001, and 2011. Based on these data, pumping was found to be lowest in January and February (4% of the annual total) and highest during the tourist season in July and August (14% of the annual total). Given the constancy of both climate and tourism seasons, it could be safely assumed that this distribution was the same for all the years [7], so monthly abstraction rates were inferred from the annual totals for the entire simulation period in this way (Figure 2(b)).

Post and Houben [35] successfully modelled downward descending salt fingers on the neighbouring island of Baltrum using $\alpha_L = 0.3$ m, but since their model had a much smaller scale, it was considered to be too small for the present study. The longitudinal dispersivity was therefore set to $\alpha_L = 0.5$ m (with $\alpha_L/\alpha_T = 10$). This value is intermediate between the values used by Stuyfzand [41] and Vandenbohede and Lebbe [42], who adopted values of $\alpha_L = 0.1$ m and $\alpha_L = 0.2$ m, respectively, for the freshwater lenses in the Dutch and Belgian coastal dunes, and the value used by Pauw et al. [43] who used $\alpha_L = 2$ m for the larger barrier island of Texel in the Dutch part of the Wadden Sea. The effect of this parameter will be discussed in more detail below. Effective molecular diffusion coefficients of 5×10^{-10}, 6.7×10^{-10}, and 2×10^{-9} m^2/s were used for Cl, ^{3}H, and ^{3}He, respectively [44].

4. Results and Discussion

4.1. Transient Effects. The results of simulations A1 and A2 are shown in Figure 4. It can clearly be seen that the temporal variability of the recharge results in a widening of the transition zone between fresh and saline groundwater in simulation A2 (compare Figures 5(a) and 5(b)). At the left model boundary, the distance between the chloride contour lines representing 2.5 and 97.5% of the seawater chloride concentration is less than 8 metres for simulation A1, whereas it is ~25 metres for simulation A2. The variability of the recharge causes a net groundwater movement that promotes mixing between the fresh- and saltwater. This effect is similar to the widening of the transition zone caused by tidal fluctuations [45].

This result highlights the importance of explicitly modelling rainfall recharge as a transient process for understanding the development of the transition zone in coastal aquifers. The importance of the temporal rainfall recharge variability has also been recognized in other modelling studies of island aquifers. For example, Griggs and Peterson [46] modelled the freshwater lens of the Laura area on the Majuro Atoll, Marshall Islands. They found that the high temporal variability of the recharge rate resulted in an absence of steady-state conditions and concluded that the sustainable yield could not be modelled if yearly instead of monthly averages were used. Both Ghassemi et al. [47] and Post et al. [48] were only able to reproduce the temporal variability of the salinity of abstracted groundwater from an atoll freshwater lens if they adopted monthly averaged recharge rates.

The effect of the ^{3}H bomb peak can clearly be recognized as a quasihorizontal, elongated zone of high ^{3}H concentrations, which starts at a depth of 20 to 40 m below sea level near the left model boundary and gradually rises closer to the surface with decreasing distance to the shoreline (Figure 5). This pattern is due to the freshwater flow pattern within the lens. The peak concentrations in simulation A2 are lower than those in A1, which is partially because of the dispersive spreading effect caused by the temporally variable recharge rates. Another important reason though is that around the time when the atmospheric ^{3}H concentrations were at their highest, groundwater recharge rates were

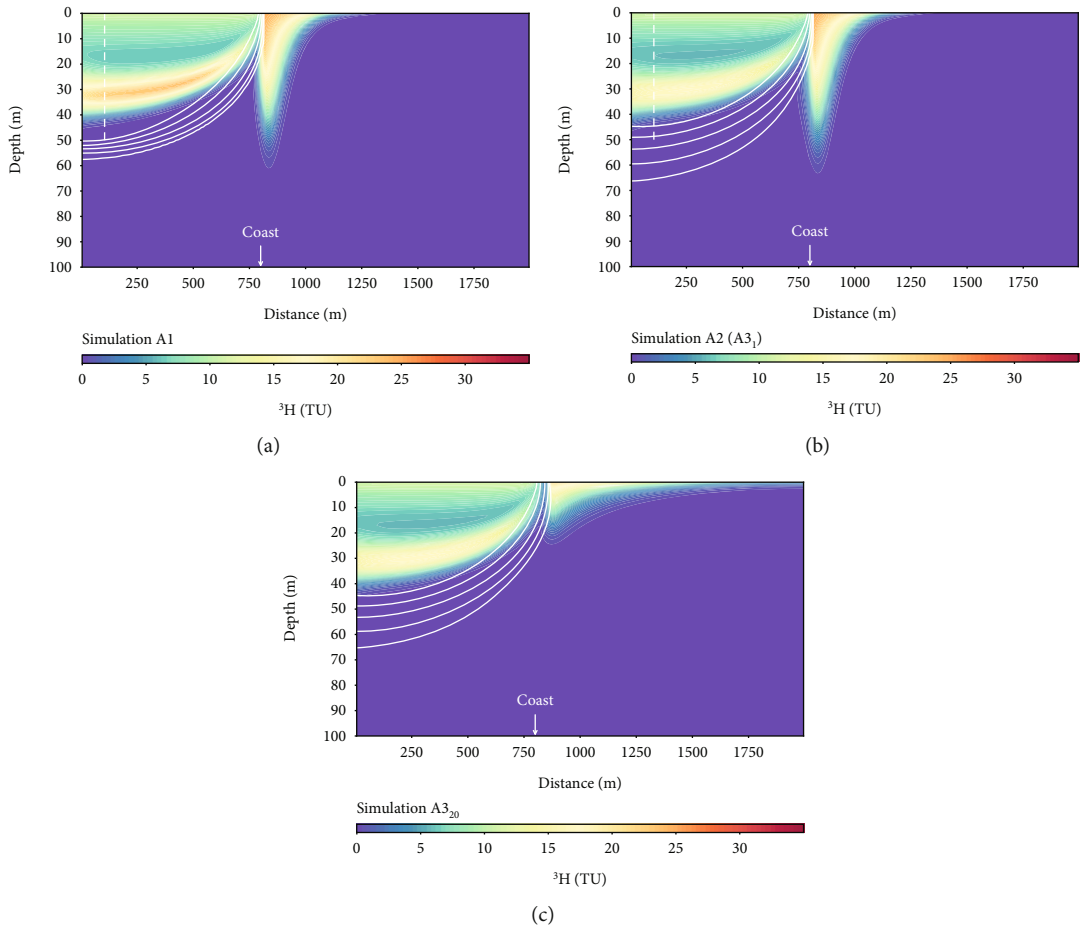

FIGURE 5: Cross sections showing contour plots of the simulated ^{3}H concentrations (shaded colours) and Cl concentrations (white lines) at the end of the simulation period (31 December 2013). The five white lines represent Cl concentrations equal to 2.5%, 16%, 50%, 84%, and 97.5% of the seawater chloride concentration (17 g/L). Results are shown for simulations (a) A1, (b) A2 (=A3$_1$), and (c) A3$_{20}$. The dashed white line in (a) and (b) indicates the position of the vertical profiles shown in Figure 7.

relatively low (Figure 2(b)). Therefore, the total mass of ^{3}H that entered the freshwater lens was considerably lower and resulted in a lower total ^{3}H mass value for simulation A2 than for simulation A1 (Figure 6). For example, at the peak in September 1966, total ^{3}H contained within the freshwater lens amounted to 1.4×10^8 Bq for simulation A2, compared to 1.8×10^8 Bq for simulation A1.

The graph in Figure 6 further shows the total ^{3}He produced from tritium in the freshwater lens. The maximum was reached during the mid-1980s but, as ^{3}He production in the freshwater lens fell because of the declining ^{3}H concentrations, the ^{3}He lost by discharging groundwater started to exceed production and total ^{3}He has been decreasing since then. Nevertheless, most (about 80%) of this ^{3}He was still present within the freshwater lens by the end of the simulation. Groundwater dating back to the 1960s thus remains identifiable by high ^{3}He concentrations it acquired due to the ^{3}H peak in recharge at that time. This provides opportunities to use ^{3}He in lieu of ^{3}H to characterise groundwater flow patterns in freshwater lenses where the groundwater residence times are on the order of a few decades.

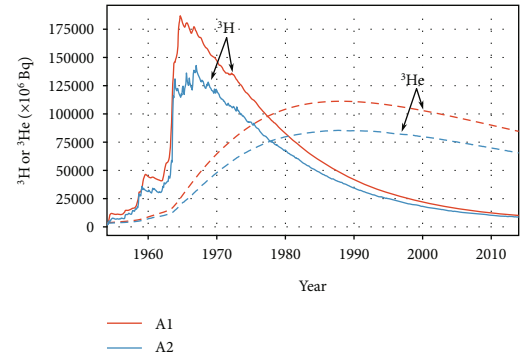

FIGURE 6: Temporal evolution of the total ^{3}H in Bq (solid lines) and ^{3}He (dashed lines) in the freshwater lens (groundwater with less than 2.5% seawater) for simulations A1 (red) and A2 (blue).

Solomon and Sudicky [49] investigated the effect of ^{3}H in rainfall being variable in time on the apparent age τ. Tritium enters the saturated zone with the recharge, but the decay product ^{3}He forms in situ in the aquifer. When the input signal of ^{3}H is steady, steady-state ^{3}He and ^{3}H concentration

profiles form, and the effect of dispersive mixing of groundwater of different ages on the calculated value of τ is small [49]. When the input of ^{3}H is variable in time, such as in the case of the ^{3}H bomb peak, ^{3}He is being produced at different rates in different parts of the aquifer. The resulting concentration gradients drive dispersive and diffusive transport away from the zones of the highest ^{3}He concentrations. As the concentration gradients of both ^{3}H and ^{3}He vary with time, this results in temporally variable dispersive and diffusive transport rates of both tracers. Solomon and Sudicky [49] found that this can result in an error of τ of up to 5 years in the groundwater above the tritium peak. Running simulations A1 and A2 with a constant atmospheric background ^{3}H input (simulations $A1_c$ and $A2_c$) and comparing the differences show that groundwater above the peak is seemingly older by 10.3 and 8.7 years (simulations A1 and A2, respectively) (Figure 7). The model parameters used in this study are comparable to those used by Solomon and Sudicky [49], and the higher age mismatch found here is therefore mainly because in our case the comparison is made about 50 years after the bomb peak, versus about 20 years in their study. Solomon and Sudicky [49] also found younger apparent ages below the tritium peak, and this is also the case here (Figure 7). Because groundwater ^{3}H concentrations in this part of the lens have fallen to below detection limits, the difference is no longer of any practical consequence. This bomb peak-impacted groundwater remains identifiable though based on its elevated ^{3}He concentration.

Comparing simulations $A1_c$ and $A2_c$ shows that the transience of the recharge similarly results in a small error of the calculated ^{3}He/^{3}H ages even when the ^{3}H input signal is constant in time. In the case of simulation $A2_c$, the maximum difference of the ^{3}He/^{3}H age compared to simulation $A1_c$ is 1.8 years. The difference is due to the greater dispersion in simulation $A2_c$ than in simulation $A1_c$, but the magnitude of the effect is only of secondary order compared to that of the bomb peak ^{3}H input.

The apparent age shift due to the nonconstant ^{3}H input is also apparent when the sum of ^{3}H and ^{3}He is plotted as a function of τ (equation (1)), which is often done to identify mixing effects in field data (e.g., [8]). If ^{3}H and its daughter ^{3}He were to remain within the same parcel of groundwater, their sum would reflect the ^{3}H concentration at the time of recharge. In that case, a groundwater sample would have a matching data point somewhere on the atmospheric ^{3}H concentration input signal in the graph of Figure 8. In reality of course, dispersive mixing causes attenuation of the peak input concentration. Moreover, because of the aforementioned dispersive separation of ^{3}H and ^{3}He and its effect on τ, the peak of the summed modelled ^{3}H and ^{3}He concentrations of the groundwater does not coincide with the peak of the atmospheric ^{3}H concentrations. Both simulations A1 and A2 fail to match the measured data of samples recharged before 1974, which could be because the models underestimate mixing effects, which will be discussed further below.

4.2. Tritium Behaviour in the Coastal Discharge Zone. The recirculation of seawater results in an asymmetric funnel-shaped zone of elevated ^{3}H concentrations in the saline groundwater just seaward of the coastline (Figure 5). In simulation A1, this zone even reaches below the transition zone at the bottom of the freshwater lens. In simulation A2, the ^{3}H-enriched seawater penetrates to an even greater depth, albeit that it does not reach below the transition zone anymore, because the latter expands more strongly. Since the circulatory flow of seawater [50] is driven by dispersive mixing [51, 52], the reconfiguration of the zone of high ^{3}H concentrations is expected and can be attributed to the enhanced mixing in simulation A2 compared to simulation A1. These results also emphasise the difficulty of using lateral changes of ^{3}H (or τ) to infer seawater intrusion rates, because of the strong vertical age stratification within the saltwater wedge [53]. This complicates the selection of a saltwater end member to correct for mixing effects in the interpretation of age tracers in coastal aquifers [54, 55] and calculating the rate of seawater intrusion [12].

An important factor that determines the circulatory flow pattern of seawater is the vertical hydraulic conductivity [52]. The effect of this parameter was explored in a set of models based on simulations A2 and A3 by letting the anisotropy ratio K_x/K_z be 1, 2, 5, 10, and 20 by varying K_z. It is noted that the simulation results show that the freshwater lens is affected only to a small degree (compare Figures 5(b) and 5(c)), because there is little change in the groundwater pressure distribution within the lens between the simulations. The reason for this is that the latter is primarily controlled by K_x and the recharge R, which both remained unchanged between the simulations, and consequently, the water table elevation changed by less than a centimetre at the inland boundary. Near the coast, the differences were larger, and this is reflected by a different shape of the transition zone in the interval $\sim 600 < x < \sim 800$ m.

In contrast to the relative constancy of the freshwater lens geometry, Figure 5(c) clearly shows that the decrease of K_z significantly reduces the maximum penetration depth of the funnel-shaped body of high ^{3}H saltwater (measured by z_{min}, the elevation of the deepest point where $^3\text{H} > 0.02$ TU) below the seafloor. This indicates an adjustment of the flow field in the subsea part of the aquifer. To analyse this in more detail, the flux across the top model boundary in the specified-head cells (representing the seafloor) was calculated. As the magnitude and direction of the flux depend strongly on the recharge rate [48, 56], the fluxes at the end of each monthly stress period were averaged over the duration of entire simulation. Discharge of land-derived freshwater mixed with recirculated seawater occurs across the cells nearest to the coast. The width of the discharge zone widened from one cell (10 m) to 7 cells (70 m) as K_x/K_z changed from 1 to 20. The effect on the inflow of seawater across the seafloor (Q_s) is shown in Figure 9. The shape of the relationship between Q_s and K_z is the same as the relationship between Q_s/Q_f and V^* defined by Smith [52] (his Figure 2), where $V^* = K_z/q_f \times (\rho_s - \rho_f)/\rho_f$. In the setup used by Smith [52], Q_f and q_f represented the lateral freshwater inflow across the inland model boundary per unit shoreline length and per unit cross-sectional area, respectively. In our simulations, the freshwater derives from recharge across the top model boundary. Nevertheless,

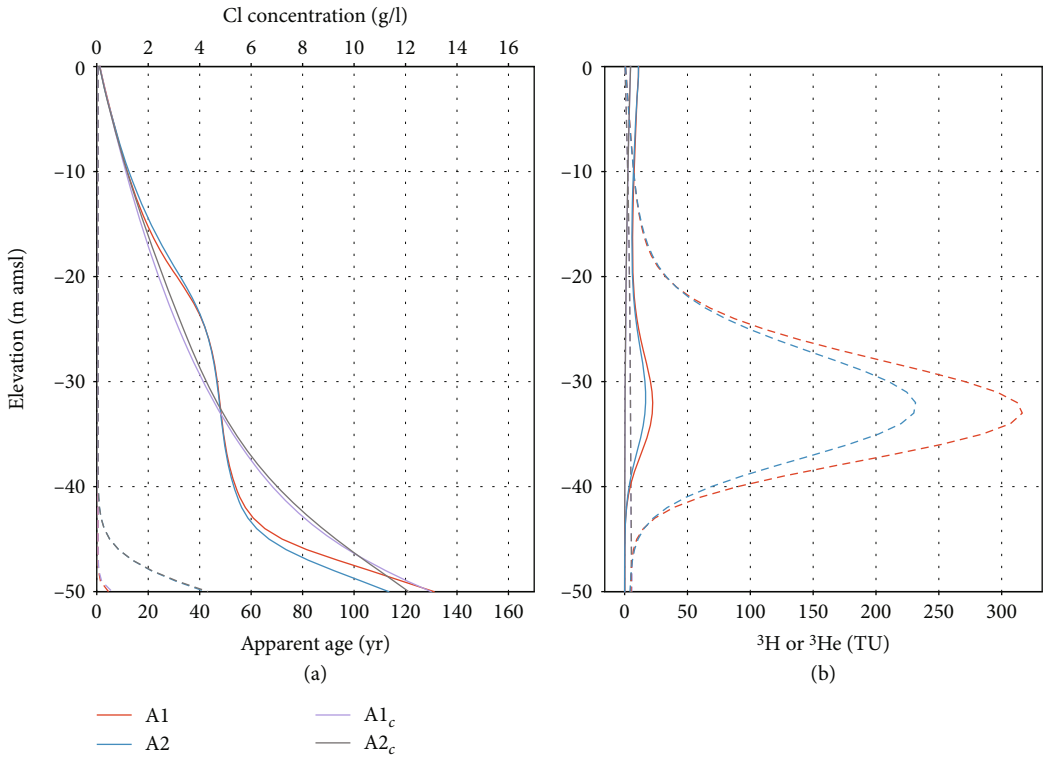

FIGURE 7: (a) Apparent age τ (solid lines) and chloride concentration (dashed lines) for simulations A1 and A2 and (b) the ^{3}H (solid lines) and ^{3}He (dashed lines) concentration versus elevation at the end of the simulation period (31 December 2013). The location of this profile is indicated in Figure 5. Results are shown both for a constant ^{3}H input of 9 TU (as indicated by the subscript c) and for the ^{3}H input according to the curve in Figure 2(b).

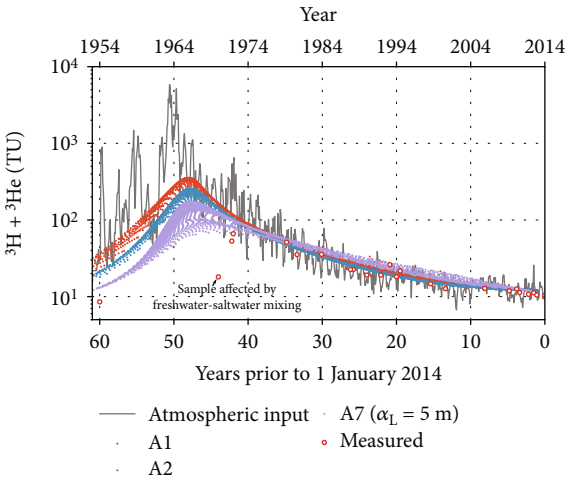

FIGURE 8: Comparison of the ^{3}H concentration in precipitation with time (same data as shown in Figure 2(b)) to the sum of the simulated and measured ^{3}H and ^{3}He concentrations in groundwater versus τ for simulations A1 (red dots), A2 (blue dots), and A7 with α_L = 5 m (purple dots). Each dot represents the simulated value for a model cell. Only values of cells or samples with less than 2.5% seawater are shown.

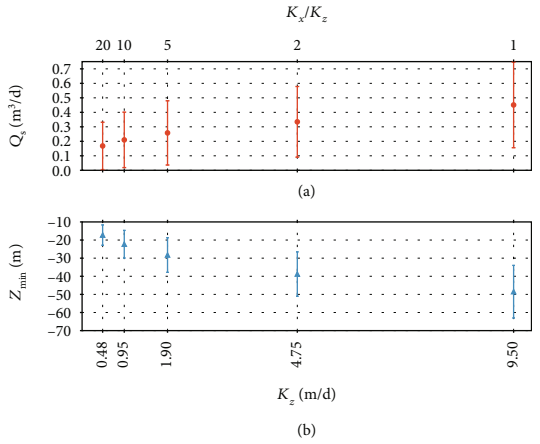

FIGURE 9: Dependency of (a) seawater inflow Q_s and (b) z_{min} (the elevation of the deepest point where ^{3}H> 0.02 TU) on vertical hydraulic conductivity K_z for simulation A3 with different anisotropy ratios. The corresponding anisotropy ratios are displayed along the top horizontal axis of the graph. Q_s was calculated by summing the inflow across the specified head cells along the seafloor. The vertical error bars represent one standard deviation of the temporal variability of Q_s and z_{min}, which is caused by the transient recharge (Figure 2(c)).

the resemblance of the results is expected, as only K_z changed between the simulations and all other parameters that determine V^* remained constant.

The practical implication of this finding is that for studies of submarine groundwater discharge it may be possible to use ^{3}H to constrain the recirculated seawater component. For

conditions similar to those simulated here (i.e., a sufficiently homogeneous aquifer) and assuming the seawater is well mixed and the vertical anisotropy is constrained, ^{3}H measured in water samples from a multilevel observation well at the shoreline might be used to infer the magnitude of Q_s. A relatively high ^{3}H content of seawater, as in the case of the North Sea, is clearly advantageous for that purpose.

4.3. Heterogeneity Effects. In simulation A4, the horizontal hydraulic conductivity of the upper 40 m was lowered (Figure 3), in accordance with the available geological information for Langeoog. Predictably, this resulted in a significant thickening of the lens (Figure 10(a)) which is caused by an increased water table elevation (i.e., higher groundwater pressures) as the freshwater in the lens experiences a greater resistance as it flows towards the sea. The presence of a continuous or discontinuous clay layer (Figures 10(b) and 10(c), respectively) adds to the resistance against freshwater flow to the sea and thereby caused the freshwater lens to thicken by a few metres in simulations A5 and A6 relative to simulation A4. The higher conductivity layer beneath 40 m depth caused a minor, barely perceptible dissection of the main ^{3}H plume, as flow velocities in this layer are higher than in the overlying less permeable layer. In both simulations A5 and A6, the freshwater lens and the transition zone extended into the offshore part of the aquifer, which is attributed to a diversion of the freshwater flowing towards the coast. The clay layer prevents it from flowing upward, and instead, a part of the freshwater is forced to flow laterally underneath the clay. In simulation A5, the freshwater tongue beneath the clay layer had not reached a stable position by the end of the simulation and kept slowly expanding in a seaward direction.

A complex distribution of chloride and ^{3}H developed above the clay layer. The reason for this is that the clay has a dispersing effect on the groundwater discharge near the coast. Rather than being focussed in a relatively narrow zone, the discharge extends over circa 200 m in simulations A5 and A6 (as well as A8 and A9). Hence, the upward flow rates decrease, and the propensity for density-driven downward flow becomes greater. Consequently, a complex pattern of upwelling and downwelling occurred, and water fluxes across the aquifer-seawater interface were spatially and temporally variable. Similar effects have been noted in numerical simulations of submarine groundwater discharge by Kooi and Groen [57]. While the complex dynamics of convective fingering may not be accurately captured by numerical models at this scale, this result indicates that some of the variability of SGD may be due to the presence of large-scale geological features and that small-scale heterogeneity is not necessarily a precondition for spatial variations of the SGD flux. Similar behaviour has also been observed in physical sand tank experiments of heterogeneous coastal aquifers [58]. When these conditions occur, the presence of ^{3}H below the seafloor in the discharge zone is associated with downwelling salt fingers. The funnel shape observed in simulations A1–A4 only developed seaward of the discharge zone, although in simulation A5 (as well as A8) its development was very much suppressed due to the presence of the continuous clay layer (Figure 9(b)).

With respect to the role of the clay layer, it is also interesting to note that simulations A5 and A6 had almost the same chloride and ^{3}H concentration patterns below the dune area (Figure 10). This means that the uncertainty about the offshore geology did not impart great uncertainty on the onshore solute transport simulation results. This is attributed to the fact that almost stagnant flow conditions exist in the aquifer below the seafloor, and therefore, the presence of a low-permeability unit did not alter the flow field significantly. Given that there is a lack of offshore geological data, this is a favourable outcome, but to what extent this holds for coastal aquifer studies more generally is uncertain.

Simulations A7–A9 included the effect of groundwater abstraction. Comparing Figures 10(a)–10(c) to 10(d)–10(f) shows that the effect was that the freshwater lens thinned by about 6 m, as measured by the vertical position of the 2.5% seawater salinity contour at the left model boundary. The distribution of ^{3}H was affected in two ways: first, the upward movement below the zone of pumping drew in water with bomb peak tritium from the deeper parts of the lens. Second, ^{3}H activities were generally lower in the simulations with abstraction. This is attributed partially to the removal of water containing ^{3}H through the abstraction wells, but it cannot be excluded that enhanced dispersive spreading due to the more irregular plume shape may have played a role. A widening of the fresh-saltwater transition zone below the abstraction wells can be recognized, which is consistent with observations in laboratory sand tank experiments of pumping-induced up-coning [59].

4.4. Comparison to Measured Data. The simulated and measured variations of the chloride concentration as well as the ^{3}H and ^{3}He concentrations with depth are shown in Figures 3(a)–3(d), alongside with the data published by Marggraf [30] and Houben et al. [7]. Arguably, a direct comparison between the simulation results and field data is difficult because of the limitations of the two-dimensional model and the required projection of the samples onto the modelled transect, but nonetheless, the simulations' resemblance of the overall observed trends with depth is encouraging. Visually, simulation A7 appears to better match the ^{3}H data in the upper 20 m of the profile as measured in 2013 than simulations A8 and A9 (Figure 3(c)). Simulation A7 also appears to best capture the ^{3}H peak observed in January 2002 (Figure 3(b), note the difference in scale with the graph of Figure 3(c)) as well as the measured ^{3}He activities (Figure 3(d)).

This outcome is somewhat surprising as simulation A7 did not include the clay layer, which is known to exist in the area albeit that there is uncertainty about its hydrogeological significance. Possibly, this result indicates that simulations A8 and A9 overestimated the effect of the clay layer on solute transport in the lens. This might be because its permeability is higher than the value used in the model (Figure 4) or that the clay layer is too discontinuous to act as a real aquitard. It is known that its continuity has been

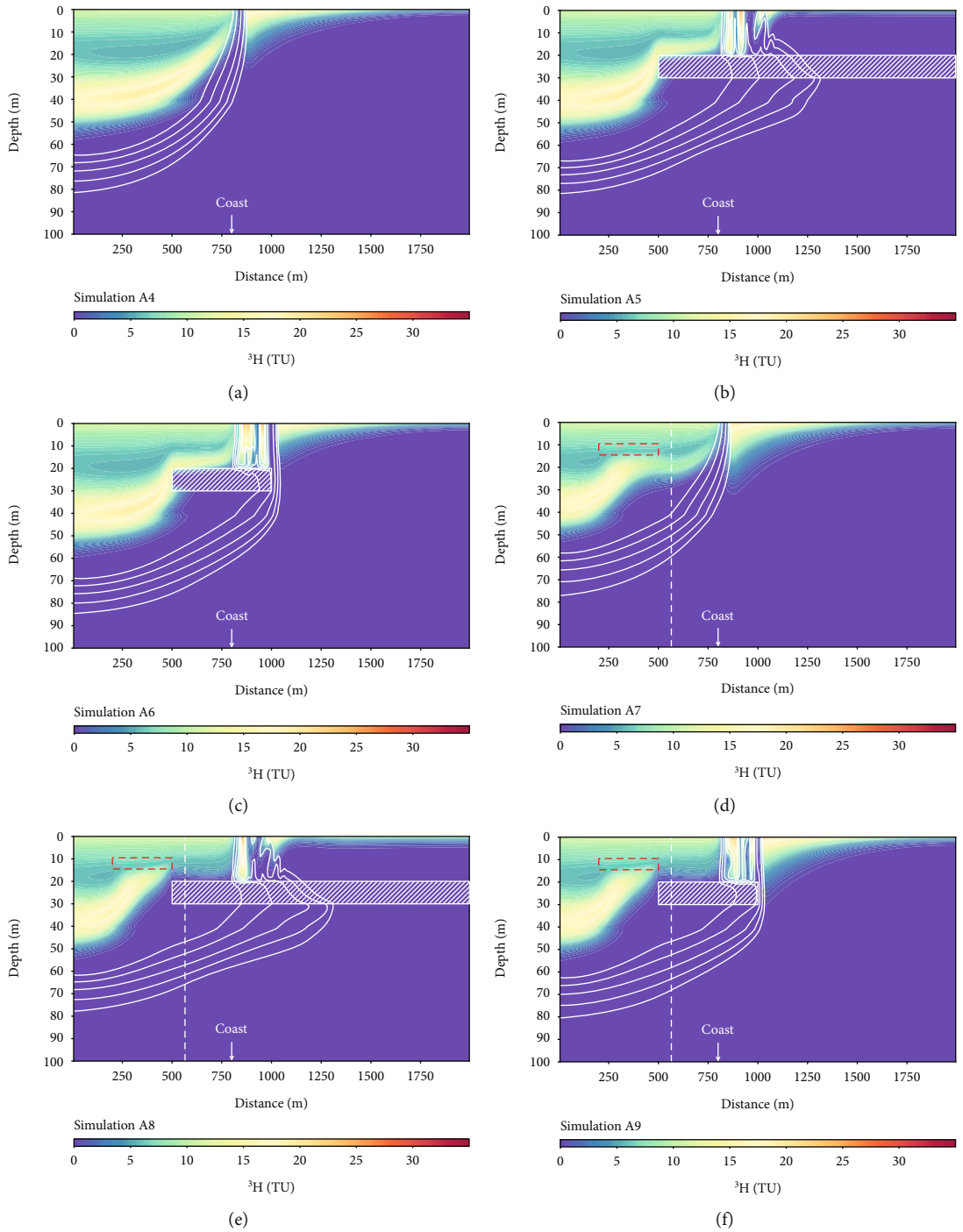

Figure 10: Contour plots of the simulated ^{3}H concentration activities (shaded colours) and Cl concentrations (white lines) at the end of the simulation period (31 December 2013). The five white lines represent Cl concentrations equal to 2.5%, 16%, 50%, 84%, and 97.5% of the seawater chloride concentration (17 g/L). Results are shown for simulations (a) A4, (b) A5, (c) A6, (e) A7, (f) A8, and (g) A9. The location of the clay layer is indicated by the hatched white rectangle. The open red rectangle in (d)–(f) encloses the cells with groundwater abstraction, and the dashed white line indicates the projected location of observation well 17.

affected by glaciotectonic effects [23]. Further simulations, based on a three-dimensional representation of the system, are required to better understand the role of the clay layer and the effect of abstraction.

The depth of the transition zone at the projected location of well 17 was overestimated in simulations A8 and A9. The midpoint of the transition zone was well matched by simulation A7 (Figure 10(e)), but the simulated width was too small relative to its observed width. It is likely that the field data are not an artefact caused by the long well screen or sampling procedures, because geophysical data (HEM and time-domain electromagnetic measurements) for Langeoog

Table 2: Time since recharge for freshwater and seawater depending on groundwater ^{3}H and ^{3}He concentration (all numbers in TU) for simulation A7 with $\alpha_L = 5$ m.

	^{3}H < 0.2	0.2 < ^{3}H < 12 ^{3}He < 10	0.2 < ^{3}H < 12 ^{3}He ≥ 10	^{3}H > 12
Freshwater	≥60 yr (^{3}He ≈ 5)	<10 yr	≥20 yr	<10 yr (^{3}He < 5)
Saltwater	≥40 yr (^{3}He ≈ 0.2)	Mixture of old seawater and seawater < 20 yr	Mixture of seawater and ≥20 yr freshwater (brackish)	<10 yr (^{3}He < 12)

Island also suggest the presence of a thick (20 to 30 m) transition zone beneath the freshwater lens [23]. This implies that dispersive mixing between the freshwater and saltwater was underestimated by the model. Simulation A7 was therefore run with a longitudinal dispersivity $\alpha_L = 5$ m (i.e., ten times the original value, and α_T increased by the same factor). The results in Figure 3(a) show that the simulated transition zone width closely resembled the observed width (Figure 3(a)). While the peaks for ^{3}H and ^{3}He in the overlying freshwater lens became more attenuated, the model results still resembled the patterns displayed by the field data.

In none of the simulations did ^{3}H originating from intruded seawater reach the location of the observation well, which most likely rules it out as a source of the observed ^{3}H in the transition zone at appreciable inland distances from the shore. This contrasts the findings by Stuyfzand et al. [14], but in their case, a significant horizontal inland movement of the saltwater wedge occurred by excessive pumping, which is not seen in our models. The model with a longitudinal dispersivity $\alpha_L = 5$ m did result in elevated ^{3}H concentration in the transition zone, suggesting that the mechanism put forward by Sivan et al. [12], i.e., freshwater containing bomb-derived ^{3}H mixes with ^{3}H-free seawater, can be responsible for ^{3}H in the transition zone in coastal aquifers.

But even with a longitudinal dispersivity $\alpha_L = 5$ m, the Langeoog models underestimated the measured ^{3}H concentrations in the transition zone. The underrepresentation of mixing processes is most likely because important confounding factors were not simulated. The consideration of tides is known to lead to a significant widening of the transition zone [45] but is computationally too expensive at the decadal timescale of our models. Multidomain solute mass exchange effects can also cause a widening of the transition zone [60] and may be important here as the tidal deposits are characterised by decimetre scale grain size variations. Also, even though pumping rates were varied using monthly time steps (Figure 2(a)), the temporal dynamics caused by pumping may be even greater; as in practice, individual wells are operated on a rotational basis whereby they are operated for periods lasting up to 24 hours and are then switched off. This is done to minimise up-coning, but the highly transient flow field that results from this way of operating the well field may induce greater mixing than what is being simulated in the model. Moreover, the combination of three-dimensional flow and subsurface heterogeneity may lead to more dispersion than was captured by the two-dimensional simulations. Dispersivity values greater than $\alpha_L = 5$ m were not considered but may be required to explain the width of the transition zone.

5. Conclusions

The model results presented in this paper demonstrate how atmospherically derived tritium behaves in freshwater lens groundwater systems under different combinations of recharge variability, aquifer anisotropy, lithological heterogeneity, and groundwater abstraction. The results reinforce earlier findings by Solomon and Sudicky [49] that the highly transient input of bomb ^{3}H in groundwater recharge results in a significant age bias for groundwater recharged around the time of the bomb peak in the 1960s, which is due to the difference in dispersive spreading of ^{3}H and its daughter ^{3}He in the aquifer.

The model results can be synthesised in terms of groundwater age classes as shown in Table 2, which is expected to be applicable to other freshwater lens systems along the shorelines of the southern North Sea. A finding that is expected to be generally applicable is that, since most of the tritiogenic ^{3}He was found to still be present within the freshwater lens, it may be possible to use ^{3}He as a tracer to identify freshwater recharged around the time of the bomb peak (a role traditionally fulfilled by ^{3}H). Because ^{3}He was also sequestered into the transition zone, it can also be used to study fresh-saltwater mixing relationships, which can contribute to the understanding of the formation of brackish groundwater in coastal areas.

Using a transient recharge input as opposed to a constant recharge had only a secondary effect on apparent ages but did result in a significant widening of the transition zone between fresh- and saltwater. While the width of the transition zone (as measured at well 17) could be approximated by increasing the dispersivity by an order of magnitude (simulation A7), the simulated ^{3}H concentrations for the transition zone underestimated the measured values. This suggests that the model still underrepresented mixing between fresh- and saltwater, despite the adopted dispersivity value of $\alpha_L = 5$ m being higher than what was used in modelling studies of comparable freshwater lenses [41–43]. The limitations of the present model complicate a direct comparison to the field data, and a fully three-dimensional model with appropriate consideration of local heterogeneity effects is required to better understand the formation of the wide transition zone. If time series data become available, lumped parameter models could further be used to investigate the role of dispersion [61].

Despite uncertainty about the magnitude of the dispersion coefficient and processes that control the width of the transition zone, our models suggest that the ^{3}H observed in the transition zone on Langeoog more likely derived from the freshwater lens than from the North Sea. In none of the simulations did ^{3}H from the North Sea reach far enough inland to explain the observed values.

In the offshore part of the aquifer, there can be a pronounced funnel-shaped zone of elevated ^{3}H concentrations that stems from the circulation of seawater driven by dispersion in the transition zone. The vertical hydraulic conductivity and the presence of a clay layer were found to exert a strong control on the maximum depth to which measurable ^{3}H can be found in the subsea portion of the aquifer, as well as on submarine groundwater discharge patterns. Therefore, groundwater ^{3}H measurements at the coastline or below the seafloor could see application as an indicator of the strength of the seawater circulation and SGD in the southern North Sea area and other coastal sites where ^{3}H or ^{3}He variations can be resolved with sufficient analytical precision.

Data Availability

Previously reported field data were used to support this study and are available at [doi 10.1002/2014WR015584, doi: 10.1016/j.jappgeo.2016.11.007, and https://d-nb.info/975110349/34]. These prior studies (and datasets) are cited at relevant places within the text as references [[7, 23]; and [30]].

Additional Points

Key Points. Numerical models provide insight into the behaviour of ^{3}H and ^{3}He in island aquifers. Bomb-related tritiogenic ^{3}He still provides a dating tool even though all ^{3}H has decayed. Bomb-pulse ^{3}H input causes an apparent age bias on the order of up to 10 years. Saltwater ^{3}H distribution is sensitive to seawater recirculation and submarine groundwater discharge. Sequestration of bomb-pulse ^{3}H in transition zone requires vigorous mixing.

Conflicts of Interest

The authors declare that they have no conflicts of interest.

Acknowledgments

The authors would like to thank the Landesamt für Bergbau, Energie und Geologie (LBEG), of Lower Saxony for the technical support during the sampling of the wells on Langeoog and the Oldenburgisch-Ostfriesischer Wasserverband (OOWV) for providing data. Dr. Matthew Currell provided thoughtful reviewer comments that led to significant improvements of the manuscript.

Supplementary Materials

This file contains a table with the data previously published by Houben et al. [7], extended with the data for well 17 in the transition zone. *(Supplementary Materials)*

References

[1] D. K. Solomon and P. G. Cook, *^{3}H and ^{3}He. Environmental Tracers in Subsurface Hydrology*, P. G. Cook and A. L. Herczeg, Eds., Springer US, Boston, MA, USA, 2000.

[2] F. Eyrolle, L. Ducros, S. Le Dizes et al., "An updated review on tritium in the environment," *Journal of Environmental Radioactivity*, vol. 181, pp. 128–137, 2018.

[3] B. C. Jurgens, J. K. Böhlke, L. J. Kauffman, K. Belitz, and B. K. Esser, "A partial exponential lumped parameter model to evaluate groundwater age distributions and nitrate trends in long-screened wells," *Journal of Hydrology*, vol. 543, pp. 109–126, 2016.

[4] B. C. Jurgens, J. K. Böhlke, and S. M. Eberts, *TracerLPM (version 1): an Excel® workbook for interpreting groundwater age distributions from environmental tracer data*, U.S. Geological Survey, Reston, VA, 2012.

[5] C. Turnadge and B. D. Smerdon, "A review of methods for modelling environmental tracers in groundwater: advantages of tracer concentration simulation," *Journal of Hydrology*, vol. 519, pp. 3674–3689, 2014.

[6] B. Hagedorn, A. I. El-Kadi, A. Mair, R. B. Whittier, and K. Ha, "Estimating recharge in fractured aquifers of a temperate humid to semiarid volcanic island (Jeju, Korea) from water table fluctuations, and Cl, CFC-12 and ^{3}H chemistry," *Journal of Hydrology*, vol. 409, no. 3-4, pp. 650–662, 2011.

[7] G. J. Houben, P. Koeniger, and J. Sültenfuß, "Freshwater lenses as archive of climate, groundwater recharge, and hydrochemical evolution: insights from depth-specific water isotope analysis and age determination on the island of Langeoog, Germany," *Water Resources Research*, vol. 50, no. 10, pp. 8227–8239, 2014.

[8] T. Röper, K. F. Kröger, H. Meyer, J. Sültenfuss, J. Greskowiak, and G. Massmann, "Groundwater ages, recharge conditions and hydrochemical evolution of a barrier island freshwater lens (Spiekeroog, Northern Germany)," *Journal of Hydrology*, vol. 454-455, pp. 173–186, 2012.

[9] J. C. Vogel, "Investigation of groundwater flow with radiocarbon," *Isotopes in Hydrology*, pp. 355–369, 1967.

[10] S. Stein, A. Russak, O. Sivan et al., "Saline groundwater from coastal aquifers as a source for desalination," *Environmental Science & Technology*, vol. 50, no. 4, pp. 1955–1963, 2016.

[11] C. Andrié, P. Jean-Baptiste, C. Pierre et al., "Pore water geochemistry and mixing processes within the Tahiti barrier reef," *Geochimica et Cosmochimica Acta*, vol. 62, no. 16, pp. 2809–2822, 1998.

[12] O. Sivan, Y. Yechieli, B. Herut, and B. Lazar, "Geochemical evolution and timescale of seawater intrusion into the coastal aquifer of Israel," *Geochimica et Cosmochimica Acta*, vol. 69, no. 3, pp. 579–592, 2005.

[13] L. Bouchaou, J. L. Michelot, A. Vengosh et al., "Application of multiple isotopic and geochemical tracers for investigation of recharge, salinization, and residence time of water in the Souss–Massa aquifer, southwest of Morocco," *Journal of Hydrology*, vol. 352, no. 3-4, pp. 267–287, 2008.

[14] P. J. Stuyfzand, F. Schaars, and K. J. Van der Made, "Multi-tracing the origin of brackish and saline groundwaters near a dune catchment area with beach nourishment (Monster, Netherlands)," in *Proceedings of the 22nd Salt Water Intrusion Meeting*, pp. 93–96, Buzios, Brazil, 2012.

[15] D. M. Han, X. F. Song, M. J. Currell, and M. Tsujimura, "Using chlorofluorocarbons (CFCs) and tritium to improve conceptual model of groundwater flow in the South Coast Aquifers of Laizhou Bay, China," *Hydrological Processes*, vol. 26, no. 23, pp. 3614–3629, 2012.

[16] E. Bryan, K. T. Meredith, A. Baker, V. E. A. Post, and M. S. Andersen, "Island groundwater resources, impacts of abstraction and a drying climate: Rottnest Island, Western Australia," *Journal of Hydrology*, vol. 542, pp. 704–718, 2016.

[17] P.-E. Oms, P. Bailly du Bois, F. Dumas et al., "Inventory and distribution of tritium in the oceans in 2016," *Science of the Total Environment*, vol. 656, pp. 1289–1303, 2019.

[18] H. Nies, I. Goroncy, J. Hermann et al., *Kartierung von Tc-99, I-129 und I-127 im oberflächenwasser der Nordsee [Mapping of Tc-99, I-129 and I-127 in the surface water of the North Sea]*, Bundesamt für Strahlenschutz, Salzgitter, Germany, 2010.

[19] V. E. A. Post, A. Vandenbohede, A. D. Werner, Maimun, and M. D. Teubner, "Groundwater ages in coastal aquifers," *Advances in Water Resources*, vol. 57, pp. 1–11, 2013.

[20] S. Ueda, H. Kakiuchi, K. Kondo, and J. Inaba, "Tritium concentration in fresh, brackish and sea-water samples in Rokkasho-Village, Japan, bordered by nuclear fuel cycle facilities," *Journal of Radioanalytical and Nuclear Chemistry*, vol. 267, no. 1, pp. 29–33, 2005.

[21] J. Barckhausen, "Entstehung und entwicklung der insel Langeoog [origin and development of the island of Langeoog]," *Oldenburger Jahrbuch*, vol. 69, pp. 239–281, 1969.

[22] W. Voß, B. Siemon, J. Pielawa, M. Bock, and M. Ibs-von Seht, *Technischer bericht hubschraubergeophysik befliegung Langeoog 2008/09 (technical report helicopter geopyhical survey Langeoog 2008/2009)*, Bundesanstalt für Geowissenschaften und Rohstoffe, Hannover, Germany, 2015.

[23] S. Costabel, B. Siemon, G. Houben, and T. Günther, "Geophysical investigation of a freshwater lens on the island of Langeoog, Germany – insights from combined HEM, TEM and MRS data," *Journal of Applied Geophysics*, vol. 136, pp. 231–245, 2017.

[24] F. Bungenstock and A. Schäfer, "The Holocene relative sea-level curve for the tidal basin of the barrier island Langeoog, German Bight, Southern North Sea," *Global and Planetary Change*, vol. 66, no. 1-2, pp. 34–51, 2009.

[25] G. J. Houben, "300 years of coastal salinization research in Germany - the Homann (1718) map of the Christmas Flood of 1717," in *25th Salt Water Intrusion Meeting (SWIM 2018)*, pp. 102–104, Gdańsk, Poland, 2018.

[26] J. Sültenfuß, W. Roether, and M. Rhein, "The Bremen mass spectrometric facility for the measurement of helium isotopes, neon, and tritium in water," *Isotopes in Environmental and Health Studies*, vol. 45, no. 2, pp. 83–95, 2009.

[27] S. Lee, M. Currell, and D. I. Cendón, "Marine water from mid-Holocene sea level highstand trapped in a coastal aquifer: evidence from groundwater isotopes, and environmental significance," *Science of the Total Environment*, vol. 544, pp. 995–1007, 2016.

[28] K. R. Rushton, "Differing positions of saline interfaces in aquifers and observation boreholes," *Journal of Hydrology*, vol. 48, no. 1-2, pp. 185–189, 1980.

[29] J. H. Tellam, J. W. Lloyd, and M. Walters, "The morphology of a saline groundwater body: its investigation, description and possible explanation," *Journal of Hydrology*, vol. 83, no. 1-2, pp. 1–21, 1986.

[30] G. Marggraf, *Geogene und anthropogene einflüsse auf ein isoliertes system (Düneninseln) in bezug auf die hydrochemie des grundwassers [Geogenic and anthropogenic influences on an isolated system (Dune islands) with respect to groundwater hydrochemistry]*, Thesis, Technische Universität Braunschweig, Braunschweig, Germany, 2005.

[31] C. D. Langevin, D. T. Thorne Jr., A. M. Dausman, M. C. Sukop, and W. Guo, "SEAWAT version 4: a computer program for simulation of multi-species solute and heat transport," Geological Survey (U.S.), 2008.

[32] V. Bedekar, E. D. Morway, C. D. Langevin, and M. J. Tonkin, *MT3D-USGS version 1: a U.S. Geological Survey release of MT3DMS updated with new and expanded transport capabilities for use with MODFLOW*, U.S. Geological Survey, Reston, VA, 2016.

[33] L. Stoeckl, *Dokumentation der numerischen grundwasserströmungs- und transportmodellierung von Langeoog [explanatory note for the numerical groundwater flow and transportmodel of Langeoog]*, Federal Institute for Geosciences and Natural Resources (BGR), Unpublished report, 2018.

[34] G. Marggraf and K. Naumann, *Hydrogeologie und grundwasserdynamik (hydrogeology and groundwater dynamics). Umweltverträgliche Grundwasserbewirtschaftung in hydrogeologisch und ökologisch sensiblen Bereichen der Nordseeküste (Sustainable exploitation of groundwater in hydrogeologcally and ecologically sensitive areas along the North Sea coast)*, J. Petersen, R. Pott, P. Janiesch, and J. Wolff, Eds., Husum Druck- und Verlaggesellschaft, Husum, Germany, 2003.

[35] V. E. A. Post and G. J. Houben, "Density-driven vertical transport of saltwater through the freshwater lens on the island of Baltrum (Germany) following the 1962 storm flood," *Journal of Hydrology*, vol. 551, pp. 689–702, 2017.

[36] IAEA/WMO, "Global Network of Isotopes in Precipitation. The GNIP Database," 2016, http://www.iaea.org/water.

[37] S. C. Doney and W. J. Jenkins, "The effect of boundary conditions on tracer estimates of thermocline ventilation rates," *Journal of Marine Research*, vol. 46, no. 4, pp. 947–965, 1988.

[38] W. Weiss and W. Roether, "The rates of tritium input to the world oceans," *Earth and Planetary Science Letters*, vol. 49, no. 2, pp. 435–446, 1980.

[39] E. H. De Jong and O. C. Swertz, *Radioactieve stoffen in de zoute wateren (radioactive substances in the saline waters)*, Rijksinstituut voor Kust en Zee/RIKZ, Den Haag, The Netherlands, 2000.

[40] C. Wedekind, "Tritium distribution and spreading in the North Sea and the Baltic Sea in 1980/81, as well as in the surface water of the North Atlantic in 1979," *Deutsche Hydrographische Zeitschrift*, vol. 35, no. 4, pp. 177–186, 1982.

[41] P. J. Stuyfzand, *Hydrochemistry and Hydrology of the Coastal Dune Area of the Western Netherlands*, KIWA N.V., Research & Consultancy Division, 1993.

[42] A. Vandenbohede and L. Lebbe, "Effects of tides on a sloping shore: groundwater dynamics and propagation of the tidal wave," *Hydrogeology Journal*, vol. 15, no. 4, pp. 645–658, 2007.

[43] P. Pauw, P. G. B. de Louw, and G. H. P. O. Essink, "Groundwater salinisation in the Wadden Sea area of the Netherlands: quantifying the effects of climate change, sea-level rise and

anthropogenic interferences," *Netherlands Journal of Geosciences - Geologie en Mijnbouw*, vol. 91, no. 3, pp. 373–383, 2014.

[44] E. M. LaBolle, G. E. Fogg, and J. B. Eweis, "Diffusive fractionation of ^{3}H and ^{3}He in groundwater and its impact on groundwater age estimates," *Water Resources Research*, vol. 42, no. 7, article W07202, 2006.

[45] M. R. Underwood, F. L. Peterson, and C. I. Voss, "Groundwater lens dynamics of Atoll Islands," *Water Resources Research*, vol. 28, no. 11, pp. 2889–2902, 1992.

[46] J. E. Griggs and F. L. Peterson, "Ground-water flow dynamics and development strategies at the atoll scale," *Groundwater*, vol. 31, no. 2, pp. 209–220, 1993.

[47] F. Ghassemi, J. W. Molson, A. Falkland, and K. Alam, "Three-dimensional simulation of the Home Island freshwater lens: preliminary results," *Environmental Modelling & Software*, vol. 14, no. 2-3, pp. 181–190, 1998.

[48] V. E. A. Post, A. L. Bosserelle, S. C. Galvis, P. J. Sinclair, and A. D. Werner, "On the resilience of small-island freshwater lenses: evidence of the long-term impacts of groundwater abstraction on Bonriki Island, Kiribati," *Journal of Hydrology*, vol. 564, pp. 133–148, 2018.

[49] D. K. Solomon and E. A. Sudicky, "Tritium and helium 3 isotope ratios for direct estimation of spatial variations in groundwater recharge," *Water Resources Research*, vol. 27, no. 9, pp. 2309–2319, 1991.

[50] P. M. Barlow, *Ground water in freshwater-saltwater environments of the Atlantic Coast*, U.S. Geological Survey, 2003.

[51] H. H. Cooper Jr., "A hypothesis concerning the dynamic balance of fresh water and salt water in a coastal aquifer," *Journal of Geophysical Research*, vol. 64, no. 4, pp. 461–467, 1959.

[52] A. J. Smith, "Mixed convection and density-dependent seawater circulation in coastal aquifers," *Water Resources Research*, vol. 40, no. 8, p. 40, 2004.

[53] L. Stoeckl and G. Houben, "Flow dynamics and age stratification of freshwater lenses: experiments and modeling," *Journal of Hydrology*, vol. 458-459, pp. 9–15, 2012.

[54] C. I. Voss and W. W. Wood, *Synthesis of geochemical, isotopic and groundwater modeling analysis to explain regional flow in a coastal aquifer of southern Oahu, Hawaii. Mathematical models and their applications to isotope studies in groundwater hydrology, IEAE-TECDOC-777*, International Atomic Energy Agency (IAEA), Vienna, Austria, 1994.

[55] Y. Yechieli, R. Yokochi, M. Zilberbrand et al., "Recent seawater intrusion into deep aquifer determined by the radioactive noble-gas isotopes ^{81}Kr and ^{39}Ar," *Earth and Planetary Science Letters*, vol. 507, pp. 21–29, 2019.

[56] H. A. Michael, A. E. Mulligan, and C. F. Harvey, "Seasonal oscillations in water exchange between aquifers and the coastal ocean," *Nature*, vol. 436, no. 7054, pp. 1145–1148, 2005.

[57] H. Kooi and J. Groen, "Offshore continuation of coastal groundwater systems; predictions using sharp-interface approximations and variable-density flow modelling," *Journal of Hydrology*, vol. 246, no. 1-4, pp. 19–35, 2001.

[58] G. J. Houben, L. Stoeckl, K. E. Mariner, and A. S. Choudhury, "The influence of heterogeneity on coastal groundwater flow - physical and numerical modeling of fringing reefs, dykes and structured conductivity fields," *Advances in Water Resources*, vol. 113, pp. 155–166, 2018.

[59] D. Jakovovic, A. D. Werner, and C. T. Simmons, "Numerical modelling of saltwater up-coning: comparison with experimental laboratory observations," *Journal of Hydrology*, vol. 402, no. 3-4, pp. 261–273, 2011.

[60] C. Lu, P. K. Kitanidis, and J. Luo, "Effects of kinetic mass transfer and transient flow conditions on widening mixing zones in coastal aquifers," *Water Resources Research*, vol. 45, no. 12, 2009.

[61] L. M. Bexfield, B. C. Jurgens, D. M. Crilley, and S. C. Christenson, *Hydrogeology, water chemistry, and transport processes in the zone of contribution of a public-supply well in Albuquerque, New Mexico, 2007-9*, U.S. Geological Survey, Reston, VA, 2012.

Hindawi
Geofluids
Volume 2019, Article ID 9484657, 15 pages
https://doi.org/10.1155/2019/9484657

Research Article

Modeling the Evolution of a Freshwater Lens under Highly Dynamic Conditions on a Currently Developing Barrier Island

Tobias Holt, Janek Greskowiak, Stephan L. Seibert, and Gudrun Massmann

Institute for Biology and Environmental Sciences, Carl von Ossietzky University of Oldenburg, Ammerländer Heerstraße 114-118, D-26129 Oldenburg, Germany

Correspondence should be addressed to Tobias Holt; tobias.holt@uni-oldenburg.de

Received 26 February 2019; Revised 18 April 2019; Accepted 21 May 2019; Published 14 August 2019

Academic Editor: Constantinos Loupasakis

The drinking water supply on barrier islands largely depends on freshwater lenses, which are also highly relevant for island ecosystems. The freshwater lens presented in this study is currently developing (since the 1970s) below the very young eastern part of the North Sea barrier island Spiekeroog, the so-called "Ostplate." Due to the absence of coastal protection measures, formation, shape, and extent of the freshwater lens below the Ostplate are unaffected by human activities but exposed to dynamic changes, e.g., geomorphological variations and storm tides. The main aim of this paper was to reconstruct the evolution of the freshwater lens over several decades in order to explain the present-day groundwater salinity distribution. In addition, the study assessed the impact of geomorphological variations and storm tides on the freshwater lens formation. Detailed field observations were combined with a transient 2-D density-dependent modeling approach. Both field observations and simulations show an asymmetric freshwater lens after ~42 years of formation, whereby the horizontal extent is limited by the elevated dune area. The simulations indicate that the young freshwater lens has nearly reached quasi-steady-state conditions mainly due to the continuous mixing with seawater infiltrating during storm tides, which inhibits further growth of the freshwater lens on the narrow island. The findings further show that (i) a neglection of storm tides results in a significant overestimation of the freshwater lens extent, and (ii) the modeled present groundwater salinity distribution and shape of the freshwater lens are predominantly determined by the position and extent of the elevated dune area at the past ~20 years. Hence, annual storm tides have to be directly implemented into numerical models to explain the groundwater salinity distribution and the extent of young freshwater lenses located in highly dynamic tidal environments.

1. Introduction

The water supply in coastal regions largely depends on groundwater from local aquifers. Since almost 25% of the global population lives within 100 km of a coastline, the high demand for freshwater creates an immense pressure on the coastal groundwater resources [1–3]. With the expected doubling of the population density in coastal regions by 2030 [4], the demand for freshwater and its extraction will further increase. The available freshwater resources in coastal areas and related ecosystems are highly vulnerable and often threatened by salinization due to seawater infiltration and overuse. The vulnerability of coastal aquifers is additionally enhanced by saltwater intrusion and more frequent inundations due to increasing storm frequencies both coming along with climate change and predicted sea level rise [1, 5, 6].

Barrier islands are commonly characterized by underlying fresh groundwater resources, which typically exist in the form of freshwater lenses (FWLs) [7, 8]. On dune islands, like the barrier islands located in the southern North Sea, the formation of dunes allows for the development of FWLs due to their elevation and infiltration capability. Reaching heights above the maximum level of storm tides, elevated areas are no longer prone to inundations, and the previously saline unconfined aquifer gets recharged by precipitation, displacing the saltwater and reducing the groundwater salinity [9–11]. Due to density differences between fresh and saline groundwater, the freshwater floats on top of the underlying saltwater (e.g., [12–16]). The transition zone that separates

fresh and saline groundwater normally is not a sharp boundary as assumed by analytical solutions [7, 8]. It is rather a zone of up to several meter thickness due to mixing and hydrodynamic dispersion, displaying an increase in salinity with depth (e.g., [10, 13, 17, 18]).

Both the FWL and the transition zone are dynamic and influenced by natural factors including tides, seasonal changes in groundwater recharge/discharge, ground surface elevation, and island stratigraphy [14, 17–21]. In the absence of coastal measures like dykes, inundation events can cause salinization of the FWL, posing a serious threat to local water supply [22–26]. The inundation frequency is, thereby, mainly determined by ground surface elevation above sea level [27]. Given the fact that sea level and the frequency of storm tides are predicted to rise, barrier islands and the available freshwater resources, respectively, will become even more vulnerable to inundations and saltwater intrusion, especially on islands where topography constrains the rise of the FWL [5, 28, 29].

According to Illangasekare et al. [30], the infiltration of saltwater through the unsaturated zone during inundation events has the largest spatial impact on the FWL. Its impact on the FWL depends, thereby, on the thickness of the unsaturated zone, i.e., the thicker the unsaturated zone, the larger the amount of saltwater intruded [30, 31]. The FWL recovery after salinization due to storm tides to preinundation levels can range between months [2, 22, 32] and several years [23, 25, 33]. It is mainly driven by recharge from precipitation flushing out the saltwater [30], and therefore, the time of recovery is a function of the recharge rate [34, 35]. Besides the thickness of the unsaturated zone, hydraulic properties of the aquifer, i.e., hydraulic conductivity, and geological heterogeneities also exert control on the recovery of the FWL [22]. For instance, Yang et al. [36] conducted a modeling study and showed that a low horizontal permeability and a high vertical permeability increase the aquifer vulnerability during inundation events. Infiltrating seawater may appear as descending saltwater fingers due to density differences between the fresh- and saltwater, causing a rapid downward migration of the intruded saltwater after inundation events resulting in an acceleration of the recovery of the upper parts of the FWL, but a long-lasting deterioration of the deeper parts [22, 25, 32, 33, 37–39].

Furthermore, overextraction of fresh groundwater resulting in saltwater intrusion but also contamination with biological and chemical pollutants from surface sources are anthropogenic factors affecting thickness, quality, and quantity of FWLs [18, 21, 24, 40].

A FWL is currently developing below the eastern part of the North Sea barrier island Spiekeroog, the so-called "Ostplate," representing the study area. The formation of the FWL started in the 1970s, when the first dunes covered with *Ammophila arenaria* (European beachgrass) appeared [41]. As a nature conservation area located within the national park "Nationalpark Niedersächsisches Wattenmeer" and thus part of the World Heritage Site "Wadden Sea," declared in 2009, the Ostplate remains largely unaffected by human activities. The island's village and infrastructure, including the groundwater abstraction wells, are all located in the western part of Spiekeroog, whereas the younger Ostplate and the formation of the associated FWL are unaffected by anthropogenic activities. Coastal protection measures do not exist, and the FWL is exposed to natural dynamic changes like storm tides and geomorphological variations. The FWL of the Ostplate has so far not been monitored, and except for preliminary estimates from numerical simulations by Röper et al. [41], vertical extent, tidal and seasonal dynamics, and temporal evolution of the FWL are yet unknown. However, Holt et al. [27] reported that the shallow groundwater salinities (groundwater salinity near the water table) are influenced by storm tides and inundation frequency. The near-surface extent of the FWL of the Ostplate is therefore characterized by spatial and temporal variations.

Processes affecting FWLs were analyzed in many numerical modeling studies. These studies cover natural and anthropogenic influences regarding the (formation of) FWLs (e.g., [18, 21]) and response and recovery of FWLs after saltwater intrusion due to inundation with seawater (e.g., [25, 26, 32]) or are generic model approaches investigating impacts of potential and future storm tide and inundation events (e.g., [22, 31, 42]). Thereby, a range of simulations conducted on islands are restricted in the sense that they only take one sea boundary into consideration, i.e., the model domain does not cover the entire island width, that effects of storm tides on the formation of FWLs are neglected, or only single storm tide and inundation events are considered. In contrast, Huizer et al. [43] showed for an artificial environment (beach nourishment) at the coast of the Dutch mainland how storm tides and geomorphological changes affect the formation of a very young FWL.

In the present study, we combine detailed field observations of a currently developing FWL at a barrier island with a comprehensive modeling approach. In contrast to a previous study at the site [27] that focused on the spatial and temporal dynamics of shallow groundwater salinities as a function of inundation frequency, the aims of this study were (i) to reconstruct the evolution of a currently developing FWL impacted by tides and storm tides over several decades in order to explain the present-day groundwater salinity distribution within the aquifer and (ii) to assess the impact of geomorphological changes and storm tides on the FWL formation.

2. Study Area

The barrier island Spiekeroog is part of the East Frisian Island chain, located ~6.5 km in front of the northwest coastline of Germany in the North Sea. It lies between the islands of Langeoog to the west and Wangerooge to the east. The west-east and north-south extents of the present island are ~9.8 km and 2.3 km, respectively, resulting in a total area of the island of ~21.3 km^2. Whereas the older western part of the island (~4.5 km) is inhabited, the younger eastern part (~5.3 km), the Ostplate (Figure 1), is uninhabited and highly protected by nature conservation regulations [44, 45].

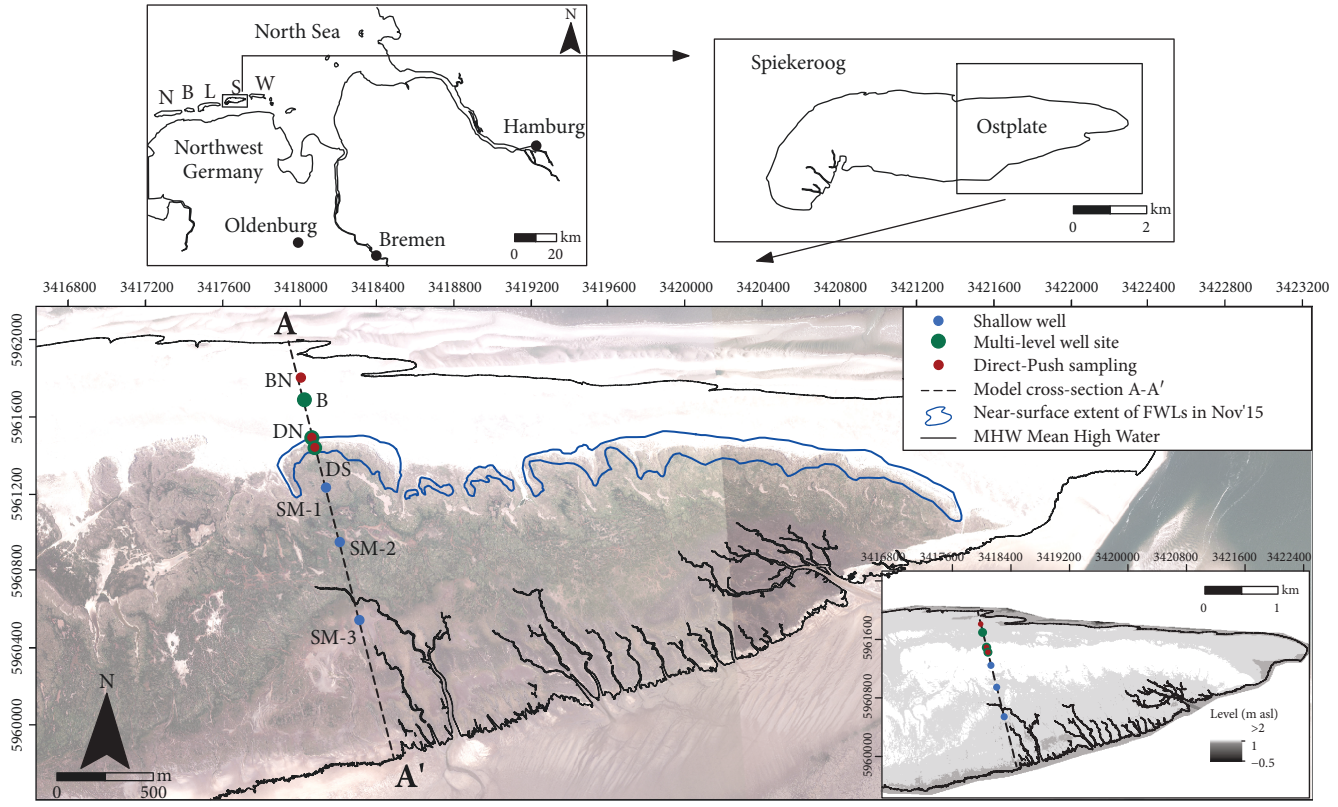

Figure 1: Overview of the Ostplate with the location of the monitoring sites, modelled cross-section A-A', and near-surface extent of FWLs in November 2015, which are restricted to the elevated dune areas [27]. Aerial picture of 2013 as well as the laser-scan elevation model of 2014 was provided by the Lower Saxony Water Management, Coastal Defense and Nature Conservation Agency (NLWKN) [59]. East Frisian Islands (top left): N: Norderney, B: Baltrum, L: Langeoog, S: Spiekeroog, W: Wangerooge.

2.1. Geomorphology of the Ostplate. Around 1940, the Ostplate was no more than a periodically flooded sand flat. The development of the Ostplate towards a dune island was caused by land reclamation and embankment activities at the mainland [41]. According to Röper et al. [41], the dune formation started with the initial growth of unstable pioneer dunes due to aeolian processes in the 1940s. Using Optically Stimulated Luminesce (OSL) age dating on core sediments, which were extracted at the dune base, Seibert et al. [46] could confirm that the aeolian sediments of the upper dune parts are younger than ~80 years. The first appearance of *A. arenaria* around 1970 marked the formation of white dunes (secondary dunes) and the start of the freshening process in the dunes [44, 47]. With a maximum height of ~11 m above sea level (asl), the present dunes of the Ostplate are mainly characterized as white dunes and partly grey dunes (tertiary dunes) [41]. The shelter of the dunes also enabled an extensive growth and spreading of salt marsh vegetation [27, 41]. For more detailed information on the evolution of the Ostplate, see Holt et al. [27], Röper et al. [41], and Seibert et al. [46].

2.2. Hydrology and Hydrogeology. Spiekeroog is affected by semidiurnal tides, with the tidal regime (mean tidal range of 2.72 m) being mesotidal according to the classification of Hayes [48]. Mean High Water (MHW) reaches 1.39 m asl and Mean Low Water (MLW) 1.33 m below sea level (bsl; annual means from 1995 to 2015 [49]). The mean spring range is 3.09 m, whereas the mean neap range is 2.23 m [50]. Three storm tides, reaching a maximum height of 3.05 m asl, were recorded during data collection in the winter 2016/2017 [49].

Affected by a temperate climate with all-season rainfall, the average annual precipitation amounts to 808 mm at Spiekeroog (from 1984 to 2011 [51]). With respect to the historical island formation [52], the evolution of the FWL in the western part of Spiekeroog started ~350 years ago, and the present FWL has a thickness of ~44 m and is being used for the island's drinking water production [53]. Based on apparent ^{3}H-^{3}He ages, Röper et al. [53] calculated groundwater recharge rates of 300-400 mm a^{-1} for the western dune area of Spiekeroog, while other references reported on recharge rates between 301 and 640 mm a^{-1} [54, 55]. The salt marsh, in contrast, is characterized by lower recharge rates due to the less permeable fine-grained sediments (clay, silt) and drainage due to the existence of tidal creeks (as suggested by [56, 57]).

The sediments of the western part of Spiekeroog consist of fluviatile Pliocene sand deposits partly with enclosed peat layers, which are overlain by sandy glaciofluvial Pleistocene deposits and fine- to coarse-grained Holocene sands. At a depth of 40 to 60 m bsl, the sand deposits

are underlain by a clay layer of 1.5-15 m thickness [55] (compare [53, 58]).

Röper et al. [41] also proved the existence of freshwater below the dunes at the Ostplate, and Holt et al. [27] could show that several separated FWLs, restricted to the elevated dune area, exist here (Figure 1). Strongly affected by spatial and temporal water-level variations, most importantly the storm tides mainly occurring in winter, the largest near-surface extent of the FWLs was observed in summer, whereas the winter storm tides lead to a shrinkage. The northern beach area and the broad salt marsh covering most of the southern area of the Ostplate are characterized by underlying brackish to saline groundwater as a consequence of frequent inundations [27]. However, a reconstruction of past shallow groundwater salinities indicates an expansion of areas underlain by freshwater due to dune growth and a simultaneous saltwater decrease for the past 15 years [27]. Seibert et al. [46] could further show that the groundwater salinity at the margin of the here investigated FWL also shows high temporal variations in greater depth and is largely determined by storm tides. Seawater infiltration during inundations and salinization of the former fresh margin of the FWL results in an abruptly steep rise of the salinity followed by a gradual salinity decrease over time.

3. Material and Methods

3.1. Instrumentation and Sampling. Six monitoring sites were installed in a north-south trending transect at the western part of the Ostplate (A-A', Figure 1) in March 2016, to facilitate groundwater level and electrical conductivity (EC) measurements. The transect is oriented along the principle assumed north-south groundwater flow direction that follows the general topographic gradient (Figure 1). Multilevel observation wells (OWs) were installed at the beach (monitoring site B, 3 piezometers with a single screen each; B-a: 0.83 m asl, B-b: -5.31 m asl, and B-c: -12.69 m asl) and at the northern (monitoring site DN, 4 piezometers with a single screen each; DN-a: 1.54 m asl, DN-b: -1.54 m asl, DN-c: -4.55 m asl, and DN-d: -6.44 m asl) and southern (monitoring site DS, 3 piezometers with a single screen each; DS-a: 1.70 m asl, DS-b: -1.04 m asl, and DS-c: -3.07 m asl) dune base, respectively (Figure 2). Three shallow single screen OWs were installed within the salt marsh south of the dunes (Figure 1), screening near-surface groundwater at 1.29 m asl (SM-1), 1.34 m asl (SM-2), and 0.97 m asl (SM-3) (Figure 2). All of the installed piezometers have a screen length of 1 m.

Groundwater levels were continuously measured at all OWs (except for B-b and DN-b) with CTD-Divers (DI271, Schlumberger Water Services) and with Mini-Divers (DI501, Schlumberger Water Services), respectively, using 10-minute intervals from April 2016 to August 2017. The EC was measured manually during six hydrochemical sampling campaigns (bimonthly) described in Seibert et al. [46]. Groundwater samples were extracted from all OWs (Figure 2) using a submersible pump (Gigant, Eijkelkamp). In addition, the Direct-Push method (probe: water sampler DP32/42 with 1 inch internal filter of 0.5 m length, Stitz) was applied at the monitoring sites BN, DN, and DS in September 2016, which allowed for the depth-specific extraction of additional groundwater samples ($n = 11$) and a higher spatial resolution of the vertical FWL extent compared to the permanent monitoring sites DN and DS alone. Samples were collected every meter (Figure 2) using a foot valve pump (S-60, Stitz). Table S.1.1 (see Supplementary Material) gives an overview of the instrumentation of the installed OWs and Direct-Push drillings as well as time periods of the water level and EC measurements.

The EC of all samples was measured using a Hach HQ40d multidevice (automatic temperature correction to 25°C) and subsequently converted into salinity using the method described in Holt et al. [27]. Groundwater salinities were classified according to Freeze and Cherry [60], with freshwater, brackish water, and saltwater having a salinity of <1, 1-10, and >10 ($g\,L^{-1}$), respectively.

3.2. Numerical Model. Assuming the principle north-south groundwater flow direction (see Section 3.1 and Supplementary Material S.2), a transient vertical density-dependent 2-D groundwater flow model was set up for the cross-section A-A', i.e., along the transect of OWs (Figure 1), using the software SEAWAT [61].

The north-south oriented model cross-section A-A' (Figures 1 and 3) is bounded at the MHW-mark (1.39 m asl) north and south of the Ostplate and includes the beach in the north (~520 m length) with a slope of about 0.002, as well as dune (~100 m length) and salt marsh areas in the south (~1,610 m length). The extent of the model is 2,230 m in the horizontal direction, with a discretization of 10 m. The topography was obtained from a laser-scan elevation model of 2014 (provided by the NLWKN [59]), interpolated with the field interpolator of the groundwater simulation software PMWIN (Processing Modflow, Version 8.0.47, www.simcore.com) to the model grid, and assigned to the top of the uppermost model layer. Except for the first two model layers, the vertical discretization is 1 m. The thickness of layer 1 ranges from 0.75 m to ~8 m, and the thickness of layer 2 ranges from 0 m to 0.9 m. This was done to circumvent the SEAWAT-specific rewetting process of dry cells during groundwater table movement across model layers, which sometimes causes numerical problems.

A no-flow boundary was assigned to the bottom boundary, assuming that the clay layer detected at the western part of the island (see Section 2.2) also exists at the eastern part of the island. Because of the extremely low morphological gradients of the beach and salt marsh areas and the correspondingly extremely small time steps (in the order of seconds) that would be needed to adequately resolve the extremely fast pressure propagation of the tidal signal at the top boundary, tide-averaged constant heads rather than real tides (following the approach of Vandenbohede and Lebbe [11, 62]) were defined at the northern and southern vertical model boundaries at the MHW-mark (Figure 3). The assigned heads were based on field measurements near the MHW-line at the beach at the western part of Spiekeroog [63] and slightly calibrated to 0.8 m asl (northern boundary) and 0.9 m asl (southern boundary). Reflecting the so-called tidal overheight

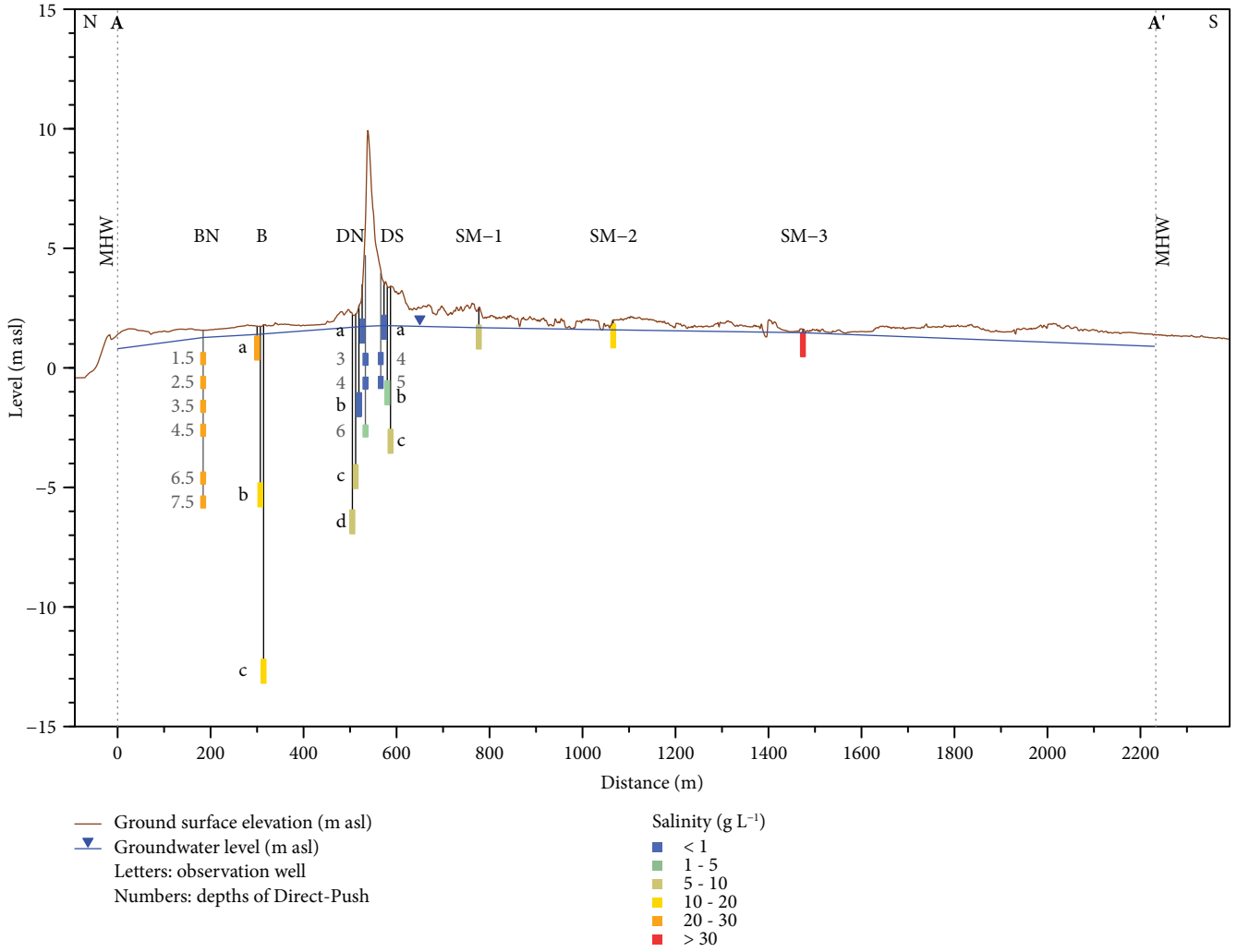

FIGURE 2: Location and mean screen depths of the OWs (marked with letters in black) and the Direct-Push drillings (depths marked with numbers in grey). Groundwater salinities measured in September 2016 are shown. The groundwater level (blue line) in this and following figures corresponds to the mean point water head between April 2016 and December 2016 (period without storm tides). The distance (*x*-axis) in this and following figures refers to the distance between the MHW-mark north of the dunes (distance = 0 m) and the MHW-mark south of the dunes. The level in m asl (*y*-axis) in this and following figures is equivalent to height above vertical datum NHN.

due to asymmetric in- and outflow conditions during high and low tide, respectively, at a sloping beach [64], the hydraulic heads at the MHW-line are elevated compared to the mean sea level. A direct implementation of the tides (e.g., semidiurnal, spring, neap, and storm tides) would lead to excessively large computing times (similar to, e.g., Comte et al. [65]) and is to the author's knowledge not feasible for a simulation of >40 years. Furthermore, a detailed analysis of the daily tides would be beyond the scope of this study, as it is focusing on the FWL evolution on a decadal time scale. The northern and southern vertical boundaries for the transport model were defined as non-dispersive flux boundaries [66]. Here, the salinity of the water entering the model domain through the constant head flow boundary was set to seawater salinity (32 g L^{-1}), whereas for outflow conditions, it was set to the salinity of the water computed at the boundary cell. The non-dispersive flux boundary is commonly applied to simulate seawater-groundwater interaction at the costal boundary (e.g., [67, 68]).

The horizontal hydraulic conductivity served as a calibration parameter, and the final calibrated value of 2×10^{-4} m s^{-1} agreed well with the hydraulic conductivity derived from grain size analysis and Darcy experiments (see Supplementary Material S.3, Fig. S.3.1). It is within the range of values for sand [69] and in line with results of pump tests conducted at the western part of Spiekeroog (1.4×10^{-4} and 2.9×10^{-4} m s^{-1}) [55]. The vertical anisotropy of the hydraulic conductivity was set to 1 : 1, as anisotropic hydraulic conductivities yielded poorer model results (similar to Schneider and Kruse [21]). The effective porosity was set to 0.35, which is a similar value found in related studies (e.g., [10, 11, 41, 62]). The longitudinal dispersivity and the vertical transverse dispersivity were $\alpha_L = 4$ m and $\alpha_{VT} = 0.04$ m, respectively, and found during model calibration. The model parameters are listed in Table 1.

Assuming that the FWL formation started around 1975 (based on Röper et al. [41]), the total simulation time was 42 years (1975-2016).

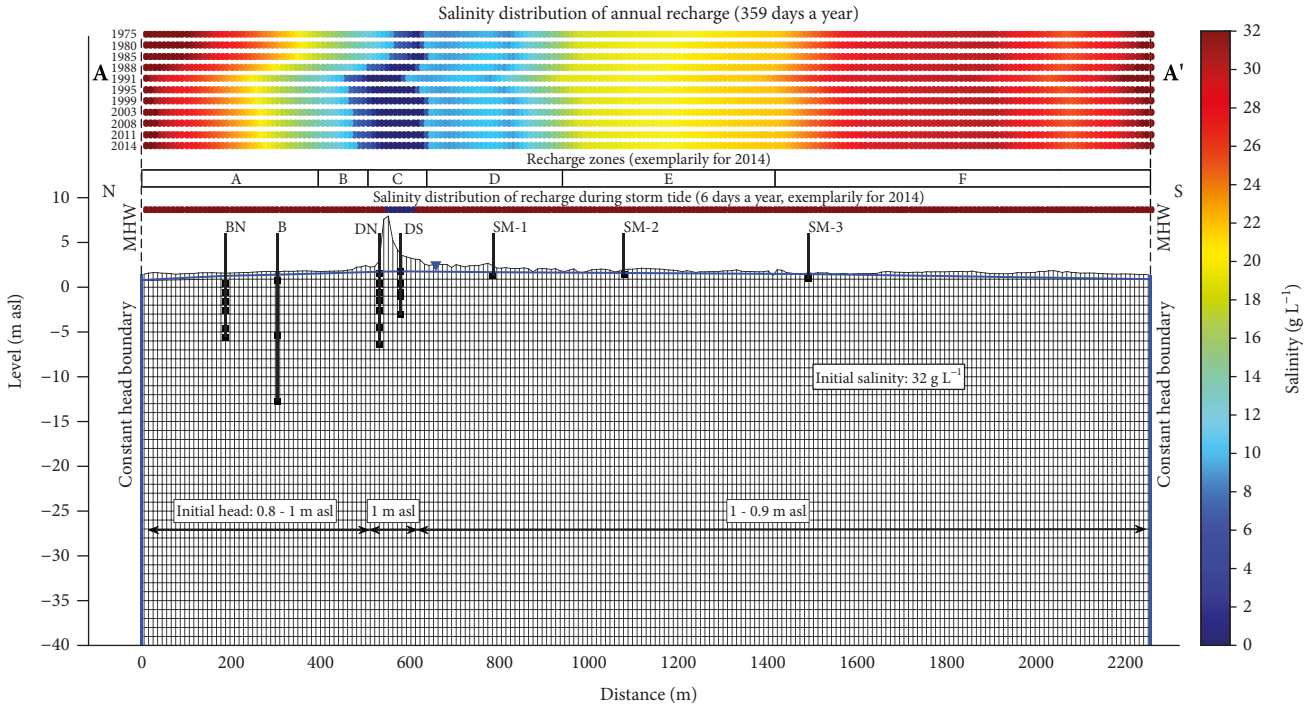

FIGURE 3: Model set-up of the north-south oriented cross-section A-A' (Figure 1) with initial and boundary conditions. Fresh recharge areas indicate variations of the position and extent of the elevated dune area for the depicted years considered in the VG-model. Between these years, the recharge salinity of the previous year was assigned. In the CG- and CGWST-model, the salinity distribution of 2014 was kept constant. Salinities are indicated by the color scale (this also applies to the following figures). Zones A-F represent zones of different recharge rates kept constant in the CG- and CGWST-model. In the VG-model, zones depended on the geomorphology of the respective year.

The conceptual model described above was used to explain the present-day groundwater salinity distribution and extent of the FWL, and to reconstruct a temporal evolution of the FWL below the dune belt in the western part of the Ostplate. Due to missing historical data, the simulation is only calibrated with respect to the present groundwater levels and groundwater salinities (2016-2017). The simulation assumed at first a constant geomorphology, i.e., only the geomorphology of the year 2014 was considered. This base case is referred to as Constant Geomorphology-model (CG-model) in the following. Furthermore, two additional model cases based on the CG-model were considered. The first additional case indirectly accounted for geomorphological changes (in the following referred to as Variable Geomorphology-model (VG-model)). Within the second additional case, the CG-model was run without implementing annual storm tides (in the following referred to as Constant Geomorphology Without Storm Tides-model (CGWST-model)). Comparing both additional cases to the base case (CG-model) allowed to study how the FWL and the groundwater salinity distribution depend on geomorphological variations and storm tides that are characteristic for the highly dynamic environment investigated here. We would like to emphasize here that the simulations are not intended to exactly replicate the observed hydraulic heads and groundwater salinities over time at the cross-section investigated here which is not possible for the lack of data before 2016. Rather, the simulations were conducted to reflect the observed pattern of hydraulic heads and ground-

TABLE 1: Overview of model parameters. Parameters marked with (*) were calibration parameters. Hydraulic conductivity, porosity, and longitudinal and vertical transverse dispersivities were set constant across the model domain, i.e., homogeneity of the porous medium was assumed.

Parameter	Value	Units
Constant heads[1] (*)	0.8 (northern boundary) 0.9 (southern boundary)	m asl
Hydraulic conductivity (horizontal, vertical) (*)	2×10^{-4}	$m\,s^{-1}$
Initial groundwater salinity	32	$g\,L^{-1}$
Seawater salinity[2]	32	$g\,L^{-1}$
Freshwater salinity	0	$g\,L^{-1}$
Porosity	0.35	—
Longitudinal dispersivity (*)	4	m
Vertical transverse dispersivity (*)	0.04	m
Recharge/infiltration rates (*)	See Table 2	$m\,a^{-1}$
Recharge salinity	See Table 2	$g\,L^{-1}$

[1]0.1 m difference between the calibrated constant hydraulic head at the southern boundary compared to the northern boundary corresponds well to the observed difference of 0.07 m between the measured MHW-levels in the back barrier tidal flats in the south and the open ocean in the north of the East Frisian Islands (see Supplementary Material Table S.4.1). [2]Salinity of the North Sea at the study area (mean salinity of sampled seawater [58]).

Table 2: Overview of the implemented recharge and infiltration rates, respectively, and recharge salinities under normal conditions (359 days a year) and during storm tides (6 days a year).

Recharge zones	359 days a^{-1} (normal conditions)			6 days a^{-1} (storm tides)		
	Recharge rate ($m\ a^{-1}$)	Total recharge (mm)	Recharge salinity ($g\ L^{-1}$)	Infiltration rate ($m\ a^{-1}$)	Total infiltration (mm)	Recharge salinity ($g\ L^{-1}$)
A	0.4	393	32-15[1]	0.6-31[2]	10-510	32
B	0.5	492	14-1.4	33-50	542-822	32
C	0.52	511	0	0.52[3]	9[3]	0[3]
				9-19[4]	148-312[4]	32[4]
D	0.35	344	6-16	13-10	214-164	32
E	0.2	197	16-22	9-2	148-33	32
F	0.15	148	22-32	2-0.02	33-0.3	32

[1]Assigned recharge salinities are a function of ground surface elevation and resulting inundation frequency and were based on salinity measurements of near-surface groundwater [27]. [2]Assigned infiltration rates during yearly storm tides were linked to the thickness of the unsaturated zone, presuming that the entire unsaturated zone of impacted areas gets filled up with seawater in a single storm tide. [3]Non-inundated part of the dune area. [4]Inundated part of the dune area.

water salinities over time in a more generic, however, real-data oriented sense, in order to analyze the significance of a varying geomorphology and storm tides on the evolution of a FWL on a young barrier island.

The groundwater flow was numerically solved with the Geometric Multigrid Solver (GMG) and advection-dispersion with the Hybrid Method of Characteristics (HMOC) in conjunction with the Generalized Conjugate Gradient (GCG). The HMOC scheme provides a solution with virtually no numerical dispersion independent from the Grid Peclet number [66] but is prone to small mass balance errors. In all our simulations, a mass balance error of <1.5% as well as grid-independent of the simulation results were ensured.

3.2.1. Constant Geomorphology with Storm Tides: CG-Model. A specified flux boundary for the flow model with different recharge rates was assigned along the top boundary, coupled with a non-dispersive flux boundary for the transport model characterized by the salinities of the recharge water (shown by the salinity distribution of annual recharge in the last row from above labelled "2014" and by the salinity distribution of recharge during storm tide in Figure 3). Recharge rates were considered as calibration parameters. Nevertheless, the calibrated rates correspond to the sediment type along the cross-section A-A', the unsaturated zone thickness and the geomorphology of the year 2014. Due to the lack of historical data prior to 2014, rates were applied to the entire simulation time (1975-2016). The highest recharge rates were assigned to the dune area (fine to coarse sand, recharge zone C, Figure 3 and Table 2) and a 30 m wide area north of the dunes. The beach was divided into two recharge zones (recharge zone A and B, Figure 3 and Table 2). Although other studies conducted on Frisian Islands reported on lower recharge rates (e.g., [25, 56, 70, 71]), the range of recharge rates used in this study is in line with previously determined rates at Spiekeroog (see Section 2.2). Salt marsh areas were divided into three recharge zones (recharge zone D, E, and F, Figure 3 and Table 2) with lower recharge rates as those areas are characterized by less permeable near-surface fine-grained sediment layers (i.e., clay and silt), which were also described in Sulzbacher et al. [56], as well as by draining tidal creeks. Also, a denser vegetation cover occurring in salt marshes typically diminishes recharge due to enhanced transpiration [21].

Fresh recharge (salinity $0\ g\ L^{-1}$) was implemented in the elevated dune area (≥3 m asl). The recharge salinity increases with increasing distance from the dunes and decreasing ground surface elevation at the beach and salt marsh areas (shown by the salinity distribution of annual recharge in the last row from above labelled "2014" in Figure 3). The implementation of this salinity gradient enabled an indirect but efficient way of accounting for an increase of inundation frequency and its bulk effect on introduced salt mass with increasing distance from the dunes. Again due to the lack of historical salinity measurements, we applied the present-day near-surface groundwater salinity distribution [27] for the entire simulation period.

Severe flooding events inundate the entire Ostplate except for the elevated dune areas [27] roughly two times per year on average [49] (tides reaching a height >1.40 m above MHW, referred to as storm tides in the following) affecting the groundwater salinity distribution at the margin of the FWL [46]. To account for these, transient recharge rates (instead of recharge rates, we refer to infiltration rates for seawater infiltration in the following) and recharge salinities were implemented into the model. Volumes of infiltrating seawater were estimated based on the thickness of the unsaturated zone and the porosity (0.35), presuming that the entire unsaturated zone of inundated areas gets filled up with seawater during an inundation event (as suggested by Illangasekare et al. [30] and Chui and Terry [31]). The thickness of the unsaturated zone was calculated for the locations of the monitoring sites and linearly interpolated in between. Consequently, the highest infiltration rates were assigned to the northern and southern dune base.

Based on the two storm tides per year on average, we assumed that the unsaturated zone gets filled up with seawater twice a year. For numerical reasons, i.e., a long computing time due to small computational time steps and the vulnerability of the simulation to numerical instabilities, we

distributed the respective infiltration volume evenly over a period of six days. Since salinities directly at the margin of the FWL were, however, overestimated (results not shown), seawater infiltration rates were subsequently reduced to one third in areas characterized by ground surface elevations >2.40 m asl. This is a reasonable assumption as these areas are submerged in seawater only during very short periods of time. Contrary to Chui and Terry [31], we assumed that this time is insufficient to fill up the entire unsaturated zone. The non-inundated part of the dune area is characterized by an infiltration rate of 0.52 m a^{-1} at all model times. Because of low permeabilities and a denser vegetation cover, only half of the calculated infiltration volumes were assigned at the salt marsh areas during storm tides.

Recharge salinities during storm tides correspond to local seawater salinity (32 g L^{-1}), except for the non-flooded parts of the dune area (0 g L^{-1}, shown by the salinity distribution of recharge during storm tide in Figure 3).

Table 2 gives an overview of the implemented infiltration/recharge rates, the total infiltration/recharge, and the corresponding recharge salinity distribution during storm tides as well as during the remainder of the year, respectively.

3.2.2. Variable Geomorphology with Storm Tides: VG-Model. Temporal changes of the geomorphology at the Ostplate were evident based on (a) the analysis of aerial and infrared pictures, and digital elevation models for the years 1985, 1991, 1999, and 2011 by Röper et al. [41] and (b) digital elevation models of the years 2008 and 2014 (provided by the NLWKN [59]). We presume that these geomorphological variations influenced the formation of the FWL. Areas with fresh recharge relevant for the FWL formation (dune area ≥3 m asl) were located for the years 1985, 1991, 1999, 2008, 2011, and 2014 using ArcGIS (see Supplementary Material Fig. S.5.1).

In cases where the time intervals between the mentioned years is >5 years, the extent of the dune area was linearly interpolated (Table S.5.1), resulting in interpolated extents for the years 1988, 1995, and 2003. The extent of the dune area was set to 10 m, as the minimal extent of a model cell, for the year 1975 (assumed start of the FWL formation [41]) and to the half of the dune extent of 1985 for the year 1980.

The implementation of the temporally varying geomorphology into the model set-up was done by adjusting the recharge zones and salinities, respectively, which were identified and used in the CG-model, while the remainder of the model parameters (Table 1) was left unchanged. Figure 3 gives a schematic overview of the changing geomorphology implemented indirectly in the model by an altering domain of fresh recharge (blue color) for the aforementioned years (shown by the salinity distribution of annual recharge). For simplicity, the storm tide salinity distribution is displayed for the year 2014 only, but also changed depending on the geomorphology for the years before (Figure 3). The same applies to the location and extent of the recharge zones. Recharge and infiltration rates, respectively, and recharge salinities depending on the position and extent of the dune area in the respective years are listed in Table S.5.2 and Table S.5.3 (see Supplementary Material).

3.2.3. Constant Geomorphology without Storm Tides: CGWST-Model. Apart from the infiltration rates and recharge salinities assigned for the storm tides in the CG-model, the model parameters were the same as in the CG-model (Tables 1 and 2).

4. Results and Discussion

4.1. Present-Day Groundwater Salinity Distribution and Extent of the FWL: Field Data. The schematic cross-section shown in Figure 2 gives an overview on the groundwater salinity distribution along A-A' and shows the results of the sampling campaign in September 2016. Freshwater (salinity ≤1 g L^{-1}) was only found in the upper OWs and Direct-Push locations below the dunes (DN-a, DN-3,4, DN-b, DS-a, and DS-4,5), indicating a FWL with an asymmetric shape. The change from fresh (salinity ≤1 g L^{-1}) to brackish groundwater (salinity 1-10 g L^{-1}) occurs at ~5 m below ground surface (m bgs) at both the northern (between DN-b and DN-6) and southern dune base (between DS-5 and DS-b). Hence, the maximum vertical extent of the FWL is ~4 m at the northern margin of the FWL (related to the mean depth between DN-b and DN-6). Compared to the FWL thickness of 14-25 m bsl suggested by preliminary numerical simulations of Röper et al. [41], the actual FWL extent is significantly smaller.

The brackish transition zone below the FWL is not a sharp boundary but a diffuse zone of several meter thickness with increasing salinities with increasing depth (DN-6, DN-c, DN-d, DS-b, and DS-c). However, the exact vertical extension of the brackish zone remains unclear, since it was not possible to drill deeper and saline groundwater was not intersected even at the deepest wells at the dunes (i.e., DN-c, DN-d).

The storm tides in December 2016 and January 2017 resulted in inundations of the Ostplate leading to a shrinkage of the FWL at the northern margin, and freshwater was only found at the uppermost OW south of the dunes in January 2017 (DS-a, see Supplementary Material Fig. S.6.1).

4.2. Model Results. The groundwater salinity distribution in different years after the onset of the freshening process is illustrated in Figure 4 for all three model cases. Videos of the evolution of the FWL are available in the Supplementary Material (videos S.7.1, S.7.2, and S.7.3).

4.2.1. Temporal FWL Evolution until Present with and without Geomorphological Variations. Both the CG- and the VG-model show the development of an asymmetric FWL which horizontal extent is limited by the elevated dune area (≥3 m asl), i.e., the area of fresh recharge (CG- and VG-model in Figure 4). The asymmetrical shape of the FWL is caused by the location of the water divide south of the dunes in the upper part of the salt marsh at a distance of about 1,000 m (CG-model) and 980 m (VG-model) from the northern model boundary, respectively. Hence, all freshwater that infiltrates in the dunes flows towards the beach and the northern MHW-boundary, respectively. Initial freshwater bodies (salinity ≤1 g L^{-1}) developed after

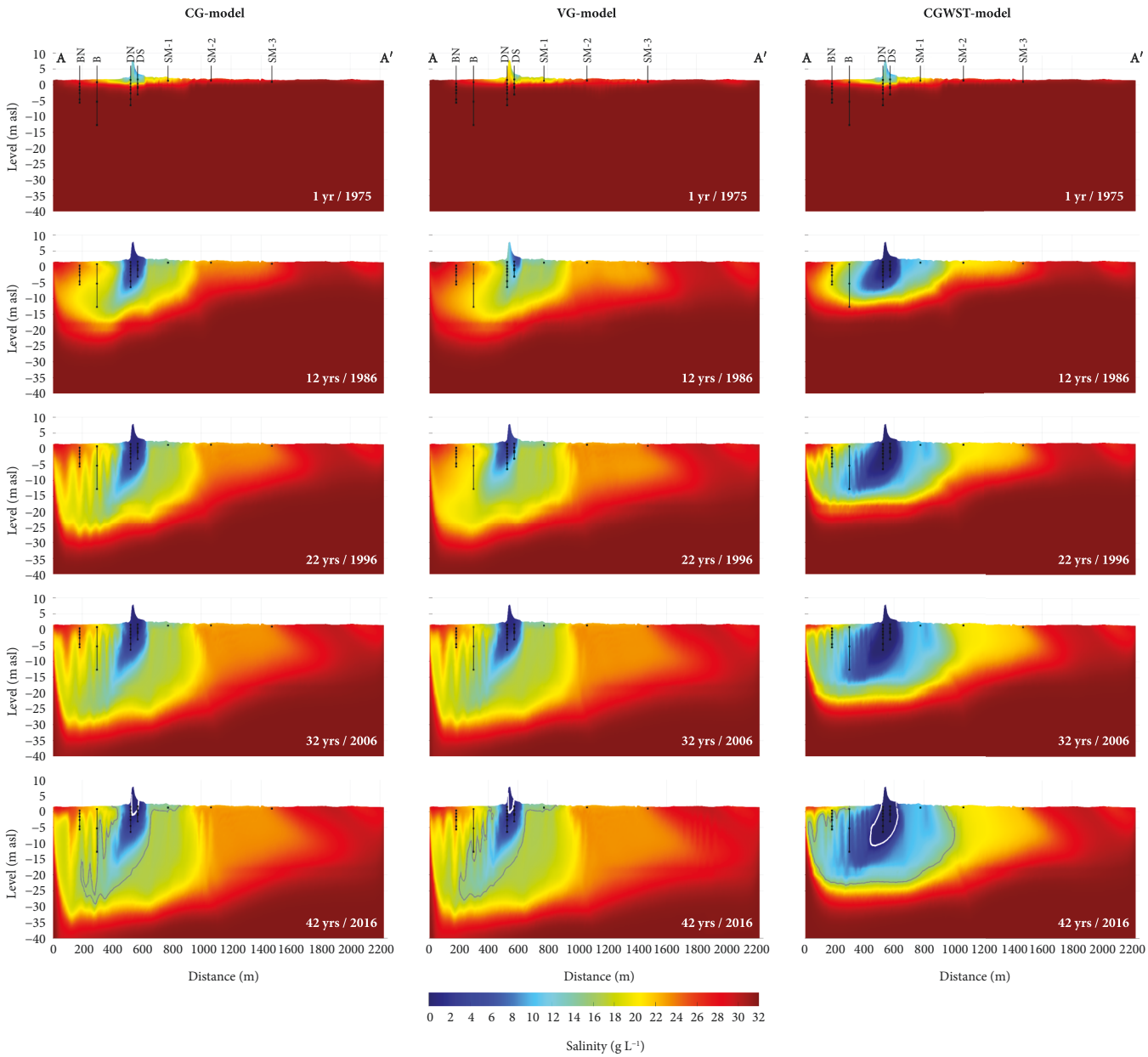

Figure 4: Temporal evolution of the groundwater salinity distribution and FWL along cross-section A-A' for the CG- (left column), VG- (central column), and CGWST-model (right column). Model results are presented for various simulation times, with the present situation after 42 years at the bottom row. The 1 g L^{-1} (white line) and the 16 g L^{-1} (i.e., 50% seawater, gray line) contour lines, respectively, are displayed for the present situation. Note that the salinities represent the distribution before storm tides occur at the end of each respective year.

11 and 25 years in the CG-model and the VG-model, respectively. The time lag between the two model approaches is due to the strong movement of the dunes in the first simulation years, which was only accounted for in the VG-model.

The simulated maximum vertical extent of the present FWL is about 3-4 m, which is well in line with the vertical thickness observed in the field (Figure 2). The horizontal extent varies between 50 m (CG- model) and 40 m (VG-model). Considering a west-east extent of 1 m and a porosity of 0.35, the volume of the FWL is estimated to be ~65 m^3 (CG- model) and ~38 m^3 (VG-model), respectively, along the cross-section A-A'. Assuming one connected FWL below the dunes on the entire Ostplate with a west-east extent of ~3,600 m and a constant width of the dune ridge, the freshwater volume would amount to ~234,000 m^3 (CG-model) and ~137,000 m^3 (VG-model). The dimensions of the freshwater volume calculated here deviates strongly from the preliminary numerical simulations of Röper et al. [41], who calculated a freshwater volume ranging between 42 and 92 million m^3. Reasons for the larger freshwater volume of their model may be the combined effect of assumed lower horizontal and vertical hydraulic conductivities, a wider area of fresh recharge, and the omission of storm tides.

The formation of the FWL is accompanied by the establishment of a wide brackish transition zone. Similar to field observations, the transition zone is not a sharp boundary but a diffuse zone of >10 m thickness showing increasing salinities with increasing depth (CG- and VG-model in Figure 4). The transition between freshwater and brackish water is located at ~5 m bgs (CG-model) and ~4 m bgs (VG-model). The distinctly thicker transition zone, compared to the vertical extent of the FWL, is in line with White and Falkland [18], after which FWLs characterized by a vertical extent of <5 m often are underlain by a transition zone larger than the FWL itself. The thickness of the transition zone is influenced by dispersive mixing, tides, temporal variabilities of recharge, hydraulic properties of the aquifer, and inundations evoked by storm tides [17, 18, 72].

Both simulation outcomes clearly suggest the appearance of saltwater fingering (onset in the CG-model: after 19 years, VG-model: after 26 years), especially below the beach due to infiltrating seawater. The development of saltwater fingers migrating from the upper beach towards the northern boundary at the MHW-line is caused by density differences between the groundwater characterized by lower salinities than seawater and the seawater which infiltrates in particular during storm tides. Such a behavior in the intertidal zone has previously been proposed by modeling and laboratory studies [39, 73–75]. Saltwater fingers are also recognizable at the northern margin of the FWL.

To assess the model performance, modelled groundwater salinities and hydraulic heads (point water heads) after 42 years were compared to field observations from 2016, as no historical exists. The calculated heads of both models agree well with the observations, and the Nash-Sutcliffe model efficiency coefficient and the Root Mean Square Error (RMSE) only differ slightly between both models (Nash-Sutcliff: 0.93-0.94; RMSE: 0.03-0.04 m, see Supplementary Material Fig. S.8.1).

The comparison of mean calculated (last five years of simulations, see Supplementary Material Fig. S.9.1) and mean observed salinities (bimonthly sampling campaigns, see Section 3.1 and S.1.1) also shows a reasonable correlation for both models, despite some over- and underestimations. Again, both models exhibit only minor differences regarding the model fit with Nash-Sutcliffe coefficients of 0.90 and 0.91 for the CG-model and the VG-model, respectively (Figure 5). Since the saltwater fingering flow causes the groundwater salinity to vary substantially over time on the beach, a direct comparison between calculated and observed salinities for the year of sampling was not appropriate (similar to Post and Houben [25]). Particularly, the upper OWs at the northern margin of the FWL (DN) are characterized by a wide range of observed salinities (compare horizontal error bars in Figure 5). This is due to the highly dynamic environment, most importantly storm tides during winter and the associated salinization. Similar findings were also reported by Huizer et al. [76] for a beach nourishment site. The steep rise of the groundwater salinity following storm tides and the subsequent freshening which was also reported by Holding and Allen [22] for recent sedimentary islands, could be simulated (see Supplementary Material Fig. S.9.1, CG- and VG-model: DN-a) and are also visible in the calculated salinities at these OWs (vertical error bars in Figure 5, CG- and VG-model).

Apart from rather small differences in the spatial extent of the present FWL, the comparison of both models shows that the overall pattern of the current groundwater salinity distribution is very similar (CG- and VG-model in Figure 4). Modeled present-day groundwater salinity distribution and shape of the FWL are predominantly determined by the position and extent of the elevated dune area during the past ~20 years, when only slight variations of the fresh recharge area occurred (Figure 3). Geomorphological changes at the early stage of the FWL formation (VG-model, Figure 4) have only little impact on the present-day situation. Since a consideration of the geomorphological changes did not result in a better model fit, the simulation outcomes suggest that the geomorphological variations are not crucial for the present-day situation of the here investigated FWL. Hence, an overestimation of the FWL volume in the CG-model neglecting geomorphological changes, as reported by Huizer et al. [43], is not expected. This is because strong geomorphological changes only appeared at the beginning of the FWL formation, and the fresh recharge area has since continuously grown, while in the study of Huizer et al. [43], erosion was reported on.

4.2.2. Effect of Storm Tides on Groundwater Salinity Distribution and FWL Development. In contrast to the temporal variability of the geomorphology, the influence of storm tides is very pronounced. The comparison between the cases with (CG-model) and without (CGWST-model) the effect of storm tides clearly indicates that FWLs are very sensitive to storm tides and associated inundations (Figure 4). Furthermore, it shows that the lateral and vertical extent of the FWL largely depends on saltwater infiltration during inundation events. Similar to the findings of, e.g., Anderson Jr [23], Holding and Allen [22, 35], Huizer et al. [76], and Post and Houben [25], the vertical infiltration of seawater caused by storm tides resulted in severe groundwater salinization. It was not possible to achieve a satisfying model fit between observed and modelled data without accounting for storm tides. When neglected, simulated groundwater salinities were considerably underestimated, which especially holds for the salinities at the margin of the FWL and within the transition zone (Figure 5, CGWST-model). Moreover, the neglection of storm tides resulted in a significant overestimation of the FWL extent 42 years after formation (Figure 4), with a maximum vertical and horizontal extent of ~13 m and 180 m, respectively. Thus, considering storm tides is crucial for an adequate simulation of a long-term evolution of a FWL on a whole island width. Otherwise, the amount of infiltrating seawater impacting the development of a FWL would be underestimated, which was also reported by Huizer et al. [43] but neglected by Röper et al. [41]. However, the situation is likely to be different on older islands with higher morphology not prone to inundations.

Similar to the CG-model, saltwater fingers occurred that moved from the upper to the lower beach. Respective

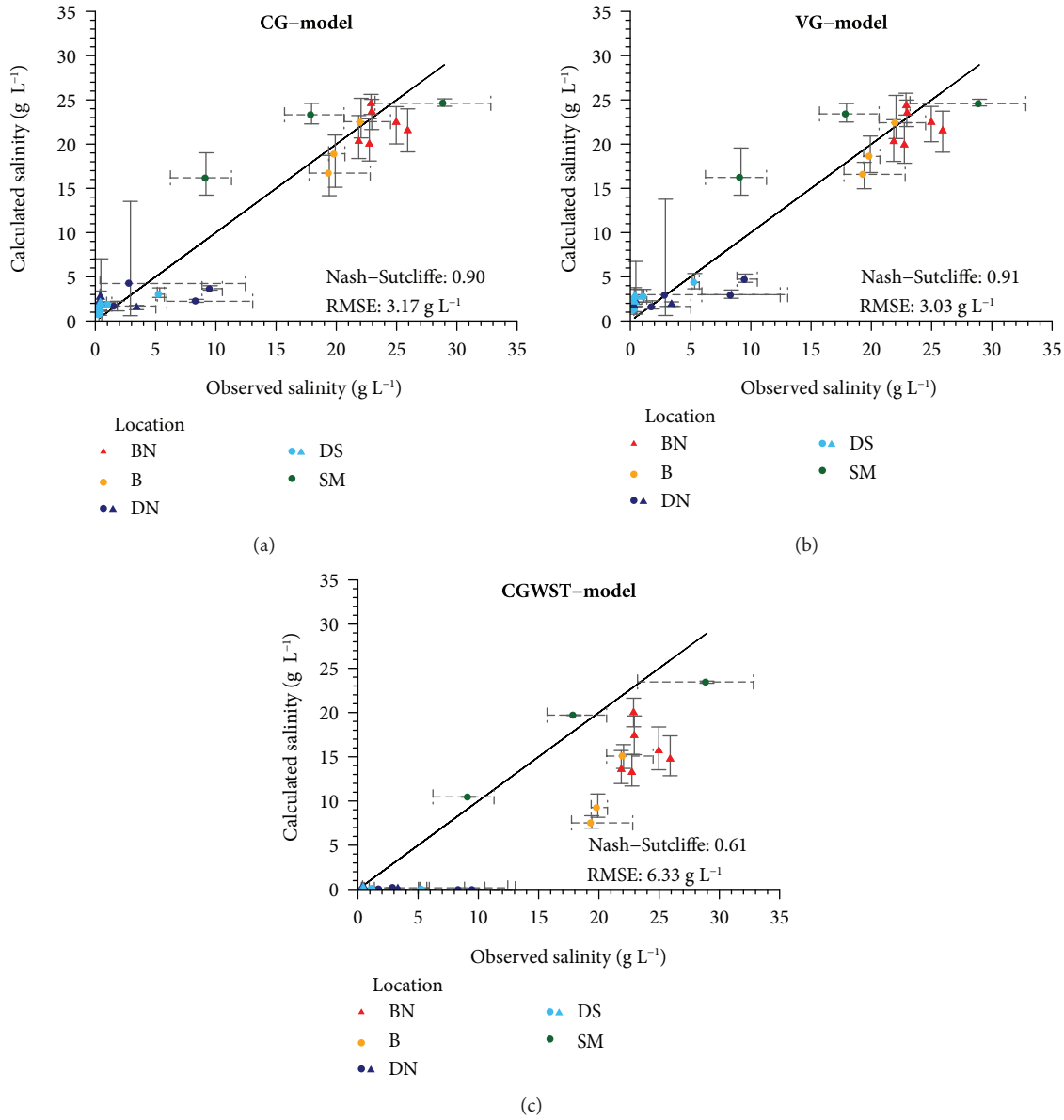

Figure 5: Scatter plots of observed versus calculated groundwater salinities after 42 years of simulation for the CG- (a), VG- (b), and CGWST-model (c). Vertical error bars represent the range of simulated salinities; horizontal error bars correspond to the range of observed salinities. In addition, one-off Direct-Push measurements of September 2016 are displayed (marked with triangles).

salinities were lower due to mixing with freshwater flowing from the larger FWL towards the sea and the missing salt mass from seawater infiltrating during storm tides (Figure 4). In the CGWST-model, the appearance of the fingering was caused by the tidal beach inundation inducing seawater infiltration which was simulated by the increasing recharge salinity towards the northern MHW-line.

4.2.3. Time of Equilibrium and Future FWL Development. The FWL in the CG-model approaches nearly steady-state conditions after ~35 years of formation (with regard to cells with salinity $\leq 1\,g\,L^{-1}$; video S.7.1), while the FWL of the VG-model reaches nearly steady-state conditions after ~70 years of formation (results not shown). Further growth of the FWL is inhibited by the repeated infiltration of seawater caused by storm tides, and its final extent is very similar in both models after steady-state conditions are reached. Note that steady-state conditions in the VG-model would only be realized when the geomorphology is stagnant in the future. The extent of the ≤50% seawater area reaches steady-state after ~100 years of formation (CG-model, Figure 6), i.e., somewhat later than the FWL. Even the larger zone characterized by salinities $\leq 20\,g\,L^{-1}$ does not expand further after 100 years due to downward migrating saltwater fingers.

However, transient conditions of the geomorphology, e.g., further dune growth due to accretion or dune erosion—which are likely to occur in such a highly dynamic environment studied here—will most likely affect the extent of the investigated FWL in the future, since variations of the coastal landscape have impact on the shape and volume of a FWL

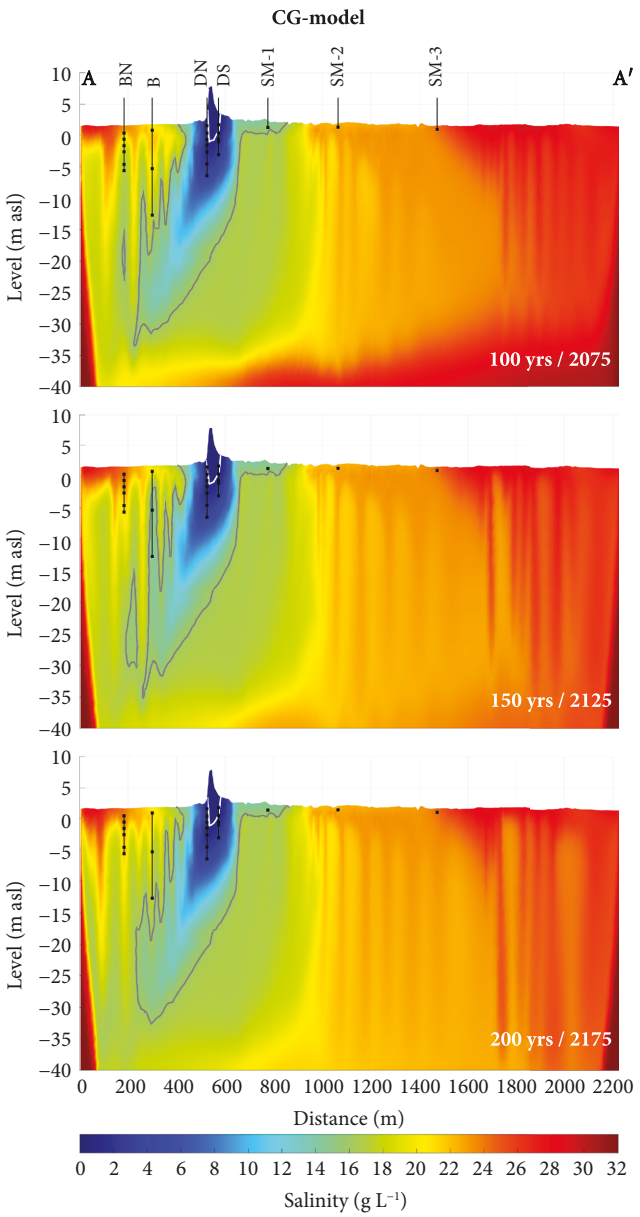

FIGURE 6: Predicted groundwater salinity distribution along cross-section A-A' without further geomorphological changes (CG-model) after a simulation time of 100 yrs (top row), 150 yrs (2nd row), and 200 yrs (bottom row). The 1 g L^{-1} (white line) and the 16 g L^{-1} (i.e., 50% seawater, gray line) contour lines are displayed.

[77, 78]. This was also visible in the onset of the FWL formation in the VG-model (Figure 4). It has been shown previously that the topography of coastal landscapes significantly influences groundwater salinization of coastal aquifers following storm tides [79]. Linked to climate change and expected future sea level rise in the southern North Sea [5], length and frequency of storm tides and resulting inundations with seawater as well as the amount of fresh recharge are further constraints on the future FWL development [56, 80]. Moreover, fresh recharge depends on the vegetation cover in the dunes. As the dunes develop, vegetation will presumably increase and become denser, thereby causing a decrease in the recharge rate, which would consequently affect the FWL development [19, 65, 81]. Hence, real steady-state conditions will likely never be reached.

5. Conclusions

This study provides a comprehensive overview of the evolution of a FWL below a currently developing young barrier island located in a highly dynamic mesotidal environment unaffected by anthropogenic activities. Numerical simulations allowed to reconstruct the temporal evolution of the FWL and to assess the effect of storm tides and geomorphological variabilities on FWL formation. The following conclusions can be made:

(1) Barrier island formation is accompanied by FWL formation as soon as the growth of dunes exceeds storm tide levels

(2) Fingering flow appears to be a likely feature below beaches subject to freshwater discharge from FWLs in combination with frequent seawater inundations

(3) For highly dynamic tidal environments subject to annual storm tides, these have to be directly implemented into models in order to explain the groundwater salinity distributions and the extents of young FWLs

(4) Accounting for flooding frequency indirectly by adjusting the salinity of the recharge water accordingly appears to be a suitable method to mimic highly transient tidal systems without explicitly incorporating tides, as shallow groundwater salinities are a function of ground surface elevation and resulting inundation frequency only

(5) Despite the young age of the Ostplate, a quasi-steady-state FWL has already been established. This is mainly a result of continuous mixing with intruding seawater due to the seasonal storm tides, which inhibits further growth of the FWL under the present geomorphological conditions at the narrow island

(6) Real steady-state conditions will most likely never be reached due to the ever varying changes of geomorphology, sea level, and fresh recharge in such a highly dynamic coastal environment

(7) A major uncertainty in the presented modeling approach are implemented recharge rates, especially the seawater infiltration rates. Future studies addressing the process of infiltration during inundation are needed

Data Availability

The observed and simulated data used to support the findings of this study are included in the article/Supplementary Material and are available from the corresponding author upon request, respectively.

Conflicts of Interest

The authors declare that there is no conflict of interest regarding the publication of this paper.

Acknowledgments

The authors wish to thank the Nationalparkverwaltung Niedersächsisches Wattenmeer (NLPV), especially G. Millat and C. Schulz for giving us the possibility to conduct studies on the Ostplate. Many thanks to the Niedersächsischer Landesbetrieb für Wasserwirtschaft, Küsten- und Naturschutz (NLWKN), mainly H. Dirks and R. Tants, for providing the laser-scan elevation models and the aerial image. We thank the Wasser- und Schifffahrtsverwaltung des Bundes (WSV) and the Bundesamt für Seeschifffahrt und Hydrographie (BSH) for providing data of the tide gauges. Many thanks are due to J. Alder, L. Diehl, T. Fresenborg, F. Grünenbaum, T. Haene, A. Harms, N. Kramer, C. H. Lünsdorf, H. Madaj, M. B. Maeso, S. Maiwald, J. Otten, F. Schindler, and S. Zahra for their support during field work. We would also like to thank U. Uebel and H. Freund for support during the construction of the observation wells. Many thanks to S. Fock, C. Heithecker, and C. Winkelmann of the Nationalparkhaus Wittbülten at Spiekeroog as well as to the team of the NLWKN located at Spiekeroog for their logistical support. Furthermore, we thank H. Nicolai and G. Behrens for the boat transfer. We also thank the German Research Foundation for project funding (DFG project number MA 3274/6-1). This publication is dedicated to our very supportive colleague Gerald Millat, who sadly passed away in 2017.

Supplementary Materials

The Supplementary Material consists of information regarding instrumentation and time of measurements (S.1), groundwater flow direction (S.2), grain size analysis (S.3), MHW-levels (S.4), temporal variability of the geomorphology at the Ostplate, recharge/infiltration rates, and recharge salinities implemented in the VG-model (S.5), present groundwater salinity distribution and extent of the FWL – Field data (S.6), videos of the temporal evolution of the groundwater salinity distribution and FWL for the CG-, VG-, and CGWST-model (S.7), comparison of the calculated and observed hydraulic heads (S.8), calculated groundwater salinities of the last five years of simulation (S.9), and the effect of choice of boundary conditions and parameter sensitivities (S.10). *(Supplementary Materials)*

References

[1] V. E. A. Post, "Fresh and saline groundwater interaction in coastal aquifers: is our technology ready for the problems ahead?," *Hydrogeology Journal*, vol. 13, no. 1, pp. 120–123, 2005.

[2] M. B. Cardenas, P. C. Bennett, P. B. Zamora et al., "Devastation of aquifers from tsunami-like storm surge by Supertyphoon Haiyan," *Geophysical Research Letters*, vol. 42, no. 8, pp. 2844–2851, 2015.

[3] C. Small and R. J. Nicholls, "A global analysis of human settlement in coastal zones," *Journal of Coastal Research*, vol. 19, pp. 584–599, 2003.

[4] W. N. Adger, T. P. Hughes, C. Folke, S. R. Carpenter, and J. Rockström, "Social-ecological resilience to coastal disasters," *Science*, vol. 309, no. 5737, pp. 1036–1039, 2005.

[5] IPCC, *Contribution of Working Group I to the Fourth Assessment Report of the Intergovernmental Panel on Climate Change*, S. Solomon, D. Qin, M. Manning, Z. Chen, M. Marquis, K. B. Averyt, M. Tignor, and H. L. Miller, Eds., Cambridge University Press, Cambridge, United Kingdom and New York, NY, USA, 2007.

[6] H. A. Michael, C. J. Russoniello, and L. A. Byron, "Global assessment of vulnerability to sea-level rise in topography-limited and recharge-limited coastal groundwater systems," *Water Resources Research*, vol. 49, no. 4, pp. 2228–2240, 2013.

[7] J. Drabbe and W. Badon Ghijben, "Nota in verband met de voorgenomen putboring nabij, Amsterdam [Note concerning the intended well drilling near Amsterdam]," *Tijdschrift van het Koninklijk Instituut van Ingenieurs*, vol. 21, pp. 8–22, 1889.

[8] A. Herzberg, "Die Wasserversorgung einiger Nordseebäder [The water supply of some North Sea spas]," *Journal fuer Gasbeleuchtung und Wasserversorgung*, vol. 44, pp. 815–819, 1901, 842–844.

[9] B. M. S. Giambastiani, M. Antonellini, G. H. P. Oude Essink, and R. J. Stuurman, "Saltwater intrusion in the unconfined coastal aquifer of Ravenna (Italy): a numerical model," *Journal of Hydrology*, vol. 340, no. 1-2, pp. 91–104, 2007.

[10] P. J. Stuyfzand, *Hydrochemistry and hydrology of the coastal dune area of the Western Netherlands, Zgl*, Univ. Diss., KIWA, Nieuwegein, Amsterdam, 1993.

[11] A. Vandenbohede and L. Lebbe, "Effects of tides on a sloping shore: groundwater dynamics and propagation of the tidal wave," *Hydrogeology Journal*, vol. 15, no. 4, pp. 645–658, 2007.

[12] M. Bakker, "The size of the freshwater zone below an elongated island with infiltration," *Water Resources Research*, vol. 36, no. 1, pp. 109–117, 2000.

[13] W. H. Collins and D. H. Easley, "Fresh-water lens formation in an unconfined barrier island aquifer," *Journal of the American Water Resources Association*, vol. 35, no. 1, pp. 1–22, 1999.

[14] A. Falkland, *Hydrology and Water Resources of Small Islands: A Practical Guide; Studies and Reports in Hydrology*, UNESCO, 1991.

[15] C. W. Fetter, "Position of the saline water interface beneath oceanic islands," *Water Resources Research*, vol. 8, no. 5, pp. 1307–1315, 1972.

[16] H. L. Vacher, "Hydrogeology of Bermuda - significance of an across-the-island variation in permeability," *Journal of Hydrology*, vol. 39, no. 3-4, pp. 207–226, 1978.

[17] W. P. Anderson Jr and R. M. Lauer, "The role of overwash in the evolution of mixing zone morphology within barrier islands," *Hydrogeology Journal*, vol. 16, no. 8, pp. 1483–1495, 2008.

[18] I. White and T. Falkland, "Management of freshwater lenses on small Pacific islands," *Hydrogeology Journal*, vol. 18, no. 1, pp. 227–246, 2010.

[19] J. C. Schneider and S. E. Kruse, "A comparison of controls on freshwater lens morphology of small carbonate and siliciclastic islands: examples from barrier islands in Florida, USA," *Journal of Hydrology*, vol. 284, no. 1-4, pp. 253–269, 2003.

[20] W. P. Anderson, D. G. Evans, and S. W. Snyder, "The effects of Holocene barrier-island evolution on water-table elevations, Hatteras Island, North Carolina, USA," *Hydrogeology Journal*, vol. 8, no. 4, pp. 390–404, 2000.

[21] J. C. Schneider and S. E. Kruse, "Assessing selected natural and anthropogenic impacts on freshwater lens morphology on small barrier Islands: Dog Island and St. George Island, Florida, USA," *Hydrogeology Journal*, vol. 14, no. 1-2, pp. 131–145, 2006.

[22] S. Holding and D. M. Allen, "Wave overwash impact on small islands: generalised observations of freshwater lens response and recovery for multiple hydrogeological settings," *Journal of Hydrology*, vol. 529, pp. 1324–1335, 2015.

[23] W. P. Anderson Jr, "Aquifer salinization from storm overwash," *Journal of Coastal Research*, vol. 18, pp. 413–420, 2002.

[24] I. White, T. Falkland, P. Perez et al., "Challenges in freshwater management in low coral atolls," *Journal of Cleaner Production*, vol. 15, no. 16, pp. 1522–1528, 2007.

[25] V. E. A. Post and G. J. Houben, "Density-driven vertical transport of saltwater through the freshwater lens on the island of Baltrum (Germany) following the 1962 storm flood," *Journal of Hydrology*, vol. 551, pp. 689–702, 2017.

[26] S. B. Gingerich, C. I. Voss, and A. G. Johnson, "Seawater-flooding events and impact on freshwater lenses of low-lying islands: controlling factors, basic management and mitigation," *Journal of Hydrology*, vol. 551, pp. 676–688, 2017.

[27] T. Holt, S. L. Seibert, J. Greskowiak, H. Freund, and G. Massmann, "Impact of storm tides and inundation frequency on water table salinity and vegetation on a juvenile barrier island," *Journal of Hydrology*, vol. 554, pp. 666–679, 2017.

[28] L. K. Morgan and A. D. Werner, "Seawater intrusion vulnerability indicators for freshwater lenses in strip islands," *Journal of Hydrology*, vol. 508, pp. 322–327, 2014.

[29] C. W. V. Wolner, L. J. Moore, D. R. Young, S. T. Brantley, S. N. Bissett, and R. A. McBride, "Ecomorphodynamic feedbacks and barrier island response to disturbance: insights from the Virginia Barrier Islands, Mid-Atlantic Bight, USA," *Geomorphology*, vol. 199, pp. 115–128, 2013.

[30] T. Illangasekare, S. W. Tyler, T. P. Clement et al., "Impacts of the 2004 tsunami on groundwater resources in Sri Lanka," *Water Resources Research*, vol. 42, no. 5, p. 508, 2006.

[31] T. F. M. Chui and J. P. Terry, "Modeling fresh water lens damage and recovery on atolls after storm-wave washover," *Ground Water*, vol. 50, no. 3, pp. 412–420, 2012.

[32] J. P. Terry and A. C. Falkland, "Responses of atoll freshwater lenses to storm-surge overwash in the Northern Cook Islands," *Hydrogeology Journal*, vol. 18, no. 3, pp. 749–759, 2010.

[33] J. Yang, T. Graf, M. Herold, and T. Ptak, "Modelling the effects of tides and storm surges on coastal aquifers using a coupled surface-subsurface approach," *Journal of Contaminant Hydrology*, vol. 149, pp. 61–75, 2013.

[34] R. T. Bailey, "Quantifying transient post-overwash aquifer recovery for atoll islands in the Western Pacific," *Hydrological Processes*, vol. 29, no. 20, pp. 4470–4482, 2015.

[35] S. Holding and D. M. Allen, "From days to decades: numerical modelling of freshwater lens response to climate change stressors on small low-lying islands," *Hydrology and Earth System Sciences*, vol. 19, no. 2, pp. 933–949, 2015.

[36] J. Yang, H. Zhang, X. Yu, T. Graf, and H. A. Michael, "Impact of hydrogeological factors on groundwater salinization due to ocean-surge inundation," *Advances in Water Resources*, vol. 111, pp. 423–434, 2018.

[37] M. S. Andersen, V. Nyvang, R. Jakobsen, and D. Postma, "Geochemical processes and solute transport at the seawater/-freshwater interface of a sandy aquifer," *Geochimica et Cosmochimica Acta*, vol. 69, no. 16, pp. 3979–3994, 2005.

[38] R. W. Buddemeier and J. A. Oberdorfer, "Hydrogeology of Enewetak Atoll," in *Developments in Sedimentology*, vol. 54, pp. 667–692, Elsevier, 2004.

[39] J. Greskowiak, "Tide-induced salt-fingering flow during submarine groundwater discharge," *Geophysical Research Letters*, vol. 41, no. 18, pp. 6413–6419, 2014.

[40] E. J. Dose, L. Stoeckl, G. J. Houben et al., "Experiments and modeling of freshwater lenses in layered aquifers: steady state interface geometry," *Journal of Hydrology*, vol. 509, pp. 621–630, 2014.

[41] T. Röper, J. Greskowiak, H. Freund, and G. Massmann, "Freshwater lens formation below juvenile dunes on a barrier island (Spiekeroog, Northwest Germany)," *Estuarine, Coastal and Shelf Science*, vol. 121-122, pp. 40–50, 2013.

[42] J. P. Terry and T. F. M. Chui, "Evaluating the fate of freshwater lenses on atoll islands after eustatic sea-level rise and cyclone-driven inundation: a modelling approach," *Global and Planetary Change*, vol. 88-89, pp. 76–84, 2012.

[43] S. Huizer, M. Radermacher, S. de Vries, G. H. P. Oude Essink, and M. F. P. Bierkens, "Impact of coastal forcing and groundwater recharge on the growth of a fresh groundwater lens in a mega-scale beach nourishment," *Hydrology and Earth System Sciences*, vol. 22, no. 2, pp. 1065–1080, 2018.

[44] J. Petersen and R. Pott, *Ostfriesische Inseln: Landschaft und Vegetation im Wandel*, Schlütersche, Hannover, 2005.

[45] H. Streif, *Das ostfriesische Küstengebiet: Nordsee, Inseln, Watten und Marschen; mit 10 Tabellen*, Borntraeger, Berlin-Stuttgart, 1990.

[46] S. L. Seibert, M. E. Böttcher, F. Schubert et al., "Iron sulfide formation in young and rapidly-deposited permeable sands at the land-sea transition zone," *Science of the Total Environment*, vol. 649, pp. 264–283, 2019.

[47] H. Eckel, *Studien zur morphologischen Entwicklung der Ostplate Spiekeroogs*, Diss., Westfälischer Wilhelms-Universität Münster, 1977.

[48] M. O. Hayes, "Barrier island morphology as a function of tidal and wave regime," in *Barrier Islands*, S. P. Leatherman, Ed., Academic, New York, 1979.

[49] Wasser- und Schifffahrtsverwaltung des Bundes (WSV) [Federal Waterways and Shipping Administration], "High and low water data at tide gauges Spiekeroog and Wangerooge 1995-2017 and mean spring tide data at tide gauge Spiekeroog 2016. Provided by Bundesanstalt für Gewässerkunde (BfG)," 2017.

[50] Bundesamt für Seeschifffahrt und Hydrographie (BSH) [Federal Maritime and hydrographic agency], "Mean neap tide data at tide gauge Spiekeroog 2016," 2017, pers. comment.

[51] Oldenburgisch-Ostfriesischer Wasserverband (OOWV) [Oldenburg-East Frisian Water Association], "Precipitation

and lysimeter data of Spiekeroog Island from 1984-2011," 2012.

[52] K. H. Sindowski, *Erläuterungen zu Blatt Spiekeroog Nr. 2212*, Niedersächsisches Landesamt für Bodenforschung, Hannover, 1970.

[53] T. Röper, K. F. Kröger, H. Meyer, J. Sültenfuss, J. Greskowiak, and G. Massmann, "Groundwater ages, recharge conditions and hydrochemical evolution of a barrier island freshwater lens (Spiekeroog, northern Germany)," *Journal of Hydrology*, vol. 454-455, pp. 173–186, 2012.

[54] Landesamt für Bergbau, Energie und Geologie (LBEG) [State Office for Mining, Energy and Geology], "Grundwasserneubildung nach Methode mGROWA 1:200 000. NIBIS Kartenserver," January 2018, http://nibis.lbeg.de/cardomap3/.

[55] Oldenburgisch-Ostfriesischer Wasserverband (OOWV) [Oldenburg-East Frisian Water Association], "Wasserrechtsantrag. Antrag auf Bewilligung einer Grundwasserentnahme über 180,000 m^3/a für das Wasserwerk Spiekeroog," 2009.

[56] H. Sulzbacher, H. Wiederhold, B. Siemon et al., "Numerical modelling of climate change impacts on freshwater lenses on the North Sea Island of Borkum using hydrological and geophysical methods," *Hydrology and Earth System Sciences*, vol. 16, no. 10, pp. 3621–3643, 2012.

[57] H. Wiederhold, W. Scheer, H. Sulzbacher, B. Siemon, and R. Kirsch, "Nordseeinseln im Klimawandel–die Nordfriesische Insel Föhr und die Ostfriesische Insel Borkum," *Coastline Reports*, vol. 25, pp. 45–48, 2015.

[58] S. L. Seibert, T. Holt, A. Reckhardt et al., "Hydrochemical evolution of a freshwater lens below a barrier island (Spiekeroog, Germany): the role of carbonate mineral reactions, cation exchange and redox processes," *Applied Geochemistry*, vol. 92, pp. 196–208, 2018.

[59] Niedersächsischer Landesbetrieb für Wasserwirtschaft, Küsten- und Naturschutz (NLWKN) [Lower Saxony Water Management, Coastal Defense and Nature Conservation Agency], "Laser-scan elevation models of 2008 and 2014, aerial image of 2013".

[60] R. A. Freeze and J. A. Cherry, *Groundwater*, Prentice hall, Englewood cliffs, N.J., 1979.

[61] C. D. Langevin, D. T. Thorne Jr, A. M. Dausman, M. C. Sukop, and G. Weixing, "SEAWAT version 4: A computer program for simulation of multi-species solute and heat transport," in *US Geological Survey Techniques Methods, Book 6 (Chapter A22)*, US Geological Survey Reston, 2008.

[62] A. Vandenbohede and L. Lebbe, "Occurrence of salt water above fresh water in dynamic equilibrium in a coastal groundwater flow system near De Panne, Belgium," *Hydrogeology Journal*, vol. 14, no. 4, pp. 462–472, 2006.

[63] M. Beck, A. Reckhardt, J. Amelsberg et al., "The drivers of biogeochemistry in beach ecosystems: a cross-shore transect from the dunes to the low-water line," *Marine Chemistry*, vol. 190, pp. 35–50, 2017.

[64] P. Nielsen, "Tidal dynamics of the water table in beaches," *Water Resources Research*, vol. 26, no. 9, pp. 2127–2134, 1990.

[65] J.-C. Comte, J.-L. Join, O. Banton, and E. Nicolini, "Modelling the response of fresh groundwater to climate and vegetation changes in coral islands," *Hydrogeology Journal*, vol. 22, no. 8, pp. 1905–1920, 2014.

[66] C. Zheng and G. D. Bennett, *Applied Contaminant Transport Modeling: Theory and Practice*, Wiley, New York, 1995.

[67] M. Walther, T. Graf, O. Kolditz, R. Liedl, and V. Post, "How significant is the slope of the sea-side boundary for modelling seawater intrusion in coastal aquifers?," *Journal of Hydrology*, vol. 551, pp. 648–659, 2017.

[68] J. Jiao and V. Post, *Coastal Hydrogeology*, Cambridge University Press, 2019.

[69] C. A. J. Appelo and D. Postma, *Geochemistry, Groundwater and Pollution*, CRC press, Amsterdam, 2005.

[70] G. J. Houben, P. Koeniger, and J. Sültenfuß, "Freshwater lenses as archive of climate, groundwater recharge, and hydrochemical evolution: insights from depth-specific water isotope analysis and age determination on the island of Langeoog, Germany," *Water Resources Research*, vol. 50, no. 10, pp. 8227–8239, 2014.

[71] P. N. Mollema and M. Antonellini, "Seasonal variation in natural recharge of coastal aquifers," *Hydrogeology Journal*, vol. 21, no. 4, pp. 787–797, 2013.

[72] A. D. Werner, M. Bakker, V. E. A. Post et al., "Seawater intrusion processes, investigation and management: recent advances and future challenges," *Advances in Water Resources*, vol. 51, pp. 3–26, 2013.

[73] T. Röper, J. Greskowiak, and G. Massmann, "Instabilities of submarine groundwater discharge under tidal forcing," *Limnology and Oceanography*, vol. 60, no. 1, pp. 22–28, 2015.

[74] C. Shen, G. Jin, P. Xin, J. Kong, and L. Li, "Effects of salinity variations on pore water flow in salt marshes," *Water Resources Research*, vol. 51, no. 6, pp. 4301–4319, 2015.

[75] C. Shen, C. Zhang, G. Jin, J. Kong, and L. Li, "Effects of unstable flow on solute transport in the marsh soil and exchange with coastal water," *Geophysical Research Letters*, vol. 43, no. 23, pp. 12,091–12,101, 2016.

[76] S. Huizer, M. C. Karaoulis, G. H. P. Oude Essink, and M. F. P. Bierkens, "Monitoring and simulation of salinity changes in response to tide and storm surges in a sandy coastal aquifer system," *Water Resources Research*, vol. 53, no. 8, pp. 6487–6509, 2017.

[77] P. J. Stuyfzand and G. A. Bruggeman, "Analytical approximations for freshwater lenses in coastal dunes," in *Proc. 13th Salt Water Intrusion Meeting*, pp. 15–33, Cagliari, Italy, June 1994.

[78] P. J. Stuyfzand, "Observations and analytical modeling of freshwater and rainwater lenses in coastal dune systems," *Journal of Coastal Conservation*, vol. 21, no. 5, pp. 577–593, 2017.

[79] X. Yu, J. Yang, T. Graf, M. Koneshloo, M. A. O'Neal, and H. A. Michael, "Impact of topography on groundwater salinization due to ocean surge inundation," *Water Resources Research*, vol. 52, no. 8, pp. 5794–5812, 2016.

[80] K. Klaassen, H. Bormann, T. Klenke, and G. Liebezeit, "The impact of hydrodynamics and texture on the infiltration of rain and marine waters into sand bank island sediments — aspects of infiltration and groundwater dynamics," *Senckenbergiana Maritima*, vol. 38, no. 2, pp. 163–171, 2008.

[81] J.-C. Comte, O. Banton, J. L. Join, and G. Cabioch, "Evaluation of effective groundwater recharge of freshwater lens in small islands by the combined modeling of geoelectrical data and water heads," *Water Resources Research*, vol. 46, no. 6, 2010.

Hindawi
Geofluids
Volume 2019, Article ID 6193134, 9 pages
https://doi.org/10.1155/2019/6193134

Research Article

The Dynamics of Sea Tide-Induced Fluctuations of Groundwater Level and Freshwater-Saltwater Interface in Coastal Aquifers: Laboratory Experiments and Numerical Modeling

Elad Levanon,[1,2] Haim Gvirtzman,[1] Yoseph Yechieli,[2,3] Imri Oz,[1,2] Elad Ben-Zur,[1] and Eyal Shalev[2]

[1]*Institute of Earth Sciences, The Hebrew University of Jerusalem, Edmond J. Safra Campus, Givat Ram, Jerusalem 91904, Israel*
[2]*Geological Survey of Israel (GSI), 32 Yesha'ayahu Leibowitz St., Jerusalem 9692100, Israel*
[3]*Department of Environmental Hydrology & Microbiology, Zuckerberg Institute for Water Research, Ben-Gurion University of the Negev, Sede Boqer 8499000, Israel*

Correspondence should be addressed to Eyal Shalev; eyal@gsi.gov.il

Received 17 April 2019; Accepted 17 July 2019; Published 5 August 2019

Guest Editor: Christopher J. Russoniello

Laboratory experiments were conducted in a vertical, two-dimensional, rectangular flow tank, simulating the response of a phreatic coastal aquifer to a sea tide. Imposed sinusoidal fluctuations of the saltwater level at one side of the flow tank caused three types of fluctuations: (a) hydraulic head throughout the aquifer, (b) saturation degree within the capillary fringe, and (c) salt concentration surrounding the freshwater-saltwater interface (FSI), all recorded by head, saturation, and salinity sensors, respectively. Significant time lags were observed both in the saturation degree within the unsaturated zone and in the salinity within the FSI. All measured values, recorded by the three types of sensors, were simulated and reproduced using a numerical model. The calibrated model was used for mapping the time lags throughout the aquifer. It was found that the time lag of saturation fluctuations within the unsaturated zone increased upward from the groundwater level as the unsaturated hydraulic conductivity decreased. Similarly, the time lag of salinity fluctuations within the FSI increased downward, with distance from the groundwater level. We interpret the low hydraulic conductivity at the capillary zone as the source of attenuation of both saturation and salinity, because both are controlled by the vertical advection of the whole freshwater body. This advection is significantly slower compared to the dynamics of pressure diffusion. The uniqueness of this study is that it provides quantitative data on the attenuation at the capillary zone and its effect on the salinity time lag in coastal aquifer systems.

1. Introduction

Seawater intrusion into coastal aquifers is of a global concern due to salinization of production wells (e.g., [1, 2]). The transition zone between the fresh groundwater that flows seaward and the saline seawater beneath that penetrates inland is referred to as the freshwater-saltwater interface (FSI). The two water bodies are in a dynamic equilibrium that is influenced by hydrodynamic processes such as sea tide oscillations and pumping [3, 4].

Sea tide oscillations influence both the groundwater level (GWL) and the location of the FSI in coastal aquifers. They induce groundwater level fluctuations with a periodicity similar to tidal periodicity [5, 6], as well as salinity fluctuations within the FSI [4, 7, 8]. GWL fluctuations in an unconfined aquifer subjected to low-frequency tidal oscillations are significantly affected by the capillary effect. Parlange and Brutsaert [9] showed that the capillary pressure above the water table varies as a consequence of GWL fluctuations. Nielsen and Perrochet [10] and Werner and Lockington [11] found a significant effect of the capillary fringe and the hysteresis phenomenon, on GWL fluctuations in an unconfined aquifer subjected to tidal oscillations. Cartwright et al. [12] showed the influence of water table shallowness on water table wave dispersion. Kong et al. [13, 14] used analytical solutions and numerical models to show that unsaturated

flow above the water table influences the amplitude of the GWL fluctuations and the lag of GWL fluctuations behind the sea level.

The depth and width of the FSI are directly influenced by the groundwater head fluctuations; thus, the FSI itself fluctuates due to sea level oscillations as well [1, 7, 15]. Ataie-Ashtiani et al. [3] showed theoretically that the sea tide widens the FSI and forces the sea water to intrude further inland. Kim et al. [8] found that the FSI and the water table in Kimje, Korea, fluctuate with a tidal periodicity. Levanon et al. [16] demonstrated that the GWL and the FSI fluctuations in the coastal aquifer of Israel are composed of the same tidal constituents as the tide wave in the Mediterranean Sea. Heiss and Michael [17] conducted a field study and numerical model and showed that the size of the mixing zone varied over the spring-neap tidal cycle. They also showed that tidal amplitude significantly affects the flow of fresh and saline groundwater toward the sea. Pool et al. [18] quantify tidal impacts on solute mixing and spreading in the FSI using a numerical model and showed that the key parameters controlling the shape and location of the FSI are the tidal amplitude, the tidal period, and the hydraulic diffusivity.

Levanon et al. [19, 20] suggested that the tidal effect on the groundwater system comprises two main processes: (1) tidal forcing at the sea floor boundary and (2) attenuation at the groundwater level due to capillary effect. They showed that even though the pressure head wave propagation into the aquifer is relatively fast, the actual movement of the freshwater body, which is reflected by fluctuations of GWL and the salinity in the FSI, is slower since it is controlled by the unsaturated hydraulic conductivity within the capillary fringe. Up to date, this thesis was shown to occur by a field study, in which the horizontal time lags of both head and salinity were measured across the aquifer using wells. However, the actual delay within the unsaturated zone and the vertical time lag that progress downwards all the way to the FSI was not shown in the field. This can be examined in a controlled laboratory setup, where it is easier to quantify the vertical time lags and unsaturated processes.

The use of physical models provides an ideal setup for conceptualization, visualization, and measurement of groundwater flow and solute transport through an aquifer [21]. Physical models have been used in a variety of groundwater studies for describing different phenomena, such as density-driven groundwater flow, saltwater intrusion, and transport of solutes and contaminants (e.g., [22–25]). Physical models were also used to show the effect of sea tides on the residence time of a plume that originated at the sea that infiltrates into the aquifer downwards during high tides and back to the sea during low tides [26–28]. However, in these experiments, the positions of the FSI were not established and monitored. The physical model in this study provides a better understanding of the dynamics in phreatic coastal aquifers subjected to sea tide influence including the FSI, water level, and saturation.

The objective of this paper is to investigate the importance of the unsaturated flow properties within the capillary fringe on the tidal dynamics of both the FSI and the water table fluctuations by controlled laboratory experiments and numerical modeling. While in previous studies [19, 20] only the horizontal time lag induced by the sea tide was analyzed at the field scale, in this study, the vertical development of the time lag is displayed; thus, a more complete picture of the tidal dynamics in coastal aquifers is achieved.

2. Methods

2.1. Laboratory Setup. Laboratory experiments were conducted in a vertical, rectangular (100 cm long, 50 cm high, and 3 cm wide) flow tank made of Plexiglas, simulating a phreatic cross-shore coastal aquifer (Figure 1). The narrow width of the flow tank ensures that the problem examined could be defined as two-dimensional, with negligible alongshore processes. It is divided into three distinct chambers: a central flow chamber that serves as an aquifer and contains the porous medium and two side chambers filled with water, which define the boundary conditions during the experiments. The left chamber represents the saltwater boundary at the seaside, and the right chamber represents the inland freshwater boundary of the regional aquifer. These side chambers are separated from the main chamber by a fine net that prevents the passage of granular material.

The initial and boundary conditions during the experiment are defined by the water levels at the side chambers. At the right boundary, freshwater is pumped from the supply reservoir into an overflow bottle connected to the right chamber. At the left boundary, the saltwater is pumped from another supply reservoir directly into the left chamber. The water level at the right boundary is higher than that at the left one; thus, an initial hydraulic gradient is formed, and the water flows through the porous medium from right to left simulating a seaward flow. The overflow at the left boundary is diluted sea water as a result of mixing between the freshwater and the saltwater which occurs along the flow paths in the FSI. The overflow pipe at the left chamber is connected to a computer-controlled engine that enables quasitidal fluctuations of the saltwater at the left boundary, which define the boundary condition at the seaside. The amplitude and the wavelength of the sinusoidal tidal wave are definable by the engine (changing vertical velocities and the time intervals for each velocity). The tidal wave used in the experiments is harmonic with constant amplitude. During all the experiments, the water levels at the boundaries were kept lower than 35 cm (Figure 1), in order to enable an unsaturated zone above the water table and to avoid problems that truncation of this area may create [29]. The freshwater in the experiment is colorless tap water, and the saline water is prepared by dissolving NaCl in tap water and adding commercial red food dye (AmeriColor Ltd.). The density of the saline water was 1.027 gr cm^{-3}, the same as the average density of the eastern Mediterranean Sea. The sand used in the experiments is silica grains which were sieved to a diameter range of 800-1,300 μm. In preexperiment treatment, it was washed with distilled water to remove dust and clay minerals and with HCl acid to remove the oxide coatings of the quartz grains. The horizontal

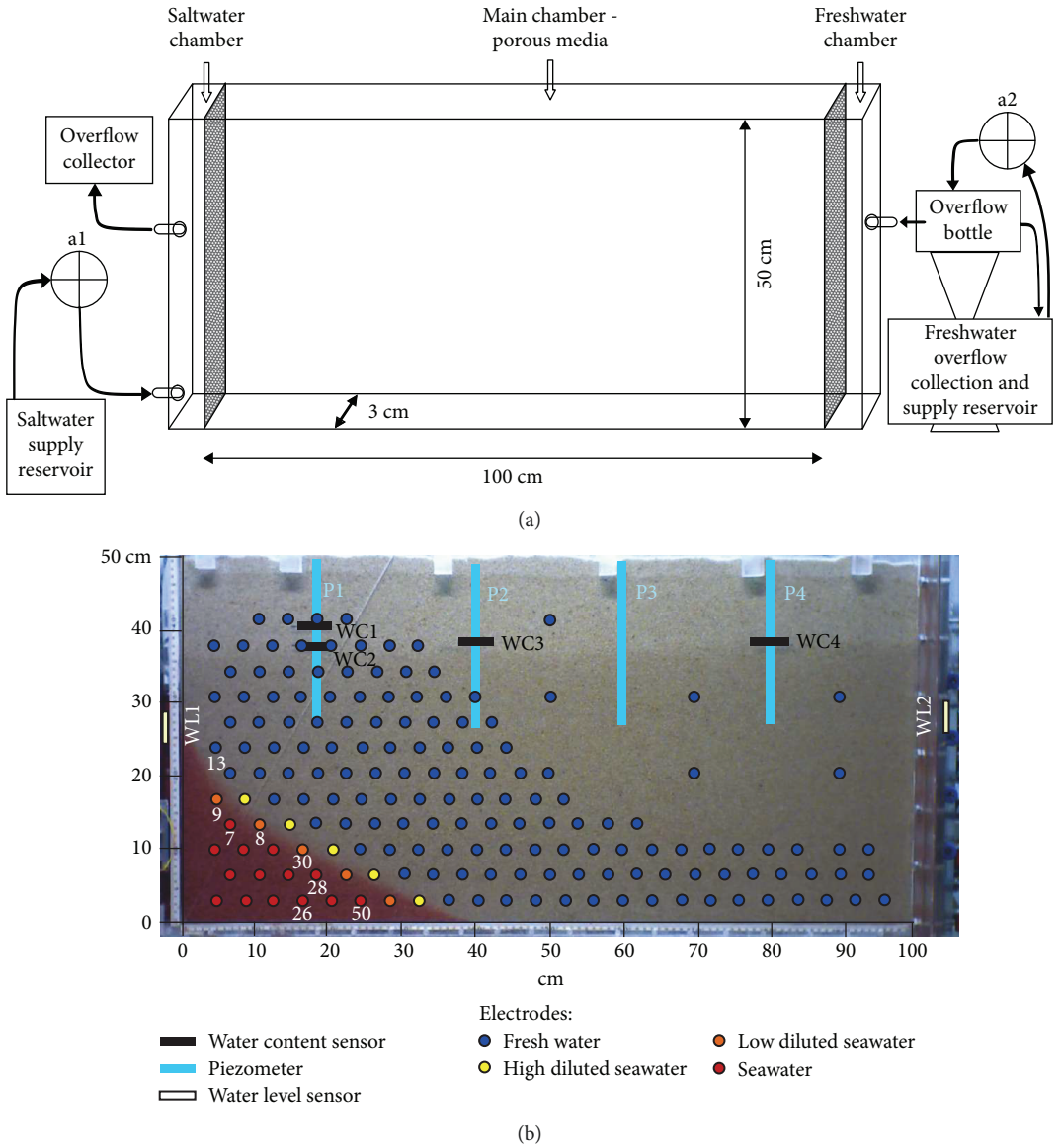

Figure 1: (a) The laboratory setup scheme. The main flow chamber simulates the aquifer, and the two side chambers create the boundary conditions during the experiments. The left chamber represents the saltwater boundary at the seaside, and the right chamber represents the inland freshwater boundary of the regional aquifer. (b) A picture of the laboratory aquifer. 168 electrodes are placed for in situ voltage measurements, which are equivalent to the salinity of the water. The electrodes, whose numbers are written, are discussed in the text. Four sensors of water content (WC1-WC4) are placed in the capillary zone above the water level. Four piezometers (P1-P4) are located a few centimeters below the water table at different distances from the left boundary. Two divers (WL1-WL2) are placed in the water chambers.

permeability was calculated from a simple steady state experiment where the hydraulic heads were constant at both ends and a freshwater was flowing from the high hydraulic head at the left boundary to the low hydraulic head at the right boundary, using the equation $K = 2QL/(h_1^2 - h_2^2)$. The porosity was measured by dividing the weight of the sand to the volume of the tank. The values of the parameters are given in Table 1.

The monitoring setup during the experiments includes several measurement systems (Figure 1(b)): (1) 168 electrodes placed at the back side of the flow tank for in situ voltage measurements, which are equivalent to the salinity of the water. The data from the electrodes is collected using LabVIEW software (National Instruments Ltd.); (2) two water level sensors (PA-36XW, Keller Ltd.) located at the side chambers; (3) four water content sensors (EC-5; Decagon Devices Inc.) placed in the capillary zone above the water level; and (4) six piezometers located a few centimeters below the water table at different distances from the left boundary. In four of these piezometers (P1-P4 in Figure 1), a thin film of red oil is added on top of the water column in order to allow easier monitoring of the changes in the water level. A high-resolution video camera (50 frames per second) records the piezometers, and the data is converted to numerical data

Table 1: Parameters used for the numerical simulations. Measured values were quantified in a specific test. Calibrated values were assessed during the numerical modeling.

	Parameter	Value	Source
Hydraulic conductivity	K horizontal	1,500 m day^{-1}	Measured
	K vertical	1,350 m day^{-1}	Calibrated
	Anisotropy (K_v/K_h)	0.9	Calibrated
Dispersivity	Longitudinal dispersivity	0.2 cm	Calibrated
	Transverse dispersivity	0.02 cm	Calibrated
Right boundary	H initial	31.85 cm	Input
	Amplitude	0.35 cm	Input
Left boundary	H initial	31.5 cm	Input
	Amplitude	3 cm	Input
Water	Saltwater	39,000 mg L^{-1}	Input
	Freshwater	20 mg L^{-1}	Input
Van Genuchten drying	Alpha	11.8 m^{-1}	Measured
	N	9	Measured
Van Genuchten wetting	Alpha	18 m^{-1}	Measured
	N	7.5	Measured
Soil properties	Porosity	0.38	Measured
	Specific storage	0.0001 m^{-1}	Calibrated

using image processing. In addition, a pressure sensor measured the barometric pressure in the laboratory during the experiment for barometric compensation of the pressure measurements at the boundaries.

2.2. Estimation of the Unsaturated Zone Characters. Unsaturated flow is an important factor in coastal aquifers under tidal influence (e.g., [11, 13, 30]). To evaluate the unsaturated properties of the sand used in the flow tank experiments, a preexperiment was conducted, in which the volumetric water content was measured under different conditions of capillary tension. Evaluation of the unsaturated characters of the sand is important for a few reasons. First, it helps plan the location of the water content sensors in the experiments. Second, according to the retention curve, the experiment is designed so that a fully unsaturated zone will develop, and third, it is important for the calibration of the numerical model.

Two sensors of water content were located just above the water table in a wide column full of sand. An overflow bottle placed on an elevator was connected to the bottom of the column, which enabled changes of its water level. The water level in the tank was lowered stepwise until residual water content was measured. Then, the water level was raised gradually, in an opposite process, to its initial height. In each step, the system was static for 10-15 minutes to allow full drainage or filling of the porous medium. The retention curve of the drying process is different from that of the wetting process due to hysteresis (Figure 2). The air entry value for the drying process is located at ~5 cm above the water table, and for the wetting, it is located at ~3 cm. The residual water content of the sand is relatively low, only 0.025, due to the high level of the sieving. The saturated water content (equal to the porosity) is 0.38 for the drying process. However, for the wetting process, it was found to be 0.35, probably as a consequence of some trapped air.

The retention curve is quantitatively described by [31]:

$$\theta(\psi) = \theta_r + \frac{\theta_s - \theta_r}{(1 + |\alpha\psi|^n)^m}, \quad (1)$$

where θ (-) is the volumetric water content, ψ (L) is the capillary tension, θ_s (-) and θ_r (-) are the saturated and residual volumetric water content, respectively, and α (L^{-1}), m (-), and n (-) are empirical constants, where $m = 1\text{-}(1/n)$.

By fitting the retention curve (equation 1) to the experimental results, the empirical unsaturated parameters for the drying and wetting processes were calibrated. The values for α are 11.8 m^{-1} and 18 m^{-1} and for n are 9 and 7.5 for the drying and wetting processes, respectively (Figure 2). These values were used in the numerical model (Table 1).

2.3. Numerical Model. Numerical simulation of the laboratory experiments is conducted using the FEFLOW code, a finite-element simulator that solves the coupled variable density groundwater flow and solute transport equations [32]. In the case of tide-induced fluctuations, both saturated and unsaturated flows are involved. The general equation for saturated-unsaturated flow, derived from the conservation of fluid mass, for variable densities is [32, 33]

$$\left(SS_s + n_e \frac{\partial S}{\partial \varphi}\right) \frac{\partial h}{\partial t} = \nabla \cdot [K(\theta)\mu_r \nabla(h + \rho_r \underline{Z})], \quad (2)$$

where S (-) is the saturation degree; S_s (L^{-1}) is the specific storage coefficient; n_e (-) is the effective porosity; φ (L) is the pressure head; h (L) is the fresh groundwater hydraulic

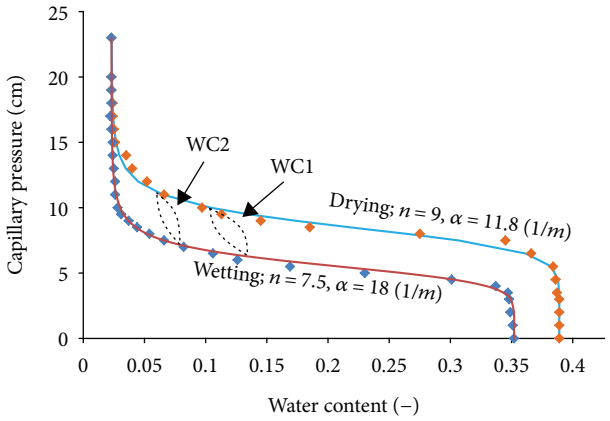

FIGURE 2: Drying and wetting retention curves of the sand used in experiments. The locations of the water content sensors, WC1 and WC2, are shown in Figure 1.

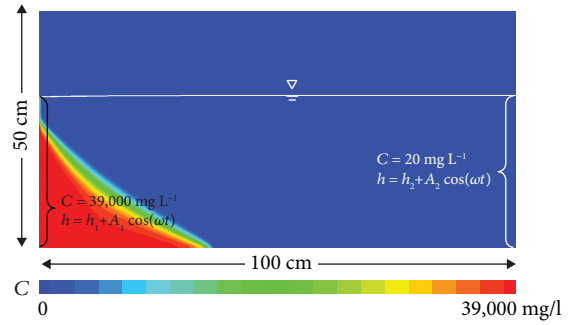

FIGURE 3: A numerical simulation of the steady state salinity distribution used as initial conditions. Boundary conditions are shown as well.

head; t (T) is the time; $K(\theta)$ ($\mathrm{L\,T^{-1}}$) is the hydraulic conductivity; $\mu_r = \mu_0/\mu$, where μ_r (-) is the relative viscosity of the fluid, μ ($\mathrm{M\,L^{-1}\,T^{-1}}$) is the viscosity of water, and μ_0 ($\mathrm{M\,L^{-1}\,T^{-1}}$) is the water viscosity at the standard state; $\rho_r = (\rho\text{-}\rho_0)/\rho_0$, where ρ_r (-) is the relative density, ρ ($\mathrm{M\,L^{-3}}$) is the fluid density, and ρ_0 ($\mathrm{M\,L^{-3}}$) is the density at the standard state; and $\underline{Z}$ is the vertical vector unit [0,0,1].

The conservation of solute mass may be written as [1]

$$\frac{\partial C}{\partial t} = \nabla \cdot (D\nabla C) - \frac{q}{n_e}\nabla C, \tag{3}$$

where C ($\mathrm{M\,L^{-3}}$) is the fluid concentration, D ($\mathrm{L^2\,T^{-1}}$) is the dispersion-diffusion coefficient, and q ($\mathrm{L\,T^{-1}}$) is Darcy's velocity of the fluid. The coupling between the solute transport equation and the flow equation is through equations of state for the fluid's density and viscosity.

The dimensions of the numerical cross-section are the same as the laboratory flow tank—a length of 100 cm and a height of 50 cm. A mesh with 228,090 elements and 114,752 nodes is used with refinement near the FSI in order to increase the stability of the numerical scheme and the accuracy of the model (Figure 3). The hydraulic heads at the left and right boundaries are defined as a tidal time series, based on the water level fluctuations that were measured during the experiment at the side chambers. The equation which defines these time series is

$$h(t) = h_i + A\cos(\omega t), \tag{4}$$

where h is the hydraulic head (L), t is time (T), h_i (L) is the initial hydraulic head, A (L) is the tidal amplitude, and ω ($\mathrm{Rad\,T^{-1}}$) is the angular frequency of the tidal wave. The amplitudes of the left and right boundaries are 3 cm and 0.4 cm, respectively, and the wavelength is 15 minutes, in accordance with the laboratory experiment. At this frequency, the hysteresis effect is very small [34]. In addition, no-flow boundaries are defined at the cross-section base. Salinity on the sea side is 39,000 mg $\mathrm{L^{-1}}$ (based on the density and the temperature of the saline water in the laboratory), and on the right boundary is 20 mg $\mathrm{L^{-1}}$. Table 1 summarizes the parameters used in the numerical model. The calibration process is detailed below.

2.4. Cross-Correlation. In order to quantitatively analyze the time lags between sea level fluctuations, salinity, water level, and saturation in the aquifer, a cross-correlation analysis was applied on both laboratory and numerical model results. Such analysis provides information about the correlation between input and output time series, along with its significance. Details about the application of the cross-correlation analysis to coastal aquifer systems can be found in Levanon et al. [20].

3. Results

3.1. Laboratory Experiments. Snapshots from one of the tidal cycles are presented in Figure 4, along with the comparable numerical results. The FSI moves forward and backward under the influence of the tidal fluctuations at the left boundary (see Supplementary Materials (available here) for a video of the full dynamic process of the experiment). At its maximum penetration, the FSI toe reaches 39 cm from the left boundary (Figure 4(b)), and at its minimum, it reaches 30 cm (Figure 4(d)). The maximum and minimum penetration distances of the FSI toe lag a few minutes behind the high and low tides (i.e., maximum and minimum water levels at the left boundary, Figures 4(a) and 4(c)). The significant difference between the salinity distributions at high and low tides is in the contact area with the left boundary, where at the high tide the saline water is higher than at the low tide.

3.1.1. Horizontal Effect. With sampling frequency of 20 msec, no time lag has been detected between the water level at P1, which is located 18 cm from the left boundary, and the water level at P4, which is located 80 cm from the left boundary (Figure 5). This is attributed to the fast pressure head wave propagation into the aquifer which is controlled by the high diffusivity (K_S/S_S) of the aquifer [20]. There is also no lag between the salinity at electrodes which are at the same depth but at different

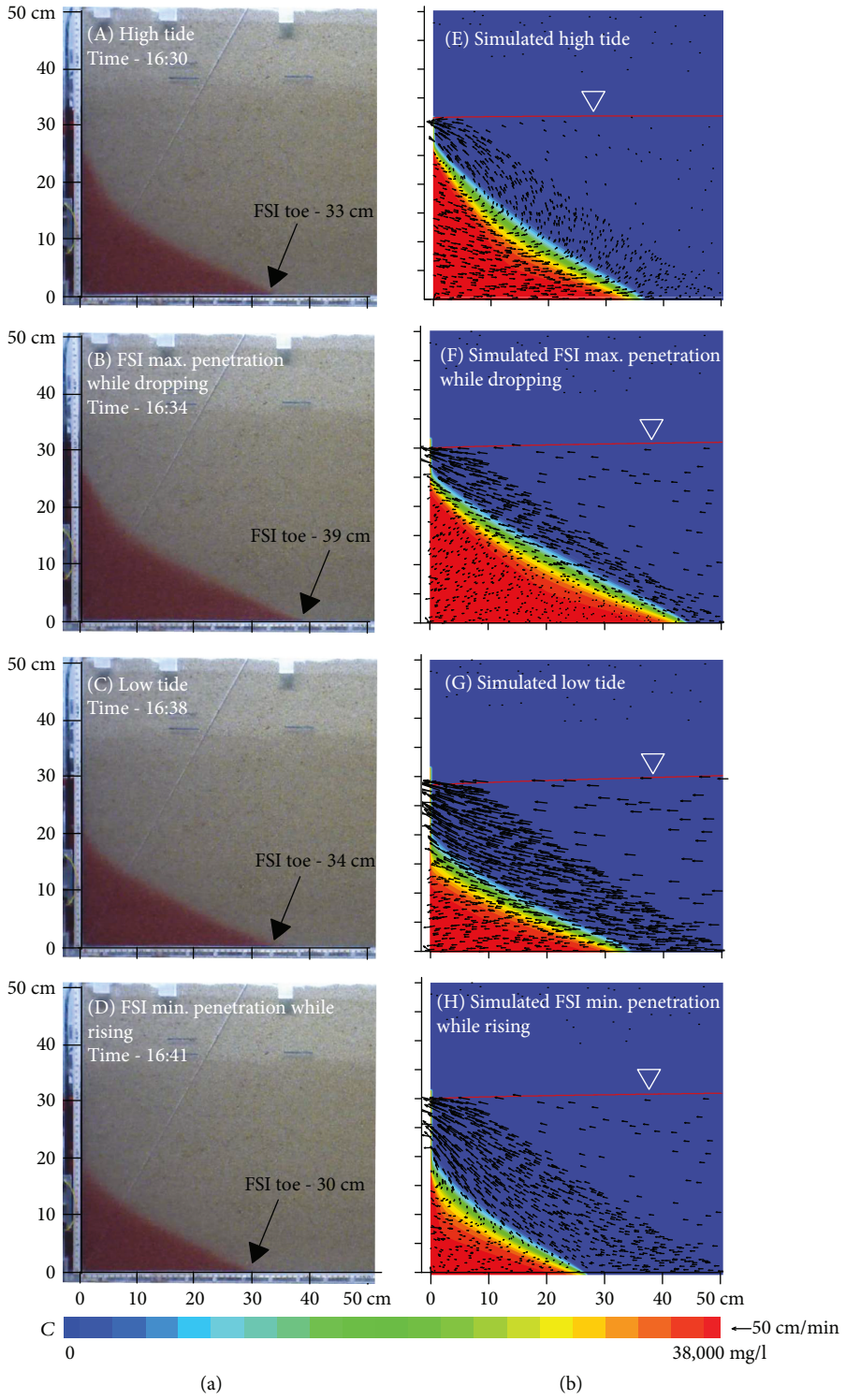

Figure 4: Four stages of a typical sinusoidal wave, each includes a snapshot of the laboratory experiment at A and the appropriate modeling result at B. Black arrows at the modeling snapshots represent the velocity vectors.

distances from the left boundary (electrodes #7 and #8 in Figure 5). However, the fluctuations of the salinity lag significantly after those of the water level. This lag between the water level and the salinity is related to vertical flow which is considered next.

3.1.2. Vertical Effect. On the other hand, there is a significant lag between sensors that are vertically aligned. Within the unsaturated zone, above the water table, the upper water content sensor (WC1) lags behind the lower water content sensor (WC2) and they both lag behind the sea level

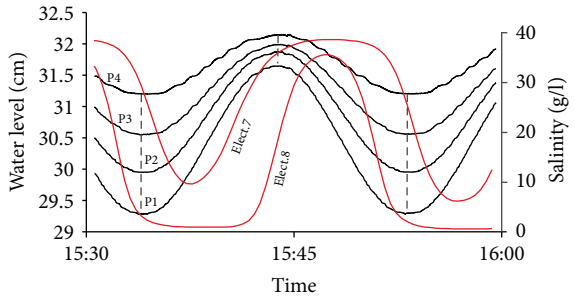

Figure 5: Water levels at all four piezometers and salinities at two electrodes which are located at the same depth (#7 and #8). Locations of the electrodes are shown in Figure 1(b). Note that the salinity peaks appear ~2 minutes after the water level peaks.

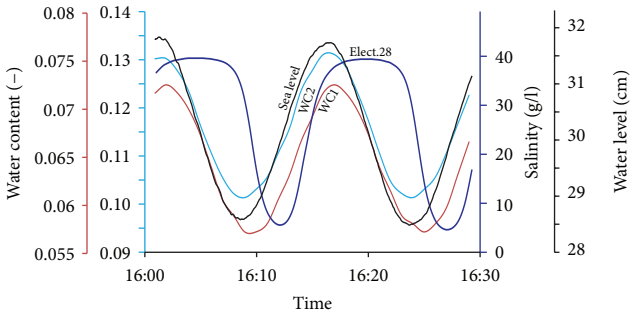

Figure 6: Vertical time lag. Upper water content sensor (WC1) lags behind the lower water content sensor (WC2), and they both lag behind the sea level fluctuations. Salinity at the FSI (electrode 28, whose location is shown in Figure 1(b)) lags behind both water content sensors. These three sensors align vertically.

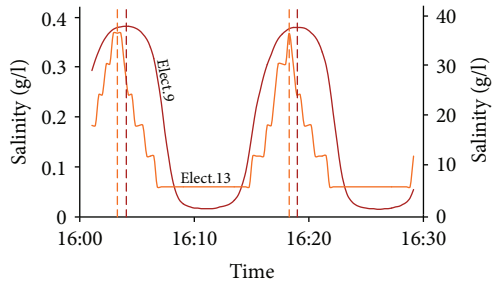

Figure 7: Vertical time lag within the FSI where the lower electrode 9 lags behind the upper electrode 13. Vertical dashed lines denote the peak timings.

fluctuations (Figure 6). The salinity at the FSI (electrode #28) lags behind both water content sensors. All these sensors are aligned vertically 18 cm from the left boundary. This vertical time lag trend exists also within the FSI where the lower electrode #9 also lags behind the upper electrode #13 (Figure 7). The mechanism for the vertical lag in saturation and salinity will be further discussed later.

3.2. Numerical Model. The hydraulic parameters (Table 1) used in the numerical simulations were calibrated to achieve a reasonable fitting between the experimental and modeled salinities (Figures 4 and 8). Even in the controlled

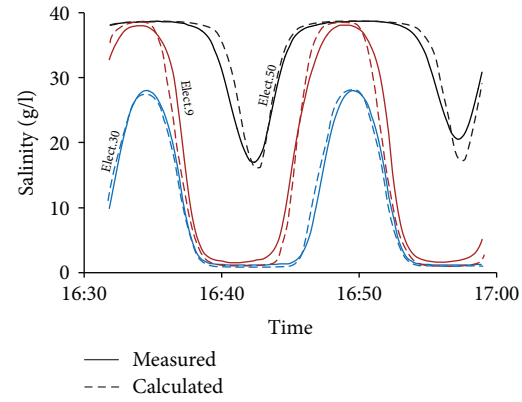

Figure 8: Comparison between observed (solid) and calculated (dashed) salinities at three electrodes whose locations are shown in Figure 1(b).

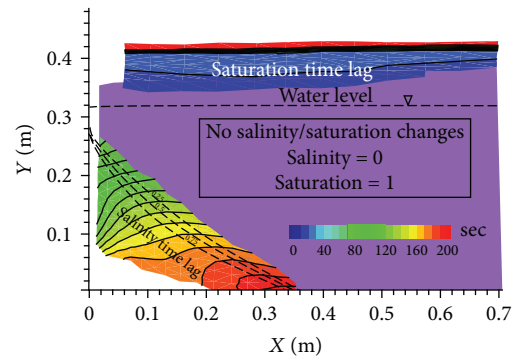

Figure 9: Time lags calculated using cross-correlation of saturation and salinity behind the sea level. Water level and contours of salinity as fraction from seawater salinity are shown for orientation.

environment of this experiment, there is some heterogeneity in the packing of the sand and some uncertainties in the measurements. Therefore, there is no attempt here to numerically reproduce the laboratory experiments exactly. Nevertheless, it helps to understand the mechanism responsible for the lags of the saturation and salinity. Based on the numerical simulation results, cross-correlation analysis was used to evaluate the correlation and the time lag between the sea level as an input and salinity and saturation as outputs.

In locations where the salinity and saturation are influenced by the sea tide, the lag after the sea level fluctuations is calculated using cross-correlation (Figure 9). Changes in salinity are observed only close to the FSI, and changes in saturation are observed only above the water level. In these locations, it is possible to calculate time lags. Because of the specific Van Genuchten parameters in this experiment, the significant drop in the saturation occurs about 9 cm above the water level. As a result, the unsaturated hydraulic conductivity also drops in this elevation and causes a significant lag for water content fluctuations. This lag of flow is transmitted to deeper parts of the aquifer and causes a lag of the salinity fluctuations around the FSI (Figure 9). The horizontal lag of the system to the imposed horizontal boundary condition is negligible because the pressure signal

is transmitted rapidly through the cross-section whereas the vertical lag of the saturation and salinity is significant because it is related to the actual advection of the water.

4. Discussion

Usually, the use of a small-scale laboratory setup has a limitation due to the downscaling problem in time and space. However, such a laboratory physical setup can provide actual results that can verify the outcome of hydrological simulation in a place where no field data can be obtained for such verification. Thus, the laboratory results can have great advantages which help in understanding the hydrodynamic processes involved in tidal influence on the coastal aquifer. As mentioned before, the effect on the vertical scale could only be obtained at the lab experiment and not in the field.

The results of this study confirm the mechanism hypothesized by Levanon et al. [19, 20] for sea tide influence on the coastal groundwater system, including both the FSI and the GWL. The tidal effect on the groundwater system comprises two main processes: tidal forcing at the sea floor boundary and attenuation at the groundwater level due to capillary effect. This mechanism was previously proven at the horizontal scale by field monitoring and numerical simulations. The horizontal pressure head wave propagation into the aquifer is fast; thus, it could be detected only at the field scale. Indeed, at the laboratory scale, there is no measured horizontal time lag between the boundary level fluctuations and the GWL (Figure 5). The current study verifies the hypothesis through controlled laboratory experiments at the vertical scale by the time lags at both the unsaturated and the saturated zones. The vertical tide-induced fluctuations of the groundwater level create an actual movement of the whole water body in a phreatic aquifer. Within the capillary zone, these fluctuations are attenuated by the relatively low hydraulic conductivity. The exact extent of the attenuation is dictated by the unsaturated hydraulic conductivity which is related to the retention curve of the matrix. The specific properties of sand used in this study (Figure 2) caused time lags of the saturation degree up to nine cm above the water level (Figure 9). At the same time, the salinity at the FSI is fluctuating with the fluctuation of the whole water body. This fluctuation is controlled by an advection wave (as opposed to the horizontal pressure wave), and therefore, the lag increases with depth (Figure 9).

This study only examined an aquifer with a vertical shoreline and no hysteresis. A sloping shoreline will likely complicate patterns and behaviors of groundwater flow and disrupt the sinusoidal tide due to the asymmetry of the tidal infiltration/draining process for a sloping beach [6, 17, 35]. It is much easier for the water to infiltrate into a sloping beach at high tide than to drain away at low tide. Hysteresis of wetting and draining water level has a similar effect, a strong asymmetry in the moisture content response to the symmetric forcing condition. For periods less than 15 minutes, the dynamics become symmetric and nonhysteretic. [34]. To avoid these complications in this study, we chose a vertical shoreline and a period of 15 minutes for the tidal wave.

5. Conclusions

Laboratory experiments conducted in a vertical, two-dimensional, rectangular flow tank exhibit a phreatic coastal aquifer. Sea tide effects on both the FSI and the GWL are analyzed in the laboratory along with numerical models that simulate these experiments. Significant time lags are observed both in the saturation degree within the capillary zone and in the salinity within the FSI. The low hydraulic conductivity in the capillary zone attenuates the movement of the water table, which controls the movement of the freshwater aquifer and causes the saturation and salinity to lag behind the fluctuating sea. The time lag of the saturation is the highest at the top of the capillary zone where the saturation and permeability is the lowest. The time lag of the salinity within the FSI increases with depth with distance from the capillary zone.

Most previous field studies in coastal aquifers neglect the dynamic nature of the attenuation caused by the nonlinearity at the capillary zone. However, these dynamics may affect significantly the transport, mobility, and removal of chemicals and their subsequent discharge to coastal waters. The attenuation at the capillary zone and its effects on the entire coastal aquifer revealed here provide new insight into the complexity, intensity, and time scales of tidal effects in coastal aquifers.

Data Availability

All data are available on request at the following e-mail address: eyal@gsi.gov.il.

Conflicts of Interest

The authors declare that they have no conflicts of interest.

Acknowledgments

This study was financed by the Israeli Water Authority and the Israel Science Foundation, grant number 942/14. We want to thank I. Simchayoff and A. Podelko from the Hebrew University of Jerusalem who helped in planning and developing the laboratory system.

Supplementary Materials

A video of the laboratory experiment showing the full dynamic process of the experiment. *(Supplementary Materials)*

References

[1] J. Bear, *Dynamics of Fluids in Porous Media*, Courier Corporation, 1972.

[2] A. D. Werner, M. Bakker, V. E. A. Post et al., "Seawater intrusion processes, investigation and management: recent advances and future challenges," *Advances in Water Resources*, vol. 51, pp. 3–26, 2013.

[3] B. Ataie-Ashtiani, R. E. Volker, and D. A. Lockington, "Tidal effects on sea water intrusion in unconfined aquifers," *Journal of Hydrology*, vol. 216, no. 1-2, pp. 17–31, 1999.

[4] E. Shalev, A. Lazar, S. Wollman, S. Kington, Y. Yechieli, and H. Gvirtzman, "Biased monitoring of fresh water-salt water mixing zone in coastal aquifers," *Ground Water*, vol. 47, no. 1, pp. 49–56, 2009.

[5] P. A. Carr and G. S. Van Der Kamp, "Determining aquifer characteristics by the tidal method," *Water Resources Research*, vol. 5, no. 5, pp. 1023–1031, 1969.

[6] P. Nielsen, "Tidal dynamics of the water table in beaches," *Water Resources Research*, vol. 26, no. 9, pp. 2127–2134, 1990.

[7] J. Wang and T.-K. Tsay, "Tidal effects on groundwater motions," *Transport in Porous Media*, vol. 43, no. 1, pp. 159–178, 2001.

[8] J. H. Kim, J. Lee, T. J. Cheong et al., "Use of time series analysis for the identification of tidal effect on groundwater in the coastal area of Kimje, Korea," *Journal of Hydrology*, vol. 300, no. 1–4, pp. 188–198, 2005.

[9] J. Y. Parlange and W. Brutsaert, "A capillarity correction for free surface flow of groundwater," *Water Resources Research*, vol. 23, no. 5, pp. 805–808, 1987.

[10] P. Nielsen and P. Perrochet, "Watertable dynamics under capillary fringes: experiments and modelling," *Advances in Water Resources*, vol. 23, no. 5, pp. 503–515, 2000.

[11] A. D. Werner and D. A. Lockington, "Influence of hysteresis on tidal capillary fringe dynamics in a well-sorted sand," *Advances in Water Resources*, vol. 26, no. 11, pp. 1199–1204, 2003.

[12] N. Cartwright, P. Nielsen, and P. Perrochet, "Behavior of a shallow water table under periodic flow conditions," *Water Resources Research*, vol. 45, no. 3, 2009.

[13] J. Kong, C. J. Shen, P. Xin et al., "Capillary effect on water table fluctuations in unconfined aquifers," *Water Resources Research*, vol. 49, no. 5, pp. 3064–3069, 2013.

[14] J. Kong, P. Xin, G. F. Hua et al., "Effects of vadose zone on groundwater table fluctuations in unconfined aquifers," *Journal of Hydrology*, vol. 528, pp. 397–407, 2015.

[15] O. D. L. Strack, "A single-potential solution for regional interface problems in coastal aquifers," *Water Resources Research*, vol. 12, no. 6, pp. 1165–1174, 1976.

[16] E. Levanon, Y. Yechieli, E. Shalev, V. Friedman, and H. Gvirtzman, "Reliable monitoring of the transition zone between fresh and saline waters in coastal aquifers," *Groundwater Monitoring & Remediation*, vol. 33, no. 3, pp. 101–110, 2013.

[17] J. W. Heiss and H. A. Michael, "Saltwater-freshwater mixing dynamics in a sandy beach aquifer over tidal, spring-neap, and seasonal cycles," *Water Resources Research*, vol. 50, no. 8, pp. 6747–6766, 2014.

[18] M. Pool, V. E. A. Post, and C. T. Simmons, "Effects of tidal fluctuations on mixing and spreading in coastal aquifers: homogeneous case," *Water Resources Research*, vol. 50, no. 8, pp. 6910–6926, 2014.

[19] E. Levanon, E. Shalev, Y. Yechieli, and H. Gvirtzman, "Fluctuations of fresh-saline water interface and of water table induced by sea tides in unconfined aquifers," *Advances in Water Resources*, vol. 96, pp. 34–42, 2016.

[20] E. Levanon, Y. Yechieli, H. Gvirtzman, and E. Shalev, "Tide-induced fluctuations of salinity and groundwater level in unconfined aquifers – field measurements and numerical model," *Journal of Hydrology*, vol. 551, pp. 665–675, 2017.

[21] I. Oz, E. Shalev, Y. Yechieli, and H. Gvirtzman, "Saltwater circulation patterns within the freshwater-saltwater interface in coastal aquifers: laboratory experiments and numerical modeling," *Journal of Hydrology*, vol. 530, pp. 734–741, 2015.

[22] Y. Katz and H. Gvirtzman, "Capture and cleanup of a migrating VOC plume by the in-well vapor stripping: a sand tank experiment," *Journal of Contaminant Hydrology*, vol. 43, no. 1, pp. 25–44, 2000.

[23] C. T. Simmons, M. L. Pierini, and J. L. Hutson, "Laboratory investigation of variable-density flow and solute transport in unsaturated - saturated porous media," *Transport in Porous Media*, vol. 47, no. 2, pp. 215–244, 2002.

[24] S. W. Chang and T. P. Clement, "Experimental and numerical investigation of saltwater intrusion dynamics in flux-controlled groundwater systems," *Water Resources Research*, vol. 48, no. 9, 2012.

[25] I. Oz, E. Shalev, Y. Yechieli, I. Gavrieli, and H. Gvirtzman, "Flow dynamics and salt transport in a coastal aquifer driven by a stratified saltwater body: lab experiment and numerical modeling," *Journal of Hydrology*, vol. 511, pp. 665–674, 2014.

[26] M. C. Boufadel, M. T. Suidan, and A. D. Venosa, "Tracer studies in laboratory beach simulating tidal influences," *Journal of Environmental Engineering*, vol. 132, no. 6, pp. 616–623, 2006.

[27] X. Geng and M. C. Boufadel, "Numerical study of solute transport in shallow beach aquifers subjected to waves and tides," *Journal of Geophysical Research: Oceans*, vol. 120, no. 2, pp. 1409–1428, 2015.

[28] X. Geng, M. C. Boufadel, Y. Xia et al., "Numerical study of wave effects on groundwater flow and solute transport in a laboratory beach," *Journal of Contaminant Hydrology*, vol. 165, pp. 37–52, 2014.

[29] S. M. H. J. Shoushtari, N. Cartwright, P. Nielsen, and P. Perrochet, "The effects of oscillation period on groundwater wave dispersion in a sandy unconfined aquifer: sand flume experiments and modelling," *Journal of Hydrology*, vol. 533, pp. 412–420, 2016.

[30] L. Li, D. A. Barry, J. Y. Parlange, and C. B. Pattiaratchi, "Beach water table fluctuations due to wave run-up: capillarity effects," *Water Resources Research*, vol. 33, no. 5, pp. 935–945, 1997.

[31] M. T. Van Genuchten, "A closed-form equation for predicting the hydraulic conductivity of unsaturated soils 1," *Soil Science Society of America Journal*, vol. 44, no. 5, pp. 892–898, 1980.

[32] H.-J. Diersch, *Finite Element Modeling of Flow, Mass and Heat Transport in Porous and Fractured Media, vol. 22*, Springer Science & Business Media, 2014.

[33] C. I. Voss and A. M. Provost, *SUTRA: A model for 2D or 3D saturated-unsaturated, variable-density ground-water flow with solute or energy transport*, Water-Resources Investigations Report, 2002.

[34] N. Cartwright, "Moisture-pressure dynamics above an oscillating water table," *Journal of Hydrology*, vol. 512, pp. 442–446, 2014.

[35] C. Robinson, L. Li, and H. Prommer, "Tide-induced recirculation across the aquifer-ocean interface," *Water Resources Research*, vol. 43, no. 7, 2007.

Hindawi
Geofluids
Volume 2019, Article ID 2316271, 17 pages
https://doi.org/10.1155/2019/2316271

WILEY | Hindawi

Research Article

Experiment and Numerical Simulation of Seawater Intrusion under the Influences of Tidal Fluctuation and Groundwater Exploitation in Coastal Multilayered Aquifers

Qiaona Guo, Jiangwei Huang, Zhifang Zhou, and Jinguo Wang

School of Earth Sciences and Engineering, Hohai University, No. 8 Focheng West Road, Nanjing 211100, China

Correspondence should be addressed to Qiaona Guo; guoqiaona2010@hhu.edu.cn

Received 2 May 2019; Revised 18 June 2019; Accepted 26 June 2019; Published 18 July 2019

Guest Editor: Xuan Yu

The dynamic behavior of groundwater flow and salt transport is affected by tide and pumping in coastal multilayered aquifers. In this paper, two groups of experiments were conducted considering different constant head inland boundaries. The fluctuation of the groundwater level and the process of seawater intrusion in the multilayered aquifers were observed. A two-dimensional SEAWAT model is developed to simulate the seawater intrusion to coastal aquifers under the influences of tidal fluctuation and groundwater exploitation. The hydrogeological parameters in the model are calibrated by the records of the groundwater level and salinity measurements. The results showed that the simulated groundwater level and salt concentration match the observation well. The groundwater level has the characteristics of periodic fluctuation with tide. The lag time of the groundwater level fluctuation in each monitoring point increases slightly with the increasing distance from the saltwater chamber. For the low tide, the inland freshwater recharge has main effect on groundwater level fluctuation. The rising tide has a negative effect on the drawdown of the groundwater level induced by pumping. For the high tide, the tide plays a major role on groundwater level fluctuation, compared with the inland freshwater recharge. Compared with the condition of high head of inland recharge, larger saltwater intrusion lengths and area have been observed and simulated in the aquifer, which means that faster inland motion of the seawater wedge would occur when the inland recharge is small in the coastal aquifers. It revealed that inland recharge plays a major role in the seawater intrusion for the same pumping rate of groundwater in different seasons. The analysis provides insights into how the tide fluctuation, groundwater pumping, and inland recharge effect on the area and rates of seawater intrusion.

1. Introduction

Coastal areas are the most active area of human economic and social activities, which is built by many cities and large projects [1, 2]. The physical and chemical equilibrium of the coastal aquifer system is easily destroyed by the human activities, resulting in the problems of land subsidence, seawater intrusion, and environment deterioration. Among them, the seawater intrusion is a problem of worldwide concern, which is caused by the overpumping of groundwater, sea level rising, change of climate, and change of land use in the coastal area [3–9]. Among these factors, groundwater pumping is considered to be one of the most important challenges that promote the extent and severity of seawater intrusion [6, 9, 10]. As a result, the groundwater salinization can be directly caused by seawater intrusion due to the exploitation of groundwater [11].

The extent of seawater intrusion has been largely aggravated by the overexploitation of groundwater in coastal areas around the world, especially in China [6, 12–15]. For example, overexploitation has resulted in seawater intrusion in the Laizhou Bay, China [16]. The salinities of many groundwater samples were greater than 1000 mg/L up to tens of kilometers inland from the coastline, and the area affected by seawater intrusion has reached larger than 700 square kilometers [17, 18]. Additionally, in the Jiaozhou Bay area of

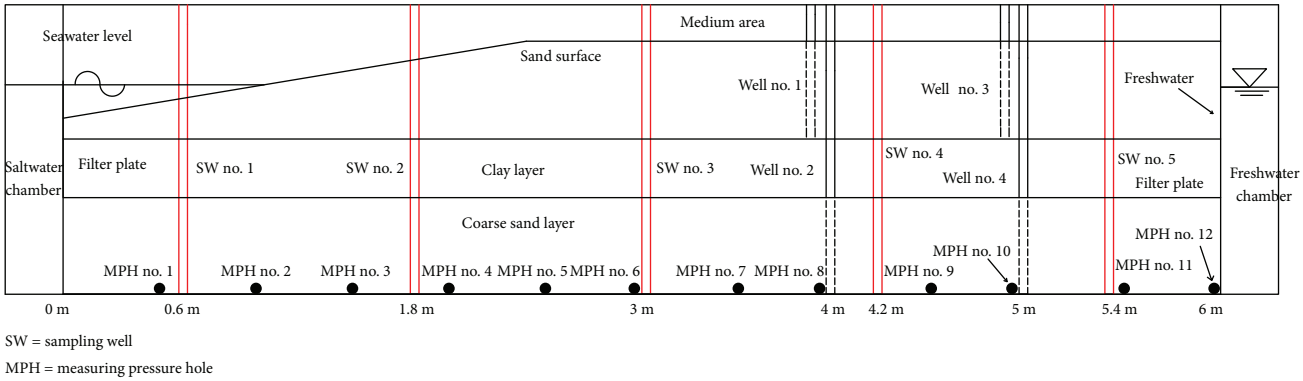

Figure 1: Schematic diagram of the test model.

China, the seawater intrusion has brought great damage in local agriculture and industry production [14]. Therefore, the mechanism, prediction, and prevention of seawater intrusion should be studied in the coastal zone.

As is known to us, the seawater intrusion process is a complex problem, because the seawater intrusion mixing with fresh groundwater couples water flow and salt transport. It involves the variable density groundwater flow, which is difficult to simulate well. Two types of flow models were developed for seawater intrusion simulation, including the sharp interface models and mixing interface models [14, 19–24]. There are many analytical solutions for variable density flow models to solve the coupled seawater intrusion equations under special conditions [6, 19, 20, 25]. Most of the analytical solutions are predominantly based on the Ghyben-Herzberg relation in the sharp interface models, in which the freshwater and saltwater are treated as separated fluids by an interface. As a consequence, the models may overestimate the actual penetration length of the seawater wedge [26]. Therefore, the analytical models of variable density flow including mixing between freshwater and seawater were provided considering the realistic condition [24, 27]. However, the analytical solutions are often derived based on some hypothetical conditions. The numerical approaches have been widely used to simulate seawater intrusion in the mixing interface [28, 29], which includes FEFLOW [30], SUTRA [31], and SEAWAT [14, 32, 33]. However, most of the numerical simulations were developed in two-dimensional cross sections, owing to the limitation of computation.

The dynamic behavior of groundwater flow induced by tidal fluctuation is an important issue in nature. There are some analytical solutions and numerical models adopted to study the influence of tides on the groundwater fluctuations and seawater interface [34–39]. The results show that the groundwater level fluctuates with a periodicity similar to tide periodicity, and the fresh saline water interface itself fluctuates due to sea level oscillations. However, the dynamic behavior of groundwater flow in a coastal aquifer is complex when considering the effect of groundwater exploitation [12, 16, 40–42]. Due to overpumping groundwater in coastal areas, the depression cones of the groundwater level can exacerbate seawater intrusion by reducing the hydraulic pressure of the freshwater. In addition, the inland boundary conditions have effects on seawater intrusion in coastal aquifers [43–46]. However, the comprehensive influence of tidal fluctuations, groundwater exploitation, and inland recharge on the location of the fresh saline water interface, including the groundwater flow in coastal aquifers, has received less attention. Moreover, the coastal aquifers are a multilayered aquifer system in most cases, and there are few studies on the seawater intrusion in the multilayered aquifers.

The objective of this study is to investigate the effects of a fluctuating sea level, groundwater pumping, and inland recharge on seawater intrusion in coastal multilayered aquifers. In this paper, two groups of experiments were conducted considering different constant head inland boundaries. The fluctuation of the groundwater level and the process of seawater intrusion in the unconfined aquifer and confined aquifer were observed. The numerical results were analyzed and compared with the experiment data. The effects of aquifer heterogeneity, boundary condition, groundwater pumping, and tide on solute mixing of saltwater and freshwater are described. The range of the saltwater and freshwater mixing zone and seawater wedge toe motion in the unconfined aquifer and confined aquifer are determined. The hydrogeological factors affecting salt distribution in the multilayered aquifer system are identified.

2. Experimental Setup and Test Cases

2.1. Experimental Setup. Figure 1 shows the laboratory tank, which is 6.6 m long, 0.6 m wide, and 1.5 m high, made of plexiglass with the thickness of 1.5 cm. The tank consists of three parts, which are the saltwater chamber, medium area, and freshwater chamber along the length direction. The medium area and the side chambers at either side are separated by two filter plates with small holes. The filter plates on both sides are 30 cm away from the left saltwater side and the right freshwater side, respectively. Geotextiles are laid on both sides of the filter plate, which acts as a barrier to sand passage. In order to avoid the deformation of the tank after filling sand, the main body of the tank is protected by a steel frame in the interval of 1 m. The seawater area and freshwater area are connected with the reservoirs, respectively. The two reservoirs are made of PVC boards, with the length of 140 cm, width of 120 cm, and height of 60 cm, placed on the ground. The right freshwater chamber is

connected to a fixed head device (an overflow device for controlling the water level), which makes the freshwater head a fixed value. The left seawater chamber is controlled by the power cabinet system (controlling the tide device). The power cabinet system can control the inlet pump or outlet pump, which is connected to the seawater area, to make the seawater level fluctuate tidally.

The experiments required the measurements of the water level and the concentration of salt. The sea level on the left side of the tank was measured using a meter stick fixed on the steel frame. There are twelve monitoring point of pressure measuring tubes placed at the bottom of the back of the sand tank to measure the water level variation with time. In order to prevent the fine sand particles from entering into the pressure measuring tubes, a filter with a mesh diameter of 0.18 mm is placed at the connection between the piezometric tube and sand tank; the interval between every two pressure tubes is 50 cm in the horizontal direction. In order to study the seawater intrusion under the effect of groundwater exploitation, two groups of wells are set in the middle of the tank, which are 4 m and 5 m far from the saltwater boundary. The shallow wells No. 1 and No. 3 are installed in the fine sand layer, with the depth of 55 cm. The bottom of the wells was placed at the interface between the fine sand layer and clay layer. The deep wells No. 2 and No. 4 are installed in the coarse sand layer, with the depth of 156 cm. The bottom of the wells was placed at the bottom of the tank. The two groups of wells are cylindrical pipes, made of PVC material, with the diameter of 80 mm. There is a silastic tube with 2.79 mm internal diameter in each deep well, which connected to a peristaltic pump head (YZ35-13 type, 3 rollers, speed less than 600 rpm, and max flow rate 11000 mL/min) to extract water at the desired flow rate. The PVC pipes in both coarse sand layer and fine sand layer were drilled with small holes. In order to prevent the fine sand particles or coarse sand particles from entering into the wells, the bottom and the holes on the sidewall of the wells are wrapped by a filter with the mesh diameter of 0.18 mm.

In order to track the variation of the length of the saltwater wedge and the migration of the seawater-freshwater interface, there are five multiport sampling wells installed in the sand tank, which are 0.6 m, 1.8 m, 3 m, 4.2 m, and 5.4 m far away from the saltwater boundary, respectively. The multiport sampling wells are made of PVC board and have 6 sampling ports. They are labeled ports from A to F from the bottom to the top; the interval distance between every two ports is 20 cm. Each port is connected to a tube, whose top was connected to a Luer lock three-way valve at the top of the well through a Typon tubing.

Considering the heterogeneity of a coastal aquifer, the main body of the tank is filled with fine sand, clay, and coarse sand from top to bottom, with the thickness of 40 cm, 25 cm, and 50 cm, respectively. The bank slope of the fine sand layer is set to 6°. The setting of the slope satisfied the requirement that it should be stable and should not collapse during the period of the experiment. The sand samples are taken from the field site, which is located in the coastal area of Longkou City (the longitude is 120°31′42″, and the latitude is 37°44′23″), China. The particle sizes of fine sand and coarse sand are ranging from 0.25 mm to 0.1 mm and from 0.5 mm to 1 mm, respectively. The particle sizes of the clay are less than 0.01 mm. The hydraulic conductivities of the fine sand and coarse sand are 4.32 m/d and 37 m/d, obtained from the slug test in the wells No. 1 and No. 2, respectively. The hydraulic conductivity of clay is 0.25 m/d, which is obtained from a variable head permeameter in the laboratory.

The bottom of the sand box is the datum level. The simulated average sea level is 0.85 m. The highest and the lowest values of the tide are 1.05 m and 0.65 m, respectively. The tidal range is 0.4 m, and the tidal cycle is 40 min. The deionized water is used to be freshwater, which is made in the laboratory. The concentration and density of the freshwater are 0 g/L and 1.00×10^3 kg/m^3, respectively. The saltwater is configured by deionized water and sodium chloride (analytical purity). The concentration and density of the saltwater are 18 g/L and 1.02×10^3 kg/m^3, respectively. The bright blue is dissolved with salt to trace the saltwater transport in the tank and monitor the seawater wedge visually, with the concentration of 2 g/L. During the experiment, the salinities were measured at various depths using the multiport wells. The shape of the seawater wedge is recorded every 10 minutes by taking photos.

2.2. Test Schemes and Flow Chart. Two groups of experiments (Cases 1 and 2) were designed and conducted to investigate the effects of tide and groundwater exploitation on groundwater flow and salt transport in a coastal multilayered aquifer system. In order to investigate the impact of inland freshwater recharge on seawater intrusion, these two cases of constant inland boundary are considered. The constant head of inland boundary is 95 cm for Case 1 and 80 cm for Case 2, which represents the high and low groundwater levels in different seasons. There are three tests in each case. The experiment starts after the sand sample installation.

For each case, the tank was initially flushed using freshwater with the saltwater chamber closed. For Case 1, the water level of freshwater on the right side was set to 95 cm. The freshwater flowed from the right side to the left side of the tank, and the excess amount of freshwater discharged from the left chamber. When the freshwater level on the left side rises to 95 cm, the steady flow was formed on both sides. Then, the tide device was applied, and the freshwater in the seawater chamber was replaced quickly with dyed seawater. The sea level fluctuated periodically, with the amplitude of 20 cm and period of 40 min. The pressure heads at the twelve measuring holes were observed. The electrical conductivity of water samples at different depths was measured by the conductivity meter. When the shape and position of the seawater wedge do not change within 10 minutes, it is assumed that the interface between saltwater and freshwater has reached a steady state condition. Subsequently, the peristaltic pump in well No. 4 started to extract water at the flow rate of 1.0 L/min. The pumping experiment stopped until a new steady state of seawater wedge was achieved. At last, the groundwater was continuously pumped with a larger flow rate of 2 L/min. The experiment stopped until the seawater wedge reached a new steady state. During the whole

experiment, the water samples in the monitoring holes were collected at the interval between 5 min and 30 min. The migration of seawater wedge was observed every 5 minutes by taking photos during this period.

The water level of freshwater on the right side was set equal to 80 cm for Case 2. The whole experiment process was similar to that of Case 1, which was not described in detail. During the experiment, the images of the saltwater intrusion were captured with a high-speed camera with a resolution of 1280×1024 pixels and an 8-bit grayscale pixel depth. After the experiment, a MATLAB code was then used to analyze all the experimental images to calculate the toe length of the saltwater wedge and provide maps of the solute concentration in the aquifers.

3. Numerical Simulations of Variable Density Flow and Solute Transport

3.1. Mathematical Model. The mathematical model for groundwater flow with variable density is applied to simulate the seawater intrusion processes. Based on the finite difference groundwater flow simulation model MODFLOW, the numerical simulation model of solute transport in groundwater flow is established using SEAWAT, considering the effect of density on groundwater flow [32]. The software has been widely applied in seawater intrusion and submarine groundwater discharge (e.g., [12, 47–49]).

The governing equation for the variable density groundwater flow can be expressed as

$$\begin{aligned}
&\frac{\partial}{\partial x}\left[\rho K_{fx}\left(\frac{\partial h_f}{\partial x}+\frac{\rho-\rho_f}{\rho_f}\frac{\partial Z}{\partial x}\right)\right] \\
&\quad+\frac{\partial}{\partial y}\left[\rho K_{fy}\left(\frac{\partial h_f}{\partial y}+\frac{\rho-\rho_f}{\rho_f}\frac{\partial Z}{\partial y}\right)\right] \\
&\quad+\frac{\partial}{\partial z}\left[\rho K_{fz}\left(\frac{\partial h_f}{\partial z}+\frac{\rho-\rho_f}{\rho_f}\frac{\partial Z}{\partial z}\right)\right] \\
&=\rho S_f\frac{\partial h_f}{\partial t}+\theta\frac{\partial \rho}{\partial C}\frac{\partial C}{\partial t}-\rho_s q_s,
\end{aligned} \tag{1}$$

where x, y, z is the flow direction; K_{fx}, K_{fy}, K_{fz} are the hydraulic conductivities in different directions (LT^{-1}); S_f is the specific storage in terms of freshwater head (L^{-1}); h_f is the equivalent freshwater head (L); θ is the effective porosity of porous medium (-); ρ is the density of saline groundwater at a point in aquifer (ML^{-3}); ρ_f is the density of freshwater (kg/m^3); ρ_s is density of water entering from a source or leaving through a sink (ML^{-3}); q_s is the volumetric flow rate of sources or sinks per unit volume of aquifer (T^{-1}); C is the solute concentration (ML^{-3}); and t is the time (T).

The process of seawater intrusion is a variable density groundwater flow, including the seepage, dispersion, and diffusion. The partial differential term of the concentration changing with time is added in the flow equation (1), and the change of concentration affects the groundwater flow of the aquifer. Therefore, the seawater intrusion requires the coupling solution of groundwater flow equation and solute transport equation. The equation of solute transport includes the groundwater convection term, hydrodynamic dispersion term, source-sink term, and reaction term, which is expressed as

$$\frac{\partial \theta C}{\partial t}=\nabla(\theta D\nabla C)-\nabla(\theta V C)+q_s C_s+R_n, \tag{2}$$

where D is the hydrodynamic dispersion coefficient tensor (L^2T^{-1}), C_s is the solute concentration of water entering from sources or sinks (ML^{-3}), V is the average linear velocity (LT^{-1}), and R_n is the reaction term of chemical substance.

3.2. Numerical Simulation Method. The aquifer system was assumed to be heterogeneous and isotropic. The length, width, and height of the simulation zone were 600 cm, 60 cm, and 115 cm, respectively. This model domain was discretized into the hexahedron elements with $4 \times 4 \times 5\ cm^3$. There were 3150 columns and 15 layers with 47250 cells in total. The top boundary was a free surface, and the bottom boundary was treated as a no-flow boundary. On the right side boundary, a constant hydraulic head of 95 cm for Case 1 (80 cm for Case 2) was set. The concentration of freshwater was 0 g/L. The flow boundary at the left side boundary was defined as a time series of the hydraulic head based on a simple harmonic tidal function:

$$h(t)=h_i+A\cos(\omega t), \tag{3}$$

where h_i (L) is the initial saltwater hydraulic head, A (L) is the tidal amplitude, and ω (Rad T^{-1}) is the tidal angular frequency. Salinity was prescribed to be 18 g/L on the sea floor. The simulation period was 1200 minutes. A constant time step of 1 min was defined for the simulations in order to enable the analysis for the results from the numerical model. For every time step, the hydraulic heads on the sea floor changed according to equation 3.

Initially, the transient simulation was used to determine the extent of seawater intrusion under the condition of tidal fluctuation, without considering the pumping in the aquifer. Then, a pumping well was introduced, and the simulation continued until the new steady state conditions were obtained in different pumping rates.

3.3. Model Calibration. In our model, the parameters of aquifers were calibrated by a trial-error method repeatedly to fit the head and salinity measurements for Case 1. The process of calibration was to adjust the values of the parameters, including the hydraulic conductivities, specific yield, specific storage, effective porosity, and dispersivity, until a good agreement between simulated and observed results is reached. Based on the empirical data, the horizontal hydraulic conductivity was assumed to be ten times of its vertical value of the aquifer system. The transverse dispersivity (α_T) was one-twentieth of the longitudinal dispersivity (α_L) [50, 51]. The longitudinal dispersivity and transverse dispersivity were determined mainly based on model calibration. The parameters used for the simulations were given in Table 1.

Table 1: Model parameters and their values used in the numerical simulations.

Parameter	Definition	Unit	Value
K_x	Hydraulic conductivity	m/d	4.3 (fine sand layer) 0.03 (clay layer) 38.0 (coarse sand layer)
μ	Specific yield	—	0.30
S_s	Specific storage	1/m	10^{-5}
ρ_f	Density of the freshwater	kg/m^3	1.0×10^3
ρ	Density of the seawater	kg/m^3	1.02×10^3
α_L	Longitudinal dispersivity	m	0.1
α_T	Transverse dispersivity	m	0.005
τD_m	Molecular diffusion coefficient in porous media	m^2/s	10^{-9}
t	Time period	min	1200
Q	Pumping rates	L/min	$Q_1 = 1.0$, $Q_2 = 2.0$

From the estimated values listed in Table 1, one can see that the hydraulic conductivity of clay is smaller, compared with those of the fine sand and coarse sand. Therefore, the clay is regarded as the semipermeable layer. The fine sand layer and coarse sand layer are the unconfined aquifer and confined aquifer, respectively.

Figure 2 shows general similar groundwater dynamics between simulated and observed groundwater level data in the confined aquifer during the simulation period of 120 minutes, despite discrepancies around the peaks and troughs. The relative error (RE) and correlation coefficient (R^2) are used to quantitatively analyze the fitting results, which can reflect the fitting degree between the calculated values and measured values. The calculated results are shown in Table 2. The RE values between observed and calculated hydraulic heads at the monitoring points are ranging from 5.79% to 13.94%, and the correlation coefficient (R^2) is between 0.8265 and 0.9659, respectively. The results showed that most of the RE values are less than 10% and the R^2 values are larger than 0.9. It indicates that the estimation of hydrogeological parameters is reasonable and the reliability of the model is high.

Figure 3 shows the observed values and the calculated values of salt concentrations at the sampling wells in the confined aquifer during the simulation period. From Figure 3, one can see that the observed and calculated values of Cl^- concentrations increased during the period of 0 to 480 minutes. Then, they became stable from 480 minutes to 1200 minutes. The Cl^- concentrations simulated by the model were consistent with the observed ones in the sampling wells No. 1 and No. 2. The concentration of saltwater in sampling well No. 2 is lower than 18 g/L, which may be due to the fact that the freshwater flows into the saltwater chamber during the experiment. These errors are small relative to the maximum concentration variations in the sampling wells. Generally, the simulated groundwater levels and salt concentrations match the observations well.

4. Results

4.1. Effect of the Tidal Level on the Groundwater Level. In order to study the fluctuation characteristics of the groundwater level caused by tidal effect in the aquifers, Case 1 is selected to analyze the variation of the tide and the groundwater level of the confined aquifer, without considering the pumping effect. The period of tidal fluctuation was 40 minutes. The amplitude of the tide was 20 cm, and the average sea level was 85 cm. The monitoring period was from 0 min to 200 min, and the groundwater level fluctuated with time during the period of 200 min.

Figure 4 reports the variation of the groundwater level at the selected seven monitoring points and the tidal level fluctuation. The graph adopts the data from 0 minute for five consecutive tidal periods since the beginning of the experiment. From the figure, one can see that the groundwater level and tidal fluctuation have the same regularity, which shows the characteristics of periodic fluctuation. The farther the monitoring point is from the left boundary (saltwater chamber), the smaller the fluctuation range of the groundwater level is. There is a lag time between the peak or valley of the tide and that of the groundwater level. In addition, there is a certain difference in the time of the peak value or the valley value at each monitoring point. The lag time between the peak value of the groundwater level at each point and that of the sea level from the shoreline (monitoring point No. 1) to inland (monitoring point No. 12) is ranging from 5 min to 10 min. It indicates that the lag time of the groundwater level fluctuation in each monitoring point increases slightly with the increasing distance from the saltwater chamber.

4.2. Effects of Pumping on the Tide-Induced Groundwater Level. In order to study the pumping effects on tide-induced groundwater level fluctuation in the coastal multilayered aquifers, two groups of experiments were conducted. During the two groups of experiments, the change of the interface between seawater and freshwater and the variation of the groundwater level at each monitoring point were observed until the system reached the final steady state. In this section, we only focus on the variation of the groundwater level.

Figure 5 shows the observed values and calculated values of the groundwater level at the low tide, average sea level, and high tide for Case 1. The match between the observed and calculated groundwater levels is well. As the tide rises from the low tide (65 cm) to high tide (105 cm), the groundwater level increases under the condition of tidal effect without pumping (blue lines of Figures 5(a)–5(c)). From Figure 5(a), one can see that the groundwater level decreases when the pumping rate Q_1 equals to 1 L/min for the low tide. The groundwater depression cone is formed in the well No. 2 due to the pumping. The drawdown of the groundwater level in well No. 2 reaches the maximum with a value of 8.5 cm. The groundwater level drawdown on both

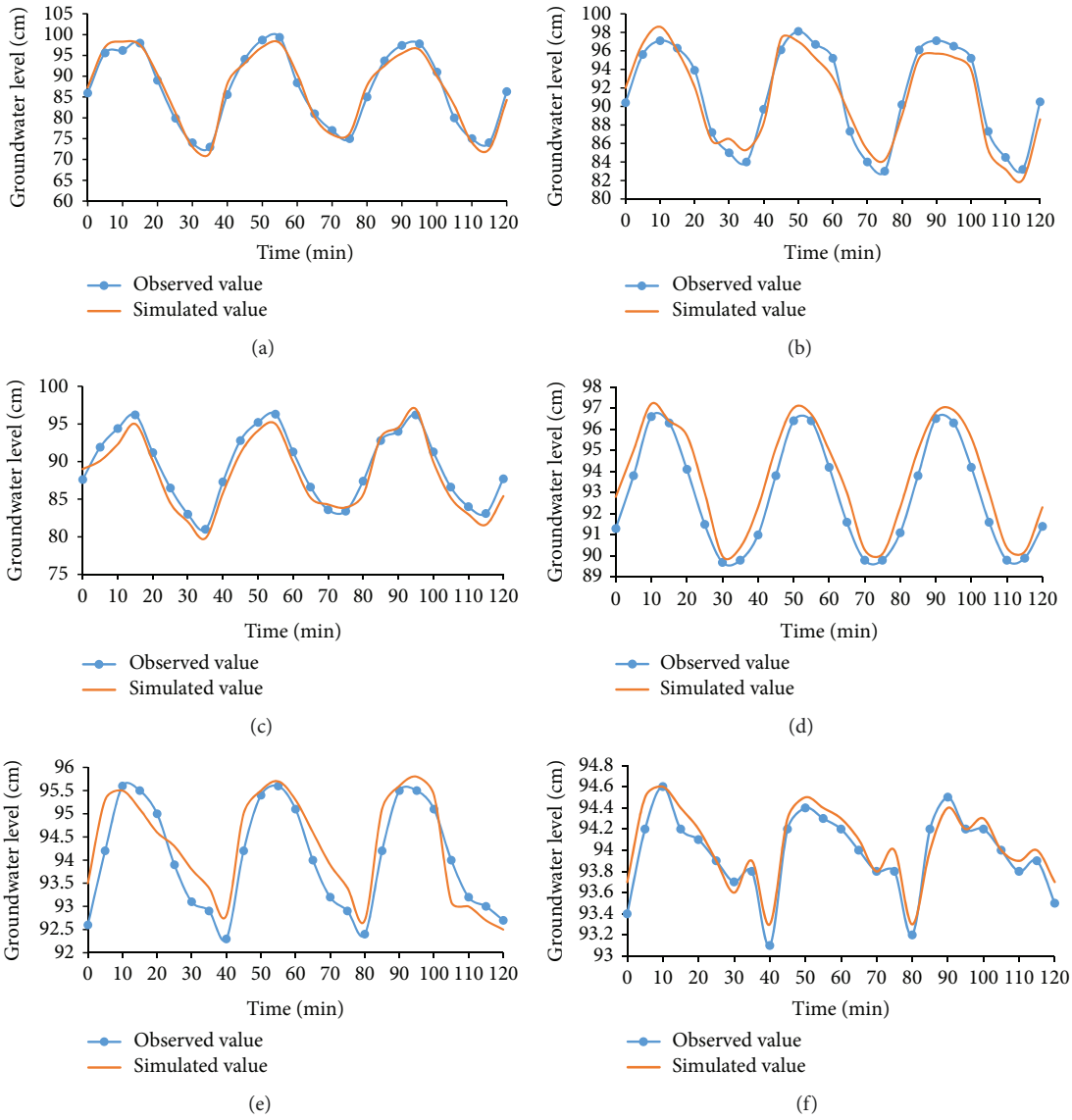

Figure 2: Observed and simulated hydraulic heads at the monitoring point of pressure measuring tubes (a) No. 1, (b) No. 3, (c) No. 5, (d) No. 7, (e) No. 9, and (f) No. 11.

Table 2: The calculated values of the fitting result at the monitoring points.

Number	No. 1	No. 3	No. 5	No. 7	No. 9	No. 11
RE (%)	5.79	8.98	8.44	12.64	13.94	7.73
R^2	0.9659	0.9316	0.9562	0.9643	0.8265	0.9037

sides of the pumping well No. 2 decreases gradually to the left boundary and right boundary. It indicates that transient pumping can significantly enhance the amplitude of the groundwater level fluctuation. A further increment of the pumping rate to $Q_2 = 2$ L/min caused faster drawdown of the groundwater level in the aquifer. The drawdown of the groundwater level in well No. 2 can reach the maximum value of 15 cm, compared with that of the case without considering pumping. From Figure 5(c), one can see that the groundwater level drawdowns in well No. 2 are 5.0 cm and 9.7 cm for the high tide, respectively, when the pumping rates are 1 L/min and 2 L/min. When the tide rises from low tide to high tide, the drawdown of the groundwater level at each point decreases (Figures 5(a)–5(c)). It indicates that the rising tide has a negative effect on the drawdown of the groundwater level induced by pumping.

In order to investigate the inland freshwater recharge on the groundwater dynamic, the freshwater head on the right boundary was set to 80 cm (Case 2), which is lower than that of Case 1 (95 cm). Figure 6 shows the observed values and calculated values of the groundwater level at low tide, average sea level, and high tide for Case 2. The simulated results captured the fluctuating trend of the groundwater level with time at the monitoring points. From Figure 6, it can be seen that the groundwater level increases under the condition of tidal effect without pumping, as the tide rises from the low tide to high tide. Thus, the variations of the groundwater level for Case 2 are similar to those of Case 1. It can be seen from

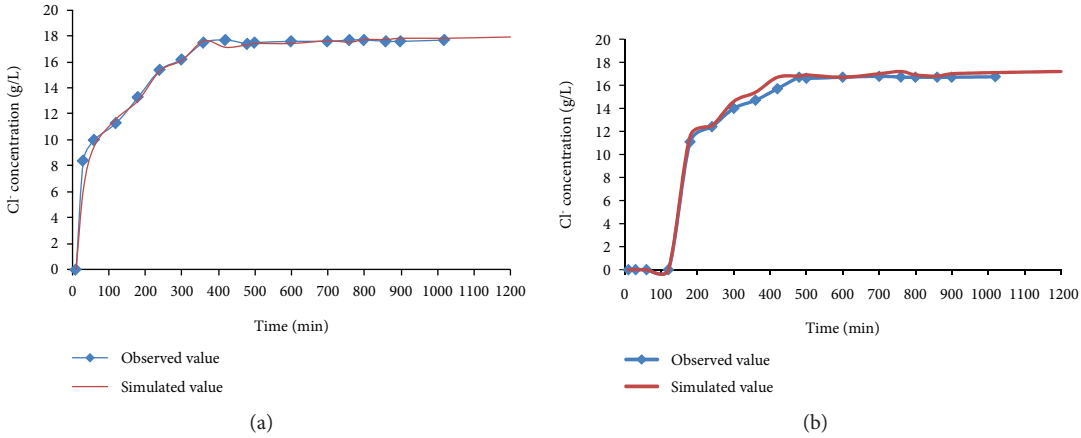

Figure 3: Fitting of observed values and calculated values of Cl^- concentration at the sampling wells (a) No. 1 and (b) No. 2.

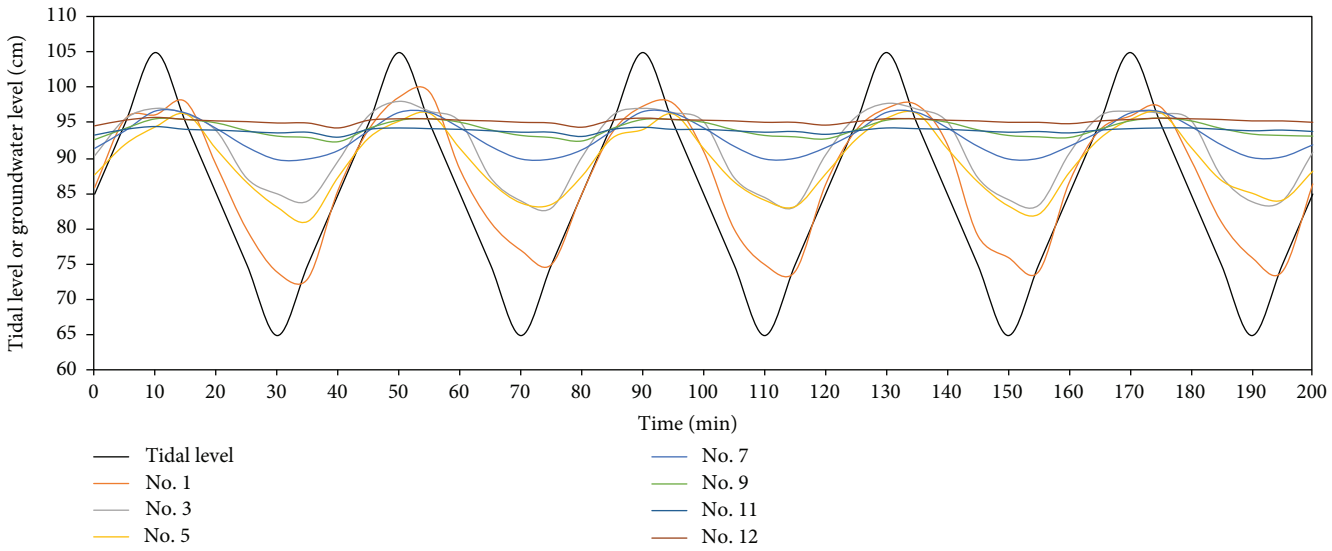

Figure 4: The variation of the groundwater level at the monitoring points (No. 1, No. 3, No. 5, No. 7, No. 9, No. 11, and No. 12) under the condition of tidal level fluctuation.

Figure 6(a) that the groundwater level drawdowns in well No. 2 can reach the maximum values of 12 cm and 18 cm, respectively, when the pumping rates are 1 L/min and 2 L/min. The groundwater level drawdown on both sides of the pumping well No. 2 decreases gradually to the seaside boundary and inland boundary under the condition of different pumping rates. Compared with Figure 6(a), from Figures 6(b) and 6(c), one can conclude that the groundwater level drawdown decreases at the monitoring points, as the tide rises under different pumping rates. When the sea level is 105 cm, the groundwater level drawdowns in well No. 2 are 5.6 cm for $Q_1 = 1$ L/min and 8 cm for $Q_2 = 2$ L/min, respectively, which are smaller than those at low tide. From Figures 5(a) and 6(a), one can see that the groundwater level drawdowns at the monitoring points for Case 1 are lower than those of Case 2, when the pumping rates are 1 L/min and 2 L/min. Especially in well No. 2, the groundwater level drawdown for Case 1 is lower than that of Case 2, with values of 3.5 cm for $Q_1 = 1$ L/min and 3.0 cm for $Q_2 = 2$ L/min. It indicates that the inland freshwater recharge in Case 2 is smaller than that of Case 1, which cannot replenish groundwater exploitation in time. However, when the sea level reaches its maximum, the difference between the groundwater level drawdowns of Case 1 and those of Case 2 is small. In well No. 2, the drawdown for Case 1 is slightly smaller than that of Case 2 with the value of 0.6 cm for $Q_1 = 1$ L/min and larger than that of Case 2 with the value of 1.7 cm for $Q_2 = 2$ L/min. It reflects that the tide plays a major role in the high tide, compared with the inland freshwater recharge. A large amount of seawater enters into the aquifer, because the groundwater level is lower than the sea level.

4.3. Saltwater Intrusion in the Multilayered Aquifers. During the experiments, there is no seawater intrusion in the middle semipermeable layer (clay layer), because of the low permeability. Therefore, in this part, we only focus on the analysis of the seawater intrusion processes in the unconfined aquifer (fine sand layer) and confined aquifer (coarse sand layer). The salinity at the mixing interface is defined as larger than 1% of salinity of seawater.

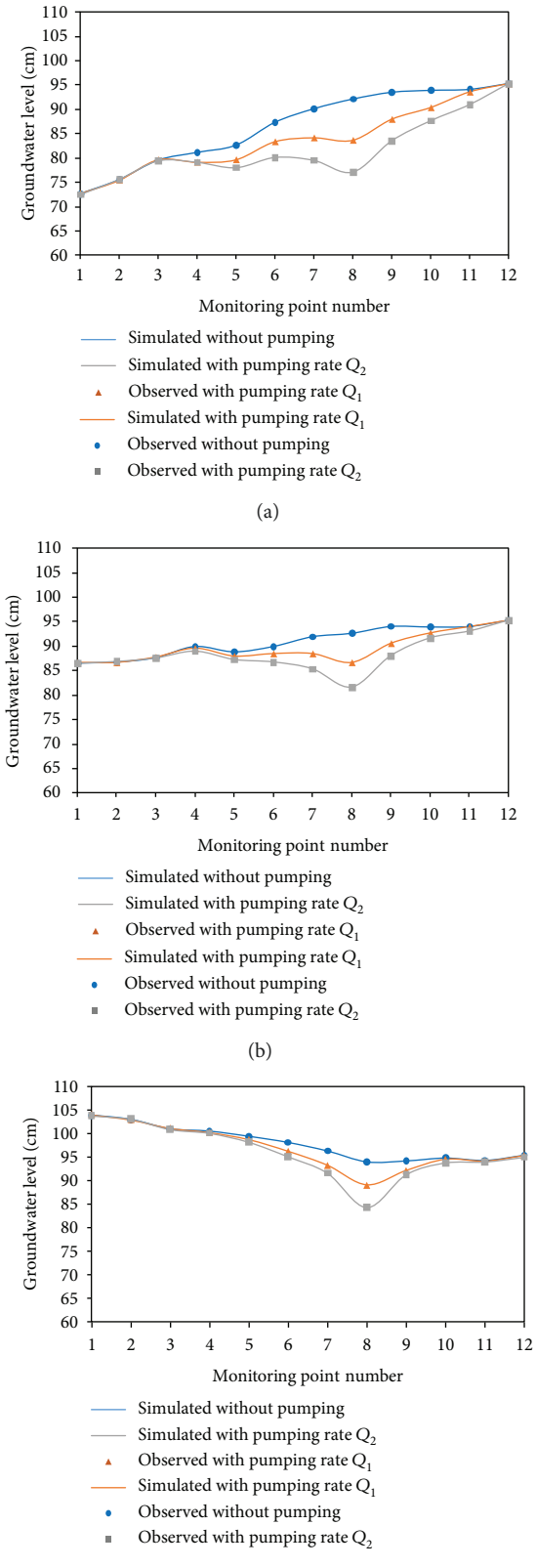

Figure 5: Observed (symbols) and simulated (solid lines) groundwater levels at the monitoring points for (a) low tide, (b) average sea level, and (c) high tide of Case 1.

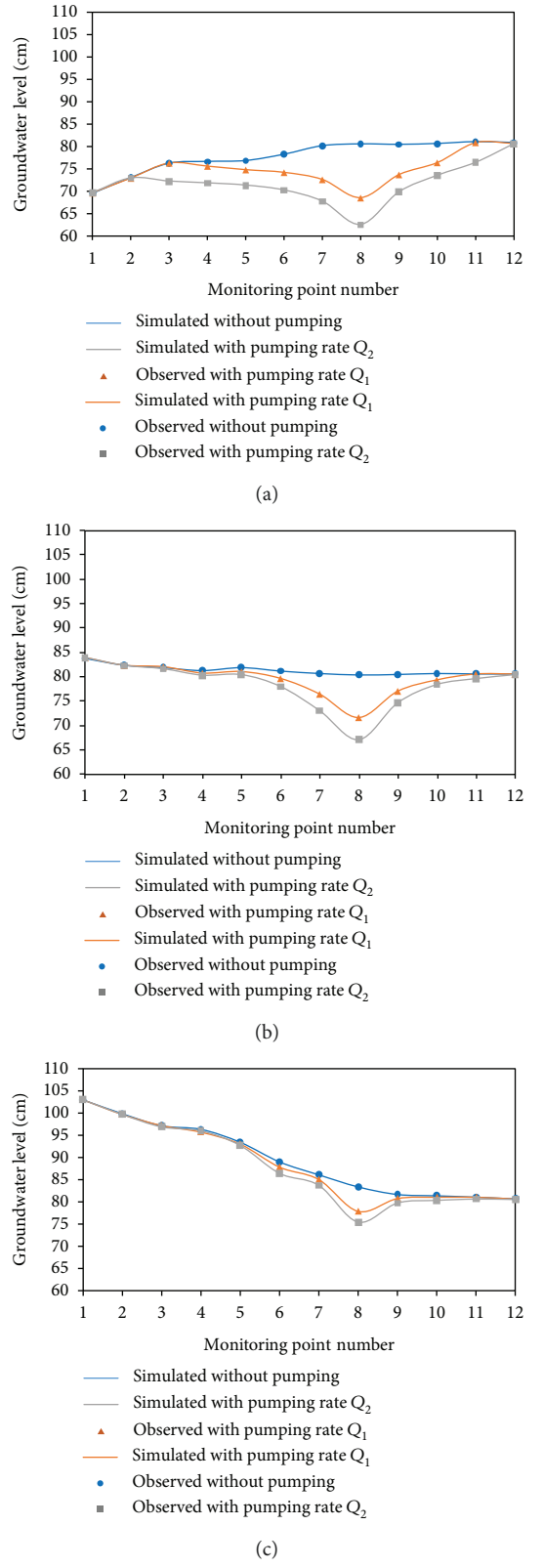

Figure 6: Observed (symbols) and simulated (solid lines) groundwater levels at the monitoring points for (a) low tide, (b) average sea level, and (c) high tide of Case 2.

Figure 7 reports the transient experimental saltwater wedges at different time intervals until the system reached a steady state condition for Case 1. From Figure 7, it can be seen that the interface between saltwater and freshwater is not clear at the initial stage of seawater intrusion (about 80 min). The curved shape of the seawater wedges in the fine sand layer and coarse sand layer is linear. As the extent of seawater intrusion increases, the saltwater wedge migrates inland, and the interface between seawater and freshwater becomes clear. The curved shape of the seawater wedge changes from linear to a concave parabolic curve. The steady state condition occurred within 480 min (12 tidal cycles) in both models for Case 1 under the influence of the tidal level. There is an obvious interface between the saltwater and freshwater. Then, in order to investigate the effect of pumping on the seawater intrusion, the groundwater in well No. 2 was pumped out with the pumping rate of Q_1 (1 L/min). The original equilibrium between the saltwater and freshwater was broken, and the saltwater wedge continued to move toward the land boundary until the secondary equilibrium was reached. Subsequently, the pumping rate in well No. 2 increases to Q_2 (2 L/min) from the time of 760 min, and the shape of the seawater wedge remains a concave parabolic curve, until a new steady state was reached. During the process of seawater intrusion, the angles of seawater wedge tip in the fine sand layer and the coarse sand layer decreases gradually with time. The results show that the mixing degree of seawater and freshwater in the aquifer is small, and the transition zone between seawater and freshwater is narrow.

Figure 8 presents the transient experimental seawater intrusion process at different time steps until the system reached a steady state condition for Case 2. Similar to Case 1, the interface between seawater and freshwater is not clear initially, and the curved shape of the seawater wedge is a straight line in the fine sand layer. As the tide fluctuates, the seawater wedge moves inland until it is stable, and the interface between seawater and freshwater becomes clear gradually. The shape of the seawater wedge changes from a straight line to a concave parabolic curve in the fine sand layer. The interface between seawater and freshwater is clear, which shows a shape of a concave parabolic curve in the coarse sand layer. The seawater intrusion in the unconfined aquifer and confined aquifer can reach a steady state at 500 min, which is relatively slower than that of Case 1. Then, in order to investigate the effects of pumping on the seawater intrusion, the groundwater in well No. 2 was pumped out with the pumping rate of Q_1 (1 L/min) from 500 min and Q_2 (2 L/min) from 840 min, respectively. During the pumping process, seawater intrudes toward inland continuously, and the shape of the seawater wedge still keeps a concave parabolic curve, until a new steady state was reached. The angles of seawater and freshwater interface tip in the fine sand layer, and the coarse sand layer decreases gradually. The widening of the seawater wedge for Case 2 was larger than that of Case 1. The reason is that the inland freshwater recharge is relatively small in Case 2 compared with that of Case 1.

4.4. Dynamics of Salt Wedge in the Multilayered Aquifers. Figure 9 shows the variation of salt wedge toe length and salt

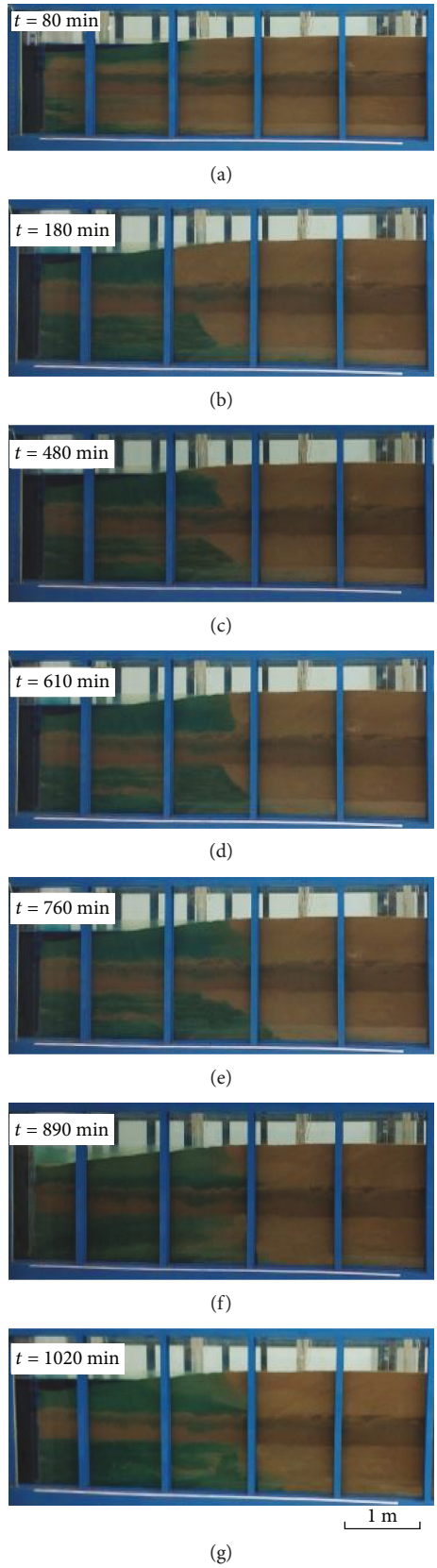

Figure 7: The experimental seawater intrusion process at different time steps: (a) 80 min, (b) 180 min, (c) 480 min, (d) 610 min, (e) 760 min, (f) 890 min, and (g) 1020 min for Case 1.

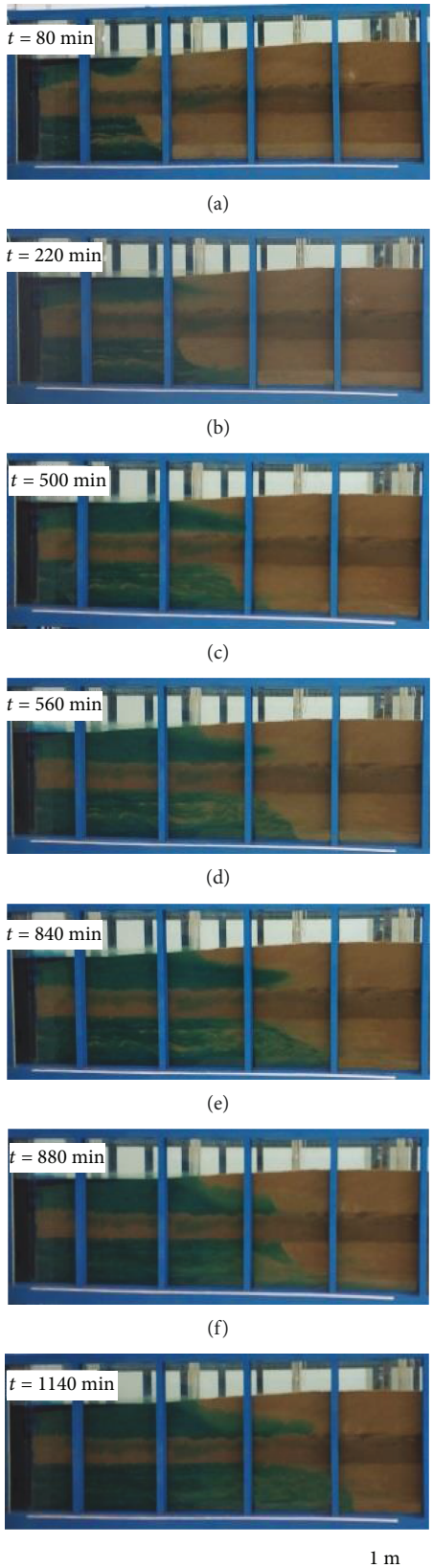

Figure 8: The experimental seawater intrusion process at different time steps: (a) 80 min, (b) 220 min, (c) 500 min, (d) 560 min, (e) 840 min, (f) 880 min, and (g) 1140 min for Case 2.

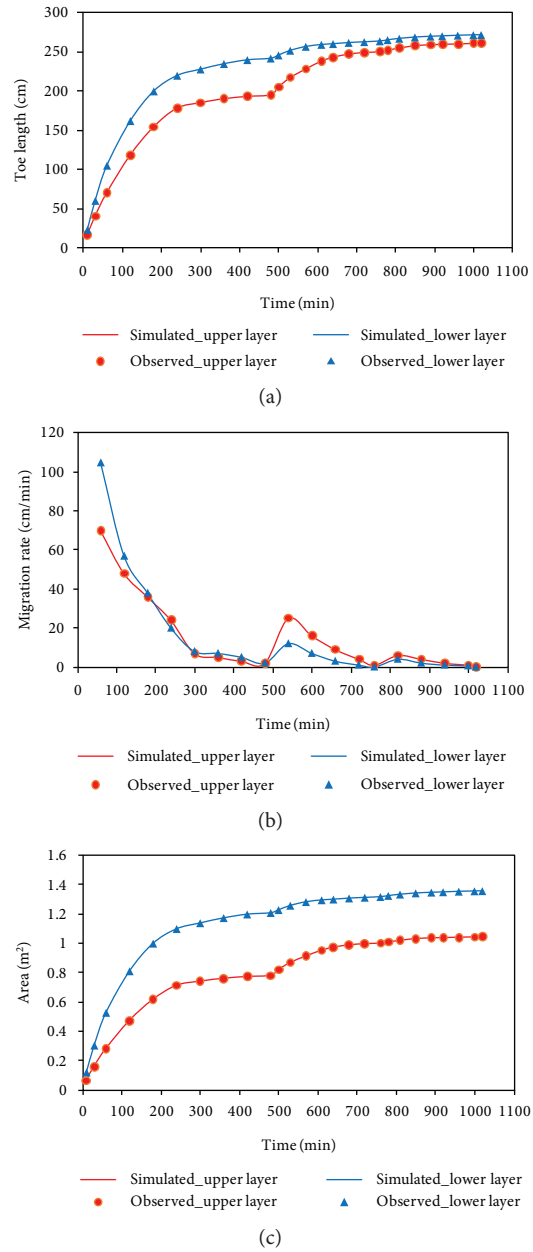

Figure 9: The variation of (a) salt wedge toe length, (b) salt wedge migration rate, and (c) salt wedge area with time in the unconfined aquifer and confined aquifer for Case 1.

wedge area with time in the unconfined aquifer and confined aquifer for Case 1. Generally, the numerical model can depict reasonably well the development of the seawater wedge variation observed in the physical experiment. Time-varying toe length of Case 1 in the fine sand layer and coarse sand layer is depicted in Figure 9(a). From Figure 9(a), one can see that the transient toe length increases with time initially and then tends to be a stable value under the condition of tidal fluctuation. When the seawater intrusion reached the steady state, the transient toe length of the upper fine sand layer is 195 cm and that of the coarse sand layer is 242 cm (Table 3). The salt wedge migration rate toward inland decreases with time dramatically initially, and then, it decreases slowly to zero

Table 3: The length and area of the seawater wedge in the steady state in each group of experiments.

Case	Average sea level (cm)	Freshwater level (cm)	Length of seawater wedge (cm)						Area of seawater wedge (m^2)					
			Without pumping		With the pumping rate of Q_1		With the pumping rate of Q_2		Without pumping		With the pumping rate of Q_1		With the pumping rate of Q_2	
			Fine sand layer	Coarse sand layer	Fine sand layer	Coarse sand layer	Fine sand layer	Coarse sand layer	Fine sand layer	Coarse sand layer	Fine sand layer	Coarse sand layer	Fine sand layer	Coarse sand layer
1	85	95	195	242	250	264	261	272	0.8	1.21	1.0	1.32	1.0	1.36
2	85	80	242	252	290	336	307	356	0.9	1.26	1.2	1.68	1.2	1.78

(Figure 9(b)). When the groundwater in well No. 2 was pumped with the rate of Q_1, the seawater further intrudes toward inland until a new steady state is reached. The transient toe length increases with time in the early state of pumping and then tends to be a stable value (Figure 9(a)). The intruding rate of seawater wedge increases with time and reaches a maximum value at the time of 540 min, and then, it decreases with time (Figure 9(b)). When the seawater intrusion reached the steady state, the transient toe length of the upper fine sand layer is 250 cm, and that of the coarse sand layer is 264 cm (Table 3). When the groundwater in well No. 2 increased to Q_2, the seawater further intrudes toward inland until a new steady state is reached. The transient toe length increases with time slightly until it is stable (Figure 9(a)). The salt wedge migration rate increases with time and reaches a maximum value at the time of 820 min, and then, it decreases to zero (Figure 9(b)). It indicates that the steady state of the seawater intrusion can be judged according to the migration rate of toe length. The maximum values of toe length are 261 cm in the upper fine sand layer and 272 cm in the lower coarse sand layer, respectively (Table 3). The toe length of the lower layer is larger than that of the upper layer, because the hydraulic conductivity of the lower layer is higher than that of the upper one. Figure 9(c) represents the time-varying curve of the seawater wedge area. Compared with Figure 9(a), one can see that the time varying of area is similar to that of length in the three stages. It indicates that the shape of the seawater wedge changes gradually during the process of seawater intrusion. The maximum area of seawater intrusion can reach 1.0 m^2 in the fine sand layer and 1.36 m^2 in the coarse sand layer, respectively.

Figure 10 presents the variation of toe length, migration rates, and area of the salt wedge with time in the unconfined aquifer and confined aquifer for Case 2. It shows that the numerical model predicted very well the inland motion of the saltwater wedge observed in the physical model. Similar to Figures 9(a) and 10(a) shows that the transient toe length increases with time initially and then tends to be a stable value under the condition of tidal fluctuation. The transient toe lengths of the steady state are 242 cm in the upper fine sand layer and 252 cm in the lower coarse sand layer, respectively (Table 3). Then, the transient toe length increases with time when the groundwater in well No. 2 was pumped with the rate of Q_1. When the seawater intrusion reached a new steady state, the transient toe length of the upper fine sand layer is 290 cm, and that of the coarse sand layer is 336 cm (Table 3). The transient toe length increases with time slightly until it is stable, when the groundwater in well No. 2 was increased to Q_2. Finally, the maximum values of toe length are 307 cm in the upper fine sand layer and 356 cm in the lower coarse sand layer, respectively (Table 3). The results show that substantially larger saltwater intrusion lengths have been observed and simulated in the unconfined aquifer and confined aquifer for Case 2 compared with those observed and simulated in Case 1. Figure 10(b) shows that the salt wedge migration rate toward inland decreases with time dramatically initially, and then, it decreases slowly to zero under the first stage. The seawater intruding rate increases with time under the condition of pumping and reaches a maximum value at the time of 560 min, and then, it decreases with time. Subsequently, it increases to be a maximum value at the time of 900 min, and then, it decreases to zero. Figure 10(b) also shows that the intruding migration rate in Case 2 was relatively larger than that in Case 1 in the three stages. This means that faster seaward motion of the seawater wedge would occur when the inland recharge is small in the coastal aquifers. Compared with Figure 10(a), from Figure 10(c), one can see that the time-varying curve of the area is similar to that of length in the three stages. The maximum area of seawater intrusion can reach 1.2 m^2 in the fine sand layer and 1.78 m^2 in the coarse sand layer, respectively, which are relatively larger than those in Case 1 during the process of seawater intrusion.

5. Discussions

5.1. Sensitivity Analysis. Different scenarios were investigated to assess the sensitivity of the seawater intrusion to the parameters' values. The above-discussed simulation is referred to as the "base case," taking the model of Case 1 as an example. The hydraulic conductivity and dispersivity are important parameters for seawater transport. Sensitivity analysis with respect to the hydraulic conductivity and dispersivity was conducted for the variation of the salt wedge. Only the values of the model parameter for sensitivity analysis were changed, and all the other parameters were fixed in each simulation.

In order to investigate the effect of hydraulic conductivity on the transport of salinity of seawater, the value of it for the unconfined aquifer and confined aquifer was changed from the base case. When the hydraulic conductivity K was increased from 4.3 m/d (base case) to 43 m/d for the fine sand, and from 38 m/d (base case) to 380 m/d for coarse sand,

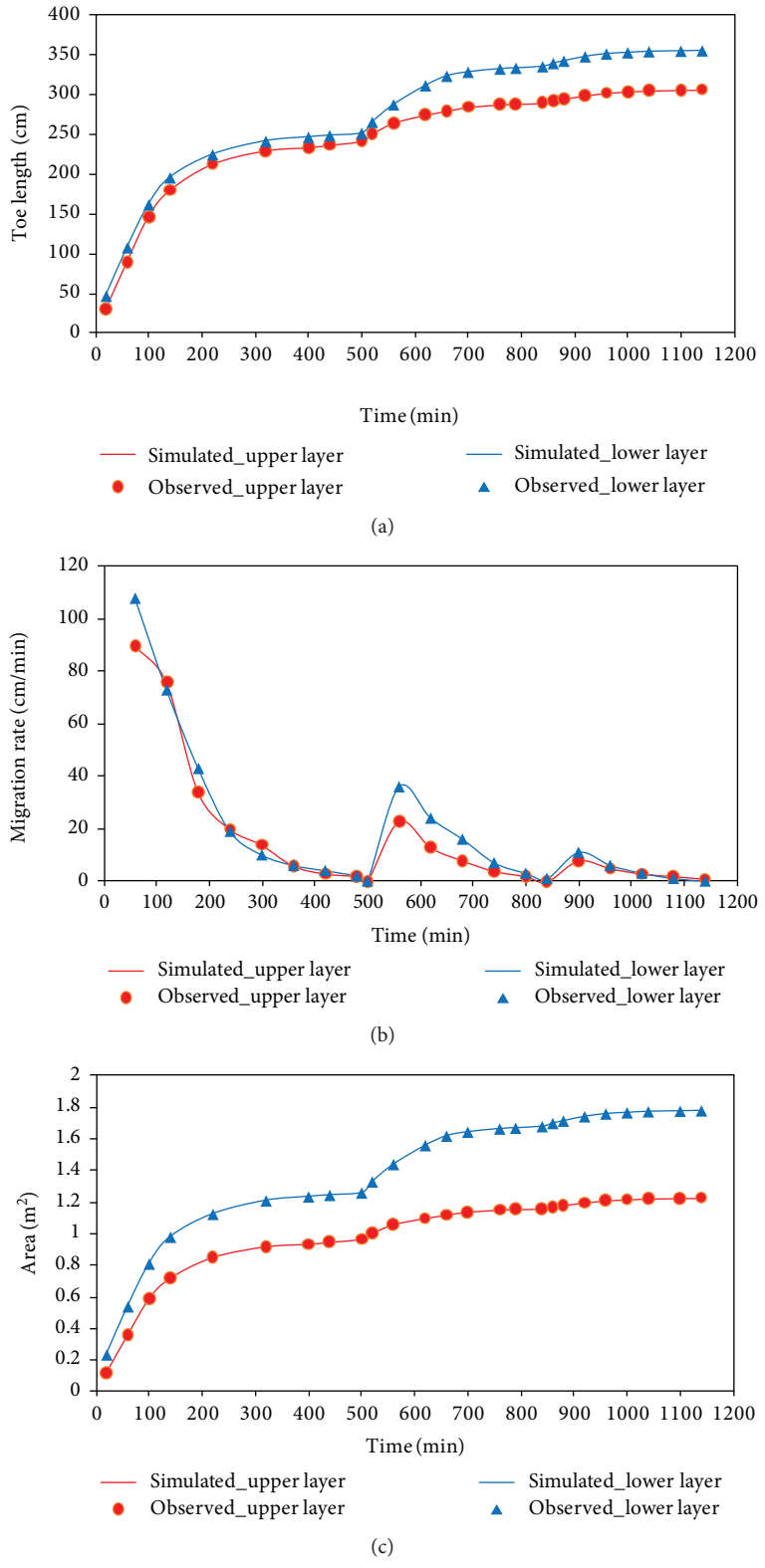

Figure 10: The variation of (a) salt wedge toe length, (b) salt wedge migration rate, and (c) salt wedge area with time in the unconfined aquifer and confined aquifer for Case 2.

the match to the observed toe length of seawater by the new model is worse than that of the base case (Figure 11(a)). The toe lengths simulated by the new model were consistently higher than the observed ones, but those of the base case were close to the observations in the upper and lower layers. The equilibrium time of the saltwater wedge of the new model is earlier than that of the basic model under the condition of tidal fluctuation and pumping. The intruding rate of the

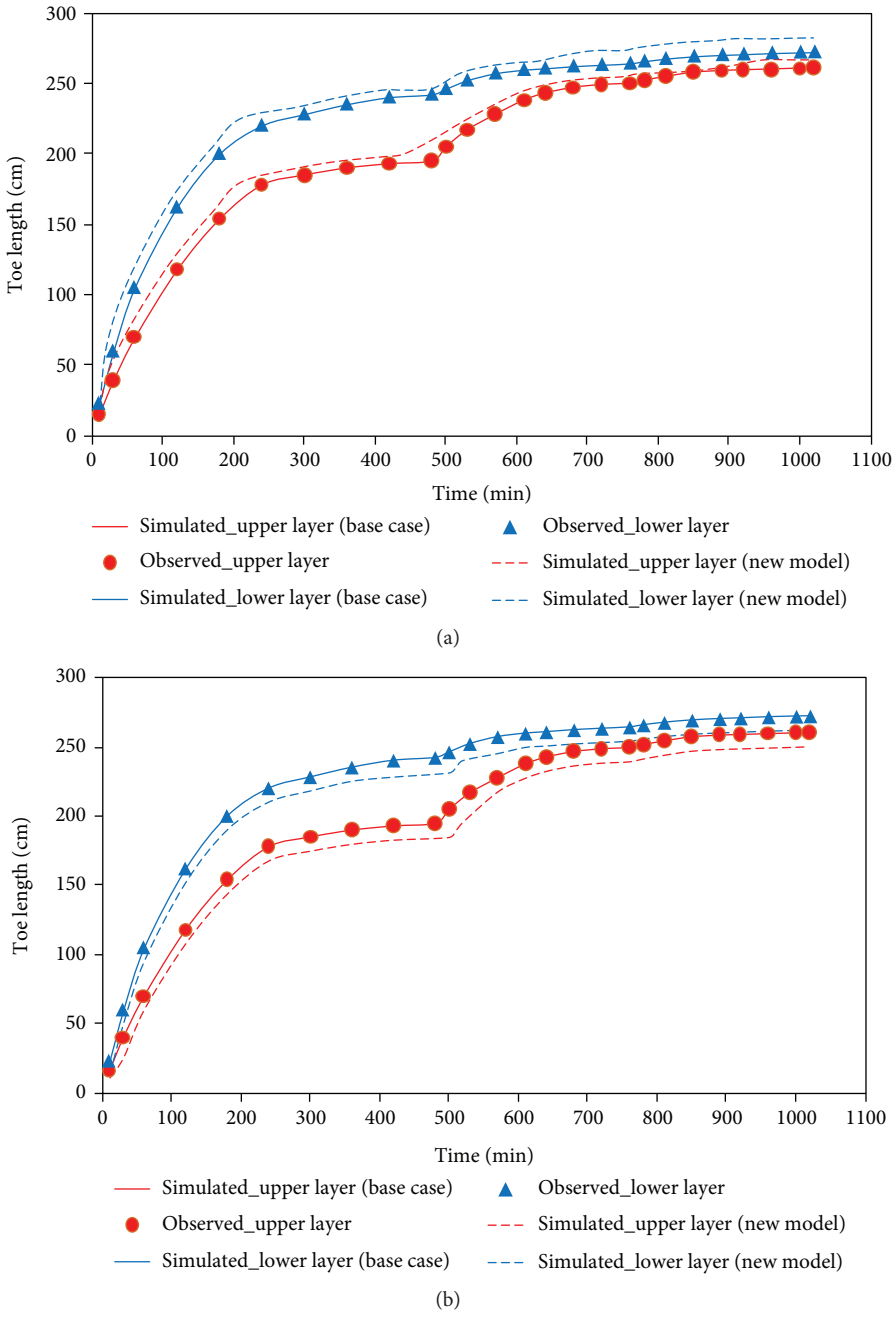

FIGURE 11: Impact of (a) increasing hydraulic conductivities and (b) decreasing hydraulic conductivities on toe lengths of seawater of the two layers.

seawater wedge in the new model is larger than that of the basic model. The results indicated that the hydraulic conductivities of the two layers are high, and a large quantity of seawater flowed into the aquifer. When the hydraulic conductivity K was decreased from 4.3 m/d (base case) to 0.43 m/d for the fine sand, and from 38 m/d (base case) to 3.8 m/d for coarse sand, the toe lengths of seawater simulated by the new model were obviously worse than those of the base case. From Figure 11(b), one can see that the arrival time of the steady state when decreasing the hydraulic conductivities of the two layers lagged behind that of the base case. Thus, one is led to conclude that the hydraulic conductivities of the two layers are too low, which are not able to reproduce the variation of the seawater wedge.

The sensitivity of toe length of seawater to dispersivity was explored to understand the contribution of dispersivity to salinization of the aquifer under pumping condition. In the simulations, the values of longitudinal dispersivity α_L and the ratio of transverse dispersivity to longitudinal dispersivity α_T/α_L were changed from the base case ($\alpha_L = 0.1$ m, $\alpha_T/\alpha_L = 0.05$). When the longitudinal dispersivity was increased to $\alpha_L = 0.5$ m (keeping the dispersivity ratio constant), the

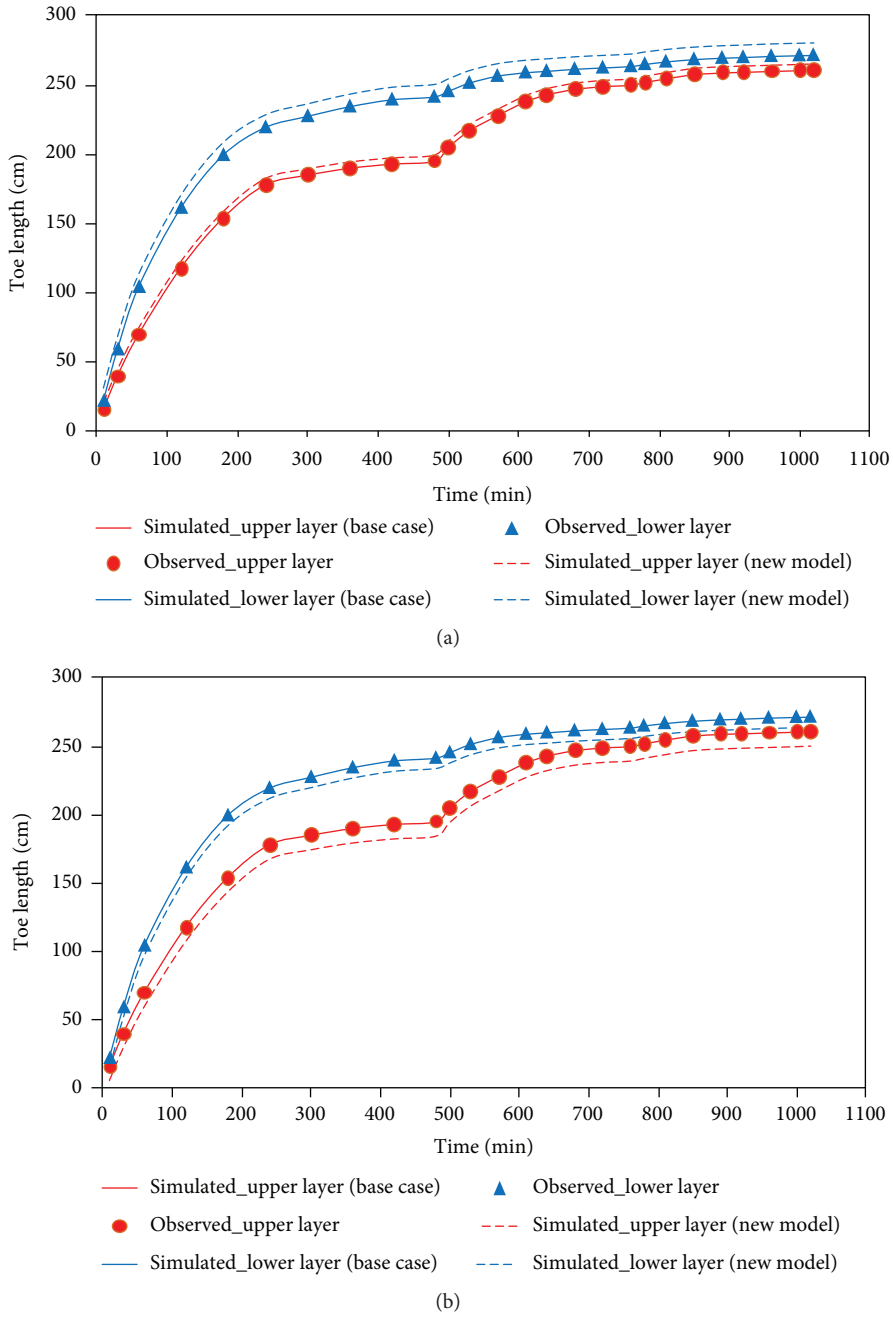

Figure 12: Impact of (a) increasing longitudinal dispersivity and (b) decreasing longitudinal dispersivity on toe lengths of seawater of the two layers.

match between the observed and simulated toe lengths became worse than those of the base model (Figure 12(a)). The toe lengths simulated by the new model were higher than those of the base model. However, the difference was not too large, suggesting that intermediate dispersivity values between the base model and new model would still be acceptable overall. When the longitudinal dispersivity was decreased to $\alpha_L = 0.05$ m, Figure 12(b) shows that the toe lengths simulated by the new model were lower than those of the base model. The results showed that changing the dispersivity has no effect on the arrival time of the steady state saltwater wedge.

5.2. Physical Mechanism. This study highlights the importance of the fluctuating sea level and inland recharge for pumping-induced groundwater salinization. The sea tide and inland freshwater recharge have impacts on the groundwater level and seawater intrusion process in the multilayered aquifers. The groundwater level has the characteristics of periodic fluctuation with the tide. The farther the position is from the sea, the smaller the fluctuation of the groundwater level is, which is similar to the results of previous studies [36, 49]. However, the groundwater level fluctuation is complex when considering the effect of pumping (e.g., [39, 42, 52, 53]). We should correct the drawdown data during the

pumping test, due to the groundwater level dynamics jointly induced by tidal forcing and groundwater pumping. In contrast to those previous studies, this study concentrates on the comprehensive effects of the fluctuating sea level and inland recharge on the pumping-induced groundwater level. The groundwater level variation in the unconfined aquifer and confined aquifer was simulated, considering different constant head inland boundaries, which represents the high and low groundwater levels in different seasons. We found that the inland freshwater recharge has main effect on the groundwater level fluctuating under the condition of low tide. The drawdown of the groundwater level decreases as the tide rises, which indicates that the rising tide has a negative effect on the drawdown of the groundwater level induced by pumping. However, the tide plays a major role compared with the inland freshwater recharge when the tide reaches maximum. Our results show that the seasonal variation of inland recharge should be considered to improve understanding of basic controls on groundwater level variation due to pumping.

In addition, we considered the variation of seawater intrusion with time in different layers. The heterogeneity of the aquifer has great effect on the seawater intrusion process (e.g., [9, 19, 41]). Our results also show that aquifer heterogeneity has an effect on salinity distributions in the fine sand layer and coarse sand layer, due to the different hydraulic conductivities in the two layers. However, there is less attention on the combined effects of the sea tide and inland recharge on pumping-induced groundwater salinization. Our results provide some insights into the toe length, migration rates, and area of seawater intrusion under the condition of tide fluctuation, groundwater pumping, and inland recharge. We found that the inland recharge in different seasons plays a major role in the seawater intrusion for the same pumping rate of groundwater. When the constant head of inland recharge is large, there is much more freshwater flowing into the aquifer, which makes the saltwater restored. When the constant head of inland recharge is small, the length and area of seawater intrusion in the aquifer are relatively large, because they are governed by the hydraulic gradient between the sea level and groundwater level. The analysis provides insights into how the tide fluctuation, groundwater pumping, and inland recharge effect on the area and rates of seawater intrusion. For future work, further efforts to do more changes of the boundary condition effects on seawater intrusion should be considered.

6. Conclusions

This study investigates the effects of a fluctuating sea level and inland recharge on pumping-induced groundwater salinization in coastal multilayered aquifers. A two-dimensional numerical model of variable density flow and solute transport is established. Using the laboratory experiments and numerical simulations, the fluctuation of the groundwater level and the process of seawater intrusion in the unconfined aquifer and confined aquifer were considered. The effects of aquifer heterogeneity, boundary condition, groundwater pumping, and tide on solute mixing of saltwater and freshwater are described. The main findings of the study are the following:

(1) The farther the monitoring point is from the left boundary, the smaller the fluctuation range of the groundwater level is. There is a lag time between the peak or valley of the tide and that of the groundwater level. The lag time of the groundwater level fluctuation in each monitoring point increases slightly with the increasing distance from the saltwater chamber

(2) In each simulation, the matches between the observed and calculated groundwater levels are well. The transient pumping can significantly enhance the amplitude of the groundwater level fluctuation. A further increment of the pumping rate caused faster drawdown of the groundwater level in the aquifer. For the low tide, the inland freshwater recharge has main effect on groundwater level fluctuation. The drawdown of the groundwater level at each point decreases as the tide rises, which indicates that the rising tide has a negative effect on the drawdown of the groundwater level induced by pumping. For the high tide, the groundwater level at the monitoring point is relatively higher when the head of inland recharge is large. It indicates that the tide plays a major role in the high tide, compared with the inland freshwater recharge

(3) The transient toe length increases with time initially and then tends to be a stable value under the condition of tidal fluctuation and pumping for different inland recharges. Larger saltwater intrusion lengths and area have been observed and simulated in the unconfined aquifer and confined aquifer for Case 2 compared with those observed and simulated in Case 1. The intruding migration rate in Case 2 was relatively larger than that in Case 1 in the three stages. This means that faster seaward motion of the seawater wedge would occur when the inland recharge is small in the coastal aquifers. There is much more freshwater flowing into the aquifer for Case 1, which makes the saltwater restored. When the constant head of inland recharge is small, the length and area of seawater intrusion in the aquifer are relatively large, which is governed by the hydraulic gradient between the sea level and groundwater level. It revealed that inland recharge plays a major role in the seawater intrusion for the same pumping rate of groundwater in different seasons

(4) The sensitivity analysis revealed that the estimated parameters of hydraulic conductivity and dispersivity are well determined. Increasing or decreasing the hydraulic conductivities of the two layers is not able to reproduce the variation of the seawater wedge. Changing the dispersivity has no effect on the arrival time of the steady state saltwater wedge. The analysis provides insights into how the tide fluctuation,

groundwater pumping, and inland recharge effect on the area and rates of seawater intrusion

Data Availability

The data used to support the findings of this study are available from the corresponding author upon request.

Conflicts of Interest

The authors declare that there are no conflicts of interest regarding the publication of this paper.

Authors' Contributions

Qiaona Guo and Zhifang Zhou conceived and designed the study; Jiangwei Huang analyzed the laboratory data; and Qiaona Guo wrote the paper with the assistance of Jinguo Wang.

Acknowledgments

This research was supported by the National Key R&D Program of China (No. 2016YFC0402803), the National Natural Science Foundation of China (No. 41772235), and the Fundamental Research Funds for the Central Universities (No. 2019B16814).

References

[1] A. Sefelnasr and M. Sherif, "Impacts of seawater rise on seawater intrusion in the Nile Delta aquifer, Egypt," *Ground Water*, vol. 52, no. 2, pp. 264–276, 2014.

[2] M. Sherif, A. Sefelnasr, and A. Javadi, "Incorporating the concept of equivalent freshwater head in successive horizontal simulations of seawater intrusion in the Nile Delta aquifer, Egypt," *Journal of Hydrology*, vol. 464-465, pp. 186–198, 2012.

[3] D. Jakovovic, A. D. Werner, P. G. B. de Louw, V. E. A. Post, and L. K. Morgan, "Saltwater upconing zone of influence," *Advances in Water Resources*, vol. 94, pp. 75–86, 2016.

[4] R. Moreno-González, S. Rodriguez-Mozaz, M. Gros, D. Barceló, and V. M. León, "Seasonal distribution of pharmaceuticals in marine water and sediment from a mediterranean coastal lagoon (SE Spain)," *Environmental Research*, vol. 138, pp. 326–344, 2015.

[5] J. Sreekanth and B. Datta, "Review: simulation-optimization models for the management and monitoring of coastal aquifers," *Hydrogeology Journal*, vol. 23, no. 6, pp. 1155–1166, 2015.

[6] A. D. Werner, M. Bakker, V. E. A. Post et al., "Seawater intrusion processes, investigation and management: recent advances and future challenges," *Advances in Water Resources*, vol. 51, pp. 3–26, 2013.

[7] Z. Xu and B. X. Hu, "Development of a discrete-continuum VDFST-CFP numerical model for simulating seawater intrusion to a coastal karst aquifer with a conduit system," *Water Resources Research*, vol. 53, no. 1, pp. 688–711, 2017.

[8] J. Yang, T. Graf, M. Herold, and T. Ptak, "Modelling the effects of tides and storm surges on coastal aquifers using a coupled surface–subsurface approach," *Journal of Contaminant Hydrology*, vol. 149, pp. 61–75, 2013.

[9] X. Yu and H. A. Michael, "Mechanisms, configuration typology, and vulnerability of pumping-induced seawater intrusion in heterogeneous aquifers," *Advances in Water Resources*, vol. 128, pp. 117–128, 2019.

[10] G. Ferguson and T. Gleeson, "Vulnerability of coastal aquifers to groundwater use and climate change," *Nature Climate Change*, vol. 2, no. 5, pp. 342–345, 2012.

[11] X. K. Zeng, J. C. Wu, D. Wang, and X. Zhu, "Assessing the pollution risk of a groundwater source field at western Laizhou Bay under seawater intrusion," *Environmental Research*, vol. 148, pp. 586–594, 2016.

[12] Y. Chang, B. X. Hu, Z. Xu et al., "Numerical simulation of seawater intrusion to coastal aquifers and brine water/freshwater interaction in south coast of Laizhou Bay, China," *Journal of Contaminant Hydrology*, vol. 215, pp. 1–10, 2018.

[13] H. Qi, C. Ma, Z. He, X. Hu, and L. Gao, "Lithium and its isotopes as tracers of groundwater salinization: a study in the southern coastal plain of Laizhou Bay, China," *Science of The Total Environment*, vol. 650, Part 1, pp. 878–890, 2019.

[14] X. K. Zeng, J. Dong, D. Wang et al., "Identifying key factors of the seawater intrusion model of Dagu river basin, Jiaozhou Bay," *Environmental Research*, vol. 165, pp. 425–430, 2018.

[15] J. Zhao, J. Lin, J. Wu, Y. Yang, and J. Wu, "Numerical modeling of seawater intrusion in Zhoushuizi district of Dalian City in northern China," *Environmental Earth Sciences*, vol. 75, no. 9, p. 805, 2016.

[16] Y. Q. Xue, J. C. Wu, C. H. Xie, and Y. X. Zhang, "Research of seawater and salt water intrusion of Laizhou Bay," *Chinese Science Bulletin*, vol. 11, no. 22, pp. 2360–2368, 1997.

[17] D. Han, C. Kohfahl, X. Song, G. Xiao, and J. Yang, "Geochemical and isotopic evidence for palaeo-seawater intrusion into the south coast aquifer of Laizhou Bay, China," *Applied Geochemistry*, vol. 26, no. 5, pp. 863–883, 2011.

[18] X. Sun, J. Xu, Q. Yang et al., "Character and prevention strategies of sea (saline) water invasion in the circum-Bohai-Sea region," *Geological survey and research*, vol. 29, pp. 203–211, 2006.

[19] C. Lu, Y. Chen, C. Zhang, and J. Luo, "Steady-state freshwater-seawater mixing zone in stratified coastal aquifers," *Journal of Hydrology*, vol. 505, pp. 24–34, 2013.

[20] C. Lu, P. Xin, J. Kong, L. Li, and J. Luo, "Analytical solutions of seawater intrusion in sloping confined and unconfined coastal aquifers," *Water Resources Research*, vol. 52, no. 9, pp. 6989–7004, 2016.

[21] C. Lu, W. Shi, P. Xin, J. Wu, and A. D. Werner, "Replenishing an unconfined coastal aquifer to control seawater intrusion: injection or infiltration?," *Water Resources Research*, vol. 53, no. 6, pp. 4775–4786, 2017.

[22] M. K. Nassar and T. R. Ginn, "Impact of numerical artifact of the forward model in the inverse solution of density-dependent flow problem," *Water Resources Research*, vol. 50, no. 8, pp. 6322–6338, 2014.

[23] W. Qu, H. Li, L. Wan, X. Wang, and X. Jiang, "Numerical simulations of steady-state salinity distribution and submarine groundwater discharges in homogeneous anisotropic coastal aquifers," *Advances in Water Resources*, vol. 74, pp. 318–328, 2014.

[24] Q. Shao, M. Fahs, H. Hoteit, J. Carrera, P. Ackerer, and A. Younes, "A 3-D semi-analytical solution for density-driven flow in porous media," *Water Resources Research*, vol. 54, no. 12, pp. 10,094–10,116, 2018.

[25] W. Shi, C. Lu, Y. Ye, J. Wu, L. Li, and J. Luo, "Assessment of the impact of sea-level rise on steady-state seawater intrusion in a layered coastal aquifer," *Journal of Hydrology*, vol. 563, pp. 851–862, 2018.

[26] C. Llopis-Albert and D. Pulido-Velazquez, "Discussion about the validity of sharp-interface models to deal with seawater intrusion in coastal aquifers," *Hydrological Processes*, vol. 28, no. 10, pp. 3642–3654, 2014.

[27] O. D. L. Strack, L. Stoeckl, K. Damm, G. Houben, B. K. Ausk, and W. J. de Lange, "Reduction of saltwater intrusion by modifying hydraulic conductivity," *Water Resources Research*, vol. 52, no. 9, pp. 6978–6988, 2016.

[28] M. M. Rajabi, B. Ataie-Ashtiani, and C. T. Simmons, "Polynomial chaos expansions for uncertainty propagation and moment independent sensitivity analysis of seawater intrusion simulations," *Journal of Hydrology*, vol. 520, no. 1, pp. 101–122, 2015.

[29] Z. Xu, Hu, B. X. Hu, and M. Ye, "Numerical modeling and sensitivity analysis of seawater intrusion in a heterogeneous coastal karst aquifer with conduits," *Hydrology and Earth System Sciences*, vol. 22, pp. 1–19, 2018.

[30] H. J. G. Diersch, *WASY Software-FEFLOW: Finite Element Subsurface Flow & Transport Simulation System. Reference Manual, WASY*, WASY Institue for Water Resources Planning and Systems Research Ltd, Berlin, 2002.

[31] C. I. Voss and A. M. Provost, "SUTRA, a model for saturated–unsaturated variable density ground-water flow with energy or solute transport," in *US Geological Survey*, pp. 2–4231, US Geological Survey Water-Resources Investigations Report, 2002.

[32] W. Guo and C. D. Langevin, "User's guide to SEAWAT: a computer program for simulation of three-dimensional variable-density groundwater flow," in *US Geological Survey*, pp. 1–434, US Geological Survey Water-Resources Investigations Report, 2002.

[33] C. D. Langevin, W. B. Shoemaker, and W. Guo, "MODFLOW-2000, the U.S. Geological Survey modular ground-water model: documentation of the SEAWAT-2000 version with variable density flow process (VDF) and the integrated MT3DMS transport process (IMT)," in *US Geological Survey*, pp. 3–426, US Geological Survey Water-Resources Investigations Report, 2003.

[34] Q. Guo, H. Li, M. C. Boufadel, Y. Xia, and G. Li, "Tide-induced groundwater head fluctuation in coastal multi-layered aquifer systems with a submarine outlet-capping," *Advances in Water Resources*, vol. 30, no. 8, pp. 1746–1755, 2007.

[35] Q. Guo, H. Li, M. C. Boufadel, and Y. Sharifi, "Hydrodynamics in a gravel beach and its impact on the *Exxon Valdez* oil," *Journal of Geophysical Research-Oceans*, vol. 115, no. C12, article C12077, 2010.

[36] E. Levanon, E. Shalev, Y. Yechieli, and H. Gvirtzman, "Fluctuations of fresh-saline water interface and of water table induced by sea tides in unconfined aquifers," *Advances in Water Resources*, vol. 96, pp. 34–42, 2016.

[37] E. Levanon, Y. Yechieli, H. Gvirtzman, and E. Shalev, "Tide-induced fluctuations of salinity and groundwater level in unconfined aquifers-field measurements and numerical model," *Journal of Hydrology*, vol. 551, pp. 665–675, 2017.

[38] H. Li and J. J. Jiao, "Tide-induced groundwater fluctuation in a coastal leaky confined aquifer system extending under the sea," *Water Resources Research*, vol. 37, no. 5, pp. 1165–1171, 2001.

[39] P. Zhou, X. Qiao, and X. Li, "Numerical modeling of the effects of pumping on tide-induced groundwater level fluctuation and on the accuracy of the aquifer's hydraulic parameters estimated via tidal method: a case study in Donghai Island, China," *Journal of Hydroinformatics*, vol. 19, no. 4, pp. 607–619, 2017.

[40] S. S. Mehdizadeh, F. Vafaie, and H. Abolghasemi, "Assessment of sharp-interface approach for saltwater intrusion prediction in an unconfined coastal aquifer exposed to pumping," *Environmental Earth Sciences*, vol. 73, no. 12, pp. 8345–8355, 2015.

[41] M. Siena and M. Riva, "Groundwater withdrawal in randomly heterogeneous coastal aquifers," *Hydrology and Earth System Sciences*, vol. 22, no. 5, pp. 2971–2985, 2018.

[42] C. Wang, H. Li, L. Wan, X. Wang, and X. Jiang, "Closed-form analytical solutions incorporating pumping and tidal effects in various coastal aquifer systems," *Advances in Water Resources*, vol. 69, pp. 1–12, 2014.

[43] C. Lu, Y. Chen, and J. Luo, "Boundary condition effects on maximum groundwater withdrawal in coastal aquifers," *Groundwater*, vol. 50, no. 3, pp. 386–393, 2012.

[44] C. Lu, P. Xin, L. Li, and J. Luo, "Seawater intrusion in response to sea-level rise in a coastal aquifer with a general-head inland boundary," *Journal of Hydrology*, vol. 522, pp. 135–140, 2015.

[45] K. Mazi, A. D. Koussis, and G. Destouni, "Tipping points for seawater intrusion in coastal aquifers under rising sea level," *Environmental Research Letters*, vol. 8, no. 1, article 014001, 2013.

[46] A. D. Werner and C. T. Simmons, "Impact of sea-level rise on sea water intrusion in coastal aquifers," *Groundwater*, vol. 47, no. 2, pp. 197–204, 2009.

[47] M. Bakker, "A Dupuit formulation for modeling seawater intrusion in regional aquifer systems," *Water Resources Research*, vol. 39, no. 5, article 1131, 2003.

[48] X. Li, B. X. Hu, W. C. Burnett, I. R. Santos, and J. P. Chanton, "Submarine ground water discharge driven by tidal pumping in a heterogeneous aquifer," *Ground Water*, vol. 47, no. 4, pp. 558–568, 2009.

[49] X. Mao, P. Enot, D. A. Barry, L. Li, A. Binley, and D. S. Jeng, "Tidal influence on behaviour of a coastal aquifer adjacent to a low-relief estuary," *Journal of Hydrology*, vol. 327, no. 1–2, pp. 110–127, 2006.

[50] D. Jakovovic, A. D. Werner, and C. T. Simmons, "Numerical modelling of saltwater up-coning: comparison with experimental laboratory observations," *Journal of Hydrology*, vol. 402, no. 3-4, pp. 261–273, 2011.

[51] S. S. Mehdizadeh, A. D. Werner, F. Vafaie, and S. Badaruddin, "Vertical leakage in sharp-interface seawater intrusion models of layered coastal aquifers," *Journal of Hydrology*, vol. 519, pp. 1097–1107, 2014.

[52] C. R. Beebe, G. Ferguson, T. Gleeson, L. K. Morgan, and A. D. Werner, "Application of an analytical solution as a screening tool for sea water intrusion," *Groundwater*, vol. 54, no. 5, pp. 709–718, 2016.

[53] C. Lu, P. Xin, L. Li, and J. Luo, "Steady state analytical solutions for pumping in a fully bounded rectangular aquifer," *Water Resources Research*, vol. 51, no. 10, pp. 8294–8302, 2015.

Hindawi
Geofluids
Volume 2019, Article ID 7191370, 11 pages
https://doi.org/10.1155/2019/7191370

Research Article

Physical and Numerical Modelling of Post-Pumping Seawater Intrusion

Leonard Stoeckl,[1] **Marc Walther**,[2,3] **and Leanne K. Morgan**[4,5]

[1]*Federal Institute for Geosciences and Natural Resources (BGR), Stilleweg 2, 30655 Hannover, Germany*
[2]*Helmholtz Centre for Environmental Research (UFZ), 04318 Leipzig, Germany*
[3]*Technische Universität Dresden, 01069 Dresden, Germany*
[4]*University of Canterbury, Christchurch 8140, New Zealand*
[5]*School of the Environment, Flinders University, Adelaide, SA 5001, Australia*

Correspondence should be addressed to Leonard Stoeckl; leonard.stoeckl@bgr.de

Received 14 February 2019; Revised 9 April 2019; Accepted 17 April 2019; Published 3 July 2019

Academic Editor: Nicoló Colombani

This paper explores post-pumping seawater intrusion (PP-SWI), which is the phenomenon of seawater intruding further inland than the location of a well, after pumping has ceased. Despite numerous papers on the topic of seawater intrusion and pumping, this is the first time that PP-SWI has been described in the literature, to our knowledge. This paper describes a laboratory-scale investigation of the phenomenon and we demonstrate that PP-SWI can be reproduced within physical experiments. We also show, using numerical modelling, that PP-SWI is caused by disequilibrium in the flow field following the cessation of pumping. Specifically, in our simulations, the cone of depression persisted after the cessation of pumping (first moving inland and then retreating toward the coastal boundary) which caused a lag in the reestablishment of fresh water flow toward the coast, after pumping had stopped. It was during this period of flow-field disequilibrium that PP-SWI occurred. We expect systems with larger postextraction disequilibrium to be most susceptible to PP-SWI and recommend future research to improve understanding of the relationship between hydrogeological parameters, extraction rates, well location, and incidence of PP-SWI. In those systems where PP-SWI is most likely, quantitative analysis of groundwater extraction and SWI will need to employ transient approaches to ensure that SWI is not underestimated.

1. Introduction

Coastal aquifers are major sources of freshwater supply in many countries [1–7]. Changes in the hydrology of the coastal zone, through groundwater pumping for example, can cause landward movement of seawater, a process referred to as seawater intrusion (SWI) [8]. SWI causes loss of water security in coastal aquifers through the displacement of fresh groundwater by seawater and through the degradation of groundwater quality whereby less than 1% of seawater (~250 mg/L chloride) renders freshwater unfit for drinking [9, 10].

SWI caused by groundwater pumping has received considerable attention over the years. In a recent review of the literature on field-based descriptions of well salinization and SWI, Houben and Post [11] noted the first systematic study to be that of Stephenson [12] who reported an increase in salt concentrations in water supply wells in Liverpool, England. This study predates by 50 years the famous paper of Herzberg [13], who described increasing salt concentrations in groundwater wells on the German tourist island of Norderney, following an unusually dry winter and spring. Herzberg [13] also described the relationship between freshwater and saltwater (i.e., the Ghyben-Herzberg approximation), which is fundamental to the quantitative modelling of SWI.

Despite the long history of studies detailing groundwater pumping and SWI, assessing the likelihood of groundwater withdrawals causing well salinization is still not straightforward. For example, the simulation of variable-density

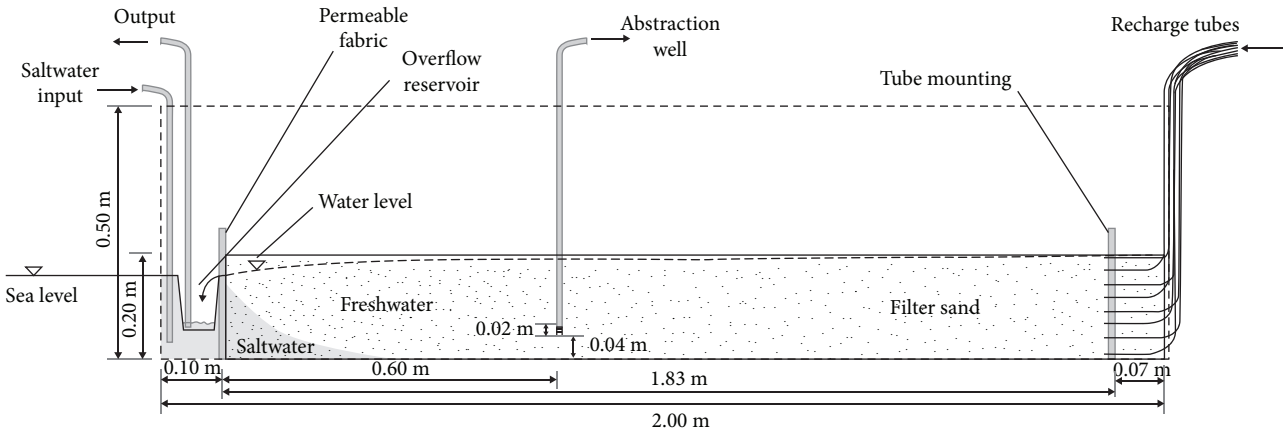

Figure 1: Schematic diagram of the physical model.

groundwater flow and solute transport in transient and heterogeneous coastal groundwater systems is computationally expensive, requires extensive field data for calibration, and is not always successful [14–16]. Data scarcity and faster computational times have meant that sharp interface analytic models are widely used to study SWI problems [e.g., 17, 18]. A well-known approach is that of Strack [19], who used potential theory to solve for the position of the freshwater-saltwater interface in regional groundwater flow systems with a pumping well. The solution also estimates the critical (i.e., maximum) pumping rate allowable before the well becomes salinized. The physics contained in analytical solutions and the simplicity of their application can provide a good balance between accounting for the relevant processes, data requirements, and calculation times [20, 21].

However, it is important to understand the implications of the simplifying assumptions underlying analytic solutions. One of the most important of these assumptions is that of steady-state conditions (i.e., the extent of seawater within the aquifer is estimated after infinite time). Research into SWI and sea-level rise (SLR) has shown that the steady-state assumption may lead to an underestimation of SWI impacts because of the so-called "seawater intrusion overshoot" phenomenon [22–26]. Seawater intrusion overshoot is the temporary movement of the saltwater-freshwater interface inland beyond the post-SLR steady-state position. Morgan et al. [25, 26] used physical and numerical modelling to show that the overshoot is physically reproducible and can occur within field-scale aquifers under realistic sea-level rise scenarios, as predicted by the Intergovernmental Panel on Climate Change [27]. Morgan et al. [26] found that the overshoot occurred during the period of flow-field disequilibrium (i.e., when the head and flow had not reached their post-SLR steady state) and was magnified when the disequilibrium was longer.

In this study, we consider a phenomenon that has not been described previously (to our knowledge) and that is likely also caused by flow-field disequilibrium, but in this case following the cessation of pumping. In a modelling study by Walther et al. [28] of the Oman coastal aquifer system (where groundwater has been intensively used for agricultural purposes for several decades under a semiarid climate conditions), scenario calculations showed that salinities in some of the wells did not immediately drop after pumping stopped. Rather, salinities in these wells increased for a certain amount of time (i.e., years to decades) suggesting that seawater continued to move landward beyond the pumping well location after the cessation of pumping. We term this phenomenon post-pumping seawater intrusion (PP-SWI) and hypothesize that disequilibrium in the flow field following pumping is causing the PP-SWI phenomenon.

In this study, we use a physical experiment in combination with numerical modelling to investigate the PP-SWI phenomenon in a systematic manner. Specifically, we aim to show that SWI does not necessarily stop immediately after the cessation of pumping in a coastal aquifer, and may penetrate further inland than the location of the pump after the cessation of pumping. Given this objective, laboratory conditions were designed to be especially conducive to PP-SWI. This included the use of a fixed-flux inland boundary condition, shown to increase flow-field disequilibrium in the seawater intrusion overshoot studies of Morgan et al. [25, 26]. Also, active seawater intrusion was instigated to enhance SWI within the study. This is because, under active SWI, the hydraulic gradient slopes from the ocean toward the well under pumping, as described previously by Badaruddin et al. [29] and Werner [30]. Unconfined conditions are considered because these types of aquifers are most commonly used for water supply purposes [22]. The present study neglects direct groundwater recharge from above, which is a valid assumption for arid regions, e.g., Arab countries and Australia.

2. Methods and Materials

2.1. Physical Model. An acrylic box of 2.0 m length, 0.5 m height, and 0.05 m width was used for physically simulating a cross section of an unconfined aquifer consisting of quartz sand (Figure 1). The apparatus used for physical modelling had essentially the same dimensions as that used by Stoeckl and Houben [31] and Strack et al. [18] in their investigation of freshwater lenses and saltwater intrusion. The box was homogeneously filled with quartz sand up to a height of

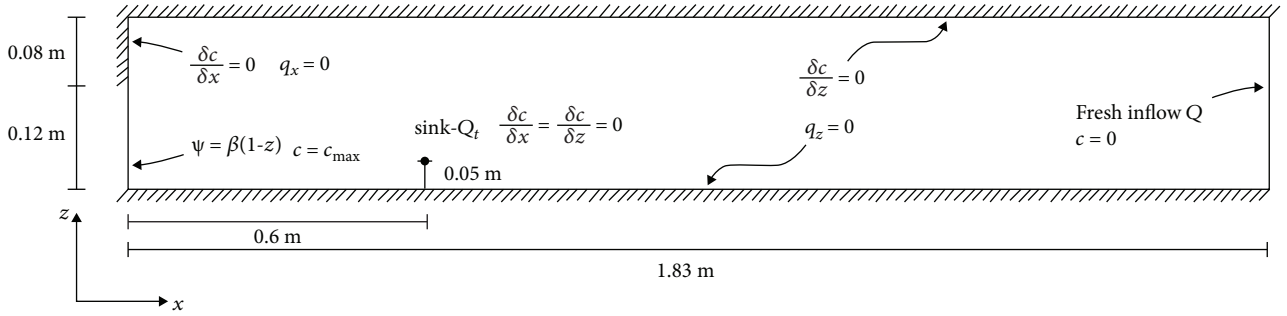

Figure 2: Conceptual model showing the boundary conditions used for numerical modelling.

0.2 m. Using a Camsizer® (Retsch Technology, Germany), with a measurement range of 30 μm to 30 mm, the grain size distribution of the filter sand ($d_{10} = 0.44$ mm and $d_{50} = 0.62$ mm) was optically determined. Applying Hazen's equation [32] on the grain size distribution, a hydraulic conductivity K(L/T) with a value of 2.2×10^{-3} m s^{-1} was determined. A mean K of 1.5×10^{-3} m s^{-1} was additionally obtained using Darcy's constant-head conductivity tests. Resulting intrinsic permeabilities are 2.0×10^{-10} m^2 and 1.4×10^{-10} m^2, respectively, considering a density of 996.9 kg m^{-3} and a viscosity of 0.00089 kg m^{-1} s^{-1}, for freshwater at 25°C [32]. Porosity n_e (-) was calculated by density measurements using a helium pycnometer (Micromeritics®, Germany) and was found to be 0.41. For visualization purposes, freshwater and saltwater were coloured using different tracer dyes, at a concentration of 0.3 g L^{-1}. Freshwater was coloured with uranine (yellow) and indigotine (blue) to distinguish flow paths, whereas saltwater was coloured with eosin (red). Dyed freshwater and saltwater densities were determined using a DMA 38 density meter (Anton Paar, Austria) and were found to be 996.9 kg m^{-3} (freshwater) and 1020.9 kg m^{-3} (saltwater) at 25 °C.

Sixteen tubes were attached to a peristaltic pump, creating a fixed-flux inland boundary condition. Tube outlets were equally spaced in the vertical direction below the water table on the right-hand edge of the acrylic box. The flow was distributed equally between the tubes, with a total flux of 0.086 m^3 d^{-1}, which was maintained throughout the entire experiment. A constant water level was maintained in the saltwater reservoir at the left side of the sand box, simulating the sea. A permeable fabric (Huesker Synthetic, Germany) with a mesh spacing of 0.45 mm was used to construct a vertical boundary, representing the coastline. According to the physical properties of the fabric, i.e., mesh spacing, no additional resistance in water flow is generated. Freshwater discharge from the aquifer into the "ocean" formed a thin layer in the saltwater reservoir, which was removed by an overflowing bucket at a tube's fixed position. The saltwater reservoir was continuously recharged with additional saltwater to maintain the water level and avoid dilution.

A tube with a 2 cm perforation at the base was placed 60 cm from the simulated coastline at a height of 4 cm above the aquifer base (i.e., the base of the sand tank), as shown in Figure 1. The tube was connected to another peristaltic pump such that water could be extracted and a well simulated in the physical model. Initially, constant boundary conditions were maintained for around 12 h to achieve a steady-state interface. Steady-state conditions were then confirmed by monitoring the interface position for a period of 1 h, over which time the interface remained stationary. The interface was visually approximated as the midpoint of the transition zone between freshwater and saltwater in the aquifer. Groundwater pumping was simulated by extracting water from the well at a constant rate of 1 m^3 d^{-1}. Water extraction was stopped just prior to the interface reaching the well, and the experiment continued until the interface returned to the original steady-state position. The entire experiment was filmed at an interval of one picture per second (Sony XDCAM EX) enabling detailed optical analyses of quantitative indicators described in Section 2.3.

2.2. Numerical Modelling. The physical experiment was simulated using the finite-element code FEFLOW 7.0, which considers variably saturated, density-dependent flow and solute transport processes [33] and is benchmarked for variable-density flow by Stoeckl et al. [34]. The numerical model was assumed to be a unit-width aquifer (2-D), and hence, the freshwater inflow at the inland boundary was scaled to $Q = 0.96$ m^3 d^{-1}.

The vertical coast was simulated using the Dirichlet boundary conditions for head and concentration (Figure 2). A constraint was applied to the Dirichlet-type concentration boundary such that seawater concentration ($C = 1$) occurred only where inflow occurs. The concentration of inflows through the inland boundary on the right-hand side was $C = 0$ (representing freshwater). Inflows at the inland boundary were applied using a Neumann boundary condition. As in Morgan et al. [25], a seepage face boundary condition was implemented in the numerical model along the vertical beach face. The seepage face boundary was implemented using a fixed-head boundary (with the head equal to the elevation of each node) that is only active if there is flow out of the model. Otherwise, the vertical beach face was a no-flow boundary above the seepage face. A mass sink term was implemented at one single node, i.e., 0.6 m inland from the coastal boundary and 0.05 m above ground, representing the center of the well screening in the physical model.

A combined quadrilateral-trapezoidal mesh with around 94,500 elements was used. The model grid was refined in the

area between the coastal boundary and the well to allow for more stable calculations. Grid discretization was $\Delta x \approx \Delta z \approx$ 2 mm, and for the refined area 1 mm. Automatic time stepping was used with an upper step size limit of 0.02 s.

The unsaturated zone was modelled using van Genuchten's [35] functions, with different curve fitting parameters for alpha (L^{-1}) and n (-). Initial values for K and n_e were taken from the physical experiment and varied during calibration, together with van Genuchten's [35] parameters. A density ratio δ (-) of 0.0241 was applied in accordance with the physical modelling values, defined as $\delta = (\rho_s - \rho_f)/\rho_f$, where ρ_f and ρ_s are freshwater and saltwater densities (mL^{-3}), respectively. Longitudinal and transverse dispersivities were set to 5×10^{-3} m and 5×10^{-4} m, respectively, and the molecular diffusion coefficient was set to 10^{-9} m^2 s^{-1}.

2.3. Quantitative Indicators. Several indicators were used to measure saltwater intrusion and retreat, as well as water level in the vicinity of the well. The wedge toe occurs at the point of intersection between the aquifer base and the freshwater-saltwater interface. The wedge toe length is defined as the distance between the vertical coastal boundary and the wedge toe. In the physical experiments, the interface was visually determined as the transition between the freshwater (yellow/blue in colour) and the saltwater (red in colour), as described above. In the numerical modelling, the interface was characterized as the 50% saltwater concentration isochlor.

The cone of depression was also used as a quantitative indicator. The cone of depression was visible as a grey-shaded area above the pump in the physical model, when pumping was enabled. For visualization purposes and for a comparison to numerical model results, a blue line was drawn onto the photographs by hand, indicating the location and extent of the cone of depression more clearly. In the numerical model, the cone of depression was visualized using a grey scale for moisture content between 0.25 (unsaturated) and 1 (fully saturated).

Freshwater flow paths were also used as indicators and were visualized by two different tracer dyes in the physical model. The changes in the flow paths were tracked over time and provided additional information relating to the transient response to pumping within the freshwater component of the aquifer. In the numerical model, velocity contours and vectors were used as indicators of flow direction for the freshwater and saltwater.

3. Results and Discussion

3.1. Physical Model. A steady-state equilibrium between saltwater and freshwater was initially established in the two-dimensional physical experiment, without pumping. At steady-state, the saltwater wedge toe length was 0.09 m due to the density contrast between freshwater and saltwater. This equilibrium condition can be seen in Figure 3(a) ($t = 0$ s). Under equilibrium conditions, flow paths can be seen to be roughly parallel to the aquifer base, except above the saltwater wedge where they are bent upwards, as expected.

The pump was switched on at time $t = 0$ s, and the saltwater wedge started to move inland (compare Figure 3(b), $t = 10$ s and Figure 3(c), $t = 60$ s). The pump was switched off at time $t = 135$ s, just before seawater entered the well. A valve stopped the water in the well from flowing back into the sand tank. After pumping had stopped, the saltwater continued moving inland until its wedge toe length reached a maximum value of 0.75 m at $t = 450$ s. That is, after the cessation of pumping, the saline interface continued to move inland beyond the pump location and at $t = 450$ s was 0.15 m further landward than the pump location. After the maximum wedge toe length was reached at $t = 450$ s, the wedge toe slowly started receding back to its original steady-state position, which was reached after around 5000 s.

Immediately after the pumping commenced (at $t = 0$ s), the yellow and blue freshwater flow paths bent toward the pumping well (see Figure 3(b), $t = 10$ s and Figure 3(c), $t = 60$ s), as expected. After pumping stopped (at $t = 135$ s), this zone of disturbed flow paths can be seen to move inland beyond the pumping well, indicating the inland movement of freshwater and saltwater. That is, freshwater as well as saltwater (within the saltwater wedge) was observed to move landward following the cessation of pumping. After around $t = 450$ s, the zone of disturbed freshwater flow paths was observed to start retreating back toward the coast.

A cone of depression was identified as a result of pumping, as expected. The position and extent were tracked over time in the video that was recorded during the experiment. In Figure 3, the position of the saturated-unsaturated interface was drawn in by hand for each of the selected time frames. The cone of depression started forming immediately after the pump was switched on and continuously extended vertically as well as horizontally until it almost reached the depth of the pump location at $t = 135$ s, at which time the pump was turned off. The pump did not take in air at any point in time, which confirms that the maximum depth of the cone of depression always remained above pump level. When the pump was switched off, the cone of depression immediately started to recover. As described previously for the zone of freshwater flow disturbance, the cone of depression moved landward after the cessation of pumping before retreating back toward the coast.

3.2. Numerical Model. The establishment of a stable simulation of the "small scale" sand tank experiment incorporating density driven flow, as well as unsaturated flow, was time consuming and difficult to achieve. The mesh was refined several times, especially in the region between the coast and the pump. The single pump location was eventually also redistributed to 10 different "well nodes," each abstracting $1/10^{th}$ of the total volume. Time steps had to be as low as 0.01 s to enable stability. In addition to the testing of grid resolution and time-stepping schemes, different solvers (e.g., pcg, pardiso, and samg) were tested and the samg solver showed the best performance and stability; it was subsequently used for the simulations. The calibration was done

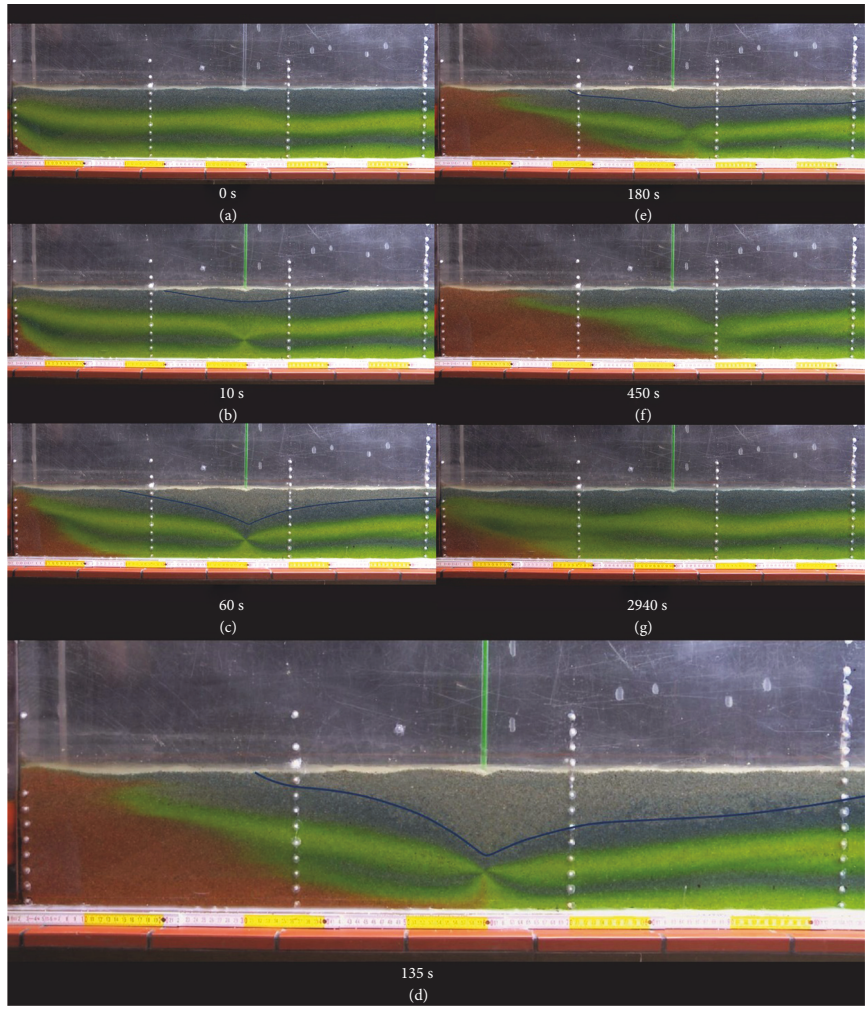

FIGURE 3: Excerpt view of the physical experiment (left-hand side and pump location) at seven different times (a-g) between $t = 0$ s and $t = 2940$ s. Red is saltwater, while yellow and blue colours indicate freshwater flow paths. The cone of depression is drawn by hand (blue line), interpreted from the unsaturated greyish area visible in the photographs.

manually, because the simulations had to be stopped and restarted to enable the switching on and off of the groundwater well for extraction (compare [22]). Every simulation was done in three steps: (a) achieving an initial steady state, (b) enabling groundwater extraction by implementing a well, and (c) disabling groundwater extraction by removing the well. The first and third phase took 5000 s each, whereas the second phase (where groundwater is being extracted) was set to 135 s, in line with the period of time that groundwater was extracted in the physical experiment.

During calibration of the numerical model, we tried to match several observations from the physical experiment:

(a) Steady-state wedge toe length of 0.09 m at $t = 0$ s

(b) Wedge toe length of 0.6 m (i.e., at the pump location) at $t = 135$ s

(c) Maximum wedge toe length of 0.75 m at $t = 450$ s

(d) A similar time (of 5000 s) for the wedge toe to return to the preextraction steady-state location

(e) A realistic saltwater wedge shape at all times that was comparable to the observations in the physical experiment

Parameters taken into account during the calibration process were K (varied between 2×10^{-3} m s^{-1} and 1×10^{-2} m s^{-1}), n_e (between 0.25 and 0.4), and van Genuchten's [35] parameters alpha (varied between 1.3 m^{-1} and 20 m^{-1}) and n (varied between 0.3 and 3). As the first two parameters were measured in the laboratory, they were varied over a smaller range than the latter two. It was observed that the variation of van Genuchten's [35] parameters had a strong influence on the temporal as well as the spatial evolution of the saltwater wedge.

Out of the approximately 150 different parameter combinations trialled, simulated wedge toe trends from a selection of 15 parameter combinations are shown in Figure 4. The toe length trend in all of these simulations reflect the typical behaviour of saltwater intruding due to pumping followed by recession due to the cessation of pumping, as observed in the physical experiment (black dots in Figure 4). However,

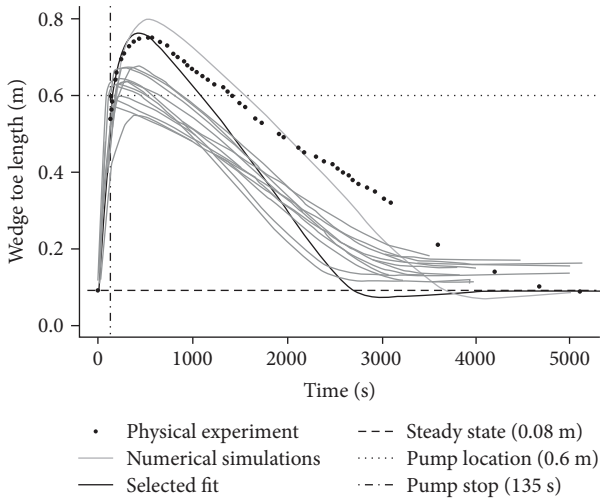

FIGURE 4: Calibration results of numerical simulations with different parameters (grey lines) and the selected fit (black line), compared to data of the physical experiment (black dots). The horizontal dashed line shows the steady-state intrusion length of 0.09 m without pumping, the horizontal dotted line shows the pump location at 0.6 m, and the vertical dash-dotted line indicates the time of pump stop after 135 s.

many parameter sets do not show a temporary continuation of saltwater intrusion after the cessation of pumping, some do not show an overall intrusion length further than the pump location at 0.6 m, and for some parameter combinations the initial and final steady-state wedge toe positions differ from those observed in the physical model (of 0.09 m). One parameter set with a porosity of 0.3, van Genuchten's [35] parameters alpha = 20 m^{-1} and $n = 2$, and K of 9×10^{-3} m s^{-1} was selected for detailed analysis (black line in Figure 4). This parameter set satisfied all but one of the previously mentioned criteria (a) to (e). The time for the saltwater wedge to return to its preextraction steady-state location was better met by using a porosity of 0.4 (compare a similar curve to the selected fit in Figure 4). However, this scenario deviates more from the observed maximum wedge toe length of 0.75 m at around $t = 450$ s. More importantly, a higher porosity leads to a quicker advance of the saltwater-freshwater interface during pumping and therefore to a significant intake of saltwater into the pump. This results in an awkward deformation of the saltwater wedge (not shown). Thus, the parameter set with the lower porosity of 0.3 was chosen to work with in the following model, even though the time of recession did not exactly match the observations in the physical experiment. The shorter recession times in the numerical model may have different causes: (a) hysteresis effects in the unsaturated zone may slow down the reequilibration process, as the drying process is faster than rewetting (the van Genuchten relationship of water suction capacity and water content in the numerical simulation does not account for hysteresis); (b) a significant portion of the sand tank is unsaturated at pump stop, thus certain pores may not have fully resaturated (due to entrapped air), which possibly leads to a reduced permeability and therefore retention in the backward movement of the saltwater-freshwater interface; and (c) the distribution of smaller and larger pores (double porosity) may additionally lead to a longer tailing (and blurring), as the coloured sea water is slowly released from the smaller pores. As the numerical model does not account for these effects, shorter times of recession are likely, compared to the physical experiment or even to real-world observations. For the interpretation of the results, however, the exact timing of the recession is less important than accurately simulating the interface movement to, beyond, and back to the pump location at 0.6 m, which is defined as PP-SWI here.

Interface location results for the selected fit simulation are shown in Figure 5. In addition to the 0.5 relative salinity contour, we also show the 0.1, 0.3, 0.7, and 0.9 relative saltwater contours as they provide information on the interface width. Between the commencement of pumping (at $t = 0$ s) and the cessation of pumping (at $t = 135$ s), the interface moved inland, as expected. At exactly $t = 135$ s, the 0.1 relative salinity contour reaches the well location, which was also the time when the pump was switched off in the physical experiment. The cone of depression (i.e., the white area above the pump) at this point is the largest. A widening of the interface was also observed and continued until a maximum wedge toe length of 0.76 cm was simulated at $t = 390$ s (compared to the physically measured time of $t = 450$ s). The wedge toe receded back to the initial steady-state position faster in the numerical modelling than was observed in the physical experiment, as noted above.

During the wedge toe recession phase of the simulation, the wedge toe was temporarily closer to the coast than the initial steady-state position. After the wedge toe reached its minimum length of around 0.07 m, it then proceeded inland to reach its final steady-state position at 0.09 m. This overshooting of the steady-state position is visible in the last two time frames in Figure 5, where it can be seen that the 0.5 relative saltwater contour is closer to the coast at $t = 2840$ s than at $t = 4500$ s. The overshoot is also evident in Figure 4, where the line of the "best fit" simulation drops below the prepumping steady-state wedge toe length of 0.09 m (indicated by a dashed line) and then returns to the steady-state position at around $t = 4500$ s. The wedge toe recession overshoot was not detected in the physical experiment, perhaps due to a blurring of the tracer dye and the small scale of the effect. The overshoot during the wedge toe recession (in response to a sea-level drop) was observed previously by Morgan et al. [25] using both physical and numerical modelling. As mentioned previously, the cause of the overshoot was shown by Morgan et al. [25, 26] to be disequilibrium between the hydraulic head and the saltwater interface as they both moved to a new steady state in response to a change in sea level. The overshoot observed in the current numerical modelling can also be attributed to this form of disequilibrium.

In Figure 5, grey shading is used to indicate the relative degree of saturation. Light grey-shaded areas at the top of the model indicate areas of lower saturation while black-shaded areas are saturated. It can be seen that at $t = 0$ s, there is a gradient in water saturation from right to left, which

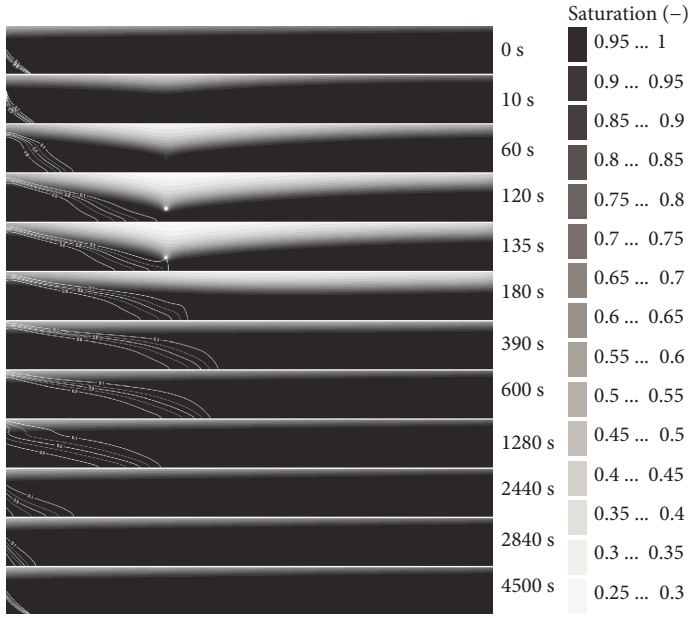

FIGURE 5: Selected time frames of the numerical simulation from $t_0 = 0$ s to $t_{end} = 4500$ s with relative concentration contours of 0.1, 0.3, 0.5, 0.7, and 0.9 in white. The different grey shadings indicate the relative degrees of saturation between 0.25 and 1.

conforms to the flow of freshwater from right to left within the model. At $t = 10$ s (i.e., 10 s after pumping has commenced) a cone of depression had already developed above the well location. The cone of depression is visible as an area of lower relative saturation and is slightly asymmetric, with lower saturation over a greater depth inland of the well, compared to the coastal side of the well. The cone of depression gets larger until the cessation of pumping at $t = 135$ s, after which time the cone of depression slowly recovers. The relative saturation contours (which also indicate the approximate water table location and hence hydraulic gradient, not accounting for density effects) show that the cone of depression is causing saltwater and freshwater to be pulled toward the well from the coastal and landward boundaries, respectively. A link between the cone of depression and the direction of the saltwater movement (i.e., intrusion versus retreat) was observed. After the cone of depression was "filled up" by both the intruding seawater from the coast boundary and the freshwater from the landward boundary, the wedge toe started to retreat (at $t = 390$ s). That is, the wedge toe began retreating once the cone of depression had recovered enough such that the hydraulic gradient and flow toward the coast in the vicinity of the saltwater wedge had reestablished, at $t = 390$ s. At $t = 4500$ s, the steady-state relative saturation condition was reestablished with a saturation gradient from the land toward the ocean.

In Figure 6, Darcy flow velocities are visualized as black contours of 0.1, 0.5, 1, 2, 5, 10, and 20 m/s. At steady state, flow directions are generally horizontal from right to left. Freshwater is only diverted upward above the saltwater wedge circulation cell, as previously observed in various studies [34, 36, 37]. As pumping commences, the saltwater wedge starts intruding inland and flow velocity vectors are directed toward the pump (not shown here). Flow velocity contours in general stay parallel until pumping is stopped at $t = 135$ s (compare Figure 5). After $t = 135$ s, semicircular flow velocity contours start to develop at the bottom of the model, to the right of the well location. These are contours of low flow velocities and they indicate a singularity, where flow from the right and left sides merge and get directed upward. An excerpt view of the singularity (from Figure 6, time frame $t = 180$ s) is shown in Figure 7 with additional flow vectors as black arrows. The full height of the numerical model is displayed, a scale in the upper-left corner shows the exact dimensions. Flow at the bottom of the model merges at the singularity from both sides where velocities are lowest (semicircular contours), and is directed vertically upward to fill the cone of depression above the singularity.

The singularity (and cone of depression above it) moved inland first (Figure 6, $t = 140$ s to $t = 245$ s), before receding back toward the pump location (Figure 6, $t = 245$ s to $t = 390$ s). As the semicircular contours surrounding the singularity reach the position of the intruding saltwater wedge at $t = 390$ s, they dissolve and form parallel lines again, until the initial condition is reached for both the concentration and Darcy velocity contours.

The singularity (and cone of depression) moved in and out of the aquifer faster than the saltwater wedge (Figure 6). We hypothesize that the occurrence and duration of this singularity dictate the extent to which seawater will continue to intrude after the cessation of pumping. Future studies are needed to investigate this further and to explore the influence of hydraulic parameters on the dynamics of the singularity. We expect that it will not be easy to draw direct linear relationships between single parameters and the extent of PP-SWI. It is rather expected that a local maximum for each parameter (or combination of parameters) exists, where the occurrence of the PP-SWI phenomenon is greatest. For

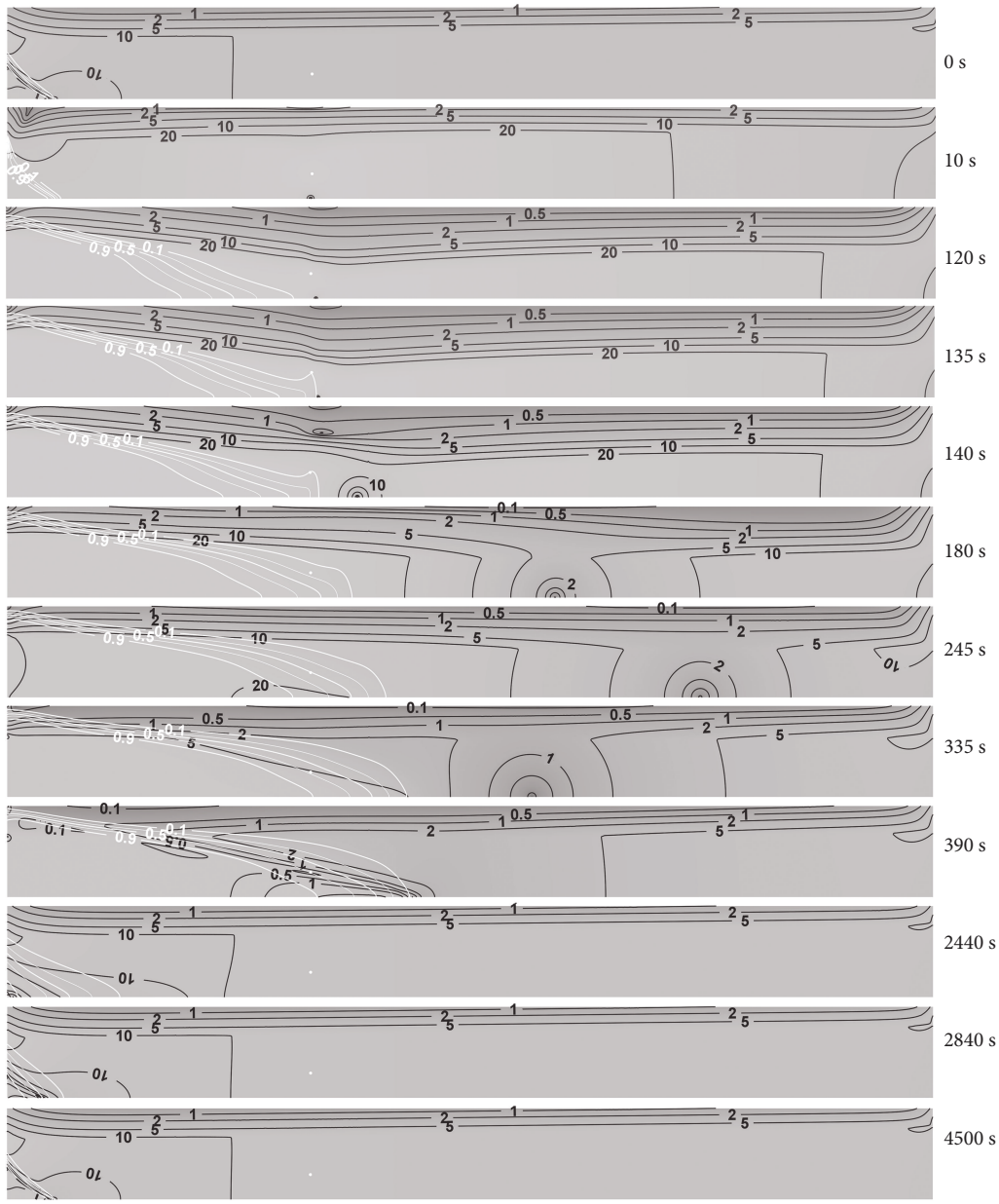

Figure 6: Selected time frames of the numerical simulation from $t = 0$ s to $t = 4500$ s. White lines are relative concentration contours of 0.1, 0.3, 0.5, 0.7, and 0.9, and black lines are Darcy flow velocity contours of 0.1, 0.5, 1, 2, 5, 10, and 20 m/s. The small white dot shows the well location at $x = 0.6$ m and $y = 0.05$ m in every frame.

example, when hydraulic conductivity is low, seawater intrusion will be slower and hence the likelihood of the PP-SWI phenomenon will be lower; however, if hydraulic conductivity is high, the cone of depression will develop more slowly and this might also reduce the likelihood of the PP-SWI phenomenon. We also expect that pump distance from the coast and extraction rate will influence the extent of PP-SWI in a nonlinear manner.

The upscaling of our findings to field-scale cases is not straight forward, as inherent difficulties in scaling sand box models exist [38]. Further discrepancies in transferring our findings to real-world cases result from neglecting, e.g., heterogeneity in the subsurface, direct groundwater recharge from above, or variable pump schemes in the sand tank experiment. The finding that PP-SWI is physically based, however, may be transferred from the two-dimensional setting used in the present study into the third dimension by considering a coastline, where pumping wells (e.g., well fields) are located a certain distance along the coastline and groundwater flow can be considered perpendicular to the coast. It is assumed that PP-SWI occurs at a field scale on much larger time scales. Here too, larger areas will be salinized that would be the case without PP-SWI, potentially threatening inland ecosystems and fresh groundwater resources.

PP-SWI might also be expected in certain cases where countermeasures are taken, for example, where pump rates are reduced (but not ceased), as well as when seawater has not reached the well but is still moving toward it. This is

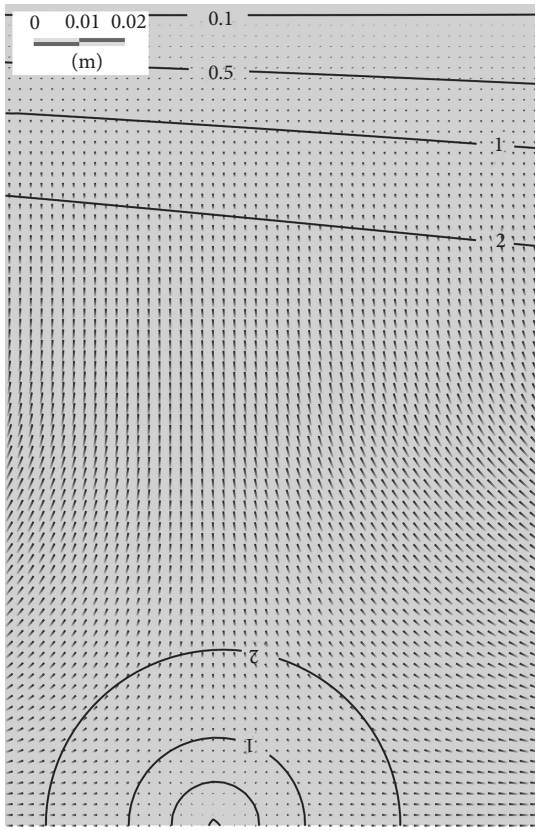

Figure 7: Excerpt view of Figure 6, at $t = 180$ s. Additional flow velocity vectors are shown for each node (small black arrows), next to black Darcy velocity contours of 0.1, 0.5, 1, and 2 m/s.

expected for cases where pump rates are not sustainable and groundwater tables are strongly lowered due to overexploitation over several decades, resulting in a large regional cone of depression in close vicinity to the coast. Times for filling up such a deficit water volume depend on recharge rates, as well as aquifer geometries. It can be stated, though, that the longer the time for reestablishing water tables and gradients from the land toward the sea, the longer SWI will take place and the more pronounced PP-SWI is expected to be. A proper analysis of field-scale cases is beyond the scope of this paper, which is about the mechanistic understanding of the PP-SWI phenomenon that was previously observed in the numerical model simulation of a coastal aquifer in Oman [28].

4. Conclusions

The physical experiment conducted here highlights the PP-SWI phenomenon, whereby seawater intrudes further inland than the location of a well, after pumping has ceased. A numerical model with the same extent as the physical model was calibrated and showed a very similar behaviour with minor differences in the overall time duration of the phenomenon. The calibration was considered adequate with a parameter set which satisfied four out of five predefined criteria: the steady-state wedge toe length without pumping, the time for the wedge toe to reach the well location after pumping had commenced, the maximum wedge toe length, and the shape of the wedge. The only predefined criteria that was poorly met was the timing of saltwater retreat.

The modelling carried out within this study offers insight into the cause of the PP-SWI phenomenon, at least for the conditions used in this study (i.e., active SWI and a fixed-flux inland boundary). In both the physical and numerical models, the driving force for the PP-SWI phenomenon was identified to be the presence, duration, and movement of the cone of depression. As a result of pumping, water entered the model from both sides, from the coastal boundary as seawater and from the inland boundary as freshwater, to fill up the "deficit volume" of the cone of depression. Under pumping, the new steady-state position of the saltwater wedge occurred at the pump and did not intrude further inland because the pumping well is the point where all waters merge. When the pump was turned off, the cone of depression moved inland (as did the singularity beneath the cone of depression), which caused water to flow from the coast and inland in order to fill the cone of depression. As a result, the saltwater wedge continued to move landward after the cessation of pumping until the cone of depression had recovered enough that a hydraulic gradient (and fresh water flow) toward the coast had reestablished. As such, it has been demonstrated that the PP-SWI phenomenon is caused by pumping-induced transience in the hydraulic gradient between the land and the ocean. The transience of the hydraulic gradient is linked to the dynamics of the cone of depression (and the associated flow singularity) following the cessation of pumping.

The PP-SWI phenomenon has not, to the best of our knowledge, been mentioned previously in the literature, except for the Oman case [28]. The observation of seawater intruding further inland than the location of an abandoned well field led us to investigate the possibility of the physical occurrence of PP-SWI and its driving mechanism. In this study, we have shown PP-SWI to be a physically reproducible phenomenon. It has important implications for coastal groundwater aquifers all around the world and shows that seawater intrusion induced by pumping (a) may not immediately stop or recede when pumping is ceased, (b) may significantly extend further inland than the actual position of a previously active pump or well field, and (c) may have a direct impact on the time scales for remediating salinized wells. This means that not only will there be salinization of much greater areas of coastal aquifers, but the times for sea water to retreat will also be much longer than expected. In (semi-)arid areas with limited groundwater recharge, such as in Arab countries, in Australia, or in other coastal areas of Africa and South America, SWI associated with groundwater pumping may have been underestimated if transient processes were not accounted for. SWI induced by freshwater abstraction from coastal aquifers is not limited to the time period of pumping, but rather extends beyond it, depending on pumping rates and locations, and aquifer characteristics, e.g., hydraulic conductivity and porosity, length-to-height relationship of an aquifer, density contrast between freshwater and saltwater, and recharge condition. It is thus important

to foster research of transient dynamics in groundwater systems rather than to assume steady-state solutions, especially when investigating the effects of groundwater abstraction in coastal aquifers.

Data Availability

Measurement data of the saltwater-freshwater interface were generated by the experimental work and are documented in the manuscript.

Conflicts of Interest

The authors declare that they have no conflicts of interest.

Acknowledgments

The authors thank Katrin Damm for helping with the physical experiments. Leanne Morgan is partly supported by Environment Canterbury, New Zealand (https://www.ecan.govt.nz/).

References

[1] P. M. Barlow and E. G. Reichard, "Saltwater intrusion in coastal regions of North America," *Hydrogeology Journal*, vol. 18, no. 1, pp. 247–260, 2010.

[2] E. Bocanegra, G. C. Da Silva, E. Custodio, M. Manzano, and S. Montenegro, "State of knowledge of coastal aquifer management in South America," *Hydrogeology Journal*, vol. 18, no. 1, pp. 261–267, 2010.

[3] E. Custodio, "Coastal aquifers of Europe: an overview," *Hydrogeology Journal*, vol. 18, no. 1, pp. 269–280, 2010.

[4] G. Steyl and I. Dennis, "Review of coastal-area aquifers in Africa," *Hydrogeology Journal*, vol. 18, no. 1, pp. 217–225, 2010.

[5] G. Ferguson and T. Gleeson, "Vulnerability of coastal aquifers to groundwater use and climate change," *Nature Climate Change*, vol. 2, no. 5, pp. 342–345, 2012.

[6] L. K. Morgan and A. D. Werner, "A national inventory of seawater intrusion vulnerability for Australia," *Journal of Hydrology: Regional Studies*, vol. 4, pp. 686–698, 2015.

[7] H. A. Michael, V. E. A. Post, A. M. Wilson, and A. D. Werner, "Science, society, and the coastal groundwater squeeze," *Water Resources Research*, vol. 53, no. 4, pp. 2610–2617, 2017.

[8] J. Bear, *Hydraulics of Groundwater*, McGraw-Hill, New York, 1979.

[9] WHO, Ed., "Water sanitation hygiene," in *Guidelines for Drinking-Water Quality*, p. 564, World Health Organization, 4th edition, 2011.

[10] A. D. Werner, M. Bakker, V. E. A. Post et al., "Seawater intrusion processes, investigation and management: recent advances and future challenges," *Advances in Water Resources*, vol. 51, pp. 3–26, 2013.

[11] G. Houben and V. E. A. Post, "The first field-based descriptions of pumping-induced saltwater intrusion and upconing," *Hydrogeology Journal*, vol. 25, no. 1, pp. 243–247, 2017.

[12] R. Stephenson, *On the Supply of Water to the Town of Liverpool*, Bradbury and Evans, London, 1850, 89 pp.

[13] A. Herzberg, "Die Wasserversorgung einiger Nordseebäder," *J Gasbeleuchtung Wasserversorgung*, vol. 44, pp. 842–844, 1901.

[14] W. E. Sanford and J. P. Pope, "Current challenges using models to forecast seawater intrusion: lessons from the eastern shore of Virginia USA," *Hydrogeology Journal*, vol. 18, no. 1, pp. 73–93, 2010.

[15] M. Walther, J.-O. Delfs, J. Grundmann, O. Kolditz, and R. Liedl, "Saltwater intrusion modeling: verification and application to an agricultural coastal arid region in Oman," *Journal of Computational and Applied Mathematics*, vol. 236, no. 18, pp. 4798–4809, 2012.

[16] F. Magri, N. Inbar, C. Siebert, E. Rosenthal, J. Guttman, and P. Möller, "Transient simulations of large-scale hydrogeological processes causing temperature and salinity anomalies in the Tiberias Basin," *Journal of Hydrology*, vol. 520, pp. 342–355, 2015.

[17] H. Ketabchi and B. Ataie-Ashtiani, "Review: coastal groundwater optimization—advances, challenges, and practical solutions," *Hydrogeology Journal*, vol. 23, no. 6, pp. 1129–1154, 2015.

[18] O. D. L. Strack, L. Stoeckl, K. Damm, G. Houben, B. K. Ausk, and W. J. de Lange, "Reduction of saltwater intrusion by modifying hydraulic conductivity," *Water Resources Research*, vol. 52, no. 9, pp. 6978–6988, 2016.

[19] O. D. L. Strack, "A single-potential solution for regional interface problems in coastal aquifers," *Water Resources Research*, vol. 12, no. 6, pp. 1165–1174, 1976.

[20] A. D. Werner, J. D. Ward, L. K. Morgan, C. T. Simmons, N. I. Robinson, and M. D. Teubner, "Vulnerability indicators of sea water intrusion," *Ground Water*, vol. 50, no. 1, pp. 48–58, 2012.

[21] L. K. Morgan and A. D. Werner, "Seawater intrusion vulnerability indicators for freshwater lenses in strip islands," *Journal of Hydrology*, vol. 508, pp. 322–327, 2014.

[22] T. A. Watson, A. D. Werner, and C. T. Simmons, "Transience of seawater intrusion in response to sea level rise," *Water Resources Research*, vol. 46, no. 12, 2010.

[23] S. W. Chang, T. P. Clement, M. J. Simpson, and K. K. Lee, "Does sea-level rise have an impact on saltwater intrusion?," *Advances in Water Resources*, vol. 34, no. 10, pp. 1283–1291, 2011.

[24] S. W. Chang and T. P. Clement, "Experimental and numerical investigation of saltwater intrusion dynamics in flux-controlled groundwater systems," *Water Resources Research*, vol. 48, no. 9, 2012.

[25] L. K. Morgan, L. Stoeckl, A. D. Werner, and V. E. A. Post, "An assessment of seawater intrusion overshoot using physical and numerical modeling," *Water Resources Research*, vol. 49, no. 10, pp. 6522–6526, 2013.

[26] L. K. Morgan, M. Bakker, and A. D. Werner, "Occurrence of seawater intrusion overshoot," *Water Resources Research*, vol. 51, no. 4, pp. 1989–1999, 2015.

[27] IPCC, "Summary for policymakers," in *Climate Change 2013: The Physical Science Basis. Contribution of Working Group I to the Fifth Assessment Report of the Intergovernmental Panel on Climate Change*, T. F. Stocker, D. Qin, G.-K. Plattner, M. Tignor, S. K. Allen, J. Boschung, A. Nauels, Y. Xia, V. Bex, and P. M. Midgley, Eds., Cambridge University Press, Cambridge, United Kingdom and New York, NY, USA, 2013.

[28] M. Walther, L. Bilke, J.-O. Delfs et al., "Assessing the saltwater remediation potential of a three-dimensional, heterogeneous, coastal aquifer system," *Environmental Earth Sciences*, vol. 72, no. 10, pp. 3827–3837, 2014.

[29] S. Badaruddin, A. D. Werner, and L. K. Morgan, "Water table salinization due to seawater intrusion," *Water Resources Research*, vol. 51, no. 10, pp. 8397–8408, 2015.

[30] A. D. Werner, "On the classification of seawater intrusion," *Journal of Hydrology*, vol. 551, pp. 619–631, 2017.

[31] L. Stoeckl and G. Houben, "Flow dynamics and age stratification of freshwater lenses: experiments and modeling," *Journal of Hydrology*, vol. 458-459, pp. 9–15, 2012.

[32] C. W. Fetter, *Applied Hydrogeology*, Waveland Press, Prentice Hall, 2001.

[33] H. J. G. Diersch, *Feflow: Finite Element Modeling of Flow, Mass and Heat Transport in Porous and Fractured Media*, vol. 996, Springer, Berlin, 2014.

[34] L. Stoeckl, M. Walther, and T. Graf, "A new numerical benchmark of a freshwater lens," *Water Resources Research*, vol. 52, no. 4, pp. 2474–2489, 2016.

[35] M. T. van Genuchten, "A closed-form equation for predicting the hydraulic conductivity of unsaturated soils," *Soil Science Society of America Journal*, vol. 44, no. 5, pp. 892–898, 1980.

[36] H. R. Henry, "Effects of dispersion on salt encroachment in coastal aquifer," in *Geological Survey Water Supply Paper 1613-C*, Prentice Hall, U.S, 1964.

[37] M. J. Simpson and T. P. Clement, "Improving the worthiness of the Henry problem as a benchmark for density-dependent groundwater flow models," *Water Resources Research*, vol. 40, no. 1, article W01504, 2004.

[38] J. Bear, *Dynamics of Fluids in Porous Media*, Elsevier, New York, 1972.

Hindawi
Geofluids
Volume 2019, Article ID 8017164, 15 pages
https://doi.org/10.1155/2019/8017164

Research Article

Analytical Solution of Tidal Loading Effect in a Submarine Leaky Confined Aquifer System

Zongzhong Song,[1] Hailong Li,[2,3] Qian Ma,[4] Chunmiao Zheng,[2,3] Jiu Jimmy Jiao,[5] and Shaohong Li[6]

[1]*Beijing Guohuan Tsinghua Environmental Engineering Design & Research Institute Co. Ltd., Beijing 100084, China*
[2]*State Environmental Protection Key Laboratory of Integrated Surface Water-Groundwater Pollution Control, School of Environmental Science and Engineering, Southern University of Science and Technology, Shenzhen 518055, China*
[3]*Guangdong Provincial Key Laboratory of Soil and Groundwater Pollution Control, School of Environmental Science and Engineering, Southern University of Science and Technology, Shenzhen 518055, China*
[4]*Tianjin University, Library, 300350, China*
[5]*Department of Earth Science, University of Hong Kong, Hong Kong, China*
[6]*State Key Laboratory of Biogeology and Environmental Geology and School of Water Resources and Environment, China University of Geosciences-Beijing, Beijing 100083, China*

Correspondence should be addressed to Hailong Li; lihailong@sustc.edu.cn

Received 23 February 2019; Revised 18 May 2019; Accepted 30 May 2019; Published 20 June 2019

Guest Editor: Leanne Morgan

Although there are many existing analytical studies of tidal groundwater level fluctuations in coastal aquifer systems, few of them focus on an offshore submarine aquifer. Here, we consider tidal groundwater head fluctuations in a submarine leaky confined aquifer overlain by a semipermeable seabed. Both the seabed and the confined aquifer are assumed to extend horizontally infinitely. A one-dimensional mathematical model is established to describe the problem, and the analytical solution is derived. The impacts of the tidal loading efficiency, hydraulic conductivity and elastic storage of the semipermeable layer and aquifer on the groundwater head fluctuations in the aquifer system are analyzed and discussed. Solution analyses indicated that tidal loading effects tend to enhance the amplitude of the tidal groundwater fluctuation in the confined aquifer system and to reduce the phase shift between the groundwater head and the sea tide fluctuations.

1. Introduction

The study of tidal groundwater level fluctuations in coastal aquifer systems is beneficial to solving various coast environmental problems. Many analytical solutions have been derived in this field since the 1950s. Jacob [1] and Ferris [2] firstly derived analytical solutions to describe the tide-induced groundwater fluctuation in a confined aquifer which ends at the coastline. The equations have been widely used in field survey and aquifer parameter estimation in coastal areas (e.g., [3–9]). Since then, various analytical solutions related to tidal head fluctuations have been derived for coastal confined aquifers. Van der Kamp [10] investigated the tidal groundwater fluctuation in an aquifer with an impermeable roof extending seaward and landward infinitely. Li and Chen [11] considered a coastal confined aquifer with an impermeable roof extending under the sea for a certain length, neglecting the vertical leakage. Jiao and Tang [12] discussed the tide-induced groundwater head fluctuation in an onshore multilayered coastal aquifer system neglecting the elastic storage of the semipermeable layer. Based on Jiao and Tang's study [12], Li and Jiao [13] took into account the elastic storage of the semipermeable layer, and they [14] considered a leaky aquifer with the roof extending under the sea. Jeng et al. [15] considered the interference of the tidal groundwater level fluctuations in a multilayered aquifer system with the

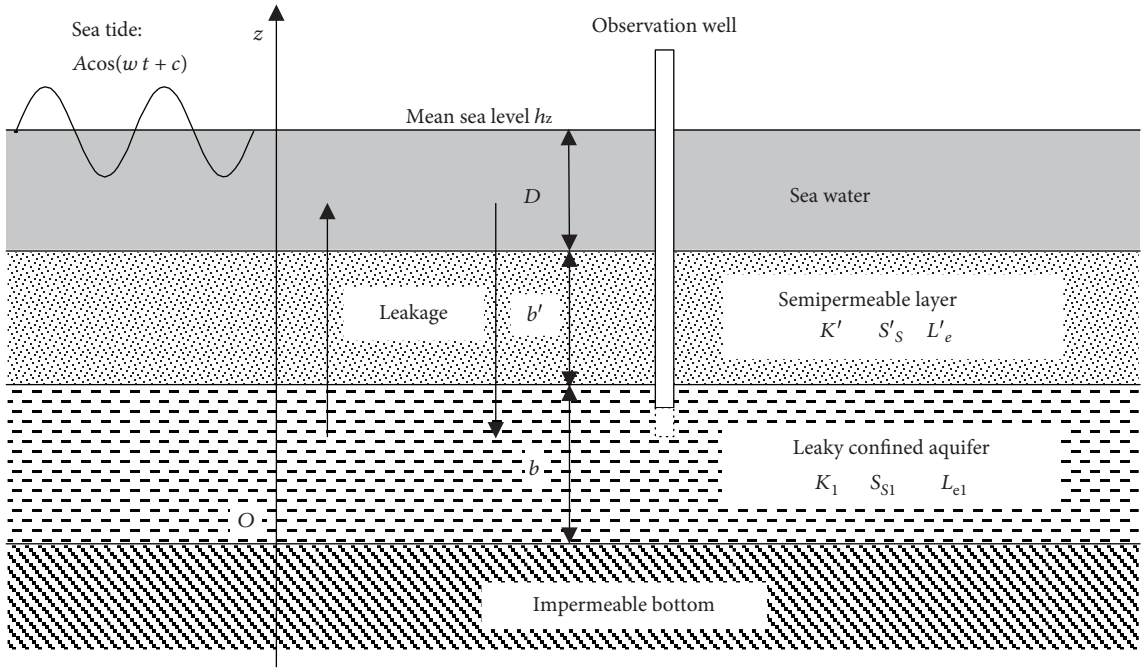

Figure 1: Schematic of a submarine leaky confined aquifer system.

leakage of a semipermeable layer considered. Li and Jiao [16] improved Jeng et al.'s work [15] in the sense that both the leakage and elastic storage of the leaky layer are considered. Li et al. [17] considered a coastal multilayered aquifer system with the confined aquifer and its semipermeable roof extending infinitely under the sea. All the effects related to the semipermeable layer such as the elastic storage, the leakage, and the tidal loading efficiency were taken into account. Guarracino et al. [18] derived an analytical solution to describe the tide-induced head fluctuation in an aquifer system that extends a finite distance under the sea, with which the extending length may be estimated from groundwater head measurement. Wang et al. [19] presented an analytical study on the loading effect of the water table variations in a coastal aquifer system consisting of an unconfined aquifer, a confined aquifer, and an impermeable layer between them.

Due to the tidal fluctuations, the total weight of the pore water (the onshore part) or sea water (the offshore part) in/overlying the aquifers will vary accordingly, which in turn can cause a considerable tidal loading effect on the groundwater flow. Many researchers [11, 14, 17–20] considered the tidal loading effect in their analytical studies, whereas almost all of the existing studies of tide-induced groundwater fluctuations focus on the tide-induced groundwater level fluctuation in onshore aquifer. Although there are some analytical solutions of tide-induced groundwater fluctuations in the submarine confined aquifer system in the offshore part (e.g., [14, 17, 18]), the dependency of the tide-induced groundwater head fluctuation in the offshore submarine aquifer on the model parameter was not analyzed or discussed. The offshore submarine aquifers are important both in water resources and in marine environments (e.g., [21–26]). Therefore, the study of the groundwater flow in offshore submarine aquifer systems is necessary and important.

This paper considered a submarine leaky confined aquifer system with the confined aquifer and its semipermeable roof extending infinitely under the sea. All effects related to the submarine leaky confined aquifer system such as the elastic storage, the hydraulic conductivity, and the tidal loading efficiency were taken into account. The mathematic model was given, and the analytical solution was derived. The influences of the tidal loading efficiency, the elastic storage, and the hydraulic conductivity on the tidal groundwater head fluctuations in the confined aquifer and in the seabed were analyzed and discussed.

2. Mathematical Model and Analytical Solution

2.1. Mathematical Model. The configuration of a submarine leaky confined aquifer system is shown in Figure 1. The aquifer is overlain by a semipermeable seabed aquifer/layer. Both the semipermeable seabed and the confined aquifer are assumed to extend horizontally infinitely. This assumption is reasonable when the considered offshore submarine aquifer is far enough from the coastline. There are even many offshore freshwater submarine aquifers extending in all horizontal directions extensively and very far from the coastline [22–26]. In addition, several existing analytical studies assume that the coastal aquifer systems extend seaward infinitely (e.g., [10, 14, 17, 27]). A vertically one-dimensional mathematical model is used to describe the problem.

Let the z axis be positive upwards (Figure 1). All the layers are homogeneous and with constant thickness. Based on these assumptions and the theories of leaky, elastic aquifers proposed by Hantush and Jacob [28] and Jacob [1], the

mathematical model to describe the groundwater fluctuations in Figure 1 is as follows:

$$S_S \frac{\partial H}{\partial t} = K \frac{\partial^2 H}{\partial z^2} + S_S L_e \frac{dH_S}{dt}, \quad -\infty < t < +\infty, 0 < z < b + b', z \neq b, \tag{1}$$

$$H\left(b + b', t\right) = H_S(t) = r_\rho A \cos\left(\omega t + c\right), \tag{2}$$

$$\lim_{z \downarrow b} H(z, t) = \lim_{z \uparrow b} H(z, t), \tag{3}$$

$$\lim_{z \downarrow b} K' \frac{\partial H}{\partial Z} = \lim_{z \uparrow b} K_1 \frac{\partial H}{\partial z}, \tag{4}$$

$$\frac{\partial H}{\partial z}\Big|_{z=0} = 0, \tag{5}$$

where $H(z, t)$, S_S, and K are the hydraulic head [L], specific storage [L^{-1}], and vertical hydraulic conductivity [LT^{-1}] of the semipermeable layer or the aquifer, respectively; L_e is the tidal loading efficiency (dimensionless) [--]; r_ρ is the density ratio (dimensionless) of the seawater to the freshwater with the range from 1.02 to 1.03; b and b' are the thicknesses [L] of the aquifer and the semipermeable layer, respectively; S_S takes the value of S_S' in the semipermeable layer and S_{S1} in the confined aquifer; K equals K' in the semipermeable layer and K_1 in the confined aquifer; $H_S(t)$ is the hydraulic head of the sea tide [L]; A is the amplitude [L] of the tidal fluctuation; ω is the angular velocity (or frequency) [T^{-1}] of tide and equals $2\pi/t_0$ with t_0 being the tidal period [T]; and c is the phase shift (in radian). The bottom of the confined aquifer is set to be the datum of the system.

Equation (1) indicates that the groundwater level fluctuation in the submarine leaky confined aquifer is caused by its elastic compression and expansion due to the tidal loading rate of the sea water above seabed ($S_S L_e (dH_s/dt)$), in addition to the tidal fluctuation at the seabed boundary $z = b + b'$ as expressed by equation (2). Equations (3) and (4) are the continuity conditions of the hydraulic head and groundwater flux, respectively. Equation (5) states the no-flow boundary condition on the upper surface of the impermeable bottom.

2.2. Analytical Solution. In order to facilitate analysis, four parameters are introduced: the main aquifer's tidal propagation parameter a [L^{-1}] defined as

$$a = \sqrt{\frac{\omega S_{S1}}{2K_1}}, \tag{6}$$

the dimensionless thickness of the seabed defined as

$$\theta = b' \sqrt{\frac{\omega S_S'}{2K'}} = \sqrt{\frac{s}{2u}}, \tag{7}$$

where s is the dimensionless storativity ratio and defined as

$$s = \frac{S_S' b'}{S_{S1} b}, \tag{8}$$

and the dimensionless leakage u defined as

$$u = \frac{K'}{\omega S_{S1} b b'}. \tag{9}$$

The solution of boundary value problem (1), (2), (3), (4), and (5) is given by the following equations (see Appendix A for the derivation):

$$H(z, t) = r_\rho A \,\mathrm{Re}\left[\exp\left(\mathrm{i}\omega t\right)\{C \cosh\left[(1 + \mathrm{i})az\right] + L_{e1}\}\right], \quad 0 < z < b, \tag{10a}$$

$$H(z, t) = r_\rho A \,\mathrm{Re}\left[\exp\left(\mathrm{i}\omega t\right)\left\{C_1 e^{((1+\mathrm{i})\theta z)/b'} + C_2 e^{-((1+\mathrm{i})\theta z)/b'} + L_e'\right\}\right], \quad b < z < b + b'. \tag{10b}$$

The analytical solutions (10a) and (10b) of the groundwater heads $H(z, t)$ can be deformed as (see Appendix B for the derivation of the analytical solutions)

$$H(z, t) = r_\rho A A_r \cos\left(\omega t - \varphi\right), \tag{11}$$

where $A_r(L_{e1}, L_e', ab, \theta, p, \tau, z)$ is the amplitude ratio and $\varphi(L_{e1}, L_e', ab, \theta, p, \tau, z)$ is the comprehensive tidal phase shift in the aquifer defined as

$$A_r\left(L_{e1}, L_e', ab, \theta, p, \tau, z\right) = \left|C \cosh\left[(1 + \mathrm{i})az\right] + L_{e1}\right|, \quad 0 < z < b, \tag{12a}$$

$$A_r\left(L_{e1}, L_e', ab, \theta, p, \tau, z\right) = \left|C_1 e^{((1+\mathrm{i})\theta z)/b'} + C_2 e^{-((1+\mathrm{i})\theta z)/b'} + L_e'\right|, \quad b < z < b + b', \tag{12b}$$

$$\varphi\left(L_{e1}, L_e', ab, \theta, p, \tau, z\right) = -\arg\left(C \cosh\left[(1 + \mathrm{i})az\right] + L_{e1}\right), \quad 0 < z < b, \tag{12c}$$

$$\varphi\left(L_{e1}, L_e', ab, \theta, p, \tau, z\right) = -\arg\left(C_1 e^{((1+\mathrm{i})\theta z)/b'} + C_2 e^{-((1+\mathrm{i})\theta z)/b'} + L_e'\right), \quad b < z < b + b'. \tag{12d}$$

The three parameters C, C_1, and C_2 are given by the following equations (see Appendix C for the derivation):

$$C = \frac{C_1 \exp\left[(1 + \mathrm{i})\tau\theta\right] + C_2 \exp\left[-(1 + \mathrm{i})\tau\theta\right] + L_e' - L_{e1}}{\cosh\left[(1 + \mathrm{i})ab\right]}, \tag{13a}$$

Table 1: Ranges of parameters ab, θ, p, and τ in the leaky confined aquifer systems reported in the literature.

Leaky aquifer			Semipermeable layer			Model parameters				References
K_1 ($\mathrm{m}\cdot\mathrm{d}^{-1}$)	S_{S1} ($\times 10^{-6}$ m^{-1})	b (m)	K' ($\mathrm{m}\cdot\mathrm{d}^{-1}$)	$S_S{}'$ ($\times 10^{-4}$ m^{-1})	b' (m)	Ab	θ	p	τ	
7.71	2.57	14	0.013	2.5	4	0.020	1.37	1.69*E*-3	3.50	[31]
11.29	3.21	14	0.013	NA	4	0.018	NA	1.15*E*-3	3.50	[32]
8.14	0.21	14	0.013	8.75	4	0.018	2.56	1.60*E*-3	3.50	[32]
579.43	4.00	28	0.0016	3.30	9.1	0.017	10.15	2.76*E*-6	3.08	[33]
579.43	4.00	28	0.0016	7.89	15.2	0.017	25.87	2.76*E*-6	1.84	[33]
1.20	16.07	6.1	0.0082	13.33	3	0.055	2.98	6.83*E*-3	2.03	[34]
45.81	5.63	16	0.0021	0.38	13.1	0.014	4.16	4.58*E*-5	1.22	[35]

NA means that data are not available.

where

$$\tau = \frac{b}{b'} \tag{13b}$$

is the thickness ratio (dimensionless) and C_1 and C_2 are two complex constants determined by equations (A.4) and (A.5) and given by

$$C_1 = \frac{1}{\Delta}\left\{e^{-(1+\mathrm{i})\tau\theta}\left[\tanh\left[(1+\boldsymbol{i})ab\right]\left(L_e' - L_{e1}\right)e^{-(1+\mathrm{i})\theta} + \left(\frac{\theta p\tau}{ab} + \tanh\left[(1+\boldsymbol{i})ab\right]\right)\left(1 - L_e'\right)\right]\right\}, \tag{13c}$$

$$C_2 = \frac{1}{\Delta}\left\{e^{(1+\mathrm{i})\tau\theta}\left[-\tanh\left[(1+\mathrm{i})ab\right]\left(L_e' - L_{e1}\right)e^{(1+\mathrm{i})\theta} + \left(\frac{\theta p\tau}{ab} - \tanh\left[(1+\mathrm{i})ab\right]\right)\left(1 - L_e'\right)\right]\right\}, \tag{13d}$$

with

$$\Delta = \frac{2\theta p\tau}{ab}\cosh\left[(1+\mathrm{i})\theta\right] + 2\tanh\left[(1+\mathrm{i})ab\right]\sinh\left[(1+\mathrm{i})\theta\right], \tag{13e}$$

$$p = \frac{K'}{K_1}. \tag{13f}$$

3. Discussion of the Solution

3.1. Value Ranges of Model Parameters. The value ranges of dimensionless model parameters ab, θ, p, and τ for the leaky confined aquifer system reported in the literature are shown in Table 1, according to the summarization of Li and Jiao ([13], Table 1). One can see that ab ranges from 0.014 to 0.055, θ from 1.37 to 25.87, p from 2.76×10^{-6} to 6.83×10^{-3}, and τ from 1.22 to 3.50. Based on these data and other situations (for example, the thickness of the submarine confined aquifer could be up to several hundred meters), the ranges of the parameters in the following discussion will be chosen: 0.001~10 for ab, 0~100 for θ, 1×10^{-5}~1×10^{-1} for p, and 1~10 for τ.

The tidal loading efficiency (L_e') in the semipermeable roof of the coastal confined aquifer system is usually very close to 1 [17]. So the value of L_e' will be fixed at 0.9 in the following discussion. Previous analytical studies and field surveys [7, 29, 30] show that the range of the tidal loading efficiency (L_{e1}) in the confined aquifer changes from 0.05 to 1.

3.2. Comparison with Existing Solutions

3.2.1. Case 1: Seabed without Elastic Storage ($S_S' \to 0$). When the elastic storage and loading efficiency of the seabed are close to zero ($S_S' \to 0$; $L_e' \to 0$), a simpler analytical solution of the confined aquifer system can be obtained. In view of equation (7), one has $\theta \to 0$. For the confined aquifer, letting $L_e' \to 0$ and $\theta \to 0$ in equation (13a) yields

$$\lim_{\theta\to0} C = \frac{1}{\cosh\left[(1+\mathrm{i})ab\right]}\cdot\left\{\frac{u + (1+i)L_{e1}\tanh\left[(1+i)ab\right]/(2ab)}{u + (1+i)\tanh\left[(1+i)ab\right]/(2ab)} - L_{e1}\right\}. \tag{14a}$$

Letting $\theta \to 0$ in equations (12a) and (12c) yields

$$\lim_{\theta\to0} A_r = \left|\frac{\cosh\left[(1+i)az\right]}{\cosh\left[(1+i)ab\right]}\cdot\left\{\frac{u + (1+i)L_{e1}\tanh\left[(1+i)ab\right]/(2ab)}{u + (1+i)\tanh\left[(1+i)ab\right]/(2ab)} - L_{e1}\right\} + L_{e1}\right|, \tag{14b}$$

$$\lim_{\theta\to0}\varphi = -\arg\left(\frac{\cosh\left[(1+i)az\right]}{\cosh\left[(1+i)ab\right]}\cdot\left\{\frac{u + (1+i)L_{e1}\tanh\left[(1+i)ab\right]/(2ab)}{u + (1+i)\tanh\left[(1+i)ab\right]/(2ab)} - L_{e1}\right\} + L_{e1}\right). \tag{14c}$$

Assuming $ab \to 0 (az \to 0)$ in equations (14b) and (14c) yields

$$\lim_{ab\to 0} A_r = \left|\frac{u+(1+i)L_{e1}\tanh\left[(1+i)ab\right]/(2ab)}{u+(1+i)\tanh\left[(1+i)ab\right]/(2ab)}\right| = \left|\frac{u+(1+i)L_{e1}(1+i)/2}{u+(1+i)(1+i)/2}\right|, \tag{14d}$$

$$\lim_{\theta\to 0}\phi = -\arg\left(\frac{u+(1+i)L_{e1}\tanh\left[(1+i)ab\right]/(2ab)}{u+(1+i)\tanh\left[(1+i)ab\right]/(2ab)}\right) = -\arg\left(\frac{u+(1+i)L_{e1}(1+i)/2}{u+(1+i)(1+i)/2}\right) \tag{14e}$$

and then yields

$$A_r = \left|\frac{u+iL_{e1}}{u+i}\right|, \tag{14f}$$

$$\varphi = -\arg\left(\frac{u+iL_{e1}}{u+i}\right). \tag{14g}$$

Substituting equations (14f) and (14g) back into equation (11), the groundwater head in the confined aquifer can be written as

$$H(z,t) = r_\rho A\left|\frac{u+iL_{e1}}{u+i}\right|\cos\left[\omega t+\arg\left(\frac{u+iL_{e1}}{u+i}\right)\right], \tag{15}$$

which is essentially the same as the equation given by Li and Jiao [14] when the roof length $L\to\infty$ and $x\to-\infty$. Therefore, our analytical solution is a generalization of Li and Jiao's solution [14] when the roof length $L\to\infty$ and $x\to-\infty$.

For the semipermeable seabed, letting $L_e'\to 0$ and $\theta\to 0$ in equations (12b) and (12d) yields

$$\lim_{\theta\to 0}A_r = \left|\frac{p\tau+(1+i)ab[(L_{e1}-1)z/b+\tau-L_{e1}(1+i)]\tanh\left[(1+i)ab\right]}{p\tau+(1+i)ab\tanh\left[(1+i)ab\right]}\right|, \tag{16a}$$

$$\lim_{\theta\to 0}\varphi = -\arg\left(\frac{p\tau+(1+i)ab[(L_{e1}-1)z/b+\tau-L_{e1}(1+\tau)]\tanh\left[(1+i)ab\right]}{p\tau+(1+i)ab\tanh\left[(1+i)ab\right]}\right). \tag{16b}$$

Substituting equations (16a) and (16b) back into equation (11), the groundwater head in the semipermeable seabed can be obtained as follows:

$$H(z,t) = r_\rho A\left|\frac{p\tau+(1+i)ab[(L_{e1}-1)z/b+\tau-L_{e1}(1+\tau)]\tanh\left[(1+i)ab\right]}{p\tau+(1+i)ab\tanh\left[(1+i)ab\right]}\right| \times\cos\left[\omega t+\arg\left(\frac{p\tau+(1+i)ab[(L_{e1}-1)z/b+\tau-L_{e1}(1+\tau)]\tanh\left[(1+i)ab\right]}{p\tau+(1+i)ab\tanh\left[(1+i)ab\right]}\right)\right]. \tag{17}$$

3.2.2. Case 2: Impermeable Seabed ($K'\to 0$). When the semipermeable seabed becomes impermeable (i.e., $K'\to 0$), in view of equation (9), one has $p\to 0$. Letting $p\to 0$ in equation (13a) yields

$$\lim_{p\to 0}C = \frac{L_e-L_{e1}+L_{e1}-L_e}{\cosh\left[(1+\mathrm{i})ab\right]} = 0. \tag{18a}$$

Letting $p\to 0$ in equations (12a) and (12c) yields

$$\lim_{p\to 0}A_r = L_{e1}, \tag{18b}$$

$$\lim_{p\to 0}\varphi = 0. \tag{18c}$$

Substituting equations (18b) and (18c) back into equation (11), the groundwater head in the confined aquifer can be written as

$$H(z,t) = r_\rho AL_{e1}\cos(\omega t). \tag{19}$$

The solution given by equation (19) is essentially the same as the solution of Van der Kamp [10] and Li et al. [17] when $K'\to 0$ and $x\to-\infty$ except some notation differences.

3.3. The Amplitude Ratio A_r and Phase Shift φ. The amplitude ratio A_r and phase shift φ of the groundwater head fluctuation in the confined aquifer and seabed are given by equations (12a), (12b), (12c), and (12d). Here, we will concentrate on the dependency of A_r and φ on the model

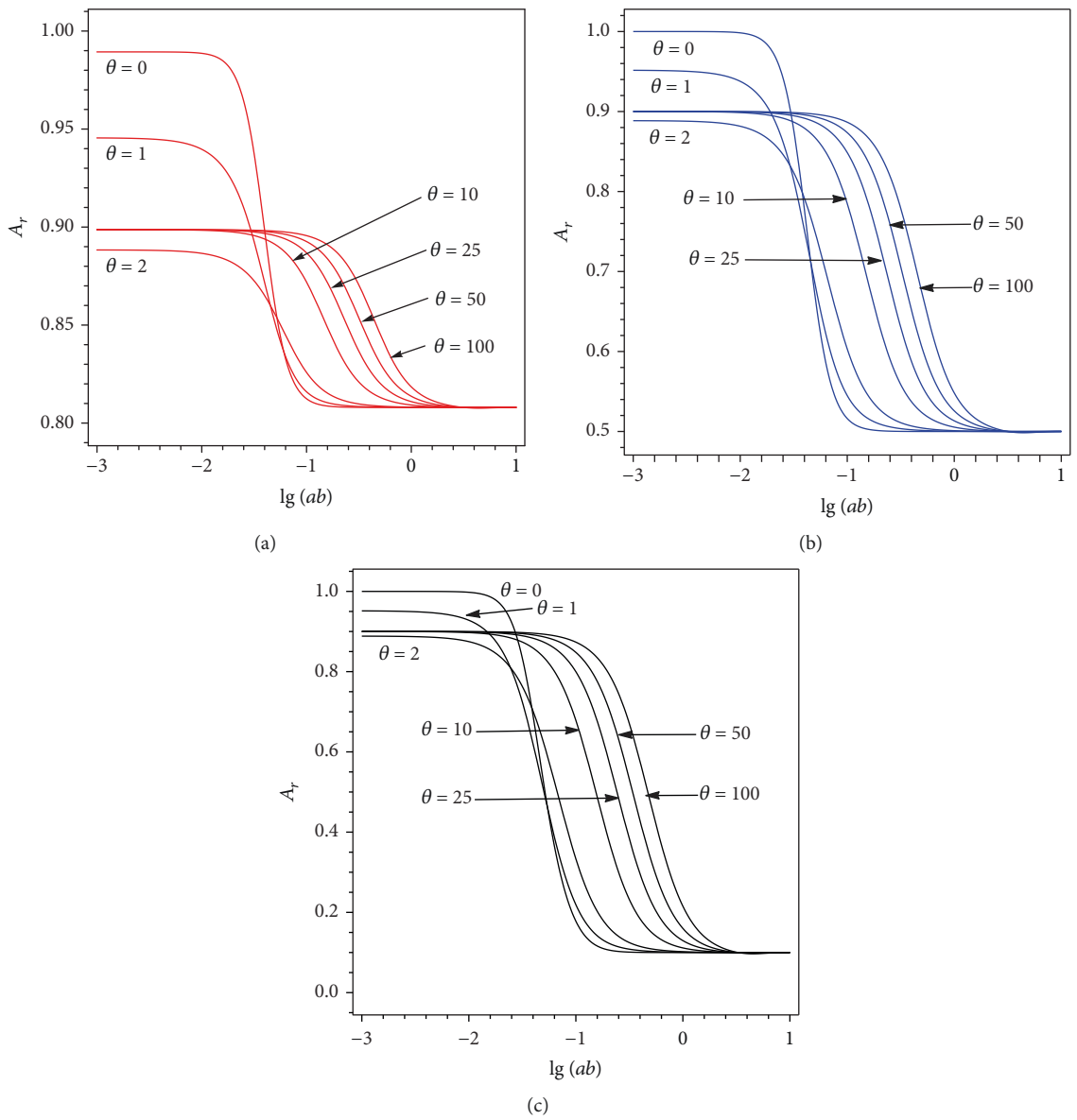

FIGURE 2: Changes of the amplitude ratio A_r at the middle of the confined aquifer $z = 0.5b$ with lg (ab) for different values of θ when L_{e1} is equal to (a) 0.8, (b) 0.5, and (c) 0.1. The loading coefficient $L_e' \equiv 0.9$.

parameters such as the tidal loading effect of the confined aquifer (L_{e1}) and of the seabed (L_e') and the dimensionless thickness θ of the semipermeable seabed and ab of the confined aquifer. Since the amplitude ratio A_r and the phase shift φ depend on z, we discuss the changes of A_r and φ when z is fixed at the middle of the confined aquifer ($z = 0.5b$) and at the middle of the semipermeable seabed ($z = b + 0.5b'$). The representative values of p and τ in the literature are chosen for the following discussion: i.e., 1×10^{-3} for p and 3 for τ (see Table 1).

3.3.1. Changes of A_r and φ in the Confined Aquifer. Figure 2 shows how the amplitude ratio A_r at the middle of the confined aquifer $z = 0.5b$ changes with lg (ab) for different values of θ and L_{e1} when $L_e' \equiv 0.9$. From Figure 2, one can see that the amplitude ratio A_r decreases from a constant close to 1 to L_{e1} (which equals 0.8, 0.5, and 0.1, respectively) as lg (ab) increases from −3 to 1. When lg (ab) is small (lg $(ab) \leq -3$), with the θ increasing, A_r decreases from 1 firstly and then increases to 0.9, which is the value of the tidal loading efficiency (L_e') of the semipermeable seabed. When lg $(ab) \to 1$, A_r approaches the fixed values of L_{e1} and becomes independent of θ. For intermediate values of ab (approximately in the range $-2.5 <$ lg $(ab) < 1$), A_r decreases significantly with ab. The curves for different θ values may cross each other near lg $(ab) = -1.4$, indicating that A_r is not always monotonic with respect to θ. In addition, A_r also increases with L_{e1} for fixed values of ab and θ. This can be observed when one compares the curves for the same values of ab and θ.

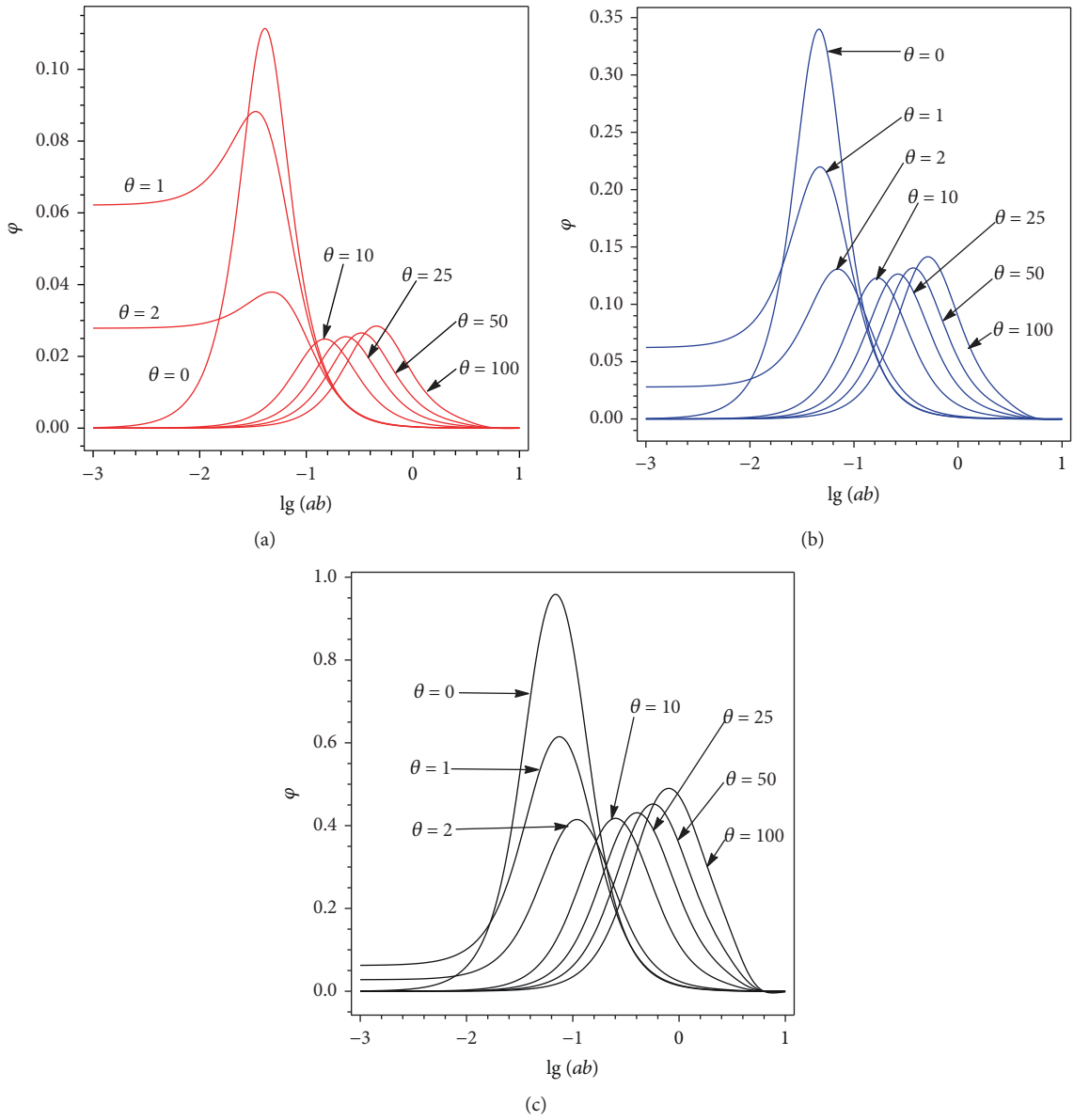

FIGURE 3: Changes of phase shift φ at the middle of the confined aquifer $z = 0.5b$ with lg (ab) for different values of θ when L_{e1} is equal to (a) 0.8, (b) 0.5, and (c) 0.1. The loading coefficient $L_e' \equiv 0.9$.

Figure 3 shows how the phase shift φ at the middle of the confined aquifer $z = 0.5b$ changes with lg (ab) for different values of θ and L_{e1} when $L_e' \equiv 0.9$. From Figure 3, one can see that the value range of phase shift φ decreases significantly with the tidal efficiency L_{e1}. The value range of φ is about (0, 0.96) for $L_{e1} = 0.1$, (0, 0.34) for $L_{e1} = 0.5$, and (0, 0.11) for $L_{e1} = 0.8$. When ab is very small (lg $(ab) \to -2.5$), with the increasing of θ, φ increases from 0 firstly and then decreases to 0. When ab is very large (lg $(ab) \to 1$), the phase shift φ tends to be zero for any values of θ and L_{e1}. From Figure 3, one can also see that φ is nonmonotonic with respect to θ and ab, which is due to the superposition of the multieffects such as the tidal loading, the downward propagation of the tidal signal, and the elastic storages of the semipermeable seabed and the aquifer. According to the curve when $\theta \to 0$ and $L_{e1} = 0.1$, the maximum phase shift is close to 1.0 (rad) which can lead to a time lag about 2 h for a semidiurnal tide and 4 h for a diurnal tide.

According to the discussions about the amplitude ratio A_r and the phase shift φ in the confined aquifer, one can conclude that tidal loading effects tend to enhance the amplitude and reduce the phase shift of the tidal groundwater head fluctuations in the confined aquifer. Figures 2 and 3 show that the increase of the dimensionless thickness of the upper semipermeable seabed may significantly enhance the tidal head fluctuation in the confined aquifer. Furthermore, Figures 2 and 3 demonstrate that an active range of lg (ab) $(-2.5.0 < \text{lg}\,(ab) < 1.0)$ exists in which both the amplitude and phase shift change with ab significantly and both become insensitive to lg (ab) outside the range (-2.5, 1).

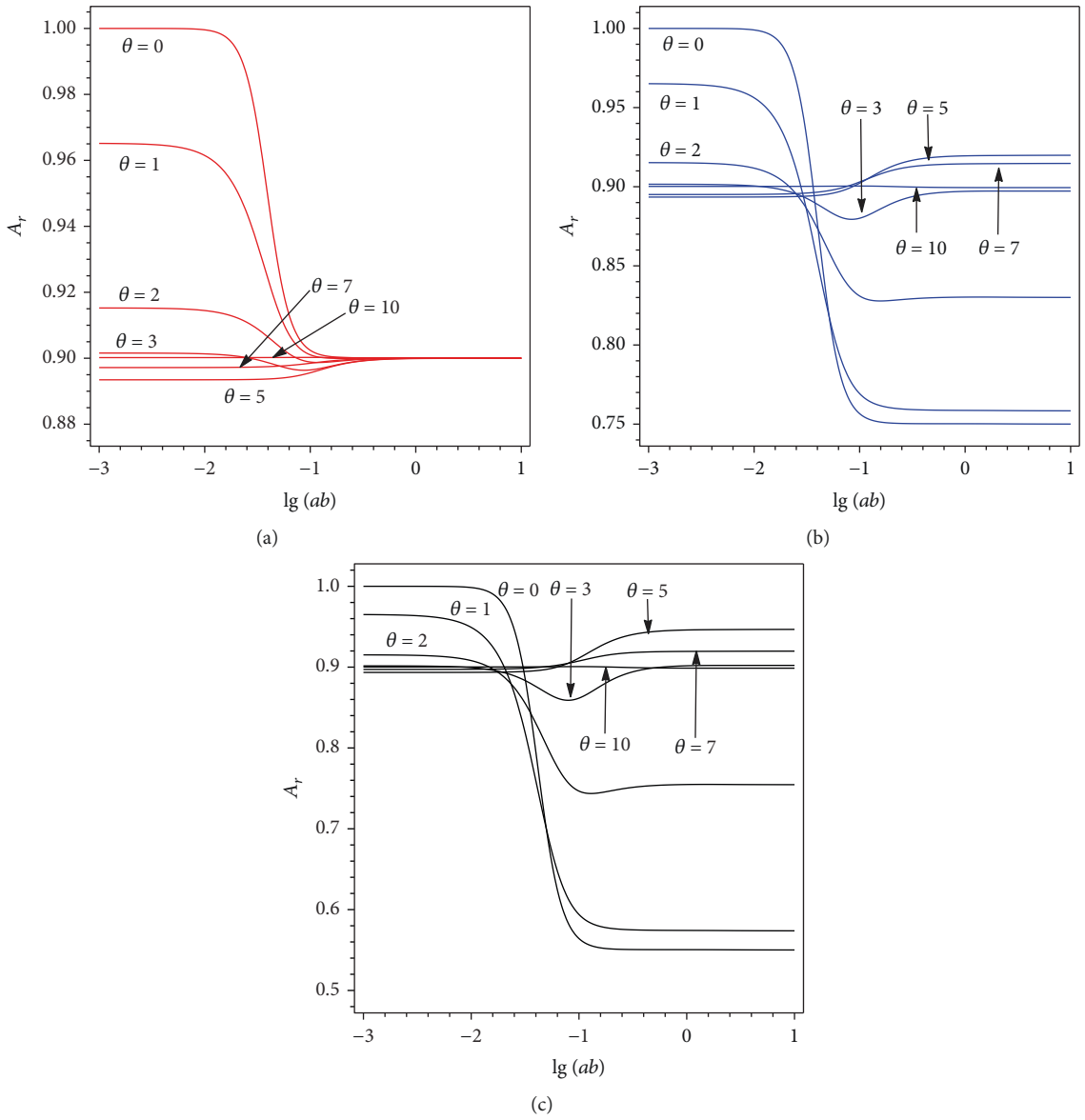

FIGURE 4: Changes of the amplitude ratio A_r at the middle of the seabed semipermeable layer $z = b + 0.5b'$ with lg (ab) for different values of θ when L_{e1} is equal to (a) 0.8, (b) 0.5, and (c) 0.1. The loading coefficient $L'_e \equiv 0.9$.

3.3.2. Changes of A_r and φ in the Seabed. Figure 4 shows how the amplitude ratio A_r at the middle of the seabed semipermeable layer $z = b + 0.5b'$ changes with lg (ab) for different values of θ and L_{e1} when $L'_e \equiv 0.9$. It is obviously that no matter how the lg (ab) and L_{e1} change, the value of A_r becomes constant when $\theta \geq 10$. However, the changes of A_r become complex when $\theta < 10$. When ab is very small (lg $(ab) \to -3$), as θ is increasing from 0 to 10, A_r decreases from 1 firstly and then increases to 0.9, which is the value of the tidal loading efficiency of the semipermeable seabed. As lg (ab) is increasing, the trends of A_r are different with θ values. When θ is small ($\theta < 5$), A_r decreases firstly and then becomes a constant independent of ab. However, when θ is in the range $5 \leq \theta < 10$, A_r increases firstly and then becomes a constant independent of ab. When θ is around 3.0, A_r decreases firstly and then increases with ab and finally becomes a constant. The curves for different θ values cross each other near lg $(ab) = -1.4$, indicating that the amplitude ratio A_r of the seabed is not always monotonic with respect to θ. Comparing Figures 4(a)–4(c), one can find that when ab is larger, A_r tends to be a constant value of 0.9 in Figure 4(a); however, A_r tends to have different values shown in Figures 4(b) and 4(c). It may be caused due to the tidal loading effect in the confined aquifer.

Figure 5 shows how the phase shift φ at the middle of the seabed semipermeable layer $z = b + 0.5b'$ changes with lg (ab) for different values of θ and L_{e1} when $L'_e \equiv 0.9$. The value range of φ changes significantly with L_{e1}, which is about (0.00, 0.05) for $L_{e1} = 0.8$, (−0.11, 0.14) for $L_{e1} = 0.5$, and (−0.28, 0.29) for $L_{e1} = 0.1$. Thus, the smaller the tidal efficiency L_{e1}, the wider the value range of the phase shift. In general, the tidal loading effect tends to reduce the phase shift

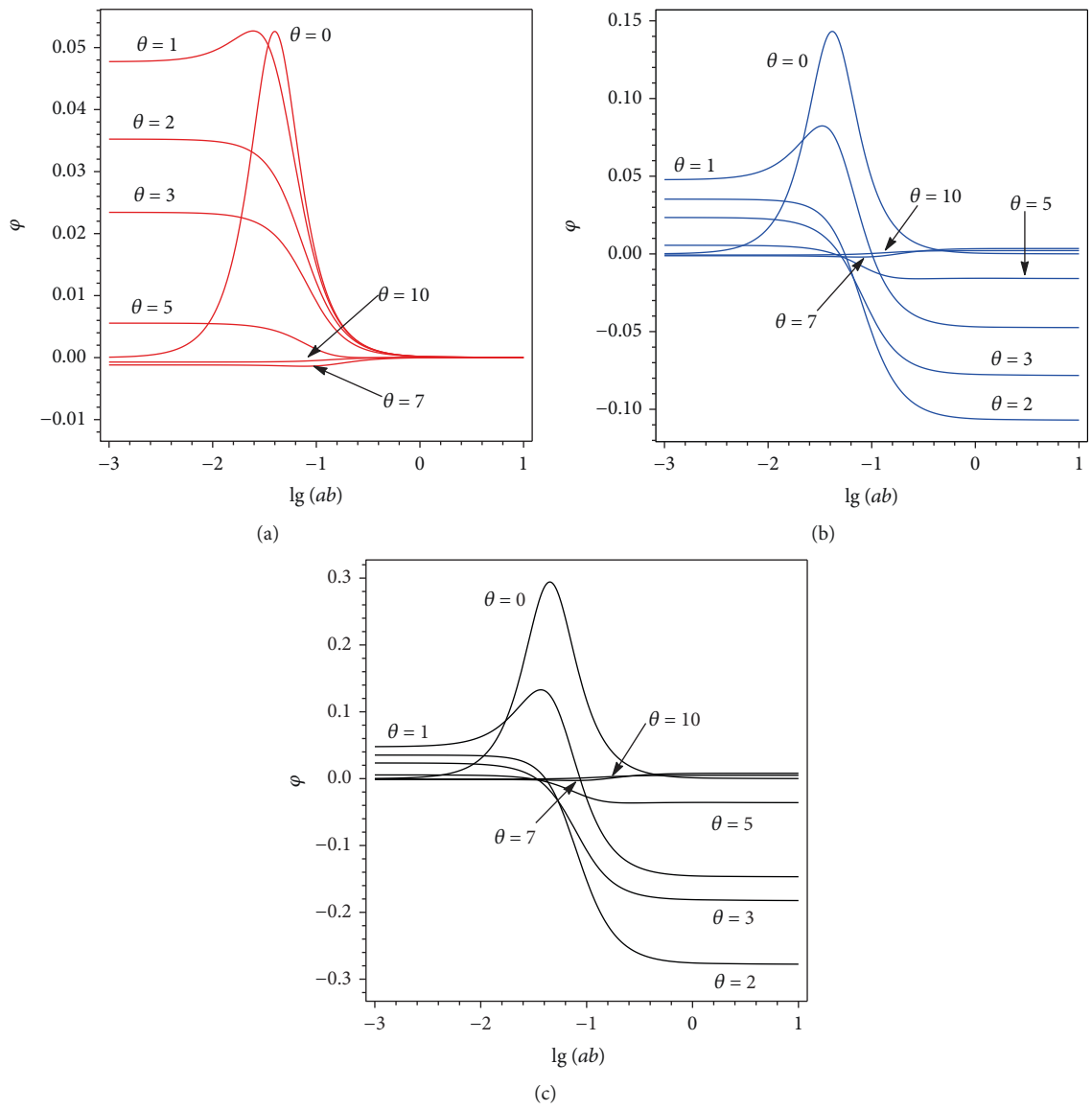

FIGURE 5: Changes of the phase shift φ at the middle of the seabed semipermeable layer $z = b + 0.5b'$ with lg (ab) for different values of θ when L_{e1} is equal to (a) 0.8, (b) 0.5, and (c) 0.1. The loading coefficient $L'_e \equiv 0.9$.

between the groundwater head and the tide fluctuations. No matter how lg (ab) and L_{e1} change, the value of φ becomes constant when $\theta \geq 10$. When θ is equal to 0 or 1, the phase shift φ increases firstly and then decreases to a constant with the increasing of lg (ab). For $2 \leq \theta \leq 5$, the phase shift φ decreases with lg (ab) monotonically to a constant. When θ is equal to or greater than 7, the phase shift φ increases with L_{e1} monotonically to a constant. Comparing Figures 5(a)–5(c), one can also find that when ab is larger, φ tends to be a constant value of 0.9 in shown Figure 5(a); however, φ tends to have different values shown in Figures 5(b) and 5(c). It may be also caused due to the tidal loading effect in the confined aquifer.

3.4. Effect of the Thickness Ratio τ and Hydraulic Conductivity Ratio p. Figure 6 shows how the amplitude ratio A_r and phase shift φ at the middle of the confined aquifer $z = 0.5b$ change with lg (ab) for different values of the thickness ratio τ. The value range of τ used is from 1 to 10, which is based on Table 2. Figure 6(a) demonstrates that when lg (ab) increases from -3 to 1, the amplitude ratio A_r decreases from L'_e to L_{e1} for any values of τ. Given any values of lg (ab) in the range of (-2, 0.4), the amplitude ratio A_r increases with τ. Outside the range of (-2, 0.4), the amplitude ratio A_r becomes insensitive to τ. In Figure 6(b), the phase shift is a monopeak function of lg (ab) for any values of τ. The increasing of the thickness ratio τ can decrease the phase shift when $-2.4 <$ lg $(ab) < -1$ and increase the phase shift when $-0.4 <$ lg $(ab) < 0.6$. The impacts are complex in other ranges. Overall, the phase shift ranges from 0 to around 0.12, a relatively narrow value range.

Figure 7 shows how the amplitude ratio A_r and phase shift φ at the middle of the semipermeable seabed layer $z = b + 0.5b'$ change with lg (ab) for different values of τ.

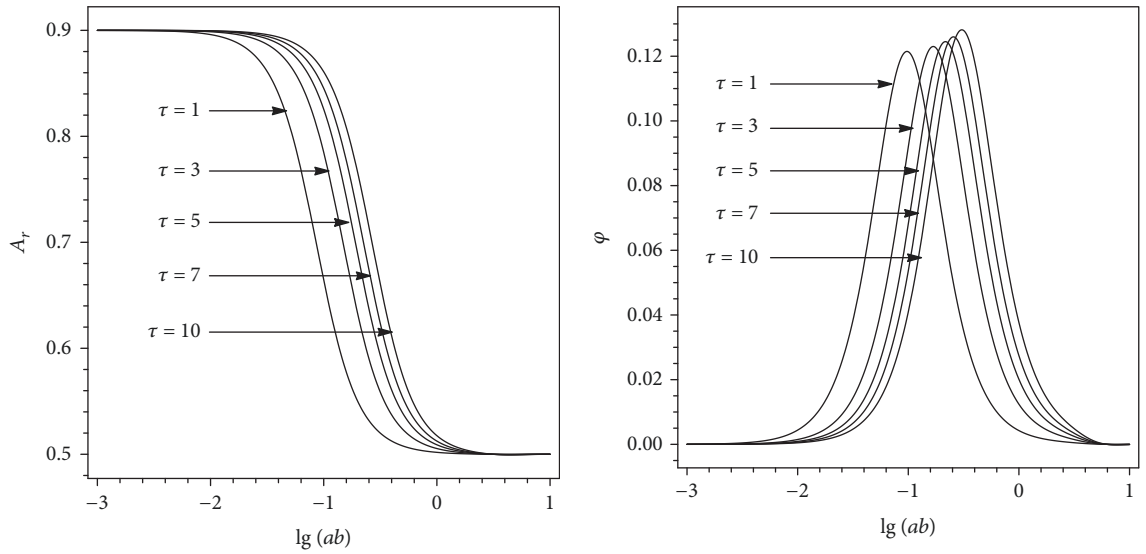

Figure 6: Changes of (a) amplitude ratio A_r and (b) phase shift φ at the middle of the confined aquifer $z = 0.5b$ with lg (ab) for different values of τ ($\tau = b/b'$). The loading coefficients $L_{e1} = 0.5$ and $L_e' \equiv 0.9$.

Table 2: Fixed parameters and their values used in the discussion.

Case no.	z	L_{e1}	θ	T	p
1	$0.5b$	0.5	10	1~10	10^{-3}
	$b + 0.5b'$	0.5	2	1~10	10^{-3}
2	$0.5b$	0.5	10	3	10^{-6}~10^{-1}
	$b + 0.5b'$	0.5	2	3	10^{-6}~10^{-1}

The parameters in Case 1 are used to discuss the effect of the thickness ratio τ ($\tau = b/b'$). The parameters in Case 2 are used to discuss the effect of hydraulic conductivity ratio p ($p = K'/K_1$).

Figure 7(a) shows that the amplitude ratio decreases with lg (ab) first and then tends to be a constant with a slight oscillations. The increasing of the thickness ratio τ can lead to the increase of the amplitude for any value of lg (ab) in the range $-2.4 <$ lg $(ab) < 0$. Figure 7(b) shows that the phase shift decreases with lg (ab) monotonically from about 0.035 to about -0.11, a very narrow value range. The increasing of the thickness ratio τ can lead to the increase of the phase shift for any value of lg (ab) in the range $-2 <$ lg $(ab) < 0.4$.

Figure 8 shows how the changes of the amplitude ratio A_r and phase shift φ at the middle of the confined aquifer $z = 0.5b$ with lg (ab) for different values of the hydraulic conductivity ratio p, which ranges from 10^{-5} to 10^{-2} according to Table 1. Figure 8(a) shows that the amplitude ratio decreases with lg (ab) monotonically from 0.9 (L_e') to 0.5 (L_{e1}) for any fixed value of p. The increasing of p can lead to the increase of the amplitude ratio for any value of lg (ab) in the range $-2.8 <$ lg $(ab) < 0.4$. Figure 8(b) shows that the phase shift is a monopeak function of lg (ab) for any given value of p. The values of lg (ab) where the curve peaks increase with p. The value range of the phase shift is from 0 to less than 0.15.

Figure 9 shows how the amplitude ratio A_r and phase shift φ at the middle of the semipermeable seabed layer $z = b + 0.5b'$ change with lg (ab) for different values of p. Figure 9(a) shows that the amplitude ratio decreases with lg (ab) first and then tends to be a constant with slight oscillations. The increasing of hydraulic conductivity ratio p can lead to the increase of the amplitude for any value of lg (ab) in the range $-3 <$ lg $(ab) < -0.6$. Figure 9(b) shows that the phase shift decreases with lg (ab) monotonically from about 0.035 to about -0.11, a very narrow value range. The increasing of hydraulic conductivity ratio p can lead to the increase of the phase shift for any value of lg (ab) in the range $-3 <$ lg $(ab) < 1$.

3.5. Groundwater Head at Different Depths of the Confined Aquifer. In order to investigate the differences of groundwater head fluctuations at different depths of the confined aquifer, we considered the changes of A_r and φ at the top and the bottom of the confined aquifer. The parameters p and τ are fixed in the following discussion: $p = 1 \times 10^{-3}$ for $\tau = 3$. Figure 10 shows how the amplitude ratio A_r at the top and bottom of the confined aquifer changes with lg (ab) for different values of θ and L_{e1} when $L_e' \equiv 0.9$. The variation patterns of A_r at the top and bottom of the aquifer are similar to that at the middle of the confined aquifer (Figure 2). When $\theta = 1$, Figure 10(a) shows that the curves of A_r at the top and bottom of the aquifer coincide completely with each other, and so do the curves for the phase shift φ in Figure 10(b). Figures 10(c) and 10(e) show that when lg $(ab) \leq -0.4$, the curves of A_r at the top and bottom of the aquifer are also entirely coincident; however, A_r at the top of the aquifer becomes larger than that at the bottom of the aquifer with θ when lg $(ab) > -0.4$. The difference in the value of A_r between the top and bottom of the aquifer decreases gradually as L_{e1} increases. Figures 10(d) and 10(f) show that the phase shift φ at the top of the aquifer becomes smaller than that at the bottom of the aquifer for large values of θ

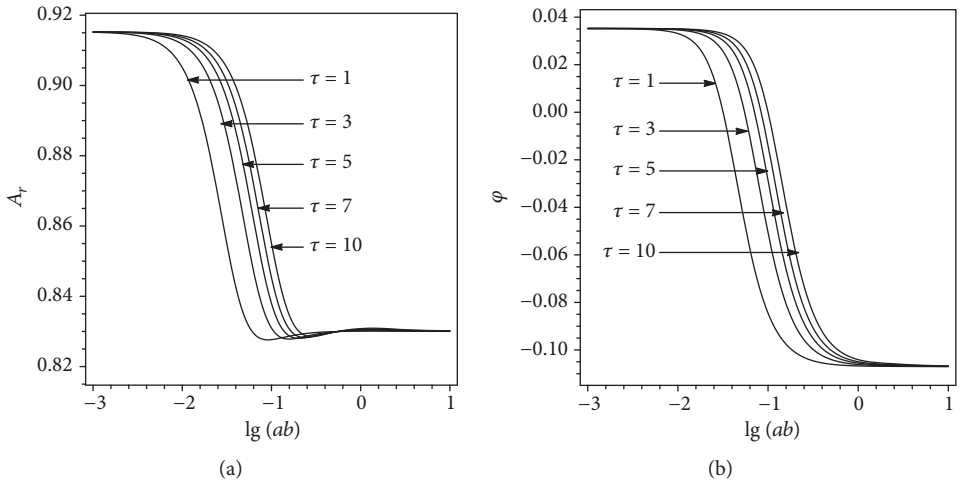

FIGURE 7: Changes of (a) amplitude ratio A_r and (b) phase shift φ at the middle of the semipermeable seabed layer $z = b + 0.5b'$ with lg (ab) for different values of τ $(\tau = b/b')$. The loading coefficients $L_{ei} = 0.5$ and $L_e' \equiv 0.9$.

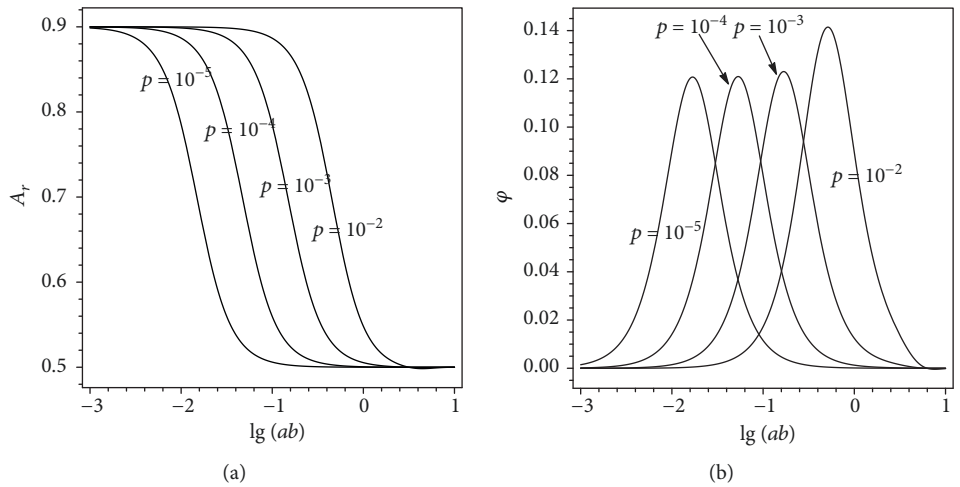

FIGURE 8: Changes of (a) amplitude ratio A_r and (b) phase shift φ at the middle of the confined aquifer $z = 0.5b$ with lg (ab) for different values of p $(p = K'/K_1)$. The loading coefficients $L_{e1} = 0.5$ and $L_e' \equiv 0.9$.

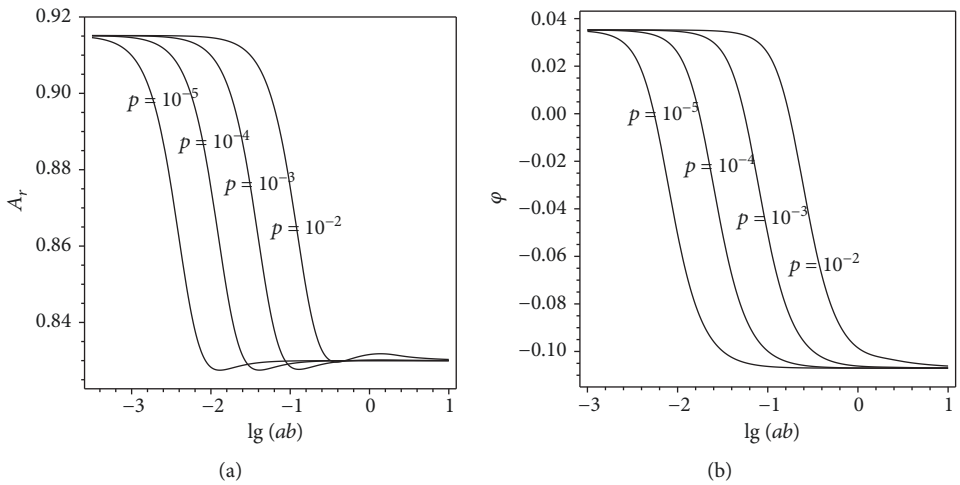

FIGURE 9: Changes of (a) amplitude ratio A_r and (b) phase shift φ at the middle of the seabed semipermeable layer $z = b + 0.5b'$ with lg (ab) for different values of p $(p = K'/K_1)$. The loading coefficients $L_{e1} = 0.5$ and $L_e' \equiv 0.9$.

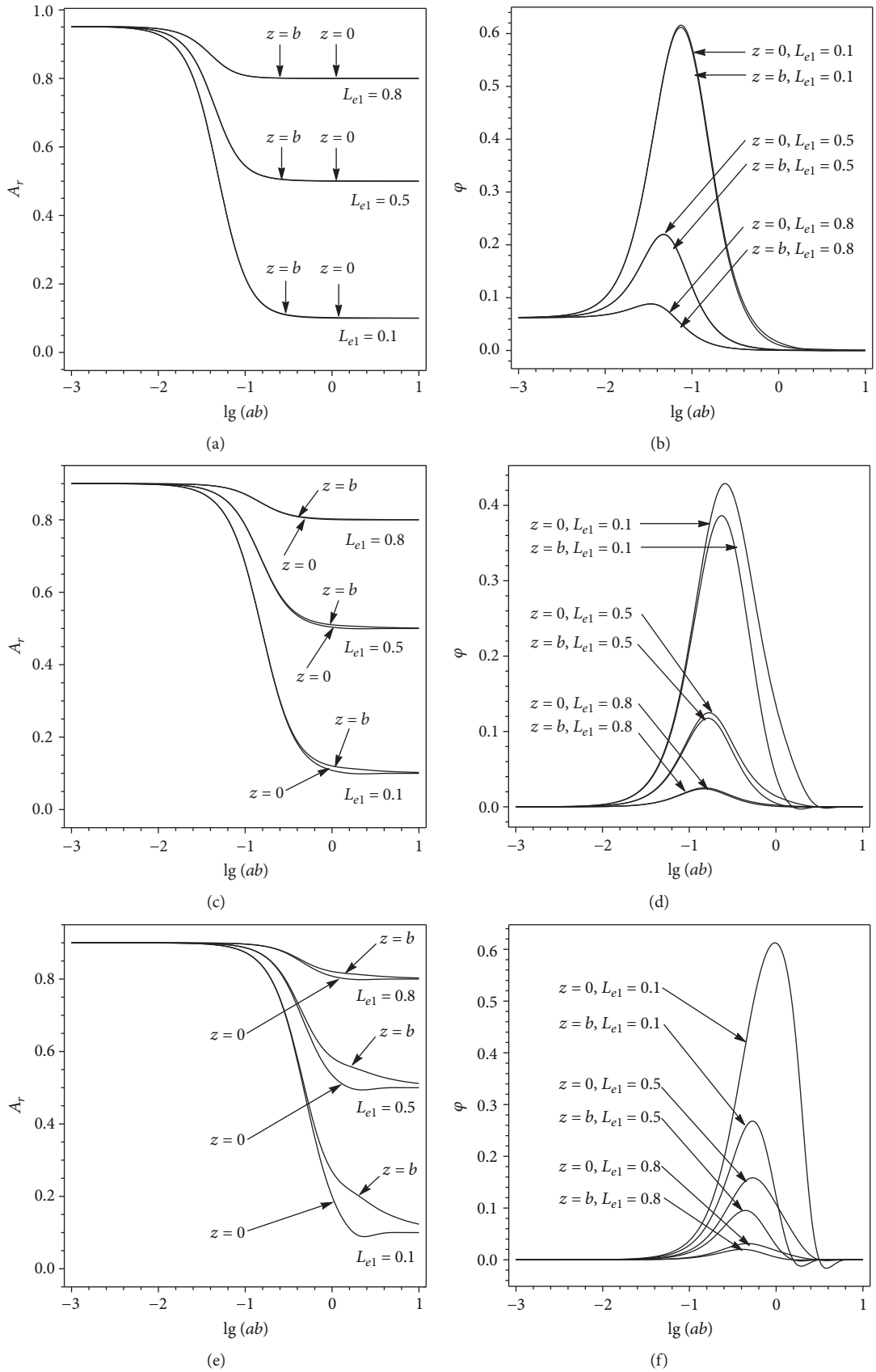

FIGURE 10: Changes of amplitude ratio A_r and phase shift φ at the top $z = b$ and bottom $z = 0$ of the confined aquifer with lg (ab) for different values of θ and L_{e1} when $L'_e \equiv 0.9$. (a, b) A_r and φ for $\theta = 1$; (c, d) A_r and φ for $\theta = 10$; and (e, f) A_r and φ for $\theta = 100$.

(10 and 100). The difference in the value of φ between the bottom and top of the aquifer decreases gradually as L_{e1} increases. It can be concluded that the discrepancy between the tidal groundwater fluctuations at the top and bottom of the confined aquifer becomes larger with the increasing of θ and the decreasing of L_{e1}.

4. Conclusion

This paper investigated the tidal groundwater head fluctuation in a submarine confined leaky aquifer system. A vertical one-dimensional mathematical model is given with the analytical solution derived. Both the leakage and elastic storage of the semipermeable seabed are considered in this model. The derived analytical solution is different from previous analytical solutions by Li and Jiao [14] and Guarracino et al. [18] which focus on the analysis in the inland portion. Although Li et al. [17] give the analytical solutions in the offshore part, they did not do sensitivity analysis of parameters of the aquifers in the offshore part to head fluctuations of the aquifers there. Our solution quantifies the tidal groundwater head fluctuations in an offshore submarine aquifer system, which contains a confined aquifer and a semipermeable seabed.

The effects of several dimensionless model parameters, including the tidal loading efficiencies (L_{e1} and L'_e) of the confined aquifer and the semipermeable seabed, the dimensionless thickness ab of the confined aquifer, and the dimensionless thickness θ of the seabed, on the tidal groundwater fluctuations are quantitatively discussed and analyzed. The following conclusions can be drawn based on the solution analyses and discussion: (1) The tidal loading effect tends to enhance the amplitude of the tidal groundwater fluctuation in the confined aquifer system, and it can also tend to reduce the phase difference between the fluctuation of the groundwater head in the aquifer (or an aquitard) and the tidal fluctuations. (2) The increase of the thickness ratio or the hydraulic conductivity ratio can not only result in a larger amplitude in the confined aquifer but also lead to a larger phase shift. (3) The discrepancy between the tidal groundwater fluctuations at the top and bottom of the confined aquifer increases when θ increases and/or L_{e1} decreases.

Appendix

A. Derivation of Solutions (10a) and (10b)

Let $F(z,t)$ be a complex function of the real variables z and t that satisfies equations (1), (2), (3), (4), and (5) after $h_S(t) = r_\rho A \cos(\omega t)$ in equations (1) and (2) is replaced by $r_\rho A \exp(i\omega t)$, where $i = \sqrt{-1}$.

Let $H(z,t)$ be the solution to (1), (2), (3), (4), and (5); it follows that

$$H(z,t) = \mathrm{Re}\,(F(z,t)), \tag{A.1}$$

where Re denotes the real part of the followed complex expression. Now suppose

$$F(z,t) = r_\rho A Z(z) \exp(\boldsymbol{i}\omega \boldsymbol{t}), \tag{A.2}$$

where $Z(z)$ is an unknown function of z. Substituting (A.2) into the five equations which $F(z,t)$ satisfies and extending the five resultant real equations into complex ones with respect to the unknown complex function $Z(z)$, then dividing the results by $r_\rho A \exp(\boldsymbol{i}\omega \boldsymbol{t})$, yield

$$K_1 Z'' - \boldsymbol{i}\omega S_{S\boldsymbol{1}} Z + \boldsymbol{i}\omega S_{S\boldsymbol{1}} L_{e1} = 0, \quad 0 < z < b, \tag{A.3}$$

$$KZ'' - \boldsymbol{i}\omega S'_S Z + \boldsymbol{i}\omega S'_S L'_e = 0, \quad b < z < b + b', \tag{A.4}$$

$$Z\left(b + b'\right) = 1, \tag{A.5}$$

$$\lim_{z \downarrow b} Z(z) = \lim_{z \uparrow b} Z(z), \tag{A.6}$$

$$K' \lim_{z \downarrow b} Z'(z) = K_1 \lim_{z \uparrow b} Z'(z), \tag{A.7}$$

$$Z'(0) = 0. \tag{A.8}$$

The solution to (A.3), (A.4), (A.5), (A.6), (A.7), and (A.8) is

$$Z(z) = \begin{cases} C \cosh\left[(1+\boldsymbol{i})az\right] + L_{e1}, & 0 < z < b, \\ C_1 e^{((1+\mathrm{i})\theta z)/b'} + C_2 e^{-((1+\boldsymbol{i})\theta z)/b'} + L'_e, & b < z < b + b', \end{cases} \tag{A.9}$$

where a and θ are the dimensionless model parameters given by equations (6) and (7), respectively, and C, C_1, and C_2 are the complex constants given by equations (13a), (13b), (13c), (13d), (13e), and (13f).

B. Derivation of Solution (11)

The following is the derivation deformation of the analytical solutions (10a) and (10b).

$$\begin{aligned} H(z,t) &= \mathrm{Re}\left[r_\rho A Z(z) \exp(\boldsymbol{i}\omega \boldsymbol{t})\right] \\ &= r_\rho A\ \mathrm{Re}\left[|Z| \exp(i \arg Z) \cdot \exp(i\omega \boldsymbol{t})\right] \\ &= r_\rho A\ \mathrm{Re}\left[|Z| \exp\left[i(\arg Z + \omega t)\right]\right] \\ &= r_\rho A\ \mathrm{Re}\left\{|Z|[\cos(\arg Z + \omega t) + i \sin(\arg Z + \omega t)]\right\} \\ &= r_\rho A |Z| \cos(\omega t - (-\arg Z)). \end{aligned} \tag{B.1}$$

C. Derivation of Solutions (13a), (13c), and (13d)

Putting equation (A.9) into equation (A.6) yields

$$C \cosh\left[(1+\mathrm{i})ab\right] + L_{e1} = C_1 e^{(1+\mathrm{i})\theta\tau} + C_2 e^{-(1+\mathrm{i})\theta\tau} + L'_e, \tag{C.1}$$

and then, the following equation can be obtained from (C.1):

$$C = \frac{C_1 \exp\left[(1+i)\tau\theta\right] + C_2 \exp\left[-(1+i)\tau\theta\right] + L_e' - L_{e1}}{\cosh\left[(1+i)ab\right]}. \tag{C.2}$$

Getting the derivative of equation (A.9) and then putting them into equation (A.6) yield

$$C\cosh\left[(1+\mathrm{i})ab\right] = \frac{\theta p\tau}{ab}\left[C_1 e^{(1+\mathrm{i})\theta\tau} - C_2 e^{-(1+\mathrm{i})\theta\tau}\right]. \tag{C.3}$$

Putting equation (A.9) into equation (A.5) yields

$$C_1 e^{(1+\mathrm{i})\theta} e^{(1+\mathrm{i})\theta\tau} + C_2 e^{-(1+\mathrm{i})\theta} e^{-(1+\mathrm{i})\theta\tau} = 1 - L_e'. \tag{C.4}$$

The solutions to (C.2), (C.3), and (C.4) are

$$\begin{aligned} C_1 &= \frac{1}{\Delta}\left\{e^{-(1+\mathrm{i})\tau\theta}\left[\tanh\left[(1+i)ab\right]\left(L_e' - L_{e1}\right)e^{-(1+\mathrm{i})\theta}\right.\right. \\ &\quad \left.\left. + \left(\frac{\theta p\tau}{ab} + \tanh\left[(1+i)ab\right]\right)\left(1 - L_e'\right)\right]\right\}, \\ C_2 &= \frac{1}{\Delta}\left\{e^{(1+i)\tau\theta}\left[-\tanh\left[(1+i)ab\right]\left(L_e' - L_{e1}\right)e^{(1+\mathrm{i})\theta}\right.\right. \\ &\quad \left.\left. + \left(\frac{\theta p\tau}{ab} + \tanh\left[(1+i)ab\right]\right)\left(1 - L_e'\right)\right]\right\}, \end{aligned} \tag{C.5}$$

with

$$\begin{aligned} \Delta &= \frac{2\theta p\tau}{ab}\cosh\left[(1+i)\theta\right] + 2\tanh\left[(1+i)ab\right]\sinh\left[(1+i)\theta\right], \\ p &= \frac{K'}{K_1}, \\ \tau &= \frac{b}{b'}. \end{aligned} \tag{C.6}$$

Data Availability

The data used to support the findings of this study are included within the article.

Disclosure

This article was modified based on the master thesis of Mr. Zongzhong Song.

Conflicts of Interest

The authors declare that they have no conflicts of interest.

Acknowledgments

This work was supported by the Key Program of the National Natural Science Foundation of China (Grant No. 41430641) and the National Basic Research Program of China ("973" Program, Grant No. 2015CB452902). This work was also sponsored by Guangdong Provincial Key Laboratory of Soil and Groundwater Pollution Control (No. 2017B030301012) and State Environmental Protection Key Laboratory of Integrated Surface Water-Groundwater Pollution Control.

References

[1] C. E. Jacob, "Flow of groundwater," in *Engineering Hydraulics*, H. Rouse, Ed., pp. 321–386, John Wiley, New York, NY, USA, 1950.

[2] J. G. Ferris, *Cyclic Fluctuations of Water Level as a Basis for Determining Aquifer Transmissibility*, IASH Publ, 1951.

[3] P. Banerjee, D. Sarwade, and V. S. Singh, "Characterization of an island aquifer from tidal response," *Environmental Geology*, vol. 55, no. 4, pp. 901–906, 2008.

[4] P. A. Carr and G. S. van der Kamp, "Determining aquifer characteristics by the tidal method," *Water Resources Research*, vol. 5, no. 5, pp. 1023–1031, 1969.

[5] E. S. Carol, E. E. Kruse, J. L. Pousa, and A. R. Roig, "Determination of heterogeneities in the hydraulic properties of a phreatic aquifer from tidal level fluctuations: a case in Argentina," *Hydrogeology Journal*, vol. 17, no. 7, pp. 1727–1732, 2009.

[6] C. Drogue, M. Razack, and P. Krivic, "Survey of a coastal karstic aquifer by analysis of the effect of the sea-tide: example of the Kras of Slovenia, Yugoslavia," *Environmental Geology and Water Sciences*, vol. 6, no. 2, pp. 103–109, 1984.

[7] A. D. Erskine, "The effect of tidal fluctuation on a coastal aquifer in the UK," *Ground Water*, vol. 29, no. 4, pp. 556–562, 1991.

[8] A. Pandit, C. C. EI-Khazen, and S. P. Sivaramapillai, "Estimation of hydraulic conductivity values in a coastal aquifer," *Ground Water*, vol. 29, no. 2, pp. 175–180, 1991.

[9] M. E. Series, "Determining the mean hydraulic gradient of ground water affected by tidal fluctuations," *Ground Water*, vol. 29, no. 4, pp. 549–555, 1991.

[10] G. Van der Kamp, "Tidal fluctuations in a confined aquifer extending under the sea," in *24th Proceedings of the International Geological Congress*, pp. 101–106, Montreal, Canada, 1972.

[11] G. M. Li and C. X. Chen, "Determining the length of confined aquifer roof extending under the sea by the tidal method," *Journal of Hydrology*, vol. 123, pp. 97–104, 1991.

[12] J. J. Jiao and Z. H. Tang, "An analytical solution of groundwater response to tidal fluctuation in a leaky confined aquifer," *Water Resources Research*, vol. 35, no. 3, pp. 747–751, 1999.

[13] H. L. Li and J. J. Jiao, "Analytical studies of groundwater-head fluctuation in a coastal confined aquifer overlain by a semi-permeable layer with storage," *Advances in Water Resources*, vol. 24, no. 5, pp. 565–573, 2001.

[14] H. L. Li and J. J. Jiao, "Tide-induced groundwater fluctuation in a coastal leaky confined aquifer system extending under the sea," *Water Resources Research*, vol. 37, no. 5, pp. 1165–1171, 2001.

[15] D. S. Jeng, L. Li, and D. A. Barry, "Analytical solution for tidal propagation in a coupled semi-confined/phreatic coastal

aquifer," *Advances in Water Resources*, vol. 25, no. 5, pp. 577–584, 2002.

[16] H. L. Li and J. J. Jiao, "Analytical solutions of tidal groundwater flow in coastal two-aquifer system," *Advances in Water Resources*, vol. 25, no. 4, pp. 417–426, 2002.

[17] G. H. Li, H. L. Li, and M. C. Boufadel, "The enhancing effect of the elastic storage of the seabed aquitard on the tide-induced groundwater head fluctuation in confined submarine aquifer systems," *Journal of Hydrology*, vol. 350, no. 1-2, pp. 83–92, 2008.

[18] L. Guarracino, J. Carrera, and E. Vázquez-Sune, "Analytical study of hydraulic and mechanical effects on tide-induced head fluctuation in a coastal aquifer system that extends under the sea," *Journal of Hydrology*, vol. 450-451, pp. 150–158, 2012.

[19] X. J. Wang, H. L. Li, L. Wan, F. T. Liu, and X. W. Jiang, "Loading effect of water table variation and density effect on tidal head fluctuations in a coastal aquifer system," *Water Resources Research*, vol. 48, no. 9, article W09501, 2012.

[20] C. Y. Wang, H. L. Li, L. Wan, X. J. Wang, and X. W. Jiang, "Closed-form analytical solutions incorporating pumping and tidal effects in various coastal aquifer systems," *Advances in Water Resources*, vol. 69, pp. 1–12, 2014.

[21] J. Y. Gao, X. J. Wang, Y. Zhang, and H. L. Li, "Estimating submarine groundwater discharge and associated nutrient inputs into Daya Bay during spring using radium isotopes," *Water Science and Engineering*, vol. 11, no. 2, pp. 120–130, 2018.

[22] J. J. Jiao, L. Shi, X. Kuang, C. M. Lee, W. W. S. Yim, and S. Yang, "Reconstructed chloride concentration profiles below the seabed in Hong Kong (China) and their implications for offshore groundwater resources," *Hydrogeology Journal*, vol. 23, no. 2, pp. 277–286, 2015.

[23] A. C. Knight, A. D. Werner, and L. K. Morgan, "The onshore influence of offshore fresh groundwater," *Journal of Hydrology*, vol. 561, pp. 724–736, 2018.

[24] V. E. A. Post, J. Groen, H. Kooi, M. Person, S. Ge, and W. M. Edmunds, "Offshore fresh groundwater reserves as a global phenomenon," *Nature*, vol. 504, no. 7478, pp. 71–78, 2013.

[25] S. C. Solórzano-Rivas and A. D. Werner, "On the representation of subsea aquitards in models of offshore fresh groundwater," *Advances in Water Resources*, vol. 112, pp. 283–294, 2018.

[26] X. Yu and H. A. Michael, "Offshore pumping impacts onshore groundwater resources and land subsidence," *Geophysical Research Letters*, vol. 46, no. 5, pp. 2553–2562, 2019.

[27] M.-H. Chuang and H.-D. Yeh, "An analytical solution for the head distribution in a tidal leaky confined aquifer extending an infinite distance under the sea," *Advances in Water Resources*, vol. 30, no. 3, pp. 439–445, 2007.

[28] M. S. Hantush and C. E. Jacob, "Non-steady radial flow in an infinite leaky aquifer," *Transactions, American Geophysical Union*, vol. 36, no. 1, pp. 95–100, 1955.

[29] D. O. Gregg, "An analysis of ground-water fluctuations caused by ocean tides in Glynn County, Georgia," *Ground Water*, vol. 4, no. 3, pp. 24–32, 1966.

[30] M. L. Merritt, *Estimating Hydraulic Properties of the Floridan Aquifer System by Analysis of Earth-Tide, Ocean-Tide, and Barometric Effects, Collier and Hendry Counties, Florida*, U.S Geological Survey: Water-Resources Investigations Report 2003-4267, 2004.

[31] N. T. Sheahan, "Injection/extraction well system-a unique seawater intrusion barrier," *Ground Water*, vol. 15, no. 1, pp. 32–50, 1977.

[32] V. Batu, *Aquifer Hydraulics: A Comprehensive Guide to Hydrogeologic Data Analysis*, Wiley, New York, NY, USA, 1998.

[33] S. P. Neuman and P. A. Witherspoon, "Field determination of the hydraulic properties of leaky multiple aquifer systems," *Water Resources Research*, vol. 8, no. 5, pp. 1284–1298, 1972.

[34] K. J. Dawson and J. D. Istok, *Aquifer Testing: Design and Analysis of Pumping and Slug Tests*, Lewis Publishers, Boca Raton, FL, USA, 1991.

[35] C. X. Chen and J. J. Jiao, "Numerical simulation of pumping tests in multilayer wells with non-Darcian flow in the wellbore," *Ground Water*, vol. 37, no. 3, pp. 465–474, 1999.